7-20-2022 1:30 PM

Development of a Cold Model Fuild Coker Pilot Plant

Jessica A. Godin, *The University of Western Ontario*

Supervisor: Briens, Cedric L., *The University of Western Ontario*
Co-Supervisor: Pjontek, Dominic, *The University of Western Ontario*
A thesis submitted in partial fulfillment of the requirements for the Master of Engineering Science degree in Chemical and Biochemical Engineering

Abstract

Fluid Coking™ is an upgrading process used to produce higher-value products from heavy hydrocarbons through thermal cracking. A Hot Pilot Plant is being designed for potential use to optimize commercial Fluid Cokers.

A Cold Model Fluid Coker was operated in this thesis to identify design limitations restricting operation at the required conditions. Design changes were implemented, and their impact on the system fluid dynamics were characterized. Successful operation of at required conditions was demonstrated.

Pressure measurements provided rapid feedback on potential issues. Models for bed expansion and entrainment flux were developed, which can be used to extrapolate to the Hot Model operating conditions. A model was developed to predict the probability of solids in the dipleg reaching a critical level, reducing solids losses. The model provided an accurate prediction of the behaviour of solids backups in the dipleg and can be used in the Hot Model Pilot Plant.

Keywords

Recirculating Fluidized bed, Fluid Coker, Entrainment

Summary for Lay Audience

Bitumen, a component present in oil sands, requires upgrading though thermal cracking to produce more valuable, lighter products. The Fluid Coking™ process utilizes two fluidized beds, units consisting of gas injected into a bed of small particles to provide liquid-like behaviour to the gas solids mixture.

A Fluid Coker Pilot Plant that will operate at conditions used in commercial Fluid Coker (a "Hot Model") is being designed for potential use in Alberta. It will be used to develop and test methods to monitor important features of commercial Fluid Cokers.

The purpose of this thesis was to operate a Fluid Coker Pilot Plant at room temperature (a "Cold Model") to identify limitations to the original design and provide insight prior to the construction of the Hot Model. Phenomena that would prevent operation at the required plant conditions were studied to suggest design improvements. The impact of design changes were characterized to demonstrate successful operation at required conditions in the Cold Model.

A pressure measurement system with a fast response time was developed to provide rapid feedback on potential operating issues. Models for bed expansion and entrainment flux were found for the Cold Model, which can be used in the design stage or to estimate the entrainment rate under other operating conditions. A model to predict the probability of solids in the dipleg reaching a critical level that would results in excessive solids losses from the Cold Model was developed.

Co-Authorship Statement

Chapter 1: Jessica Godin prepared the original manuscript, including collecting references and writing the manuscript. Prof. Cedric Briens and Prof. Dominic Pjontek reviewed the manuscript.

Chapter 2: Jessica Godin prepared the original manuscript, including collecting references and writing the manuscript. Prof. Cedric Briens and Prof. Dominic Pjontek reviewed the manuscript.

Chapter 3: Jessica Godin conducted the experimental work, analyzed the data and prepared the original manuscript, including collecting references and writing the manuscript. Prof. Cedric Briens and Prof. Dominic Pjontek reviewed the manuscript. Francisco Sanchez Careaga wrote the code to collect the data.

Chapter 4: Jessica Godin conducted the experimental work, analyzed the data and prepared the original manuscript, including collecting references and writing the manuscript. Prof. Cedric Briens and Prof. Dominic Pjontek reviewed the manuscript. Francisco Sanchez Careaga wrote the code to collect the data.

Chapter 5: Jessica Godin conducted the experimental work, analyzed the data and prepared the original manuscript, including collecting references and writing the manuscript. Prof. Cedric Briens and Prof. Dominic Pjontek reviewed the manuscript. Francisco Sanchez Careaga wrote the code to collect the data.

Chapter 6: Jessica Godin prepared the original manuscript, including collecting references and writing the manuscript. Prof. Cedric Briens and Prof. Dominic Pjontek reviewed the manuscript.

Acknowledgments

Over the course of my Masters program, I met many people who provided support, constructive criticism and offered helpful assistance and expertise. I could not have written this thesis without them.

I would like to thank both my supervisors, Prof. Cedric Briens and Prof. Dominic Pjontek. Thank you for providing me the opportunity to work at the *Institute for Chemicals and Fuels from Alternative Resources (ICFAR)*, and thank you for your support, advice and expert proof reading skills during the course of this research.

I would like to express my gratitude to the entire team of engineers at Syncrude Canada Ltd., especially Dr. Jennifer McMillan. Your guidance and insight was always appreciated in guiding this research to be as close as possible to industrial needs.

I would also like to thank Dr. Francisco Javier Sanchez Careaga for his invaluable help in developing the systems needed for this research to progress.

I would like to thank Syncrude Canada Ltd. and the Natural Science and Engineering Research Council (NSERC) of Canada for their financial support.

I would like to thank everyone who contributed to this research work at University Machine Shop (UMS) at the University of Western Ontario, especially Cody Ruthman, for all their help with unit modifications.

I would like to acknowledge my friends and colleagues at ICFAR. Davin, Jenny, Yuan and Yohann, thank you for all the laughs we could enjoy together.

Finally, I would like to express my deepest appreciation to my husband, Andrew Miller. Thank you for always pushing me to better myself, and never questioning my ability to succeed in this research work. Without you this thesis would not have been possible.

Table of Contents

List of Tables

List of Figures

Nomenclature

$A_{Cyclone\ Inlet}$	Cross sectional area of the cyclone inlet (m^2)
A_{Probe}	Cross sectional area of the probe mouth, (m^2)
b	Slope coefficient
d_b	Bubble diameter, (m)
CV	Coefficient of variation
C_d	Orifice coefficient
D	Orifice diameter (m)
D_d	Diameter of dipleg (m)
D_e	Effective orifice diameter (m)
d_{pc}	Maximum entrainable particle size (m)
D_{pi}	Particle diameter in size cut i (m)
d_{psm}	Sauter Mean diameter of the solids (Fluid Coke) (m)
F	Entrainment flux (kg/m^2s)
F_{c0}	Flux of clusters ejected from the bed surface (kg/m^2s)
F_e	Flow rate of solids entering dipleg (kg/s)
$F_{exhaust}$	Flow rate of particles escaping cyclone (kg/s)
F_{inlet}	Flow rate of particles entering cyclone (kg/s)
F_o	Flow rate of solids in dipleg (kg/hr)
F_s	Flow rate of solids measured in riser (kg/hr)
$F_{s,avg}$	Average flow rate of solids (kg/hr)
F_∞	Entrainment flux above the TDH (kg/m^2s)
g	The gravity on Earth, ($9.81\ m/s^2$)
$H_{bed,ref}$	Reference bed height (m)
$H_{Defluidized}$	Bed height when not fluidized (m)

H_e	Height of emulsion (m)
H_s	Height of the bed above the bottom of the dipleg (m)
L_{dipleg}	Length of the dipleg (from the cyclone bottom to the elbow termination) (m)
M_s	Mass of solids in dipleg (kg)
$M_{s,i}$	Mass of solids in dipleg at time i (kg)
$M_{s,i-1}$	Mass of solids in dipleg at time i-1 (kg)
P_0	Initial pressure (Pa)
P_∞	Pressure as t approaches infinity (Pa)
P_i	Pressure in dipleg (Pa)
P_o	Pressure in dipleg outlet (Pa)
$P_{o,i}$	Pressure in dipleg outlet at time i (Pa)
P(t)	Pressure at time, t (Pa)
$Q_{Sampling}$	Volumetric gas flow rate in isokinetic in probe mouth (m^3/s)
TDH	Transport Disengagement Height (m)
U_B	Bubble velocity (m/s)
U_{ej}	Ejection velocity (m/s)
u_G	Superficial gas velocity (m/s)
$U_{G,Ax}$	Superficial gas velocity of loop seal tap A_x (m/s)
$U_{G,AERATION}$	Superficial gas velocity provided by aeration (m/s)
$U_{G,\ Heater}$	Superficial gas velocity in Heater (m/s)
$U_{G,Downleg}$	Superficial gas velocity in Heater to Reactor transfer line downleg (m/s)
$U_{G,\ Reactor}$	Superficial gas velocity in Reactor (m/s)
$U_{G,Slug}$	Slug velocity (m/s)
$U_{G,Upleg}$	Superficial gas velocity in Heater to Reactor transfer line upleg (m/s)
U_{mf}	Minimum fluidization velocity (m/s)
U_{mt}	Minimum turbulent velocity (m/s)

W_s	Flux of solids in the dipleg (kg/m^2s)
x_B	Fraction of bed volume occupied by bubbles
z	Height in the freeboard above the bed surface (m)
z_c	Distance of solids in the dipleg from the bottom of the cyclone (m)
$z_{c,i}$	Distance of solids in the dipleg from the bottom of the cyclone at time i (m)
z_d	Measured level of solids in the dipleg above the reference height (m)
$z_{d,0}$	Initial level of solids in dipleg (m)
$z_{d,i}$	Level of solids in dipleg at time i (m)
α	Angle of internal friction (degrees)
α_A	Empirical orifice parameter used in dipleg solids model
β	Coefficient for mass of solids in dipleg cross-section
ΔP_c	Cyclone pressure drop (Pa)
Δt	Time interval, s
ε_e	Voidage of emulsion
ε_{mf}	Voidage at minimum fluidization
$\eta_{cyclone}$	Cyclone efficiency
μ_g	Gas viscosity (kg/m·s)
ρ_{Bed}	Bed density (kg/m^3)
ρ_B	Bulk powder density (kg/m^3)
ρ_D	Density of solids in dipleg (kg/m^3)
ρ_e	Emulsion phase density (kg/m^3)
ρ_g	Density of gas (kg/m^3)
ρ_{mf}	Density at minimum fluidization (kg/m^3)
ρ_p	Particle density (kg/m^3)
σ	Standard Deviation, various units
τ	Time constant, s

List of Appendices

Chapter 1

1 Introduction

The purpose of thesis was to operate a cold model Fluid Coker pilot plant to identify limitations to the original design and provide insight prior to the construction of a Hot Model Fluid Coker pilot plant. Phenomena that would prevent operation at the required plant conditions were studied to suggest design improvements. The impact of design changes were characterized to demonstrate successful operation at required conditions in the Cold Model.

After a general introduction to the Fluid Coking process, this chapter highlights the need for a Hot Model Fluid Coker Pilot Plant, and the requirements for the Cold Model. The research objectives of this thesis are then presented.

1.1 Oil Sands and Bitumen

While renewable sources of energy continue to grow rapidly, the uneven economic recovery from the Covid-19 induced recession has strained the energy market, with 2021 seeing a rebound in coal and oil use worldwide. The International Energy Agency predicts the demand for fossil fuels will increase for at least the next decade and remain high until 2050 as global energy demands outpace alternative fuel sources (IEA, 2021).

Conventional light oil reserves are diminishing worldwide, increasing the use of heavy oil reserves to meet global energy demands (Grey, 2015). Canada possesses the third largest reserves of heavy oil in the world, providing a reliable source of energy to North America, Europe and Asia. The oil sands, primarily located in Alberta, contain an estimated 170 billion barrels of bitumen recoverable with current technologies (The Canadian Association of Petroleum Producers (CAAP), 2019). Oil sands are composed of 10-12 wt.% bitumen, a black highly viscous oil, with the remainder composed of sand, clay, and water. Bitumen cannot be processed

in its raw form, due to higher concentrations of high molecular weight species and heteroatomic species such as nitrogen, sulphur, and metals (Soundararajan, 2001). To be processed in conventional refineries, it instead must be upgraded. Upgrading heavy oil increases the natural resource value, eases its transportation, and allows it to be further processed at existing refineries and petrochemical plants (Nikiforuk, 2008; Percy, 2012; Little, 2015).

Conventional thermal cracking commercial processes used to upgrade bitumen to lighter hydrocarbon fractions are: Delayed Coking, Flexicoking™, and Fluid Coking™. Due to its high reliability, flexibility, continuous products, and low greenhouse gas emissions, Fluid Coking™ is the preferred process for bitumen cracking (Speight, 2014). Synthetic crude produced by Fluid Cokers represents between 15 and20 % of Canada's combined oil production from conventional sources and oil sands to produce about 400,000 barrels/day of light, synthetic crude oil. The Fluid Cokers of Syncrude in Northern Alberta produced around 314,600 barrels per day in 2019 (Alberta Energy Regulator, 2021).

1.2 Fluid Coking™ Process

The Fluid Coker system consists of two vessels, a fluidized bed reactor connected to a fluidized bed burner, shown in Figure **1-1**. Coke particles are partially combusted with air in the burner to heat them to 600 to 680° C. Through pneumatic transportation, the "hot" coke particles are introduced at the top of the reactor section, where bitumen or heavy oil is sprayed with atomization steam and undergoes thermal cracking at a temperature ranging from 500-550°C, producing condensable vapours, non-condensable gases, and solid coke. "Cold" coke particles will eventually move down the reactor back to the burner to re-start the cycle (Downing and North, 1958). Attrition nozzles above the stripper sheds maintain the particle size distribution to provide good fluidization quality and good operation of the coke transfer lines while moderating particle losses in the reactor and burner (Li et al. 2012b).

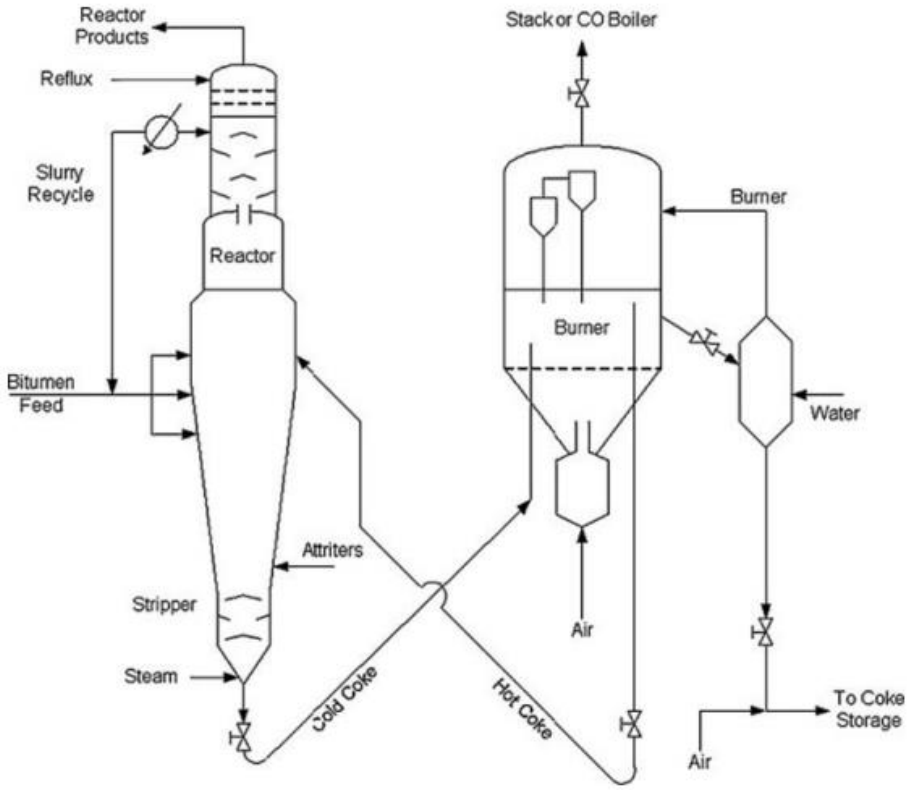

Figure 1-1. Simplified Fluid Coking^{TM} process (Prociw, 2014).

The Fluid Coker reactor can be divided into three sections:

- The reaction section where bitumen is atomized through spray nozzles using steam, with a goal to promote uniform coating of fluidized particles for a stable cracking reaction.

- The scrubber section where vapors produced through thermal cracking of bitumen flow to the top of the reactor, through the cyclones to remove entrained coke particles, and return them to the bed. Vapours pass through a scrubber to remove remaining fines and condense and recycle remaining heavy residues. The average superficial velocity of the rising gases is ranging from 0.3 m/s to 1.0 m/s depending upon the coke size, to maintain fluidization (Pfeiffer, 1959, Li et al., 2012a).

- The stripper section where “cold” coke particles that have lost their heat due to the endothermic cracking reactions and vaporization circulate down through the stripper section towards the burner. The stripper uses steam to enhance the removal of hydrocarbon vapours moving with the down-flowing fluid coke.

1.3 Pilot Plant Studies

Syncrude Canada Ltd. is designing a novel hot Fluid Coker pilot plant, in which bitumen will be converted via thermal cracking, and all products characterized at their research facilities in Edmonton, Alberta, Canada. The Hot Pilot Plant will provide information to allow Syncrude to adapt their commercial plant to the evolving economic and regulatory environments. The Hot Model Pilot Plant is being designed to provide results that are representative of Syncrude’s commercial Fluid Cokers. Additionally, the pilot plant may be used to develop and test methods to monitor several other important features of commercial cokers, including the spray nozzles, fluidization quality, coke deposits and coke transfer lines between the reactor and burner.

Studies on Fluid Cokers typically use smaller-scale equipment at room temperature or computational fluid dynamics (CFD) simulations (Briens and McMillan, 2021). Many researchers have explored bed hydrodynamics (Cui et al., 2006, Cochet et al., 2020; Sanchez Careaga, 2013; Song et al., 2004; Song et al, 2006, Li et al., 2012a/b, Xing, 2020), agglomerate break-up (Sun et al., 2020; Shi et al., 2018), entrainment (Ayatollahi, 2016), particle tracking (Cochet, 2021), spray nozzles (Joness, 2019; Prociw, 2014) and liquid distribution in the bed (Li, 2021; Li, 2016). The two types of studies were reconciled by verifying that CFD models could predict results from the cold models (Li et al., 2012a/b).

Several challenges arise with cold model studies:

- Using proper geometric scaling.
- Proper simulation of hydrodynamics at coker conditions.
- Accounting for the effect of spray jets on hydrodynamics.

Studies at the same operating conditions as commercial cokers with spray jets are more representative than similar studies at ambient conditions without injection. Therefore, the Hot Model Fluid Coker will provide valuable information for use on the commercial coker. To provide operational insight and explore design aspects of the Hot Fluid Coker pilot plant, a Cold Model was constructed and operated. The Cold Model has been operated to investigate and design for better hydrodynamics, solids circulation and entrainment, and to mitigate technical risks in the hot pilot.

1.4 Requirements for Operation

The following conditions were required for ideal operation of the Cold Model:

- The Heater vessel should operate at a freeboard superficial gas velocity ranging from 0.05 to 0.15 m/s with a nominal operating condition of 0.1 m/s at a minimum defluidized bed height of 0.65 m.
- The Reactor vessel should operate at a freeboard superficial gas velocity ranging from 0.1 to 1.2 m/s , with a nominal operating condition of 0.6 m/s at a minimum defluidized bed height of 1.6 m.
- Under the above range of conditions:
    - The Reactor and Heater fluidized beds should be well fluidized.
    - Losses of entrained solids from the cyclones should be less than 0.01 kg/min, with no pulses in entrained solids.
    - Stable recirculation rates between 3000 – 4000 kg/hr should be achieved.
    - No gas should flow from the reactor to the heater through the solids return line.

1.5 Research Objectives

The main objectives of the research described in this thesis were:

- Operate a Cold Model Fluid Coker Pilot Plant to identify limitations to the original design.
- Study phenomena that would prevent operation at the required plant conditions to suggest design improvements.
- Characterize the impact of design changes.
- Demonstrate successful operation of Cold Model at required conditions.
- Develop measurement techniques for use in both the Cold and Hot Model Pilot Plants.
- Study entrainment above the TDH in a fluidized bed of coke particles at high gas velocities.
- Develop a model to predict the probability of solids in the dipleg reaching a critical level.

1.6 References

Alberta Energy Regulator. (2022) Upgraded Bitumen Production. [cited 2022 04.24]; Available from: https://www.aer.ca/providing-information/data-and-reports/statisticalreports/st98/crude-bitumen/production/upgraded-bitumen.

Ayatollahi, S. (2016). *Particle Entrainment Studies From Dry and Wet Bed* (Issue June). MESc Thesis, Western University, London, Ontario, Canada

Briens, C., & McMillan, J. (2021). Review of Research Related to Fluid Cokers. *Energy and Fuels*, *35*(12), 9747–9774. https://doi.org/10.1021/acs.energyfuels.1c00764

Cochet, Y. (2021). *Mitigation of fouling and liquid losses in a Fluid Coker™: Influence of operating conditions and internals on wet-agglomerates contribution to liquid carry-under*. The University of Western Ontario.

Cochet, Y.; Briens, C.; Berruti, F.; McMillan, J.; Sanchez Careaga, F. J. (2020). Impact of column geometry and internals on gas and particle flows in a fluidized bed with downward solids circulation: Effect of lateral injection profile and baffles. *Powder Technol*. *372*, 275−289.

Cui, H. P.; Strabel, M.; Rusnell, D.; Bi, H. T.; Mansaray, K.; Grace, J. R.; Lim, C. J.; McKnight, C. A.; Bulbuc, D. (2006). Gas and solids mixing in a dynamically scaled fluid coker stripper. *Chem. Eng. Sci. 61* (2), 388−396.

Gray, M. R. (2002). Fundamentals of bitumen coking processes analogous to granulations: A critical review. *The Canadian Journal of Chemical Engineering*, *80*(3), 393–401. https://doi.org/10.1002/CJCE.5450800308

Gray, M. R. (2015). *Upgrading Oilsands Bitumen and Heavy Oil*; University of Alberta Press: Edmonton, Alberta, Canada. p 499.

International Energy Agency, (2021). *World Energy Outlook 2021*. www.iea.org/weo

Joness, A. M. (2019) *Effect of Scale on Spray Nozzle Performance*. MESc Thesis, Western University, London, Ontario, Canada

Li, L. (2016). *Effect of Local Bed Hydrodynamics on the Distribution of Liquid in a Fluidized Bed*. MESc Thesis, Western University, London, Ontario, Canada.

Li, T., Grace, J., Bi, X., Reid, K., & Wormsbecker, M. (2012a). Numerical investigation of FLUID COKING™ units, Part I: Hydrodynamics of a scaled cold flow model. *Canadian Journal of Chemical Engineering*, *90*(2), 442–456. https://doi.org/10.1002/CJCE.20538

Li, T., Grace, J., Bi, X., Reid, K., & Wormsbecker, M. (2012b). Numerical investigation of FLUID COKING^{TM} units, Part II: Modelling of feed vaporisation. *Canadian Journal of Chemical Engineering*, *90*(2), 457–471. https://doi.org/10.1002/CJCE.20537

Li, Y. (2021). *Impact of Fluidized Bed Hydrodynamics on the Distribution of Liquid Sprayed Into the Bed*. The University of Western Ontario.

Nikiforuk, A., (2008). Tar sands: dirty oil and the future of a continent. Greystone Books/David Suzuki Foundation; 2nd edition.

Percy, K.E. (2012). Alberta oil sands: energy, industry and the environment. Elsevier; 1st edition

Prociw NA. (2014). *Effect of Nozzle Geometry on Jet Bed Interaction: Experiments with Commercial Scale Nozzles and Eroded Nozzles*. MESc Thesis, The University of Western Ontario. https://ir.lib.uwo.ca/etd/2424/

Sanchez Careaga, F. (2013). *Hydrodynamics in Recirculating Fluidized Bed Mimicking the Stripper Section of the Fluid Coker*. Ph.D. Thesis, Western University, London, Ontario, Canada.

Shi, Q.; Li, S.; Tian, S.; Huang, Z.; Yang, Y.; Liao, Z.; Sun, J.; Wang, J.; Yang, Y. (2018). Investigating Agglomeration Behaviors in High Temperature Gas-Solid Fluidized Beds with Liquid Injection. *Ind. Eng. Chem. Res.*, 57 (15), 5482−5494

Song, X., Bi, H., Jim Lim, C., Grace, J. R., Chan, E., Knapper, B., & McKnight, C. (2004). Hydrodynamics of the reactor section in fluid cokers. *Powder Technology*, *147*(1–3), 126–136. https://doi.org/10.1016/J.POWTEC.2004.09.033

Song, X., Grace, J. R., Bi, H., Lim, C. J., Chan, E., Knapper, B., & McKnight, C. (2006). Experimental simulation of the reactor section of fluid cokers: Comparison of FCC and fluid coke particles. *Canadian Journal of Chemical Engineering*, *84*(2), 161–169. https://doi.org/10.1002/cjce.5450840203

Soundararajan, S. (2001). Determination of thermal cracking kinetics of Athabasca bitumen vacuum residue. *Edmonton (AB): University of Alberta*.

Speight JG. (2014). The chemistry and technology of petroleum. 4th ed. *Boca Raton, Florida, USA: CRC Press*. ISBN: 9781439873892. https://www.crcpress.com/TheChemistry-and-Technology-of-Petroleum/Speight/p/book/9781439873892

Sun, J.; Tian, S.; Li, S.; Yang, Y.; Huang, Z.; Shi, Q.; Wang, J.; Yang, Y.; Wang, F. (2020). Experimental and Modeling Investigation of Liquid-Induced Agglomeration in a Gas-Solid Fluidized Bed with Liquid Spray. *Ind. Eng. Chem. Res*., 59 (25), 11810−11822. (51)

The Canadian Association of Petroleum Producers (CAAP). (2019). *Crude Oil Forecast, Markets and Transportation*. Calgary. https://www.capp.ca/wp-content/uploads/2019/11/CAPP-2019-Crude-Oil-Markets-and-Transportation-338794-1.pdf.

X.T. Bi, H.P. Cui, J.R. Grace, A. Kern, C.J. Lim, D. Rusnell, X.Q. Song, C. McKnight. (2004) Flooding of gas–solids counter-current flow in fluidized beds, *Ind. Eng. Chem. Res*. 43 5611–5619.

Xing, X. (Cher). (2020). *Numerical study of the effect of gas distributors and baffles on the bubble distribution, gas and solid mixing in a fluidized bed*. 292. Ph.D. Thesis, Western University, London, Ontario, Canada. https://ir.lib.uwo.ca/etd/7474

Chapter 2

2 Experimental Setup and Measurement Techniques

2.1 Cold Model Pilot Plant

Experimental measurements were required to test the Cold Model design, define and study limitations and suggest improvements. Experiments were conducted at ambient temperature (i.e., "cold" setup) using fluid coke particles provided by Syncrude Canada Ltd. The Sauter mean diameter of the particles was 130 μm, measured by a HELOS particle size analyzer. Measurements are available in "Appendix A: Fluid coke particle size distribution." The coke particle density was measured to be 1500 kg/m^3 using a pycnometer, and are classified as a Group A powder, near the boundary between Group A and Group B powders in the Geldart classification (Geldart, 1973; Song et al., 2006). They have a minimum fluidization velocity of U_{mf} = 0.008 m/s.

Fluidization gas was compressed air at room temperature, provided by compressors at the Institute for Chemicals and Fuels from Alternative Resources (ICFAR). The relative humidity of the air used is lower than 5% at room temperature (20 °C) (Li et al., 2020).

The purpose of the experiments with the Cold Model was to provide design information and identify potential limitations to the Hot Model pilot plant. The gas density and viscosity will be higher under the Hot Model Pilot Plant conditions (ρ_g = 2.05 kg/m^3; μ_g = 0.02 cp), and results obtained under cold conditions will not be representative of results expected under hot conditions. It is, therefore, key to develop measurement techniques and models that can be extrapolated from cold to hot conditions.

The hot pilot plant is not intended to be an exact scaled-down model of a commercial Fluid Coker; Fluid Coker experts designed it at Syncrude Canada to provide information that could be used to understand and optimize the operation of commercial Fluid Cokers."

2.1.1 Unit Dimensions

2.1.2 Original Cold Model Design

The original Cold Model design consisted of two fluidized bed vessels that used a standpipe and riser to circulate solids from the Reactor to the Heater vessel. Solids overflowed into a transfer line to return solids from the Heater to the Reactor. The Cold Model consisted of eight main sections that will be discussed in this section, illustrated in Figure 2-1. The overall unit dimensions are outlined in Figure 2-6.

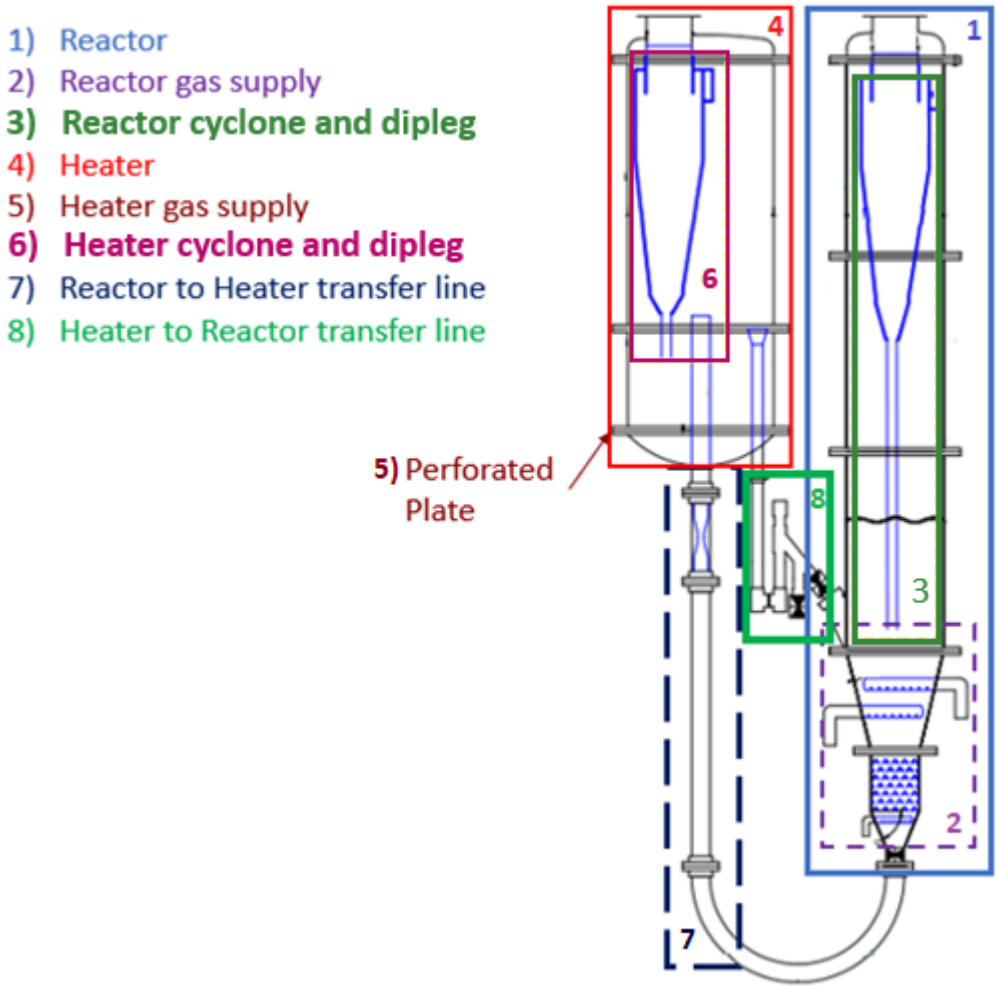

Figure 2-1. Main sections of Cold Model.

1) Reactor

The first fluidized bed used in the Cold Model was a simulated reactor section with an inside diameter of 0.6 m (24 in) and a total height of 4.9 m. Below the main cylindrical section of the Reactor was a cone with an internal angle of 57.3°, which contained the upper two gas distributors. Below the cone was a 0.3 m (12 in) diameter simulated stripper section. As solids exited the reactor, they flowed to a second cone with an internal angle of 45.9°, that contained the bottom gas distributor. A slide valve was located immediately below the second cone, used to control the flowrate of solids exiting the reactor.

2) Reactor gas supply

Three spargers were used to supply a superficial gas velocity between 0.1 and 1.2 m/s in the Reactor freeboard. The dimensions of the three spargers are shown in Figure 2-2. Sparger A and Sparger B were situated just above the stripper sheds section, and rest on the cone where the unit diameter is 0.3 m. Sparger C was situated below the stripper sheds section. All holes faced down to avoid clogging the holes. There are two main gas distributions used in this thesis, achieved by changing the amount of gas provided to the three spargers. The different gas distributions are illustrated in Figure 2-3. In the All Spargers configuration, gas supplied from a bank of sonic orifices (see Chapter 2.1.4) was supplied to all three spargers, with the control valves upstream of each sparger open 100%. In the Bottom Sparger Only configuration, the control valves to Sparger A and Sparger B were completely closed.

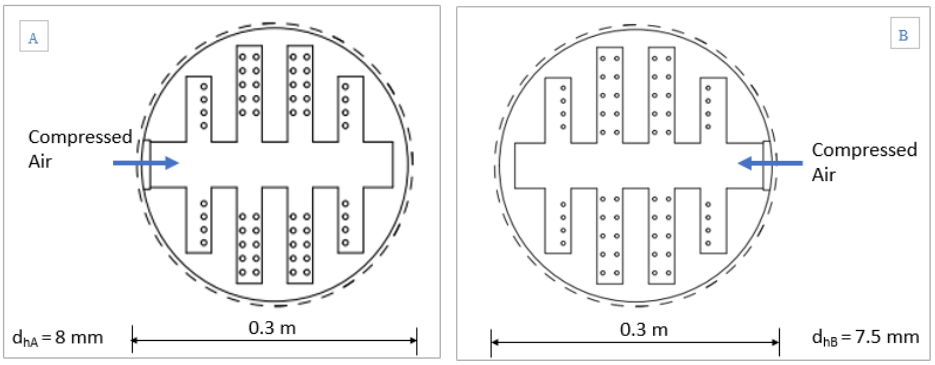

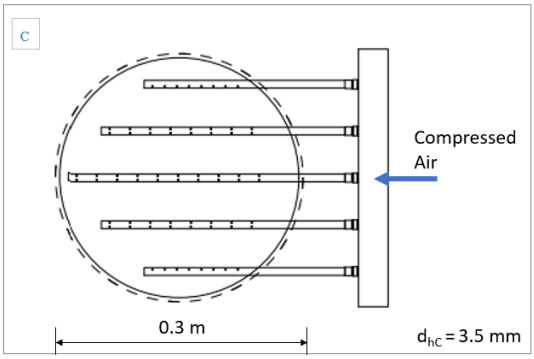

Figure 2-2. Bottom view of spargers in Reactor: A) Top of Sheds Sparger A; B) Top of Sheds Sparger B**;** C) Bottom of Sheds Sparger C.

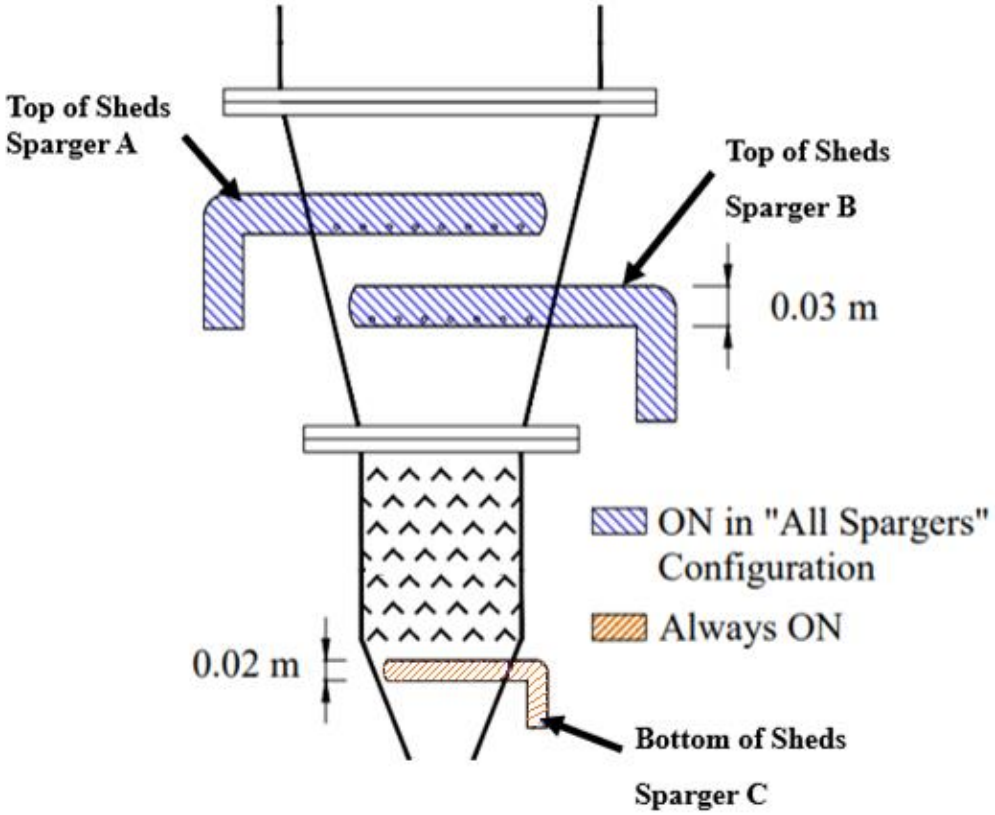

Figure 2-3. Schematic of gas distributions used in Reactor: 1) All Spargers and 2) Bottom Sparger Only for the original Cold Model design.

3) Reactor cyclone and dipleg

The reactor contained an internal cyclone with a 0.05 m (2 in) diameter dipleg to return solids to the fluidized bed. The cyclone barrel measureed 0.54 m in length, with a diameter of 0.34 m. It had a rectangular inlet measuring 0.18 m by 0.07 m. The cyclone cone measured 0.96 m with a half angle of 17°. The dipleg was 1.9 m long, and had a straight, open termination.

4) Heater

The second fluidized bed vessel was a simulated Heater with an inside diameter of 0.9 m (36 in) and a total height of 2.7 m.

5) Heater gas supply

Fluidization to the heater was provided from an independent sonic orifice (see Chapter 2.1.4) a 0.9 m diameter perforated plate with 200 3 mm holes.

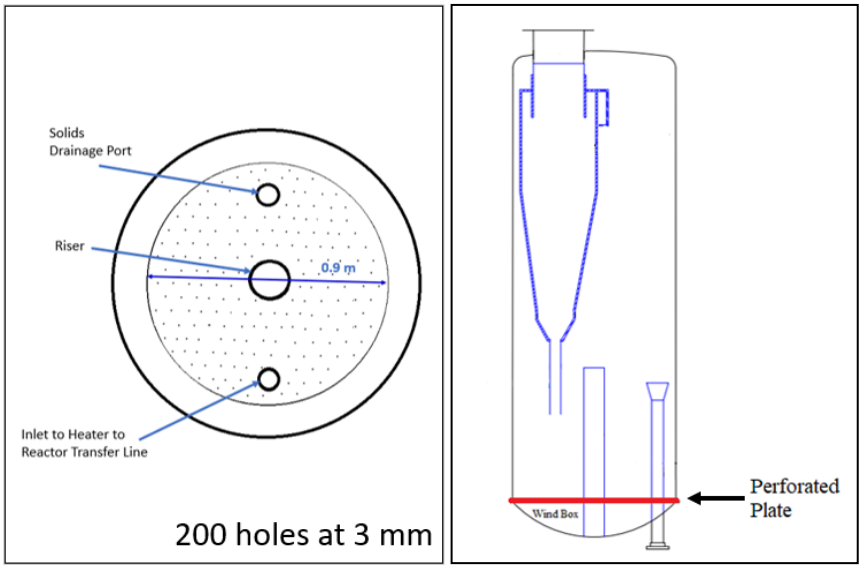

Figure 2-4. Schematic of perforated plate gas distributor in Heater.

6) Heater cyclone and dipleg

The Heater contained an internal cyclone with a 0.05 m (2 in) diameter dipleg to return solids to the fluidized bed. The cyclone barrel measured 0.48 m in length, with a diameter of 0.34 m. It had a rectangular inlet measuring 0.16 m by 0.06 m. The cyclone cone measured 0.87 m with a half angle of 16°. The dipleg was 0.25 m long, and had a straight, open termination.

7) Reactor to Heater transfer line

During recirculation, solids flowed out of the Reactor and entered the Reactor to Heater transfer line. This transfer line consisted of a 0.1 m (4 in) Sch 80 U-Bend and riser. The flowrate of solids entering the U-Bend was controlled with a gate valve at the bottom of the Reactor. The U-bend fed solids into a riser 1.8 m in length. A venturi was at the top of the riser, intended to measure the solids flow rate. Three aeration taps were installed along the U-Bend, each controlled with a separate flowmeter (8051K34, ± 6% full scale accuracy, McMaster-Carr). The riser acted as a pneumatic transport line and carried the solids up into the simulated heater fluidized bed. The outlet of the riser was 0.76 m (30 in) above the wind box, situated above the intended level of the fluidized bed in the heater of 0.64 m.

8) Heater to Reactor transfer line

The solids from the fluidized bed in the Heater overflowed into the Heater to Reactor transfer line, a 0.05 m (2 in) Sch 80 loop seal used to return solids to the Reactor fluidized bed. Figure 2-5 presents the dimensions and aeration taps of the loop seal. The inlet was 0.64 m (24.5 in) above the Heater wind box, maintaining a constant bed height due to the overflow of the solids into the inlet of the Heater to Reactor transfer line. The discharge of the transfer line was approximately 0.2 m (8 in) above the bottom of the cylindrical section of the fluidized bed reactor.

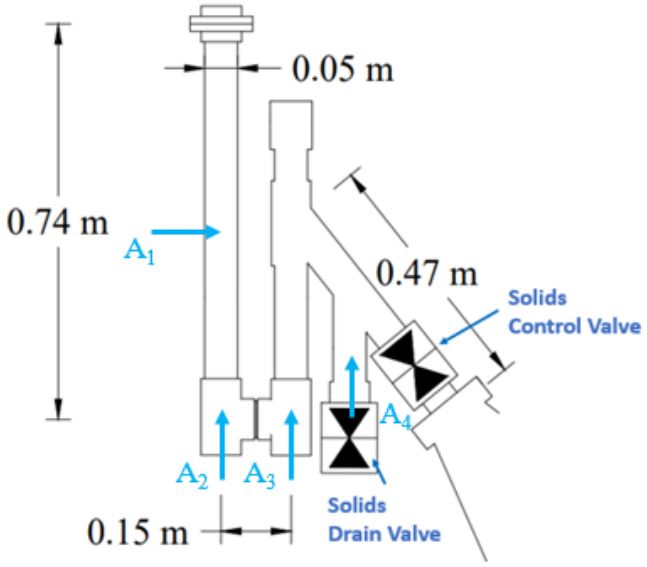

Figure 2-5. Dimensions and aeration locations of 0.05 m (2 in) loop seal.

Aeration was used to control the transfer of solids from Heater to Reactor, or to completely stop flow, controlled with separate flowmeters for each tap (A_1 & A_3: 8051K41, ±6% full scale accuracy, McMaster-Carr) (A_1: 5079K63, ± 4% full scale accuracy, McMaster-Carr) (A4: 5079K65, ±4% full scale accuracy, McMaster-Carr) The loop seal also had a valve used to completely stop solids flow into the reactor, and the valve used to drain solids from the loop seal.

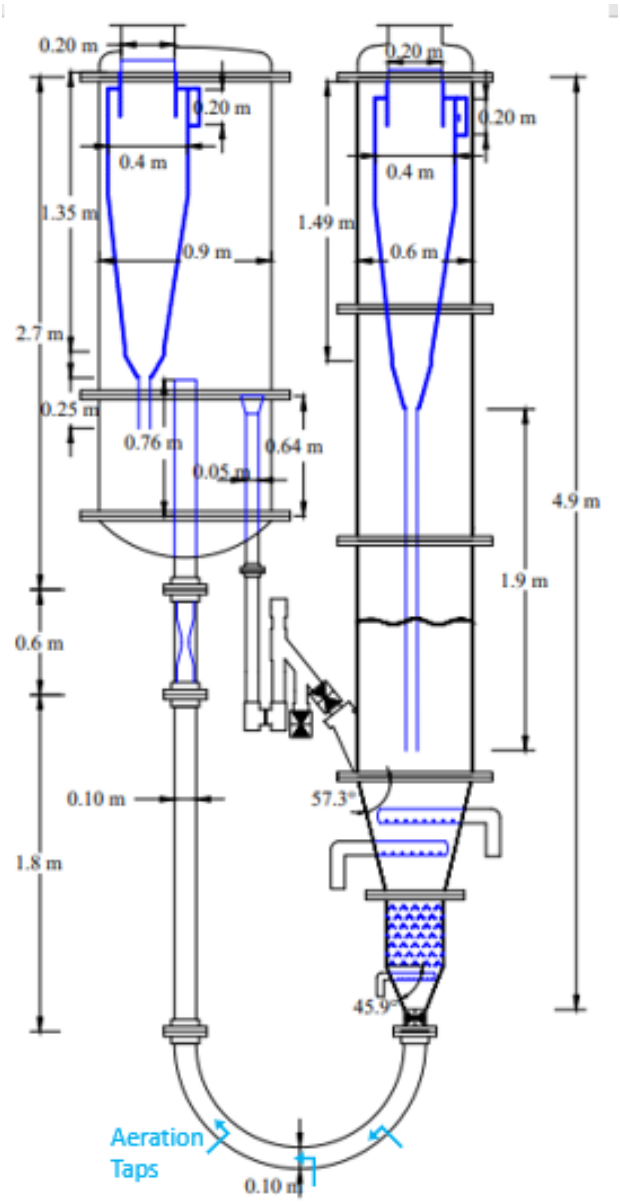

Figure 2-6. Unit dimensions for original Cold Model Configuration.

2.1.3 Summary of Unit Modifications

During preliminary testing with the original Cold Model design, the unit was found to have tight operating limits (see Chapter 4.2), and difficulties achieving high recirculation rates (see Chapter 5.2). As a result, the Cold Model was modified in two phases. The changes made to the 8 Cold Model sections are summarized below in Table 2-1. Modifications to specific unit dimensions

were recommended by an external consultant. Figure 2-12 at the end of this section shows the unit dimensions and configuration of the Cold Model after Phase 1 and 2 of modifications.

Table 2-1. Summary of modifications made to the Cold Model during Phase 1 and Phase 2.

Cold Model Section	Phase 1	Phase 2
1) Reactor	Extend freeboard by 0.9 m	Increase sheds diameter to 0.6 m
2) Reactor gas supply	NA	Modify bottom sparger to cover new cross section
3) Reactor cyclone and dipleg	1) Extend dipleg by 0.9 m 2) Add elbow termination 3) Add aeration tap	NA
4) Heater	Extend freeboard by 0.9 m	Increase overflow pipe to 0.08 m diameter
5) Heater gas supply	NA	NA
6) Heater cyclone and dipleg	1) Extend dipleg by 0.9 m 2) Add elbow termination 3) Add aeration tap	NA
7) Reactor to Heater transfer line	Venturi removed	Replace with 0.1 m (4 in) 45° angled line
8) Heater to Reactor transfer line	Replace with 0.05 m (2 in) 45° angled line	Replace with 0.08 m (3 in) diameter loop seal

1) Reactor

a. Phase 1

The freeboard of Reactor was extended by 0.9 m (36 in), to a new total height of 5.8 m. No change was made to the bottom section of the reactor containing the gas distributors or sheds, including the angles of the cones.

b. Phase 2

The diameter of the sheds section was increased to 0.6 m (24 in) to match the reactor column diameter. This eliminated one cone from the reactor, which can limit flow as cones do not build as much head as an equivalent height of fluidized bed. The second cone leading to the Reactor to Heater transfer line was increased to accommodate the larger stripper sheds, however, the internal angle of the cone remained unchanged from the original design (45.9°).

2) Reactor gas supply

a. Phase 1

No change was made to the reactor gas supply in Phase 1 of Modifications

b. Phase 2

As detailed in the original design section, the Reactor used three spargers for fluidization. The upper two spargers (A and B) were not changed in either phase of design, while the bottom sparger (C) was modified to cover the new, larger cross section of the Reactor. The hole diameter increased to 4 mm, while the tube diameter was kept constant. Figure 2-7 shows the schematic of the new bottom sparger, C. The holes were angled downward in the Cold Model.

The same two gas distributions used after Phase 2 of modifications, illustrated in Figure 2-8 In the All Spargers configuration, gas supplied from a bank of sonic orifices (see Chapter 2.1.4) was supplied to all three spargers, with the control valves upstream of each sparger open 100%. In the Bottom Sparger Only configuration, the control valves to Sparger A and Sparger B were completely closed.

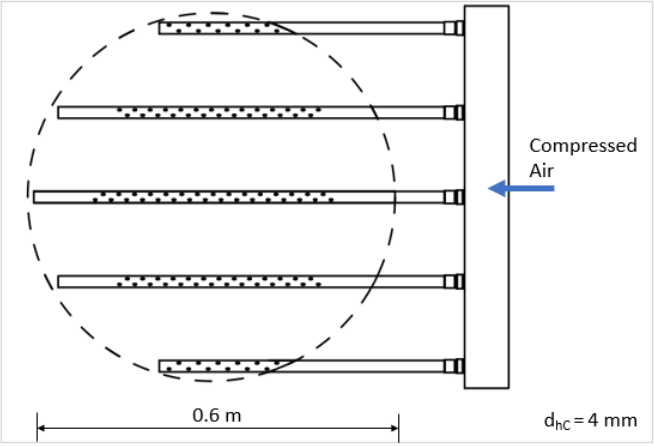

Figure 2-7. Bottom view of Bottom of Sheds Spargers C in Reactor after Phase 2 of modifications.

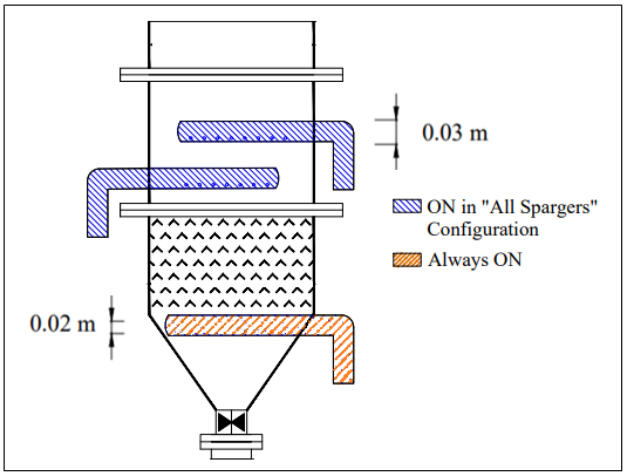

Figure 2-8. Schematic of gas distributions used in Reactor: 1) All Spargers and 2) Bottom Sparger Only after Phase 2 of modifications.

3) Reactor cyclone and dipleg

a. Phase 1

To maintain the immersion depth of the cyclone dipleg in the Reactor, the dipleg was also extended by 0.9 m (36 in), to a new total length of 2.8 m. The dipleg termination was modified from a straight pipe to a 90° elbow, with an aeration tap 2.5 cm (1 in) above the elbow.

b. Phase 2

No changes were made to the Reactor cyclone or dipleg in Phase 2 of modifications.

4) Heater

a. Phase 1

The freeboard of the Heater was extended by 0.9 m, to a new total height of 3.6 m. No change was made to the bottom section of the reactor containing the gas distributors or sheds, including the angles of the cones.

b. Phase 2

The overflow pipe that feeds solids from the Heater fluidized bed to the Heater to Reactor transfer line was increased in diameter from 0.05 m to 0.08 m. The height was maintained at a constant level, 0.64 m above the windbox.

5) Heater gas supply

a. Phase 1

No changes were made to the Heater gas supply during Phase 1 of modifications.

b. Phase 2

No changes were made to the Heater gas supply during Phase 2 of modifications.

6) Heater cyclone and dipleg

a. Phase 1

To maintain the immersion depth of the cyclone dipleg in the Heater, the dipleg was also extended by 0.9 m (36 in), to a new total length of 1.16 m. The dipleg termination was modified from a straight pipe to a 90° elbow, with an aeration tap 2.5 cm (1 in) above the elbow.

b. Phase 2

No changes were made to the cyclone or cyclone dipleg in Phase 2 of modifications.

7) Reactor to Heater transfer line

a. Phase 1

The venturi was removed and replaced with a spool piece with an ID of 0.1 m (4 in). The venturi increased the pressure drop required to seal the Heater to Reactor transfer line down-leg and restricted flow in the riser, so removal was theorized to improve the solids recirculation rate. The spool piece facilitated the replacement of the venturi for future testing if desired. The solids flowrate in the riser was calibrated using pressure measurements in the riser, below the new spool piece. The method used for calibration can be seen in Appendix C: Solids Flowrate Calibration. Figure 2-9 shows the calibration between riser pressure drop and solids flowrate used for recirculation.

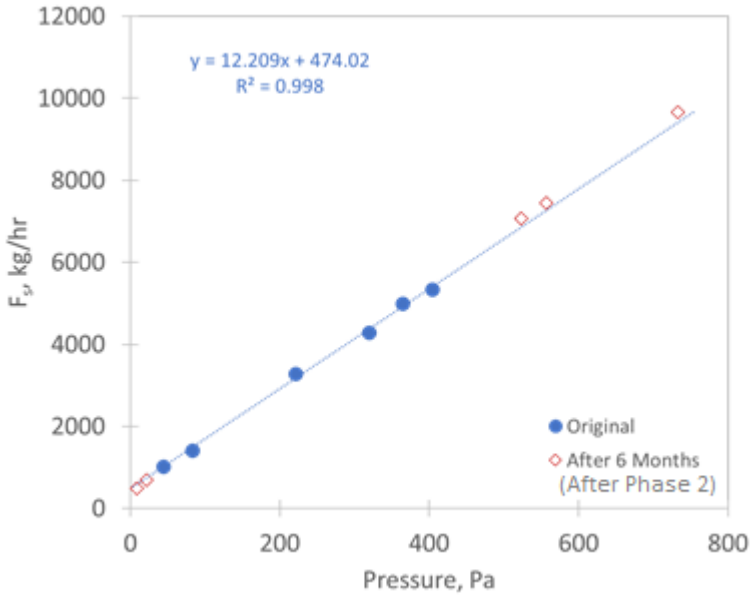

Figure 2-9. Solids flowrate calibration using riser pressure drop.

b. Phase 2

The Reactor to Heater transfer line U-Bend was replaced with a 45° angled line with a diameter of 0.1 m (4 in). U-Bend up-legs have more pressure loss than angled lines, so the change was theorized to facilitate high solids recirculation rates. Additionally, this modification simplified the system, as the 45° angled line did not require aeration to operate. The same calibration for solids flowrate was used in Phase 1 and Phase 2.

8) Heater to Reactor transfer line

a. Phase 1

The 0.05 m (2 in) loop seal was replaced with a 0.05 (2 in) 45° angled line to allow ease of operation prior to the Phase 2 modifications to the solids transfer lines. The dimensions, control valves and aeration tap of the angled line are presented below in Figure 2-10. The angled line removed the need for multiple aeration taps and can be

operated with aeration in the vertical down-leg only, using a dedicated flowmeter (8051K41, ±6% full scale accuracy, McMaster-Carr)

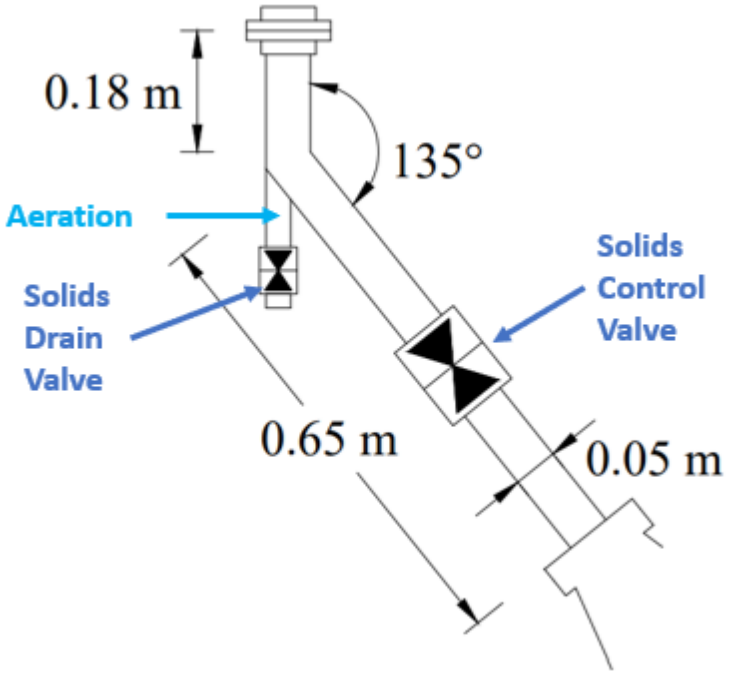

Figure 2-10. Dimensions of 0.05 m (2 in) diameter 45° angled line.

b. Phase 2

To reduce the solids flux through the transfer line and allow higher solids recirculation rates in the Cold Model, the transfer line was increased to a diameter of 0.08 m (3 in). The diameter was increased to 0.08 m (3 in) while the height above the wind box remained constant. As previously noted, under certain conditions angled lines cannot provide a dense phase of solids, allowing gas to flow from the Reactor to the Heater. Therefore, the new 0.08 m (3 in) transfer line design was a loop seal, shown below in Figure 2-11. Five flowmeters (8051K34, ±6% full scale accuracy, McMaster-Carr) are used to provide aeration to the different aeration taps.

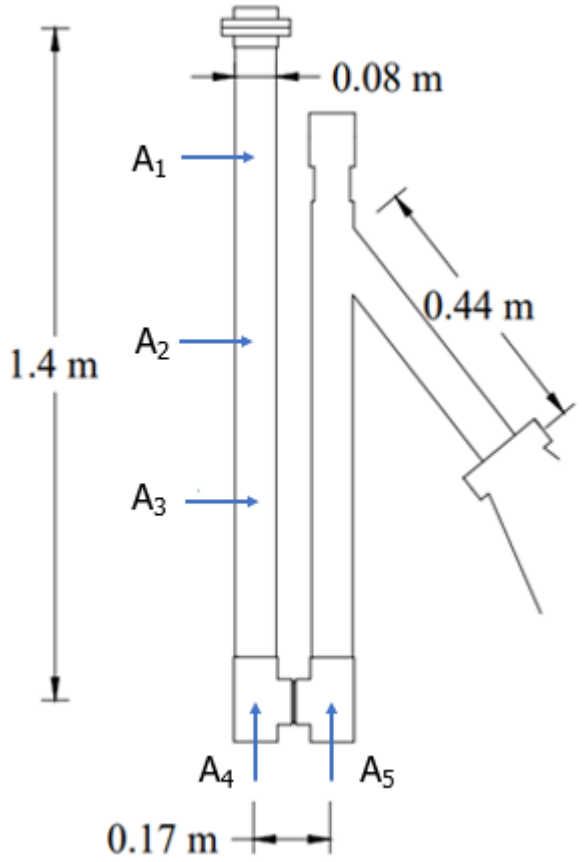

Figure 2-11. 0.08 m (3 in) diameter Loop Seal dimensions and aeration locations.

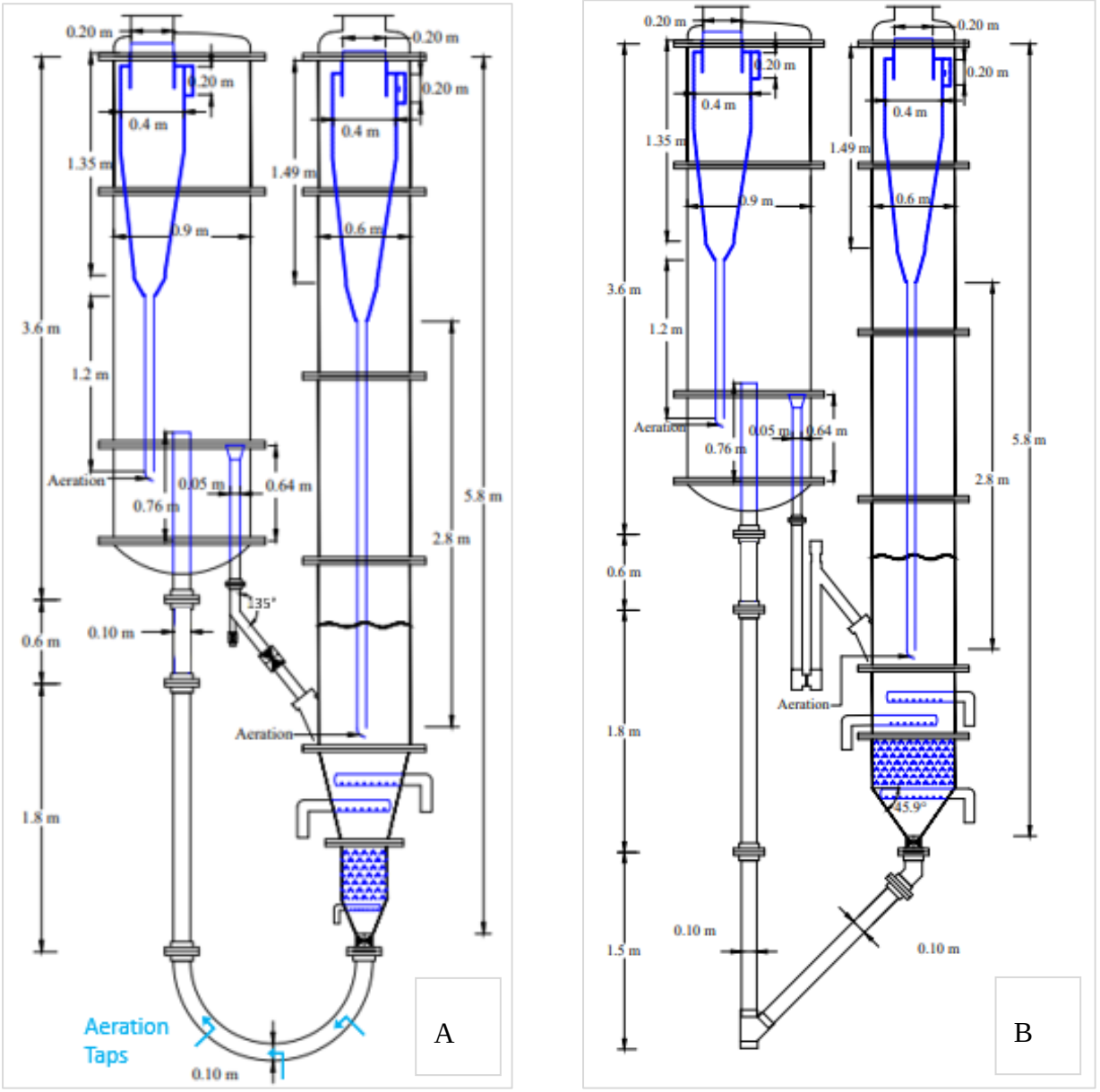

Figure 2-12. Cold Model unit dimensions after A) Phase 1 of modifications B) Phase 2 of modifications.

2.1.4 Gas Distributors

The Cold Model was fluidized with compressed air, controlled by a pressure regulator (± 3 psi accuracy, McMaster-Carr), coupled to a bank of sonic orifices to ensure a stable gas flowrate in the Reactor and Heater. The Reactor gas distributors were spargers, with two above and one below the stripper sheds, which share two sonic orifices (0.011 m ID and 0.016 m ID). The heater used an independent sonic orifice (0.012 m ID) to ensure stable flow to the perforated plate distributor. The riser fluidization gaswas provided by an additional pressure regulator (± 3 psi accuracy, McMaster-Carr) and sonic orifice (0.0083 m ID) to allow independent control from the fluidized beds (See Appendix C for calibration curves). Figure 2-13. presents the fluidization scheme used for all Cold Model configurations.

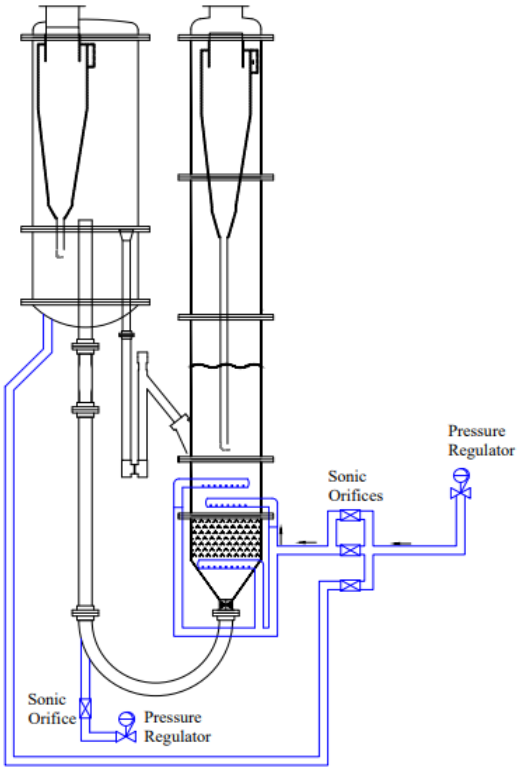

Figure 2-13. Cold Model fluidization scheme.

2.2 Pressure Measurements

Industrially, time average pressure measurements are often applied in large-scale fluidized bed to estimate the bed density or expanded bed height. When sampled at a frequency of 20 Hz or higher, pressure fluctuations can provide more information on bed hydrodynamics, bubble behaviour and flow regimes (van Ommen et al., 2004; Bi et al., 2007; Chen et al., 2015; Chen et al, 2016)

In the Cold Model, pressure measurements with a fast response time were important to monitor operating parameters and provide information on local bed hydrodynamics within the fluidized beds. Pressure measurements were used to:

1) Determine and monitor the expanded bed height to ensure that diplegs are immersed.
2) Estimate the local bed density to ensure the beds are well-fluidized.
3) Measure pressure fluctuations to detect regime transition for bubbling to turbulent, and ensure the bed is not slugging.
4) Determine and monitor the bed masses to:
    a. Ensure that solids circulation is balanced between both vessels.
    b. Ensure that solids losses are within defined limits.
5) Measure the solids flowrate from Reactor to Heater
6) Check model for dipleg stability

Typical fluctuations in a fluidized bed do not exceed 20 Hz (van Ommen et al., 2004; Bi et al., 2007), therefore, in the Cold Model the pressure measurements must have a response time faster than 0.5 s to avoid degradation of the signal. The transducers must also not get plugged by solids during regular operation. Finally, volume between the measurement point and transducer should be minimized to prevent signal degradation (van Ommen et al., 1999).

2.2.1 Transducer Response Time

To determine if the response time of the pressure transducers used was reasonable for use in the Cold Model, a transducer with the largest pressure range (PX-2650-100D5V) was connected to a 0.05 m diameter cylindrical vessel using a 2 m long line to replicate the longest distance between transducer and pressure tap on the Cold Model. The vessel was pressurized using a small air flow provided by compressed air. A back pressure regulator was used to maintain a constant pressure in the vessel, and a U-tube water manometer was used to monitor the vessel pressure. After a stable pressure was achieved and recorded, a step response was created by rapidly depressurizing the vessel. Figure 2-14 depicts a simplified diagram of the apparatus used to measure the transducer response time.

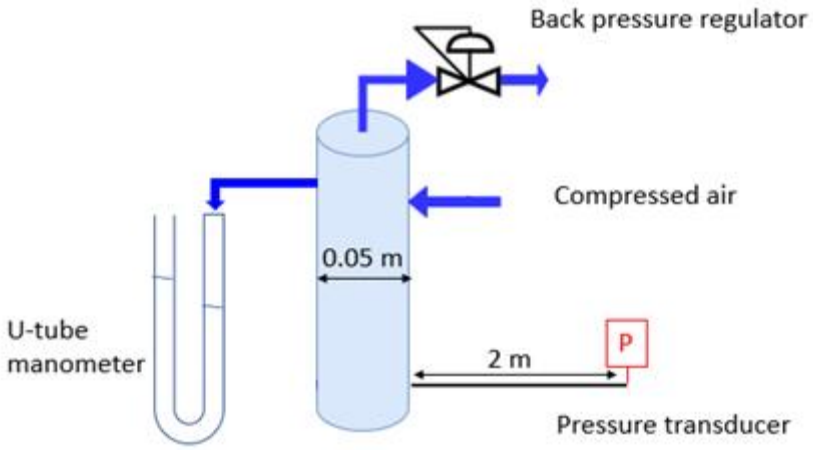

Figure 2-14. Apparatus used to determine pressure transducer with snubbers response time.

To find the response time Ƈ, the pressure response of the transducer was fit using a first order system as follows (Luyben, 1990):

$$\boldsymbol{P(t) = P_0 - (P_0 - P_\infty)(1 - e^{\frac{-t}{C}})} \quad (2.1)$$

The following sections investigate the response time of the original pressure transducers installed in the Cold Model, which used snubbers to prevent clogging the transducers, and the development and response time of transducers that used backflushing gas.

2.2.1.1 Measurements with Snubbers

The Cold Model was originally equipped with pressure transducers from the PX2650 Series Bidirectional, Differential Low Pressure Transducers (± 1% full scale (Omega, 1999)), connected to and controlled by two NI 9205 C Series DAQ (National Instruments, 2017). These transducers utilized snubbers to prevent clogs, however, snubbers can degrade pressure signals and increase response time. The location of the pressure taps using snubbers are depicted in Figure 2-15; all were in use in the original Cold Model configuration. The pressure transducers were calibrated using a u-tube water manometer (see Appendix D).

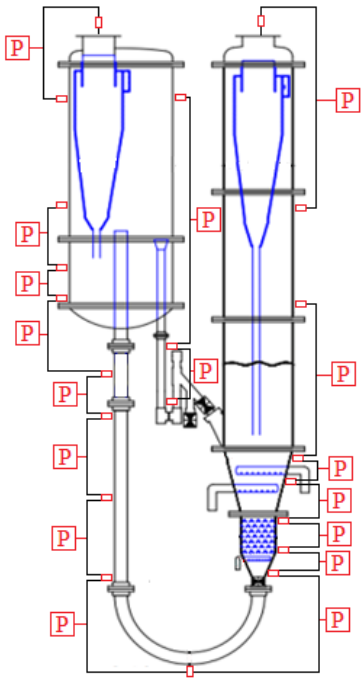

Figure 2-15. Locations of pressure transducers with snubbers on original Cold Model design.

An example of the measured and predicted pressure signal using a first order response during a step down in pressure for a single transducer (PX-2650-100D5V) is shown in Figure 2-16 for the time constant, $\tau = 0.72$ s. A response time of 0.72 s means the signal is degraded above $1/\tau = 1.4$ Hz. This does not meet the defined requirements to read a minimum of 20 Hz, therefore, the snubbers were determined to be insufficient for use in the Cold Model pilot plant.

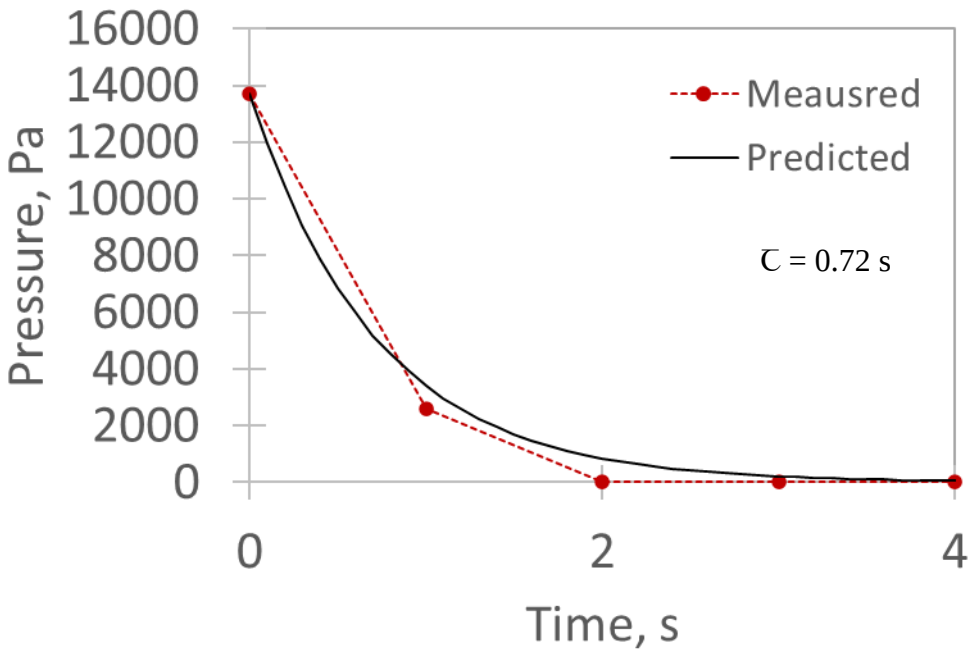

Figure 2-16. Example of pressure signal of Differential 0-100 H_2O pressure transducer (PX-2650-100D5V) fit with first order response.

2.2.1.2 Measurements with Backflushing

To improve the response time of the pressure readings in the Cold Model and measure pressure fluctuations, pressure measurements without snubbers were needed. Providing a steady stream of gas through the pressure tap prevents clogging pressure transducers without the use of snubbers. Therefore, differential pressure transducers from the Honeywell Board Mount TruStability® SSC Series (± 0.25% full scale (Honeywell, 2014)) were used with backflushing gas (compressed air). The transducers were connected to a 32 AI (16-Bit, 250 kS/s) USB Multifunction I/O Device (National Instruments, 2017) with 13 of the 32 channels in use to acquire the voltage signal at a

sampling frequency of 100 Hz (sampling every 1 ms). Figure 2-17 presents the device used to provide backflushing gas to each transducer.

Figure 2-17. Device used for pressure measurement with backflushing.

To ensure a stable flowrate of backflushing gas, compressed air at 80 psig was provided to a sonic orifice (0.1 mm ID) installed upstream of the connection to each pressure transducer. Figure 2-18 shows the location of the pressure taps on the Cold Model using backflushing, all used during operation of the Cold Model. The locations did not change during each phase of modifications.

The mass flow contribution from one backflushing tap in each fluidized bed is presented in Figure 2-19. Each individual tap provides a fraction smaller than 0.001 of the total mass flowrate of air in each unit. Five backflushing taps were used in the Reactor during typical experiments, providing a fraction smaller than 0.003 of the total mass flowrate of air. Three backflushing taps were used in the Heater during typical experiments, providing a fraction smaller than 0.002 of the total mass flowrate of air. The contribution from backflushing gas will not impact the system hydrodynamics.

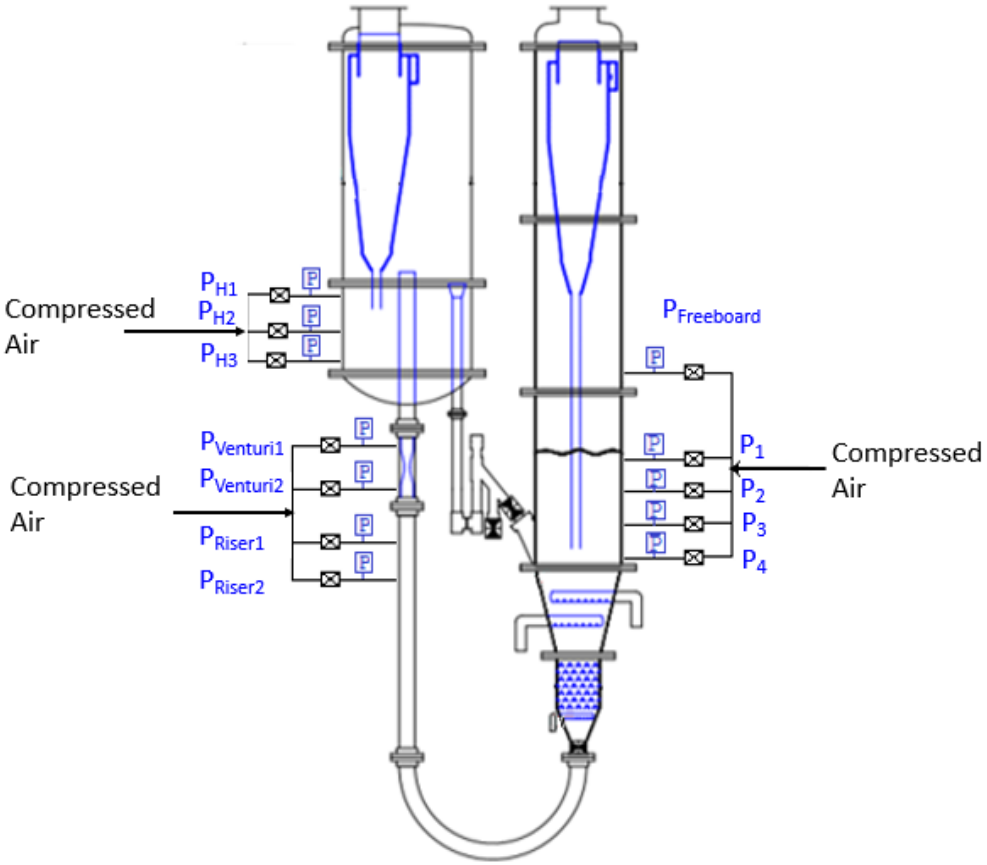

Figure 2-18. Locations of pressure taps using backflushing on original Cold Model design.

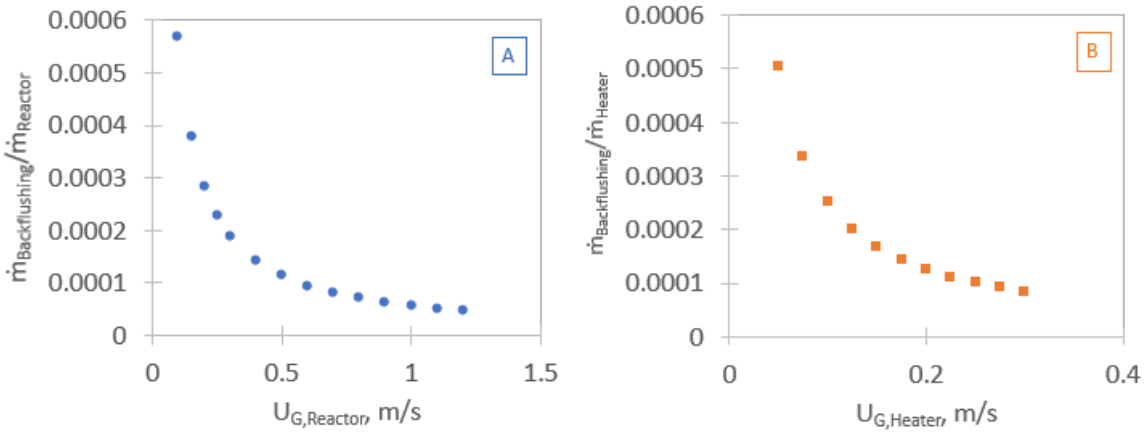

Figure 2-19. Contribution from one backflushing tap to the mass flowrate of air in the A) Reactor; B) Heater.

Response Time

As with the snubber response time, the response time of the a single transducer with backflushing (the transducer used in pressure tap P_4 – used for the dipleg fluctuation model (Honeywell TruStability SSCDRRN005PDAA5)) was fit with a first order response per Equation 2.1 during a step down in pressure. Figure 2-20. presents the measured and predicted pressure signal during the step for a time constant $\tau = 0.0156$ s. For this response time, frequencies above $1/\tau = 64$ Hz will be degraded.

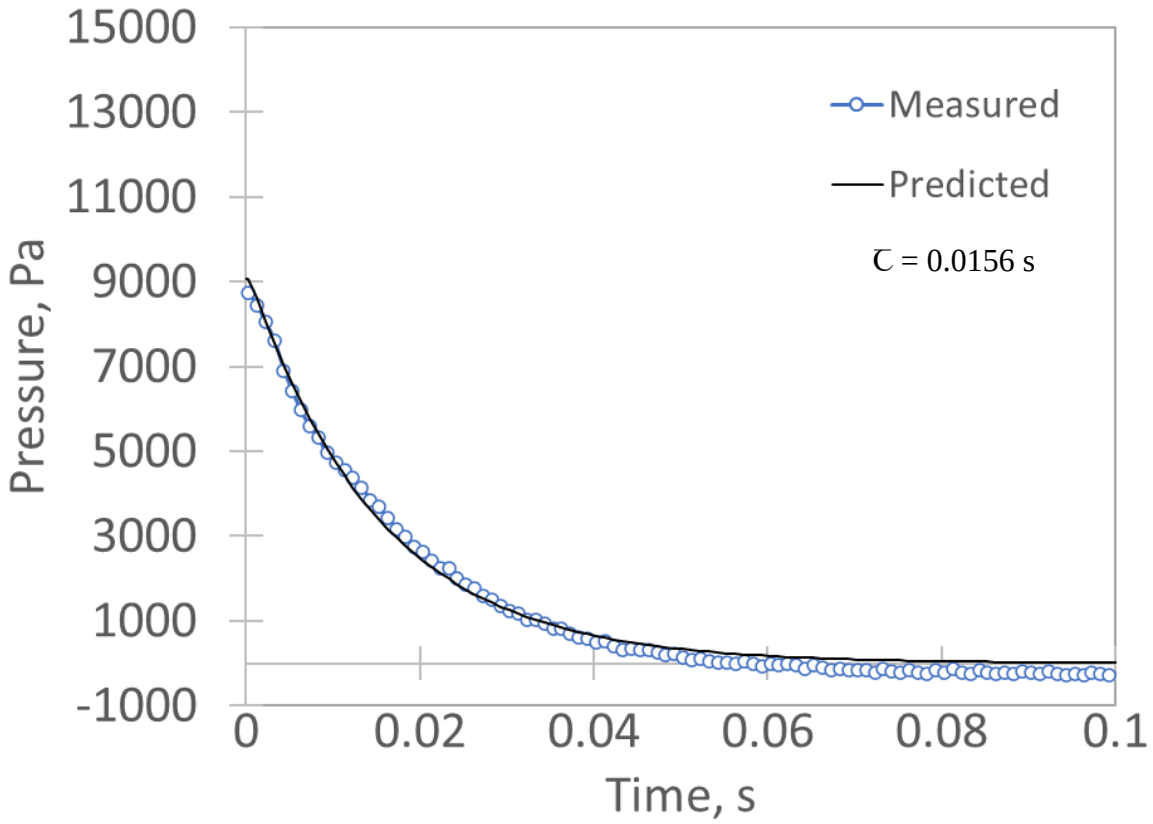

Figure 2-20. Differential 0-5 psi pressure transducer (SSCDRRN005PDAA5) in tap P_4 fit with first order response.

2.3 Entrainment Measurements

Knowledge of the entrainment flux in a fluidized bed is a key design criterion used to size and place particle recovery equipment such as cyclones and cyclone diplegs. To characterize the original Cold Model design, determine limitations and recommend improvements, the entrainment rates entering and exiting the cyclone were measured in Chapter 4.4.

Pseudo-isokinetic sampling was used as the measurement method, in which a small fraction of entrained solids is extracted using suction to match the velocity in the probe inlet with the local gas velocity. This measurement method was selected as a cyclone catch, which uses a diversion valve on the cyclone dipleg, was impractical in the Cold Model as the internal dipleg was difficult to access. Additionally, restriction on the dipleg may create operational issues. The probe was placed in the cyclone inlet for the majority of tests, as the high velocity eliminates the risk of saltation in the sampling line. The high velocity also reduces the risk of major errors in the particle size distribution if the sampling velocity is not exactly equal to the local gas velocity as the high velocity is much higher than the terminal free falling velocity of all particles.

Four ejectors, connected in parallel, were used to provide pseudo-isokinetic conditions in the probe mouth (ID 13 mm). Gas flow necessary for pseudo-isokinetic sampling was estimated using the superficial gas velocity in the reactor:

$$\boldsymbol{Q_{Sampling} = U_G \left(\frac{A_{Reactor}}{A_{Cyclone\ Inlet}} \right) A_{Probe}} \tag{2.2}$$

The velocity was controlled using a rotameter (7520 Series Flowmeter 2C-17, ± 6% full scale accuracy, King Instrument Company) for 2-30 minutes depending on solids flux in the cyclone inlet, or 2-3 hours in the cyclone outlet. Solids were collected in a bucket and measured with a balance (30000 MyWeight CTS Scale, ± 0.5 g accuracy, HBI Technologies.). Solids were stored to perform particle size analysis. Figure 2-21 shows a simplified schematic of the isokinetic sampling system used in the cyclone inlet. The setup was the same for the cyclone outlet, other than the position of the probe mouth.

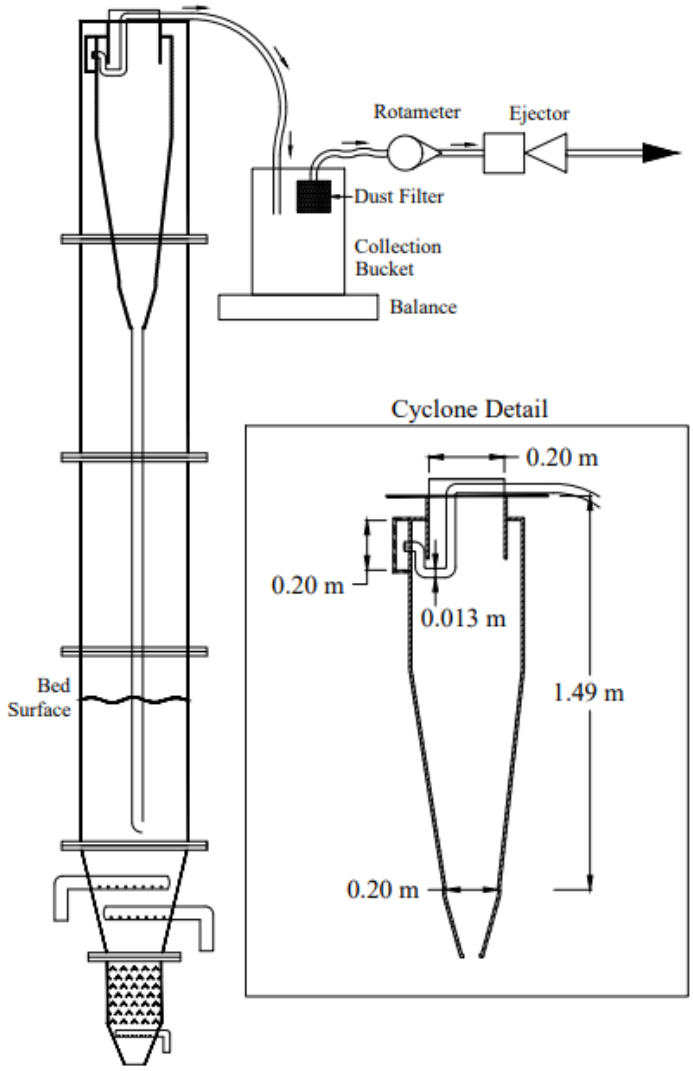

Figure 2-21. Schematic of isokinetic sampling system used to sample solids in cyclone inlet.

Due to the large scale of the unit, the pressure drop upstream of the ejectors limited pseudo-isokinetic conditions to superficial gas velocities in the reactor below 0.75 m/s. To allow sampling at higher velocities, the solids flux and particle size distributions when sampled under pseudo-isokinetic conditions and sampled at a velocity 20% lower than pseudo-isokinetic were compared after correcting the flux with the ratio of sampling velocities used. Figure 2-22. shows the flux and particle size distribution. No detectable difference in the flux or particle size distribution indicate measurements could be made at higher Reactor superficial gas velocities with no additional correction needed.

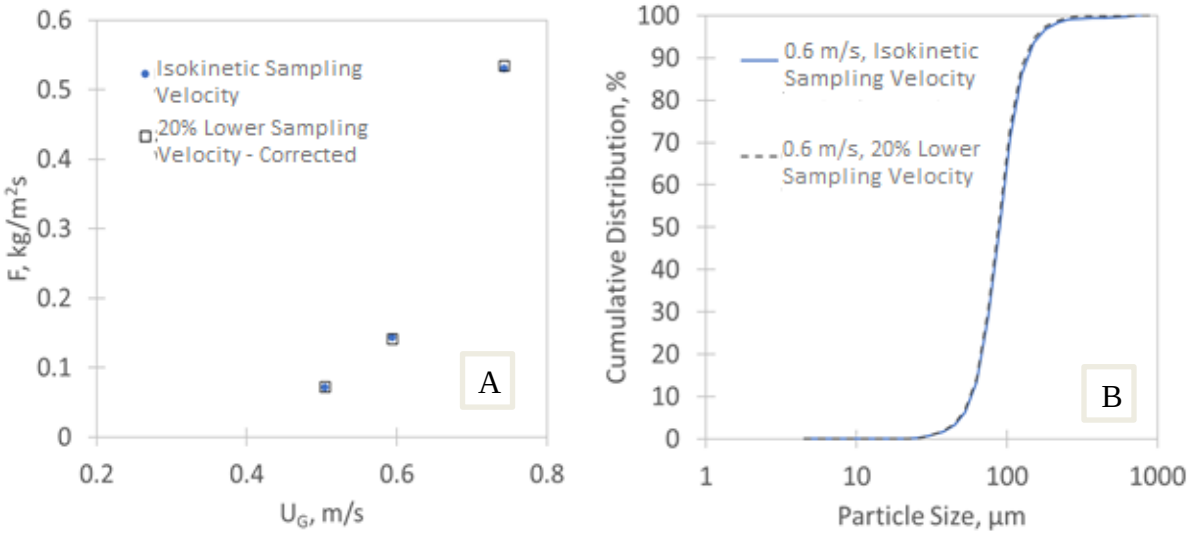

Figure 2-22. Impact of sampling velocity in probe mouth with All Spargers gas distribution at $H_{Defluidized}$ = 1.62 m on A) Entrainment Flux (F) and B) Particle size distribution (ex. at U_G = 0.6 m/s).

2.4 Dipleg Level Detection

Dipleg malfunction, either from gas flow up the dipleg, or from high solids fluxes overwhelming the dipleg capacity can result in solids backing up into the dipleg. As solids are re-entrained into the cyclone cone, the cyclone efficiency is reduced, and high levels of solids can be lost from the system. Understanding the probability of the dipleg solids reaching the bottom of the cyclone cone can provide useful information on design changes or operating limitations for the Cold and Hot Model pilot plants. A pulley and weighted float were installed in the cyclone dipleg to measure the level of solids in the dipleg under different conditions. A camera was installed at the cyclone outlet to monitor for high levels of dust emissions. Figure 2-23 illustrates the dipleg level measurement system.

The dipleg could not be easily accessed to measure the level directly, therefore a reference height was marked outside the unit before each group of measurements, assuming:

$$z_{d0} = H_{bed,ref} = 0 \quad (2.3)$$

The reference bed height was measured after fluidizing the Reactor for five minutes at U_G = 0.07 m/s. After marking a reference height, the level of defluidized solids above the reference height was measured by fluidizing the Reactor for 5 minutes at the specified superficial gas velocity. The bed was then rapidly defluidized by shutting off the fluidization gas to the system. After the solids in the dipleg have settled, the float was lowered to rest on the defluidized solids in dipleg, and the distance above the reference height recorded.

The measurements were repeated as needed, and converted to the distance of solids in the dipleg from the bottom of the cyclone cone:

$$z_c = L_{dipleg} - z_d \quad (2.4)$$

Where L_{dipleg} is the length of the dipleg from the elbow termination to the cyclone bottom (m)

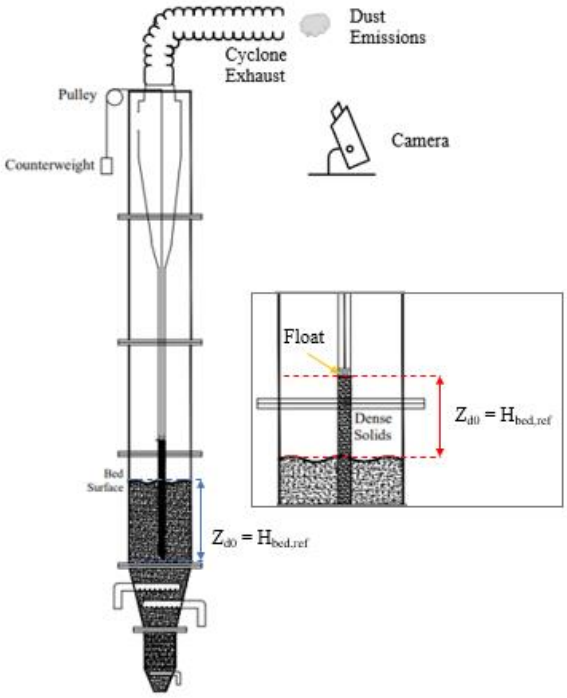

Figure 2-23. Dipleg level measurement system using pulley and float with camera at cyclone exhaust.

2.5 Gas Tracer Cross-Flow Measurements in Heater to Reactor Transfer Line

Gas tracers are often used in gas-solid fluidized systems to provide information on gas behaviour. In the Hot Model Pilot Plant, it will be important to prevent product gas from flowing from the Reactor to the Heater through the solids return transfer line (Chapter 5). Therefore, in the Cold Model, the 0.05 (2 inch) angled transfer line (see Figure 2-10) and 0.08 m (3 in) loop seal (see Figure 2-11) were tested to determine the limits of the system where no gas flowed from Reactor to Heater. Pure nitrogen gas was used as a tracer.

2.5.1 Gas Sampling Vessel and Testing Cell

A 1.7L glass container was used as a gas sampling vessel, affixed with an ejector to produce suction, and two flow control valves. The same vessel and sample bag was used throughout the experiments, connected to different porous taps in the transfer lines to prevent solids entering the sample bag. The vessel could be used in two configurations with a 1 L sample bag, shown below in Figure 2-24. Prior to taking a sample, the vessel was used in “expulsion” mode to empty the bag to prevent diluting or contaminating the sample. The sample line was closed, and the “expulsion” flow control valve was opened to use the ejector to suck gas out of the sample bag. To fill the sample bag, the “expulsion” valve is closed, and the “suction” valve is opened. With the valve to the sample line open, the ejector provided suction to fill the sample bag. The flow control valve was adjusted to ensure the sampling flowrate is small enough to not impact the local hydrodynamics within the transfer line. After the sample bag was full, the flow control valve was closed.

Each gas sample was introduced off-line to a 70 cm^3 testing cell shown in Figure 2-25 by squeezing the gas out of the bag into the cell. The shut-off valve was rapidly closed to prevent the sample from escaping while using the Premium Wideband A/F Oxygen (O_2) Sensor (Robert Bosch LLC.). The 1 L bag was sufficient to flush the cell completely and saturate the probe with sample gas.

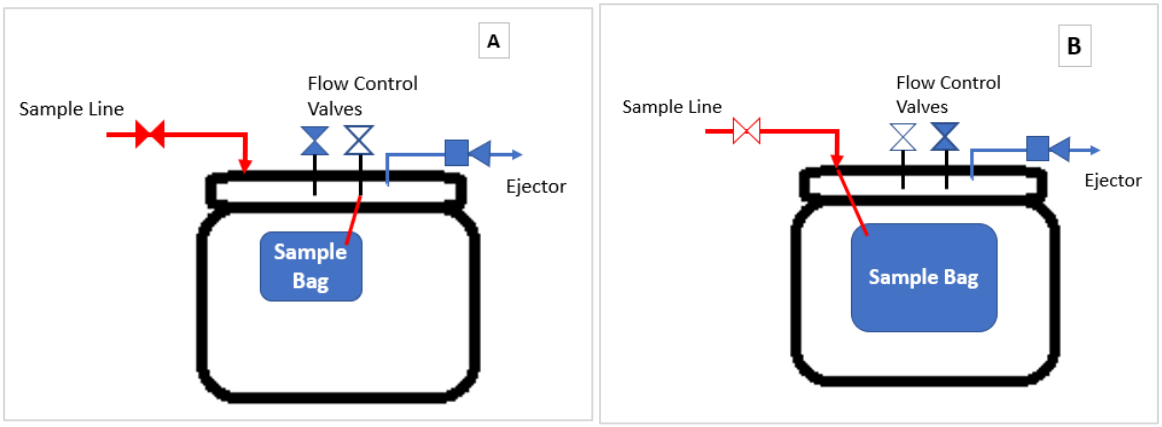

Figure 2-24. Gas sampling vessel in A) Expulsion mode and B) Suction mode.

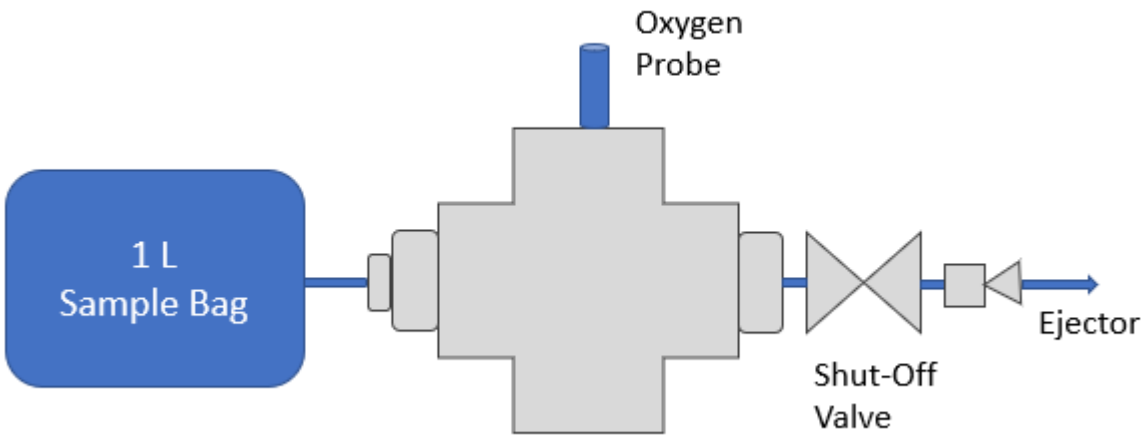

Figure 2-25. Gas tracer testing cell with oxygen probe.

2.5.2 Sampling Locations

The following section describes the nitrogen injection and sampling location in the two transfer lines tested.

2.5.2.1 0.05 m (2 in) Angled Line

Gas flow from the Reactor to the Heater was a significant concern in the angled Heater to Reactor transfer line as it did not maintain a dense phase of solids at some gas velocities. By using a high enough downflow of solids from the Heater, all the gas would be entrained downwards and thus prevent any gas from rising from the Reactor to the Heater. Nitrogen gas was used to aerate the downleg of the transfer line, as it would provide a tighter test than injection close to the reactor. The injection and sample locations for the tests performed on the angled line are presented in Figure 2-26. If nitrogen was detected in the sample bag, the flowrate of solids was not sufficient to seal the transfer line, and allowed gas to leak from the Reactor to the Heater.

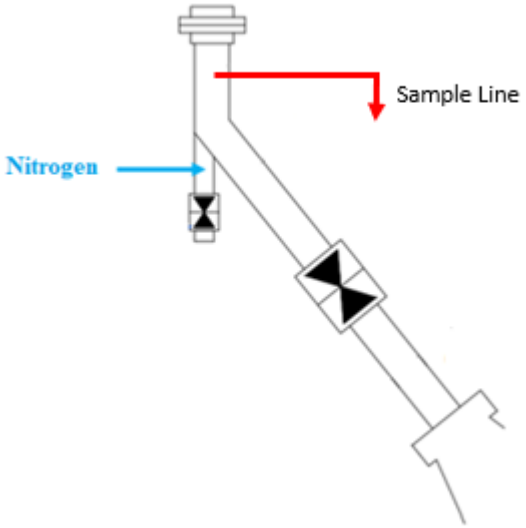

Figure 2-26. Gas sampling location to test for gas flow upwards towards Heater.

2.5.2.2 0.08 m (3 in) Loop Seal

Loop seals are designed to provide a good seal to prevent gas flow from the Reactor to the Heater. To confirm there would be no gas flow at the target operating recirculation rates, nitrogen was injected and gas sampled in the locations shown in Figure 2-27**.** If nitrogen was detected in the sample bag, the flowrate of solids was not sufficient to seal the transfer line, and allowed gas to leak from the Reactor to the Heater.

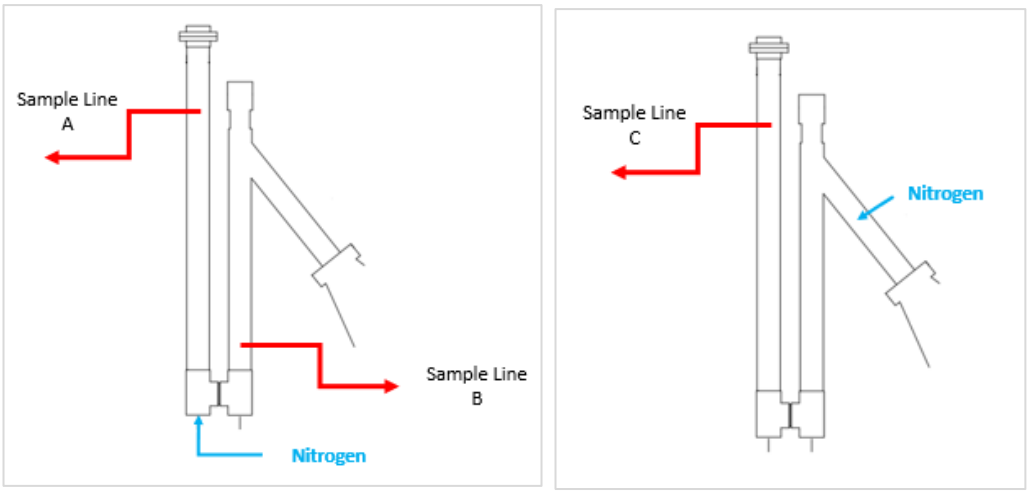

Figure 2-27. Gas sampling location to test A) direction of aeration flow B) direction of flow from Reactor to Heater.

2.6 Conclusion

Due to operational limitations, the original Cold Model was modified in two phases. The first phase focused on improving the rate of solids losses from the primary cyclone, while the second phase focused on improving the recirculation rate. Pressure measurements are a crucial measurement technique in fluidized beds; thus, the original instrumentation was improved and used to characterize the system response time. A pseudo-isokinetic probe was used to characterize the solids entrainment rate entering the cyclone throughout this research work. In addition, a pulley system was developed to measure the level of dense solids in the dipleg to characterize the level of fluctuations. Finally, a system to measure the flow of gas from the Reactor to the Heater during recirculation was developed to ensure ideal operation of the Cold Model after each phase of modifications.

2.7 References

Carl Zeiss Microscopy GmbH. (2017). *MULTILINGUAL_operating-manual_Stemi-305*. https://p.widencdn.net/15xkor/MULTILINGUAL_operating-manual_Stemi-305_1

Chen, Y., Chen, W., Grace, J. R., Zhao, Y., Zhang, J., & Li, Y. (2016). Direct resolution of differential pressure fluctuations to characterize multi-scale dynamics in a gas fluidized bed. *International Journal of Multiphase Flow*, *85*, 380–394. https://doi.org/10.1016/J.IJMULTIPHASEFLOW.2016.05.005

Chen, Y., Jim Lim, C., Grace, J. R., Zhang, J., Zhao, Y., & Zheng, C. (2015). Characterization of pressure fluctuations from a gas-solid fluidized bed by structure density function analysis. *Chemical Engineering Science*, *129*, 156–167. https://doi.org/10.1016/j.ces.2015.02.009

Honeywell. (2014). *TruStability® Board Mount Pressure Sensors*. https://prod-edam.honeywell.com/content/dam/honeywell-edam/sps/siot/en-us/products/sensors/pressure-sensors/board-mount-pressure-sensors/trustability-ssc-series/documents/sps-siot-trustability-ssc-series-standard-accuracy-board-mount-pressure-sensors-50099533-a-en-ciid-151134.pdf?download=false

Karri, S. B. R., & Knowlton, T. M. (1999). 4 - Gas Distributor and Plenum Design in Fluidized Beds. In W.-C. Yang (Ed.), *Fluidization, Solids Handling, and Processing* (pp. 209–235). William Andrew Publishing. https://doi.org/https://doi.org/10.1016/B978-081551427-5.50006-5

Kunii, D., & Levenspiel, O. (2013). Fluidization engineering: Elsevier.

Li, Y. (2021). *Impact of Fluidized Bed Hydrodynamics on the Distribution of Liquid Sprayed Into the Bed*. The University of Western Ontario.

Luyben, W.L. (1990) *Process Modeling, Simulation and Control for Chemical Engineers* (2nd Edition), McGraw-Hill, pp. 167-171, 177-182

MyWeigh. (2022). *MyWeigh CTS User Manual*. https://myweigh.com/resources/manuals/cts.pdf

National Instruments. (2017a). *Datasheet NI 9205*. https://www.ni.com/pdf/manuals/378020a_02.pdf

National Instruments. (2017b) *Specifications USB-6218* https://www.ni.com/pdf/manuals/375199d.pdf

Omega Engineering, Inc. (1999). *PX2650 Series Bidirectional, Differential Low Pressure Transducers*. https://assets.omega.com/pdf/test-and-measurement-equipment/pressure/pressure-transducers/PX2650.pdf

Robert Bosch, LLC., (2022) Premium Wideband A/F Oxygen (O2) Sensors - Premium Wideband A/F Oxygen Sensors - Bosch Auto Parts. (Accessed: April 22, 2022) https://www.boschautoparts.com/p/premium-wideband-af-oxygen-o2-sensors

van Omman, J.R., Schouten, J.C., Vander Stappen, M.L.M., and van den Bleek, C.M. (1999). Response characteristics of probe-transducer systems for pressure measurements in gas–solid fluidized beds: how to prevent pitfalls in dynamic pressure measurements. *Powder Technol.* 106: 199–218.

Van Ommen, J. R., Van Der Schaaf, J., Schouten, J. C., Van Wachem, B. G. M., Coppens, M. O., & Van Den Bleek, C. M. (2004). Optimal placement of probes for dynamic pressure measurements in large-scale fluidized beds. *Powder Technology*, *139*(3), 264–276. https://doi.org/10.1016/j.powtec.2003.12.009

Chapter 3

3 Bed Hydrodynamics

This section aims to provide detail on the behaviour of the fluidized bed at various conditions, and the methods used to obtain certain measurements made in subsequent chapters. Most experiments were carried out in the Reactor; therefore, the bed characteristics presented in the following sections are for the Reactor. All results presented were taken after Phase 2 of modifications (refer to Figure 2-8) using the All Spargers and Bottom Sparger Only gas distributions. Differences in results between the previous gas distributions were seen at lower gas velocities, so a third gas distribution was used for the results presented in this section. The third distribution uses all three spargers but provides a fluidization line directly to the Bottom Sparger using the sonic orifice typically used to fluidize the Heater, providing more uniform flow in the stripper sheds.

3.1 General Bed Characteristics

The Reactor was filled to a defluidized bed height of 2.06 m, and pressure measurements were recorded at several vertical positions along the Reactor height. Measurements were taken in descending order of fluidization velocity and recorded for 15 min each to obtain time average and dynamic pressure fluctuations. Figure 3-1 shows the pressure in the Reactor freeboard increases with gas velocity. The freeboard pressure can therefore be used as a gas flowmeter. The gas distribution did not have an impact on the pressure in the freeboard.

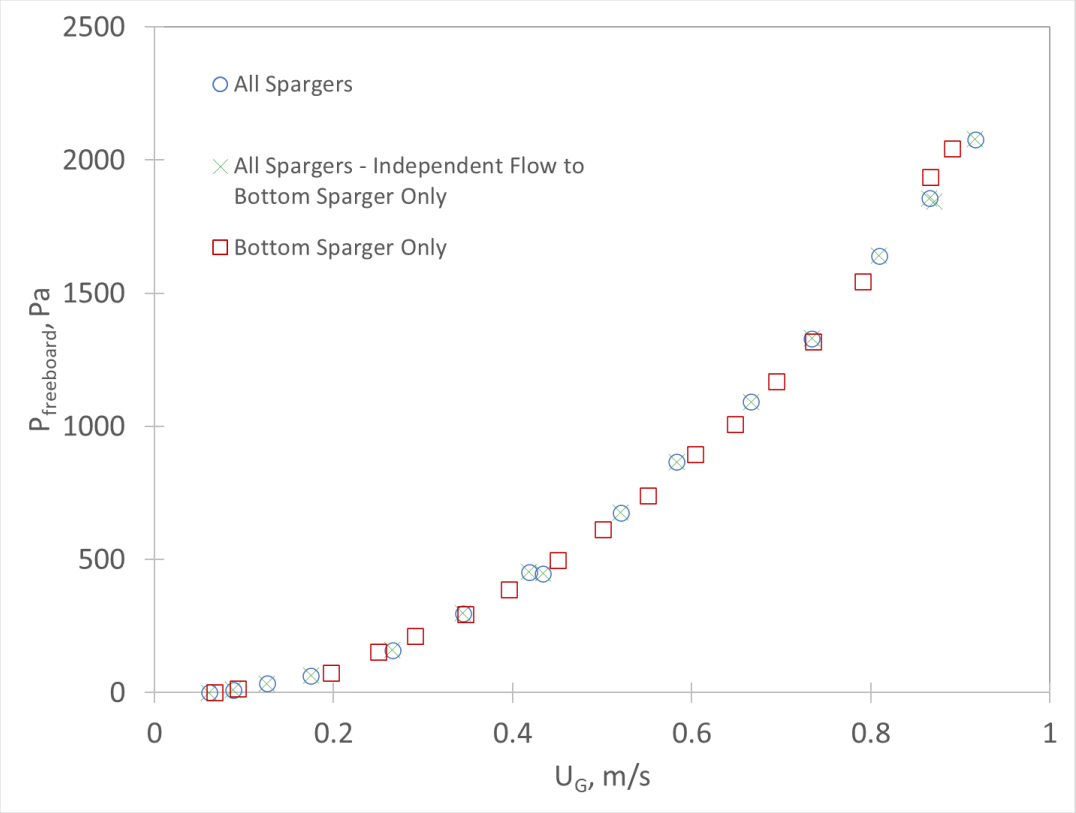

Figure 3-1. Time average gauge reactor freeboard pressure ($P_{freeboard}$) as a function of superficial gas velocity (U_G) for different gas distributions.

Pressure measurements made within the fluidized bed can be linearly correlated and extrapolated as shown in Figure 3-2. The pressure profiles shown below are for pressure taps P_1 – P_4 in the cylindrical section of the reactor above the distributors (refer to Figure 2-18). The pressure profiles for all three gas distributions and all superficial gas velocities measured are available in Appendix G. This method allows the measurement of the expanded bed height, fluidized bed pressure drop and can be used to determine the bed density or bed voidage (Knowlton, 2020). The expanded bed height, H_{Bed}, is obtained from the intercept of the pressure profiles in the dense bed and freeboard, while the bed density is obtained from the slope, or gradient of the pressure profile.

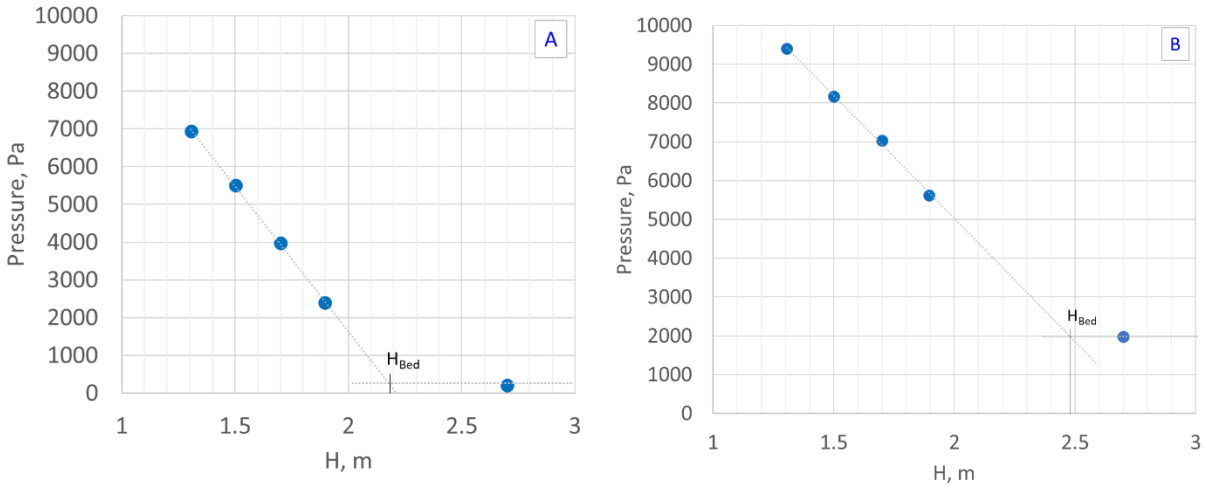

Figure 3-2. Example of pressure profile with $H_{Defluidized}$ = 2.06 m and All Spargers gas distribution at: A) U_G = 0.3 m/s; B) U_G = 0.9 m/s.

The change in bed density with superficial gas velocity (U_G) is shown in Figure 3-3. The density is observed to decrease linearly with increasing gas velocity. Above U_G = 0.2 m/s, there were minimal differences in the measured density between the three gas distributions; however, at lower gas velocities the All Spargers gas distribution was poorly fluidized in the stripper sheds section, impacting the bed density readings. If operation at low gas velocities is desired, the Bottom Sparger should have an independently controlled flow of gas. As the Bottom Sparger Only configuration provided the best distribution throughout the entire bed, the linear regression of these densities was used to extrapolate to find the bed density at minimum fluidization conditions. The emulsion density of the system is ρ_e = 848 kg/m^3.

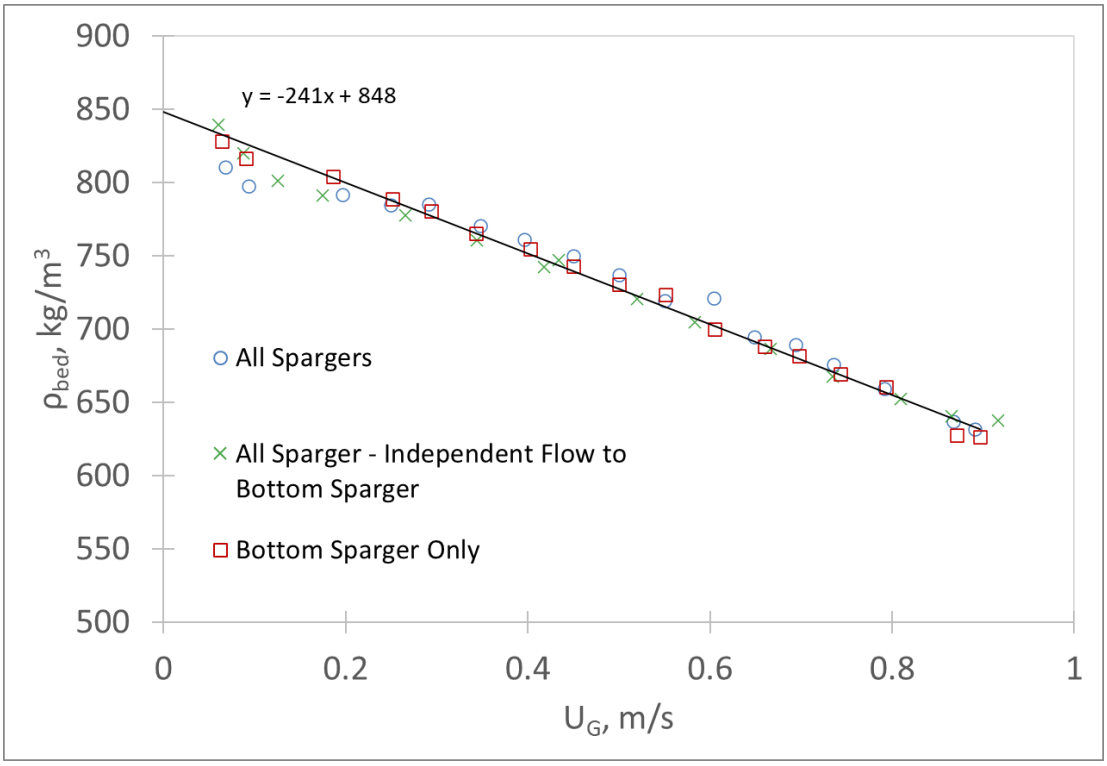

Figure 3-3. Change in bed density (ρ_{Bed}) with superficial gas velocity (U_G) for different gas distributions and $H_{Defluidized}$ = 2.06 m.

The expanded bed heights obtained from the pressure profiles are shown in Figure 3-4. The bed height consistently increased with gas velocity across the three gas distributions. The bed heights are consistently higher by up to 10 cm using the Bottom Sparger Only gas distribution. In this case, more gas is introduced lower in the bed, reducing the bed density below the upper spargers, and transferring more solids into the cylindrical region of the Reactor above the distributors (above tap P_4). The bed height in the All Spargers with Independent Flow to the Bottom Sparger configuration was lower than in the typical All Spargers configuration, indicating less gas is going to the bottom sparger with independently controlled flow. This configuration can be used for better distribution at low gas velocities, however, may not provide optimal distribution across a wide range of gas velocities.

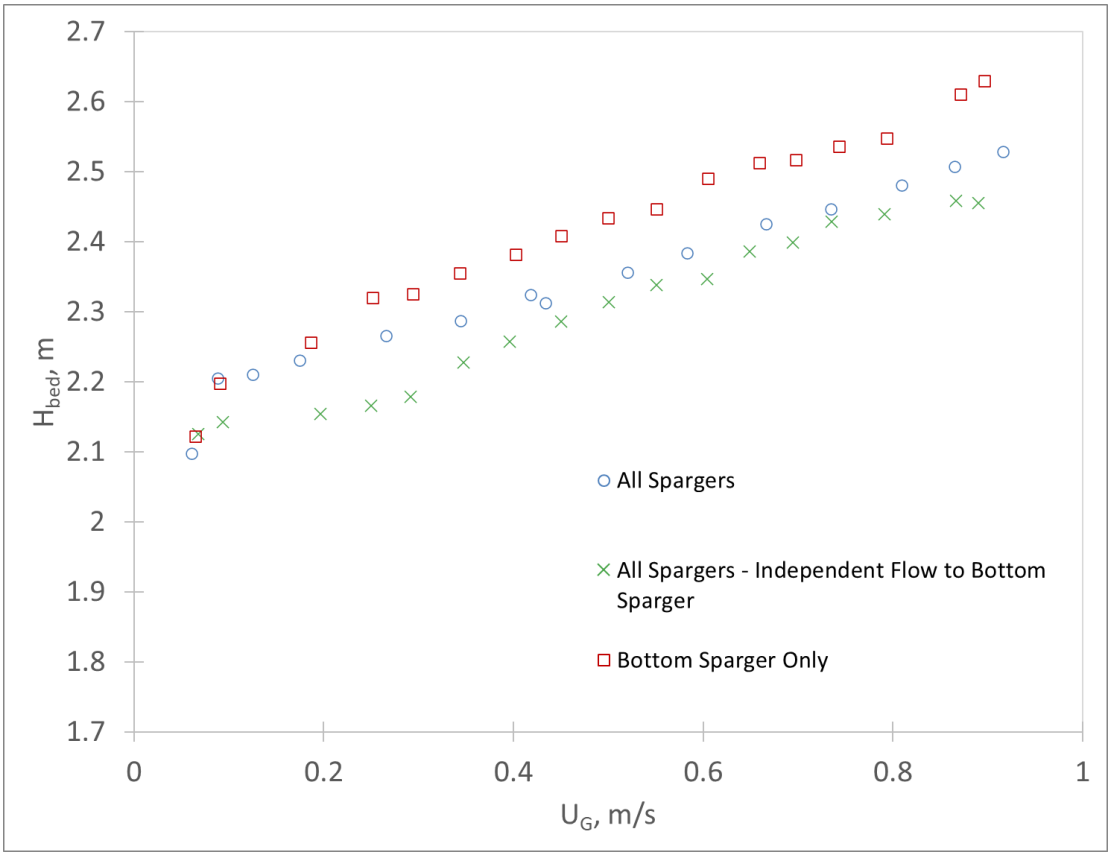

Figure 3-4. Change in bed height with superficial gas velocity for different gas distributions and $H_{Defluidized}$ = 2.06 m.

Pressure fluctuations can be used to provide dynamic information for fluidized beds, such as the transition to turbulent flow, bubble formation and splitting, and bubble coalescence and eruption (Chen et al 2015). The change in the coefficient of variation (CV) (ratio of standard deviation to the mean) of the pressure signal is presented in Figure 3-5. There is little difference between the gas distributions at the high and low velocities, but there is a slight difference in the trends around the transition velocities. Pressure fluctuations in fluidized beds can originate from several sources. The main sources of fluctuations are fluctuation caused by bubble flow past the pressure measurement location, bed level fluctuations or bed surface waves due to bubble eruption, and the vibration of the fluidized bed. Other sources can be generated from bubble/jet formation in

the distributor region and bubble coalescence and breakup in the bed (Bi et al., 2007; Chen et al., 2016).

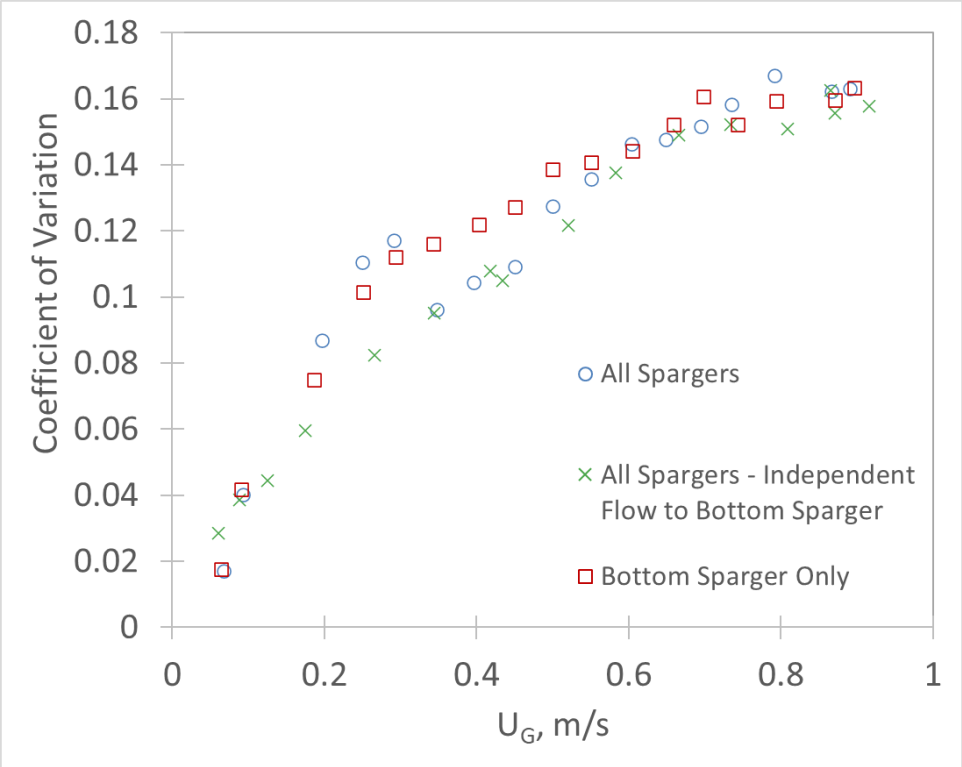

Figure 3-5. Coefficient of Variation of pressure at tap P_4 as a function of superficial gas velocity (U_G) for different gas distributions at $H_{Defluidized}$ = 2.06 m.

The power spectra can provide useful information on pressure fluctuations on fluidized bed (Chen et al., 2016; van der Schaaf et al., 2002). The power spectra were obtained using pressure measurements, recorded for 15 minutes, using a Honeywell TruStability Series model SSCDRRN005PDAA5 differential transducer. The transducer was connected to a 32 AI (16-Bit, 250 kS/s) USB Multifunction I/O Device (National Instruments, 2017), with 13 of the 32 channels in use, to acquire the voltage signal at a sampling frequency of 100 Hz (sampling every 1 ms). The power spectra was calculated using the product of its Fourier transform by its complex conjugate (Briens and Briens, 2002), and plotted for several velocities and gas distributions for a single transducer (the transducer used at P_4) and are shown in Figure 3-6. Fluidized beds rarely have fluctuations higher than 20 Hz (Bi et al., 2007). This is confirmed in

the Cold Model, as the signal peak between 0-5 Hz, with no fluctuations at frequencies higher than 10 Hz for all conditions tested. The response time of the pressure measurements was 0.0156 seconds (corresponding to 64 Hz) and would detect any fluctuations above 10 Hz if they were present. This confirms the pressure measurement response time is better than necessary.

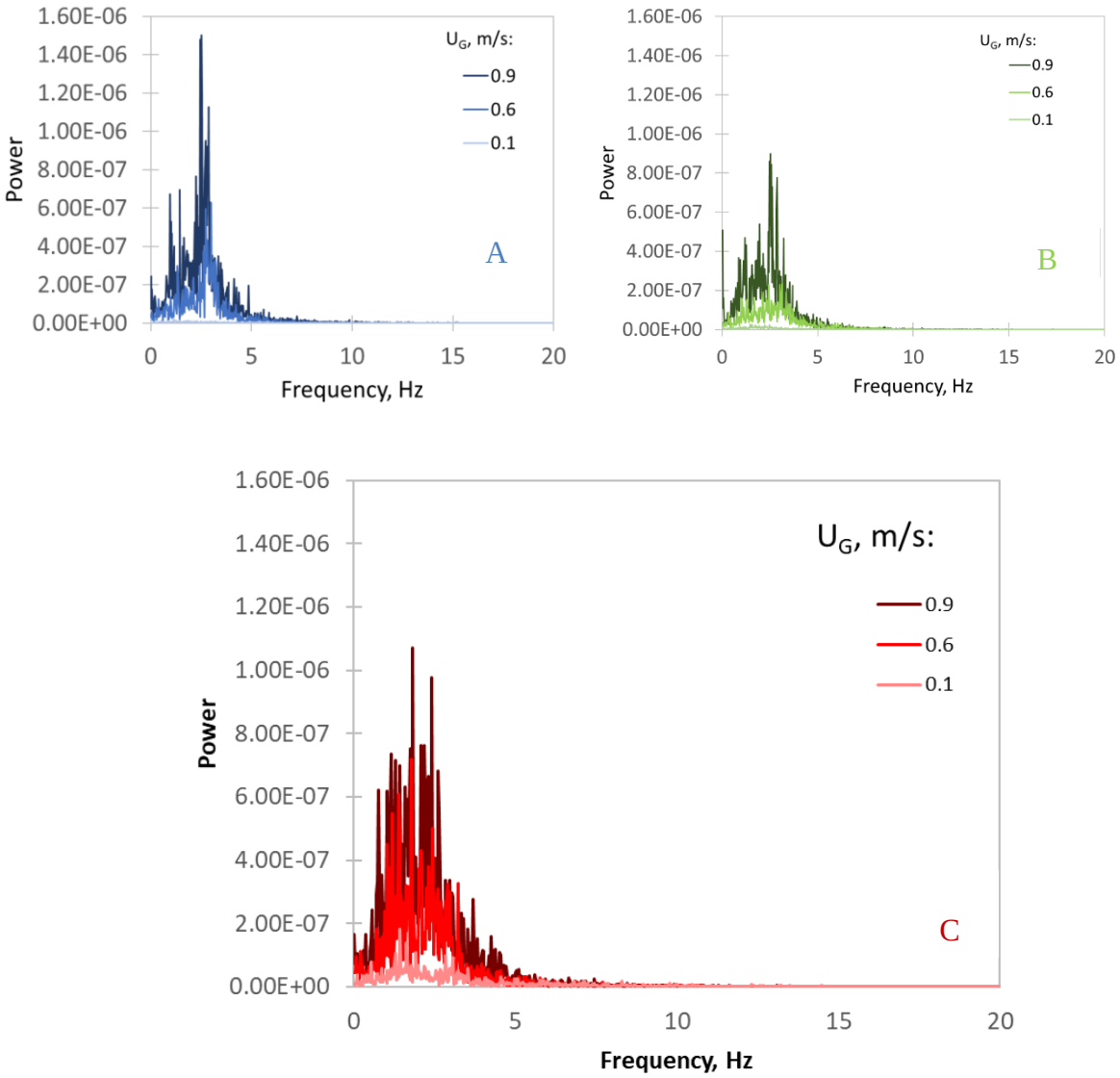

Figure 3-6. Power spectra for pressure transducer P_4 at various gas velocities for A) All Spargers; B) All Spargers – Independent Flow to Bottom Sparger; C) Bottom Sparger Only.

The cycle time has been shown to provide information on fluidized bed hydrodynamics (Li, 2021). The V statistic was developed to detect cyclic behavior (Peters, 1994) and has been applied to detect flow regimes in multiphase systems (Briens and Briens, 2002; Hurst 1951). If a signal exhibits cyclic behavior, the V-statistic versus time interval plot would peak in the plot corresponds to the cycle time. The cycle time was plotted as a function of gas velocity in Figure 3-7. The cycle time is approximately 0.5 s for both All Spargers distributions and approximately 0.6 s for the Bottom Sparger Only distribution. The response time of the pressure measurements is better than necessary to detect changes in the signal.

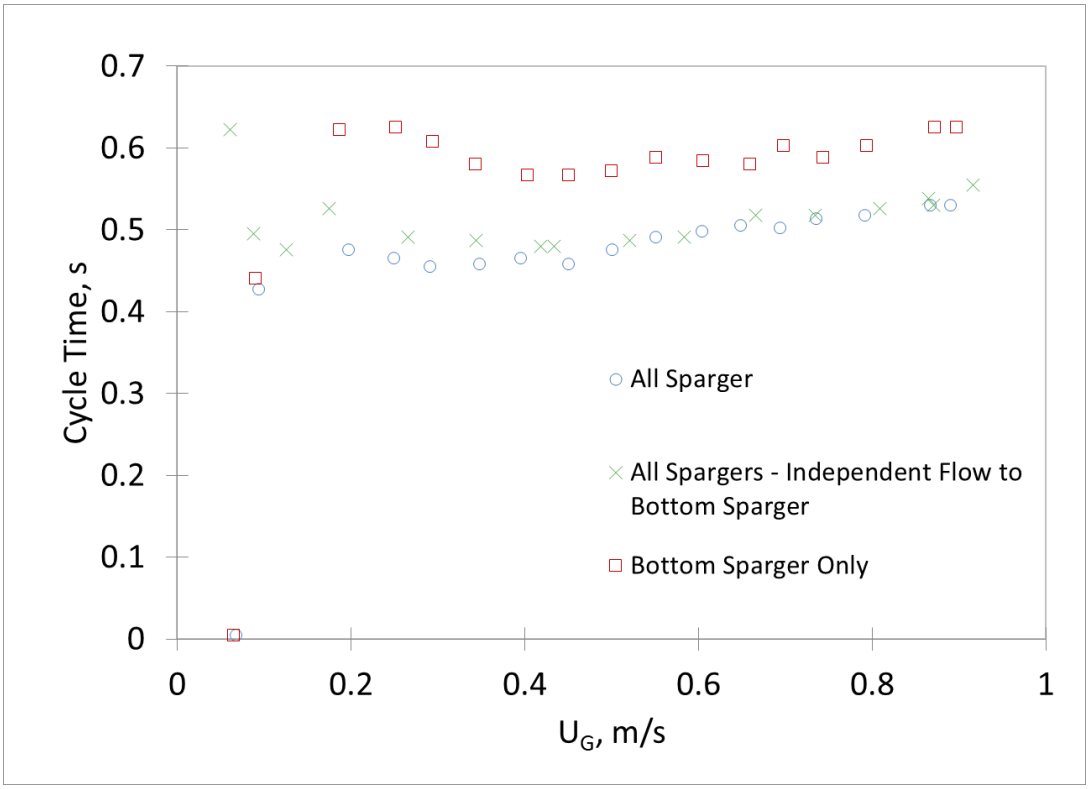

Figure 3-7. Cycle time at tap P_4 as a function of superficial gas velocity (U_G) for different gas distributions at $H_{Defluidized}$ = 2.06 m.

3.2 Transition to Minimum Turbulent Fluidization Velocity

Pressure fluctuations are commonly used to detect the transition between the bubbling and turbulent flow regimes. Many commercial fluidized bed reactors are operated in the turbulent flow regime, due to superior gas-solid contact and bed-to-surface heat transfer (Grace, Bi and Ellis, 2020; Bi et al., 2000). However, based on various models, the calculated transition velocity from bubbling to turbulent can vary significantly. The standard deviation or coefficient of variation is often used to detect the transition to turbulent flow (Arimandi-Tash et al., 2014; Brink et al., 2011; Gonzalez et al., 1995; Seo et al., 2014; Bi, 1993; Ellis et al., 2003). The maximum value of the V statistic of pressure fluctuations has also been used to detect the transition to turbulent flow (Li, 2021). These methods were applied in the Cold Model to detect the transition to turbulent flow. The differential pressure between tap P_4 and P_3 was measured. The measurement locations are illustrated in Figure 3-8.

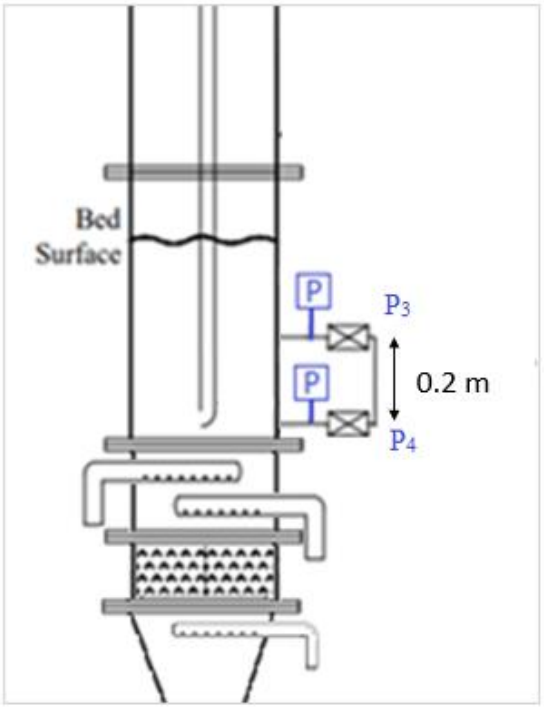

Figure 3-8. Measuring location of differential pressure fluctuations.

Figure 3-9 shows the standard deviation of the differential pressure changing with gas velocity. This is the standard method used to predict the transition from bubbling to turbulent flow, and fluctuations can be attributed primarily to local disruptions such as passing bubbles (Dubrowski et al, 2013; Zhu and Zhu, 2008) The minimum turbulent velocity (U_{mt}) predicted with this method was 0.37-0.38 m/s. This aligned well with previous studies (Li, 2021; Cochet, 2021), and gas distribution did not appear to impact the predicted transition.

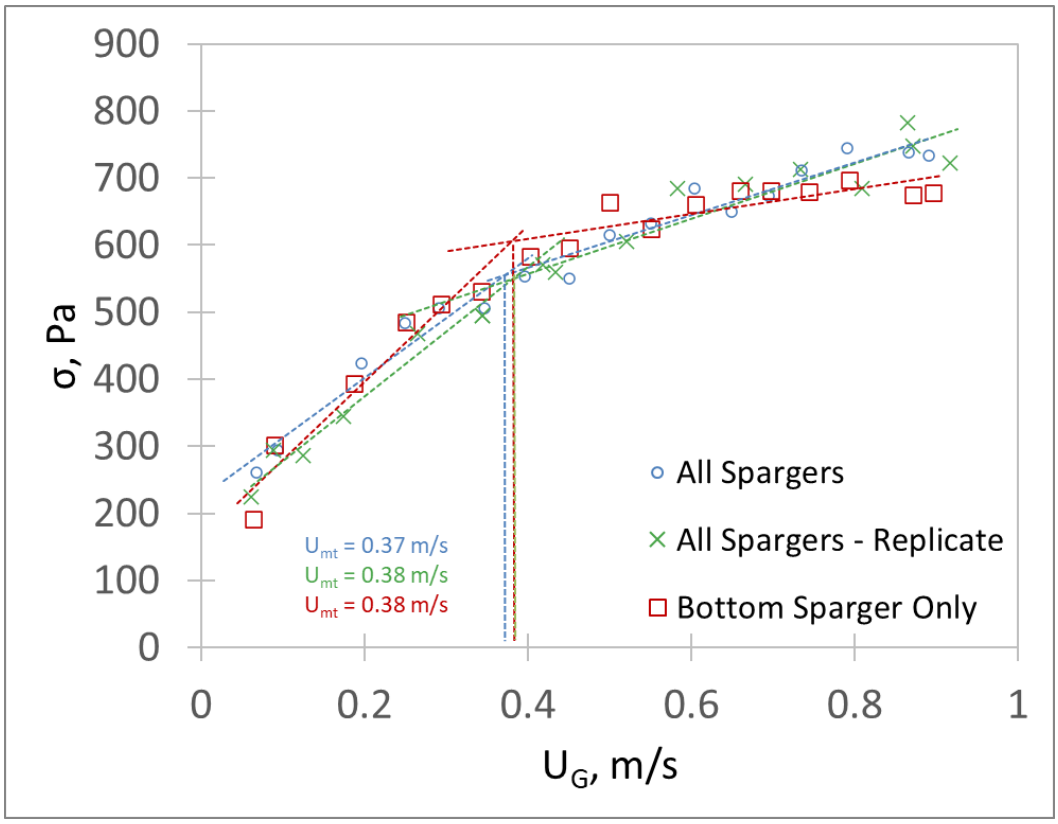

Figure 3-9. Example of the change in standard deviation (σ) of differential pressure fluctuations with superficial gas velocity (U_G) to detect minimum turbulent velocity (U_{mt}) using different gas distributions.

Due to the impact of electrostatics, the V statistic was used to confirm the transition velocity found above, as it is less sensitive to noise. Figure 3-10 shows the change in the maximum value of the V statistic of differential pressure fluctuations with gas velocity. Using this method, the predicted minimum turbulent velocity was 0.38-0.42 m/s. These values again agree with previous

study (Li, 2021). The V statistic confirms the results obtained using the standard deviation of the differential pressure signal.

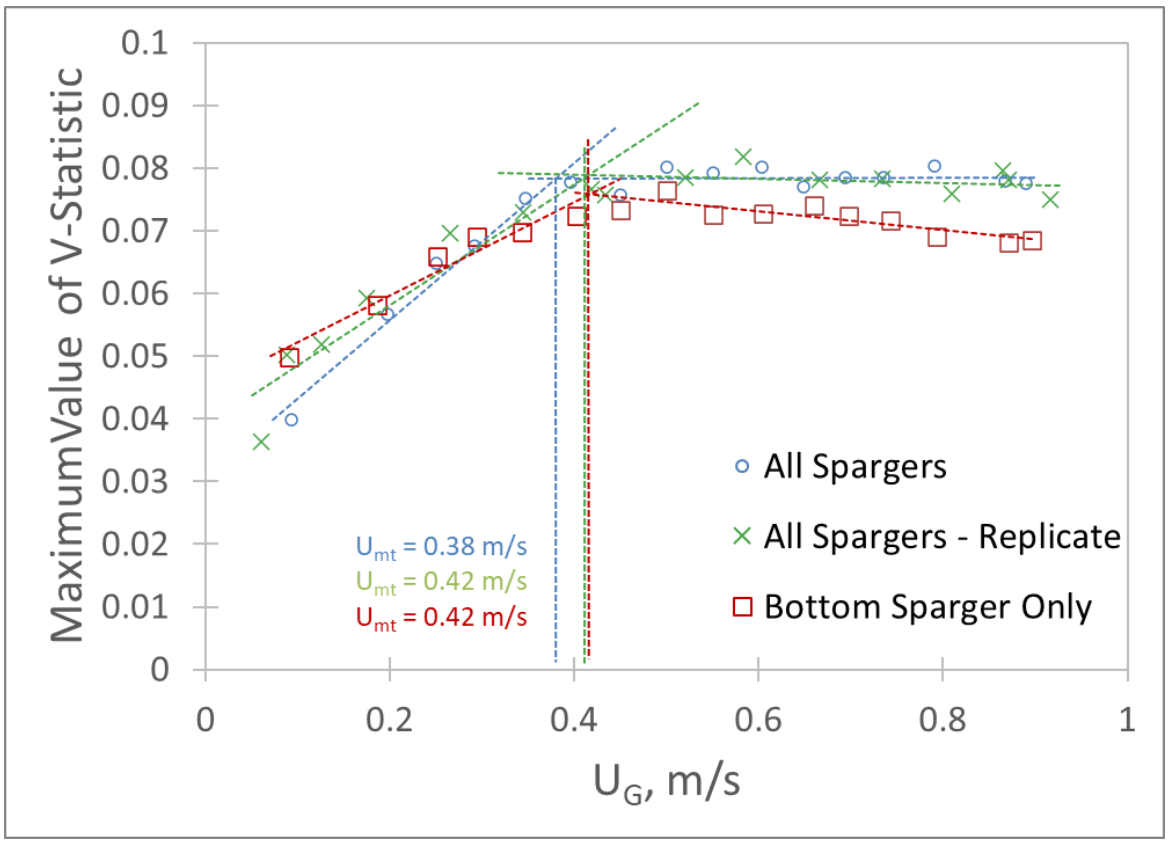

Figure 3-10. Example of the change in maximum value of V statistic of differential pressure fluctuations with superficial gas velocity (U_G) to detect minimum turbulent velocity (U_{mt}) using different gas distributions.

3.3 Bubble Velocity

The bubble velocity can be calculated from the two phase theory (Toomey, 1952), using the bed expansion. For Group A Powders, the emulsion phase voidage, ε_e is greater than the voidage at minimum fluidization, ε_{mf}. The emulsion phase density was obtained from the linear regression of the bed density as a function of gas velocity where $U_G = U_{mf}$ (see Figure 3-3). As the Bottom Sparger Only distribution provides the best fluidization at low gas velocities, that is the regression used to determine the emulsion density.

From Figure 3-3: $\rho_e = 848\ kg/m^3$

The bed density can be expressed as follows:

$$\rho_{Bed} = \rho_e(1 - x_B) \tag{3.1}$$

Therefore,

$$x_B = 1 - \frac{\rho_{Bed}}{\rho_e} \tag{3.2}$$

The fraction of bubbles can be expressed as:

$$x_B = \frac{(U_G - U_{mf})}{U_B} \tag{3.3}$$

Therefore,

$$U_B = \frac{(U_G - U_{mf})}{x_B} \tag{3.4}$$

The bubble velocity calculated using this method as a function of gas velocity is shown below in Figure 3-11. It predicts a near constant bubble velocity (U_B = 3.43 m/s) above U_G = 0.2 m/s. This

bubble velocity can be used in calculations for other bed characteristics such as bed expansion or transport disengagement height (TDH) to replace other traditional correlations.

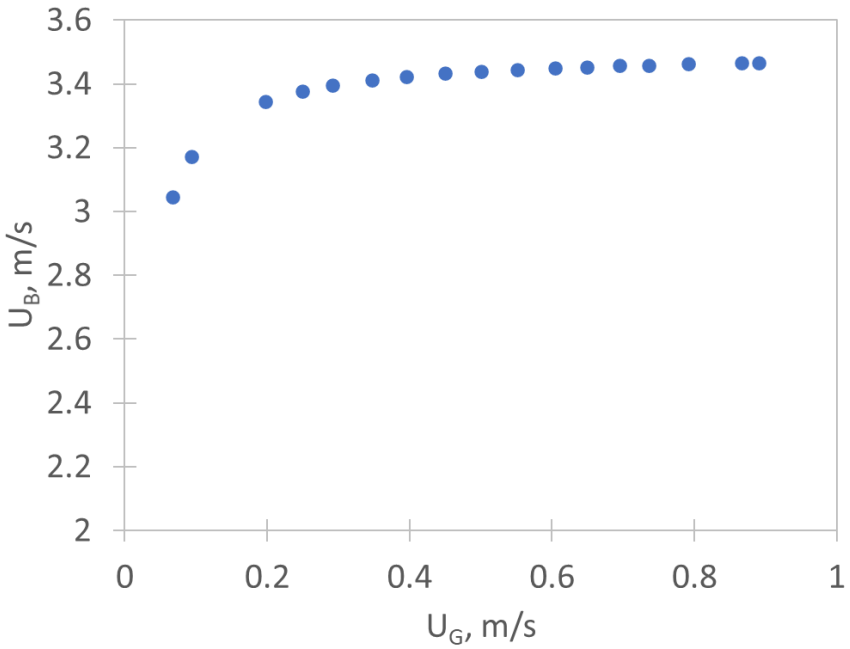

Figure 3-11. Bubble velocity (U_B) as a function of gas velocity (U_G) using the two phase theory.

3.4 Bed Expansion

Accurate predictions of the bed height are needed to estimate the gas residence time inside the bed and to position internals such as cyclone, cyclone diplegs and heat exchanger tubes. Additionally, many correlations for heat and mass transfer require the bed voidage, ε, to evaluate the total bubble volume. Therefore, the ability to model the bed height using standard theory would be helpful during the design phase.

The approximate bed voidage at minimum fluidization from the bulk density of aerated powder:

$$\boldsymbol{\varepsilon_{mf} = 1 - \left(\frac{\rho_B}{\rho_{Particle}}\right) = 1 - \left(\frac{920\,\frac{kg}{m^3}}{1500\,\frac{kg}{m^3}}\right) = 0.387} \qquad (3.5)$$

The voidage of the emulsion phase can be calculated using the correlation from Kai/Furasaki (1986):

$$\frac{H_e - H_{mf}}{H_{mf}} = 580 \mu_g^{0.8} \rho_g^{0.08} \quad (3.6)$$

where: $\varepsilon_e = 0.44$ (3.7)

This emulsion voidage gives an emulsion phase density of 840 kg/m^3, which is close to the measured value of 848 kg/m^3.

From the standard two-phase theory, bed height can be expressed as:

$$H = H_{mf} + (U_G - U_{mf}) \int_0^H \frac{dz}{U_B} \quad (3.8)$$

As a first approximation, the bubble velocity is assumed to be independent of height. The bed heights predicted using the above procedure are presented below in Figure 3-12.

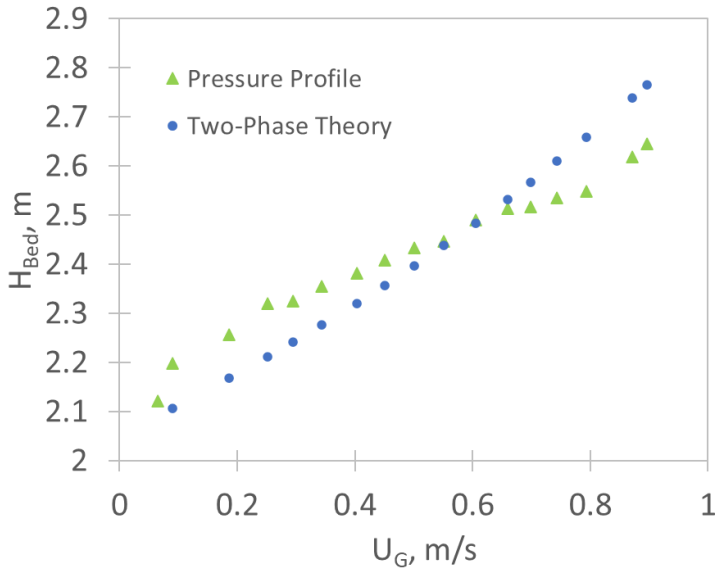

Figure 3-12. Bed height (H_{Bed}) as a function of gas velocity (U_G) predicted from the pressure profile, and the two phase theory.

The model predicts bed heights higher than measured above U_G = 0.6 m/s from the pressure profiles and lower than measured below U_G = 0.6 m/s. The prediction may be improved by considering a change in bubble velocity with height. Using the two-phase theory to extrapolate to Hot Pilot conditions, the bed expansion is expected to be higher than at the Cold Model conditions, and increase with increasing gas velocity. This indicates the entrainment rate, bubble velocity and TDH are also expected to be higher at the Hot Pilot conditions, and should be considered during design and operation.

3.5 Prediction of Transport Disengagement Height (TDH)

The transport disengagement height is the theoretical height above the bed surface above which the flux of entrained particles no longer decreases with freeboard height (Baron et al, 1998). It is a key design parameter, as most processes place the cyclone inlet above the TDH. Predicting the TDH in the Reactor is complex, as the internal cyclone reduces the freeboard cross sectional area up to 40%.

Using the ejection velocity, the TDH can be approximated using the model from Baron et al. (1998):

$$\boldsymbol{TDH = \frac{U_{ej}}{2g}} \tag{3.9}$$

where $\boldsymbol{U_{ej} = 2.1 U_B}$ (3.10)

Using the bubble velocity calculated in Chapter 3.3, the TDH was predicted and plotted as a function of superficial gas velocity in Figure 3-13. The predicted TDH is constant above U_G = 0.2 m/s, where TDH = 2.7 m

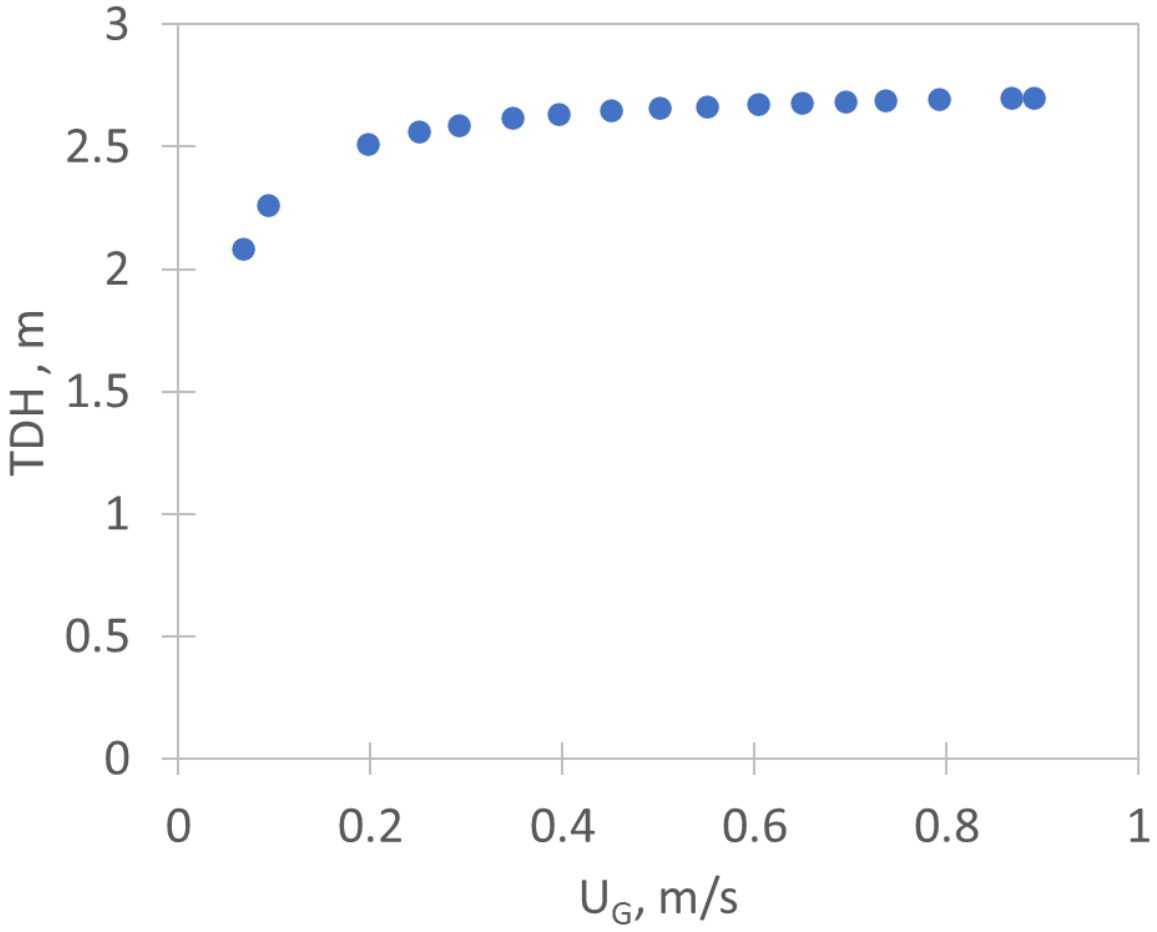

Figure 3-13. TDH using U_B calculated from the two phase theory as a function of gas velocity

Using the ratio of fluidized bed height to defluidized bed height at each gas velocity, the defluidized bed height where the TDH is at the bottom of the cyclone inlet (after the column extension) at each gas velocity was calculated, assuming the value for the TDH was constant (TDH = 2.7 m).

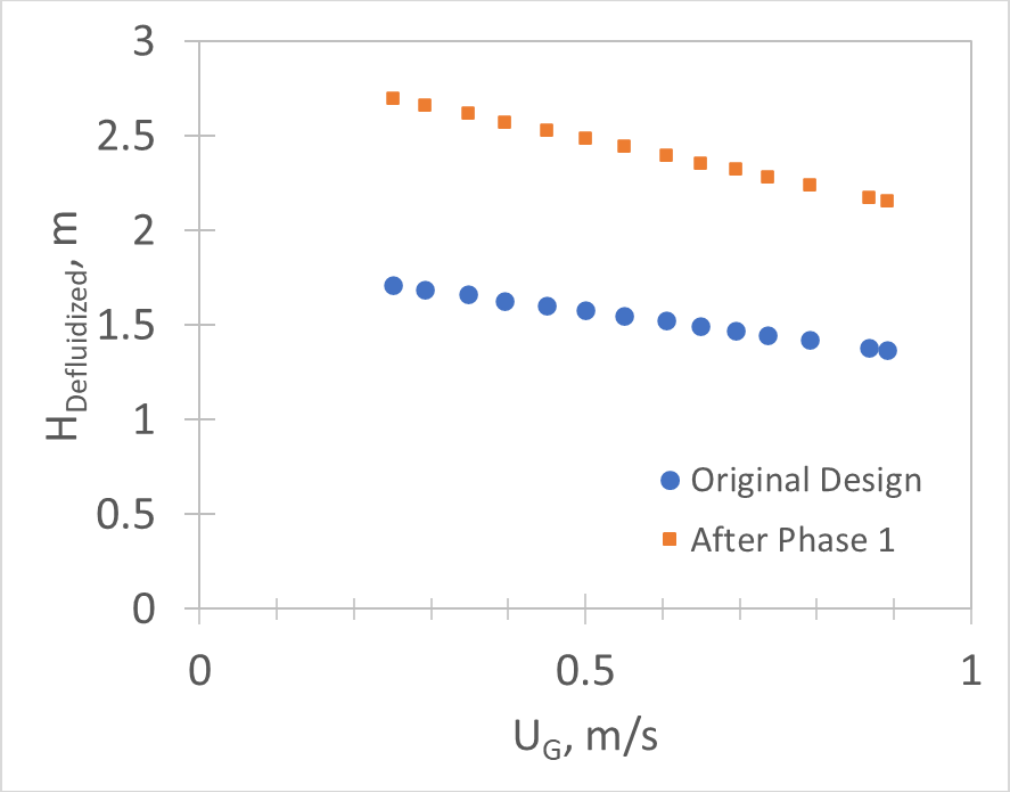

Figure 3-14. Defluidized bed height as a function of gas velocity where TDH is at the bottom of the cyclone inlet.

In practice, the TDH is likely more complex, as below the cyclone inlet there is a transition zone where the cyclone cone decreases in cross-sectional area. Based on this prediction, with the original design, the cyclone inlet would be below the TDH at superficial gas velocities of 0.4 m/s and higher as the minimum height in the Reactor is 1.6 m. After Phase 1 of modifications, operating at a defluidized bed height less than 2.15 m would ensure the cyclone inlet is above the TDH at all the considered gas velocities. The following chapter explores particle entrainment to confirm these predictions.

3.6 Summary

Reactor fluidized bed hydrodynamics were studied using the improved pressure measurements using backflushing gas described in Section 2.2.1.2. Pressure measurements were used to monitor the pressure in the freeboard, fluidized bed density and height, and pressure fluctuations using the coefficient of variation. The power spectra demonstrated that pressure measurements could provide rapid feedback on issues arising during operation due to the improved response time (τ. = 0.016 s). Two methods were used to predict the transition from the bubbling to the turbulent flow regime. It was also shown that the two-phase theory could be used to model the bed expansion and predicts a constant bubble velocity at the superficial gas velocities of interest. The bubble velocity was used to predict the TDH, which was also constant at the superficial gas velocities of interest. The model predicted the TDH at the cyclone cone at most defluidized bed heights and superficial gas velocities.

3.7 References

Arjmandi-Tash, O., A. Zarghami, and R. Zarghami, Dominant Flow Structures in Gas–Solid Fluidized Beds Using Time and Frequency Domains Analyses. *Particulate Science and Technology*, 2014. 32(5): p. 498-505.

Bai, D., Shibuya, E., Nakagawa, N., Kato, K., (1996). Characterization of gas fluidization regions using pressure fluctuations. *Powder Technol*. 87, 105–111.

Baron, T., Briens, C. L., & Bergougnou, M. A. (1988b). Study of the transport disengaging height. *The Canadian Journal of Chemical Engineering*, *66*(5), 749–760. https://doi.org/10.1002/cjce.5450660508

Bi, H. T. (2007). A critical review of the complex pressure fluctuation phenomenon in gas-solids fluidized beds. *Chemical Engineering Science*, *62*(13), 3473–3493. https://doi.org/10.1016/j.ces.2006.12.092

Bi, H. T., Ellis, N., Abba, I. A., & Grace, J. R. (2000). A state-of-the-art review of gas–solid turbulent fluidization. *Chemical Engineering Science*, *55*(21), 4789–4825. https://doi.org/https://doi.org/10.1016/S0009-2509(00)00107-X

Bi, X., Flow Regime Transitions in Gas-solid Fluidization and Transport, in Chemical Engineering. 1994, The University of British Columbia..

Bizhaem, H.K., Tabrizi, H.B., 2013. Experimental study on hydrodynamic characteristics of gas–solid pulsed fluidized bed. *Powder Technol*. 237, 14–23.

Briens, L. and C. Briens, Cycle detection and characterization in chemical engineering. *AIChE Journal*, 2002. 48(5): p. 970-980. 13.

Brink, H.G., J. Saayman, and W. Nicol, Two dimensional fluidised bed reactor: Performance of a novel multi-vortex distributor. *Chemical Engineering Journal*, 2011. 175: p. 484-493.

Chen, Y., Chen, W., Grace, J. R., Zhao, Y., Zhang, J., & Li, Y. (2016). Direct resolution of differential pressure fluctuations to characterize multi-scale dynamics in a gas fluidized bed. *International Journal of Multiphase Flow*, *85*, 380–394. https://doi.org/10.1016/J.IJMULTIPHASEFLOW.2016.05.005

Chen, Y., Jim Lim, C., Grace, J. R., Zhang, J., Zhao, Y., & Zheng, C. (2015). Characterization of pressure fluctuations from a gas-solid fluidized bed by structure density function analysis. *Chemical Engineering Science*, *129*, 156–167. https://doi.org/10.1016/j.ces.2015.02.009

de Martin, L., van den Dries, K., van Ommen, J., 2011. Comparison of three different methodologies of pressure signal processing to monitor fluidized-bed dryers/ granulators. *Chem. Eng*. J. 172, 487–499

Dubrawski, K., Tebianian, S., Bi, H. T., Chaouki, J., Ellis, N., Gerspacher, R., Jafari, R., Kantzas, A., Lim, J., Patience, G., Pugsley, T., Qi, M. Z., Zhu, J. (Jingxu), & Grace, J. (2013). Traveling column for comparison of invasive and non-invasive fluidization voidage measurement techniques. *Powder Technology*, *235*, 203–220. https://doi.org/10.1016/j.powtec.2012.10.031

Ellis, N., et al., Characterization of dynamic behaviour in gas–solid turbulent fluidized bed using chaos and wavelet analyses. *Chemical Engineering Journal*, 2003. 96(1-3): p. 105-116.

Gonzalez, A., et al., Effect of temperature on the onset of turbulent fluidization. 1995.

Grace, J.R., X. Bi, and N. Ellis, Essentials of Fluidization Technology. 2020, Wiley-VCH.

Hurst, H.E., Long-term storage capacity of reservoirs. *Trans. Amer. Soc. Civil Eng.*, 1951. 116: p. 770-808. 12.

Kai T., Furusaki S. (1986). *J. Chem. Eng*. Japan 19 67-71

Knowlton, T. M., & Reddy Karry, S. B. (2020). Essentials of fluidization technology. In *Essentials of Fluidization Technology*. https://doi.org/10.1002/9783527699483

Peters, E.E., Fractal market analysis: applying chaos theory to investment and economics. Vol. 24. 1994: John Wiley & Sons.

Saxena, S.C., Tanjore, V.N., Rao, N.S., (1992). Basic hydrodynamic characteristics of a fluidized-bed incinerator. *Energy Fuels* 6, 502–511.

Schouten, J.C., van den Bleek, C.M., (1998). Monitoring the quality of fluidization using the short-term predictability of pressure fluctuations. *AIChE J*. 44, 48–59.

Seo, M.W., et al., The transition velocities in a dual circulating fluidized bed reactor with variation of temperatures. *Powder Technology*, 2014. 264: p. 583- 591.

Toomey R.F., Johnstone H.F., Chem. Eng. Progress 48 (1952) 220-226.

van Ommen, J.R., Sasic, S., van der Schaaf, J., Gheorghiu, S., Johnsson, F., Copper, M. O., (2011). Time-series analysis of pressure fluctuations in gas–solid fluidized beds—a review. Int. J. *Multiphase Flow* 37, 403–428.

Zhu, H., & Zhu, J. (Jingxu). (2008). New investigation in regime transition from bubbling to turbulent fluidization. *The Canadian Journal of Chemical Engineering*, *86*, 553–562. https://doi.org/10.1002/cjce.20059

Chapter 4

4 Solids Losses from Primary Cyclone

4.1 Introduction

In Fluid Cokers, product vapours rise through the reactor and enter cyclones where entrained coke particles are recovered before the vapours flow to a scrubber. Fine coke particles in the cyclone gas exhaust cause operational issues and premature shut-downs (Briens and McMillan, 2021). Additionally, in the Cold Model and Hot Pilot, it is important to ensure solids losses from the system are not excessive to maintain the system hydrodynamics. Therefore, a good design of the particle recovery equipment is required to minimize shut-downs, and as such, an understanding of the entrainment of fluid coke particles into the cyclone gas exhaust is essential.

4.1.1 Requirements for Operation

During initial testing of the Fluid Coker Cold Model, the requirements for ideal operational conditions were defined as follows:

- The heater vessel operates at a freeboard superficial gas velocity ranging from 0.05 to 0.15 m/s (0.16 to 0.49 ft/s) with a nominal operating condition of 0.1 m/s (0.33 ft/s).
- The reactor vessel operates at a freeboard superficial gas velocity ranging from 0.1 to 1.2 m/s (0.33 to 3.94 ft/s), with a nominal operating condition of 0.6 m/s (1.97 ft/s).
- Losses of entrained solids from the cyclones are less than 0.01 kg/min, with no pulses in entrained solids present.
- The overall cyclone efficiency is greater than 99% for all superficial gas velocities.
- The cyclone inlet is positioned above the Transport Disengagement Height (TDH).

4.1.2 Literature Review

In gas-fluidized beds, bubbles travel upwards to the bed surface and explode, ejecting solids into the freeboard. With increasing column height, the flux of entrained solids decreases as coarser particles fall back towards the bed (Baron et al., 1988a; Large et al., 1976). The average size of the entrained particles also decreases with height (Chew et al., 2015; Cocco et al., 2010). At a certain height, called the transport disengagement height (TDH), the flux and size of solids no longer decrease and become nearly constant (Baron et al., 1988a; Chew et al., 2015; Wen and Chen, 1982; Yoon et al., 1986). In most processes, solids losses from the bed must be minimized. Even moderate solids losses reduce the fines content of the bed and, thus, adversely impact fluidization quality, heat and mass transfer, and standpipe flow. Consequently, entrained solids must be collected and returned to the fluidized bed (Kunii and Levenspiel, 1991).

Cyclones are a cost-effective method to recover solid particles from a gas, using centrifugal forces to drive suspended dust particles through the gas to the wall, where the recovered particles slide down the cyclone cone wall to a dipleg to be returned to the fluidized bed (Dehdarinejad and Bayareh, M., 2021; Mothes and Loeffler, 1985). Cyclones are often arranged in a “train”, involving several stages of collection equipment to improve the solids collection efficiency. Primary cyclones handle higher solids concentrations and collect mainly larger particles (> 30 μm). In addition, primary cyclones are operated at moderate inlet velocities to minimize particle attrition and erosion to the cyclone. Particle collection efficiency may be improved by using several small cyclones in parallel or series, which increases capital costs, or by increasing the cyclone inlet velocity, which increases operation costs and dust re-entrainment from cyclone cone, erosion, and attrition (Huard et al., 2010).

Appropriate design of primary cyclones and diplegs is key to ensuring high collection efficiencies. In most applications, the solids flow down diplegs is too high to use trickle valves that would intermittently open to let solids flow out of the dipleg and then close to prevent gas flow from the bed into the dipleg. Open-ended diplegs used to return collected particles to the fluidized bed require the cyclone inlet to be located high enough to prevent the level of dense solids in the dipleg from reaching the bottom of the cyclone cone, which would result in

significant solids losses from the bed (Bristow and Shingles, 1989; Issangya et al., 2011). Additionally, any gas flowing up from the dipleg into the cyclone cone reduces the cyclone collection efficiency and causes dust emissions (Huang et al., 2018a; Huang, et al., 2018b; Yan et al., 2020). Geldart et al. (1993) found that up to 34% of the gas entering the cyclone can be dragged downwards through the dipleg by the solids at high solids flows. While a high solids flow prevents gas from flowing up the dipleg, the extra gas being carried by the solids increases particle attrition and cyclone pressure drop. Terminations such as plates or angle bends may be used on primary cyclone diplegs to minimize gas flow up the dipleg; however, they may restrict solids flow, resulting in a backup of solids to the cyclone cone (Knowlton, Mountziaris and Jackson, 1986).

For design purposes, it can be assumed that dipleg capacity is limited to the gravity flow of solids, expressed in Equation (4.1) (Zenz, 1975):

$$W_s = \left(\frac{g}{tan\alpha}\right)^{0.5} \rho_B D_e^{0.5} \quad (4.1)$$

where:

D_e is the effective orifice diameter ($D_e = D - 1.5d_{psm}$), m

g is the gravitational constant ($g = 9.81\ m/s^2$)

α is the angle of internal friction, °

At solids fluxes higher than the dipleg capacity, solids cannot be discharged to the bed as quickly as they enter the dipleg from the cyclone. Solids thus accumulate in the dipleg, causing the dense solids level in the dipleg to reach the bottom of the cyclone cone, re-entraining solids into the cyclone vortex. Solids bridging in the dipleg can also result in flow restrictions and reduce the dipleg capacity, resulting in dipleg backup. As such, diplegs smaller than 10 cm in diameter are not recommended in commercial units (Bristow and Shingles, 1989; Dries and Bouma, 1997; Issangya et al., 2011). Aeration taps may improve solids flowability in the dipleg (Li et al., 1997; Mountziaris and Jackson, 1991; Reddy Karri and Knowlton, 2004); however, total aeration

flowrate should be such that no rising slugs are formed in the dipleg. These slugs can explode at the bottom of the cyclone, causing a sharp drop in cyclone efficiency and high dust emissions.

The top of the cyclone inlet should be as close as possible to the top of the cyclone to prevent the formation of a secondary vortex where particles accumulate. As the concentration of solids in the secondary vortex increase, they are released to the primary vortex and disrupt the cyclone flow resulting in a significant increase in dust emissions (Misiulia, Andersson, and Lundström; 2017 Qian and Zhang, 2007). As the outer gas spiral carrying particles travels down the cyclone, the gas dissipates by joining the exiting inner spiral. The natural vortex length is the height below the cyclone inlet where the strength of the rotating gas flow has completely dissipated (Hoffmann et al., 1995). Several empirical correlations have been proposed for predicting the natural vortex length L (Bryant, Silverman, and Zenz, 1983; Ji, Wu, and Shi, 1991; X. Li, et al., 2016), allowing for proper design of cyclone length. Some studies suggest that the ideal cyclone length is slightly longer than the natural vortex length and that collection efficiency is reduced when the cyclone is much longer (Hoffmann et al., 2001; Yang, et al., 2013).

Vortex instabilities can decrease the cyclone efficiency when the vortex intermittently extends down into the cyclone cone, re-entraining solids (Gao, et al., 2020; Grimble, Agarwal, and Juniper, 2017; Peng et al., 2005; Pisarev, et al., 2012; Sun, et al., 2020). Vortex instabilities can also be enhanced from gas flowing up from the cyclone dipleg into the cyclone cone (Sun et al., 2020). Internals that stabilize the vortex can reduce solids re-entrainment from the cyclone cone (Masoud and Marghzar, 2011).

Cyclone efficiency is significantly impacted by the concentration of solids in the gas, initially increasing the efficiency with increasing solids concentration (Zenz, 1982). High concentrations, however, can result in saltation in the cyclone inlet, causing the formation of dunes that move along the inlet. The cyclone operation is interrupted when a dune is introduced, creating a pulse in dust emissions (Fassani and Goldstein, 2000; Mothes and Loeffler, 1985; Trefz and Muschelknautz, 1993).

To reduce the flux of solids entering primary cyclones, they are typically installed above the TDH; however, due to cost constraints, the cyclone may be placed below the TDH. Extensive research has been dedicated to developing predictions and models of the TDH; however, most are unreliable outside of the conditions used for experimental development. The results from several correlations for the TDH were compared by Cahyadi, et al. (2015) and found that predictions of empirical correlations varied by several orders of magnitude after reviewing their application to a wide range of fluidized bed systems. Available correlations or models cannot reliably predict the TDH; this may be due to a lack of understanding of interparticle interactions such as cohesion or clustering effects and inter-species interactions such as collision momentum transfer effects (Cahyadi et al., 2015; Chew et al., 2015), or poor predictions of the ejection velocity from the bed surface. Another possible issue is that the TDH is an arbitrary concept: if the entrained particles result from the sum of the choking flux (F_∞), which does not change with height, and the clusters flux, which decreases exponentially with height above the bed (Baron et al., 1988a), the TDH can then be defined as the height at which the clusters flux becomes negligible when compared to the choking flux; different authors would then report different values depending on what they considered “negligible”.

Agglomerates or “clusters” comprise most particles ejected into the freeboard and have been directly observed in the freeboard of fluidized beds (Cocco et al., 2010). A model to predict the TDH using force balances around clusters was developed by Baron et al. (1988b), where interparticle forces and drag for the largest clusters were neglected. When used in conjunction with the appropriate correlation for the bubble velocity near the bed surface, this model could predict the impact of pressure on the TDH, and predictions agreed well with the results from (Geldart, et al., 1995). However, as mentioned previously, some of the correlations for the TDH reviewed by Cahyadi et al. (2015) could be improved with better bubble property correlations.

As cyclones are typically placed above the TDH, their design depends on good predictions of size distribution and flux of particles entrained above the TDH. Unfortunately, empirical correlations for the solids flux above the TDH (F_∞) are unreliable at conditions outside of those tested during the development of the correlation. Several models, detailed below, have been

developed to predict the properties of particles entrained above the TDH. All models assume that the flux of entrained particles above the TDH equals the maximum flux of particles carried by gas in a dilute phase pneumatic transport line. All models also assume that above the TDH, there are no inertial effects; thus, entrained particles have a terminal free-falling velocity (U_t) that is smaller than the superficial gas velocity in the freeboard (U_G) (Briens, 2021).

In the model developed by Zenz and Weil (1958), entrainment was assumed to be unaffected by fluidization characteristics of the dense bed, while the freeboard was assumed to function as a dilute phase pneumatic transport line. Therefore, this model does not provide an advanced assessment of the entrained particles size distribution. The same assessment for entrained particle size distribution was utilized by Gugnoni and Zenz (1980) as the previous model; however, they accounted for the fluidization characteristics of the dense bed by introducing (U_g - U_{mb}).

Briens et al. (1988) used a different method for predicting the size distribution than Zenz and Weil (1958), and their model fully incorporated the effect of the bed fluidization characteristics. Benoni et al. (1994) considered that entrainment is affected by particle agglomeration. They found that many fine particles are stuck to larger particles and not present as individual particles in the bed. The agglomeration function can be obtained from experimental data and depends on gas, particle, and fluidization properties. Agglomeration is often a result of electrostatic effects, which cause smaller particles to preferentially adhere to larger particles or the column wall (Baron et al, 1992; Benoni et al, 1994; Nakazato and Kato, 2008). Eliminating electrostatic effects by neutralizing particle charges can increase the entrainment flux above the TDH by up to two orders of magnitude (Baron et al., 1987; Baron et al, 1992).

Another consideration in fluidized beds is the flux of solids entrained below the TDH. Several models and correlations have been developed to predict the change in solids flux in the freeboard with height and ejection flux from the bed surface (Kunii and Levenspiel, 1977; Large et al., 1976; Wen and Chen, 1982). Many studies have observed the gradual decrease in the entrained solids flux below the TDH with distance from the bed surface, described by the empirical relationship in Equation (4.2) (Kunii and Levenspiel, 2013):

$$F = F_\infty + (F_0 - F_\infty) \exp(-a \cdot z) \quad (4.2)$$

Wen and Chen (1982) concluded that parameter a is not firmly related to gas velocity or bed characteristics and is typically between 3.5 and 6.5 m^{-1}.

Measurements of the flux and size distribution of entrained particles by Baron et al. (1988a) indicated the flux of clusters decreased exponentially with height, while the flux of individual particles was nearly independent of height. Therefore, they assumed most particles ejected to the freeboard belong to clusters to allow better predictions of the total flux at different heights, using Equation (4.3):

$$F_c = F_{c0} \exp(-a \cdot z) = F_0 \exp(-a \cdot z) \quad (4.3)$$

Clusters are affected by fluctuations in freeboard gas velocity caused by bubble eruptions at the bed surface (Fung and Hamdullahpur, 1993); however, cluster formation is not solely due to hydrodynamics. For example, Cocco et al. (2010) found that cohesive forces, including electrostatics, capillary and van der Waals forces, significantly impact cluster formation.

It is difficult to measure the ejection flux of particles from the bed surface, as it fluctuates significantly even under specific operating conditions. Nevertheless, the flux of solids at the bed surface can be obtained by extrapolating measured values of the flux below the TDH to obtain F_0 in Equation (3.2). Baron et al. (1988b) assumed nearly all ejected particles belong to the clusters to employ this technique. It uses the flux of ejected particles at various vertical positions in the freeboard and the size distribution of these particles by assuming that particles in clusters have the same size distribution as the bed particles. Wen and Chen (1982), Pemberton and Davidson (1986), Chen and Saxena (1978), Saxena and Mathur (1989) proposed empirical correlations to predict the flux of particles ejected from the bed surface; however, none provided satisfactory predictions.

4.1.3 Study Objectives

As a result of the potential operational issues described in the previous section, the objectives pursued in this section of the thesis are:

1. A definition ofthe operational limits of the Cold Model Fluid Coker where solids losses are tolerable (< 0.01 kg/min).
2. Measurement ofthe total flux and size distribution of solids entrained into the cyclone at varying bed masses.
3. Calculation of the TDH using experimental data and comparison with correlations and available models.
4. Development of a model to predict the probability of solids in the dipleg reaching a critical level based on measured fluctuations in the level of solids in the dipleg and pressure fluctuations near the dipleg termination.

4.2 Operational Limits

Prior to performing experiments in the Cold Model, the ideal range of gas velocities was tested in the heater and reactor vessels separately to observe the behaviour of the fluidized bed and identify any operational issues. In addition, cameras at the cyclone exhaust of the reactor and heater vessels were used to monitor operation and identify operational issues.

4.2.1 Original Cold Model Configuration

Refer to Chapter 2.1.2 for details on the Original Cold Model design. The heater cyclone dipleg length limited operation to a defluidized bed height of 0.65 m. Below this height, the dipleg may become uncovered as waves at the bed surface naturally fluctuate, resulting in solids losses from the heater cyclone (Bi, 2007). Above a defluidized bed height of 0.65 m, the solids level may rise higher than the bottom of the cyclone barrel, interfering with the cyclone efficiency and resulting in unacceptable solids losses. The heater vessel was filled to $H_{Defluidized}$ = 0.65 m and fluidized using compressed air at room temperature. The initial superficial gas velocity in the freeboard

was set to 0.05 m/s (0.16 ft/s), then gradually increased to 0.15 m/s. No issues in operation were identified in the heater at this bed level.

The reactor cyclone dipleg allowed operation at several defluidized bed heights; however, when $H_{Defluidized}$ is less than 1.6 m, the dipleg could be uncovered, resulting in significant solids losses from the reactor cyclone. Therefore, preliminary trials were performed at a defluidized bed height of 2.1 m and fluidized using compressed air at room temperature in the All Spargers gas distribution configuration (refer to Figure 2-3). The unit was initially fluidized at a freeboard superficial gas velocity of 0.1 m/s; the gas velocity was then gradually increased, and the unit was allowed to stabilize for 5 minutes at each incremental velocity. As the gas velocity in the freeboard approached 0.4 m/s, high levels of dust emissions were identified at the cyclone exhaust. The appearance of the reactor cyclone exhaust during regular operation and periods of high dust emissions is presented in Figure 4-1.

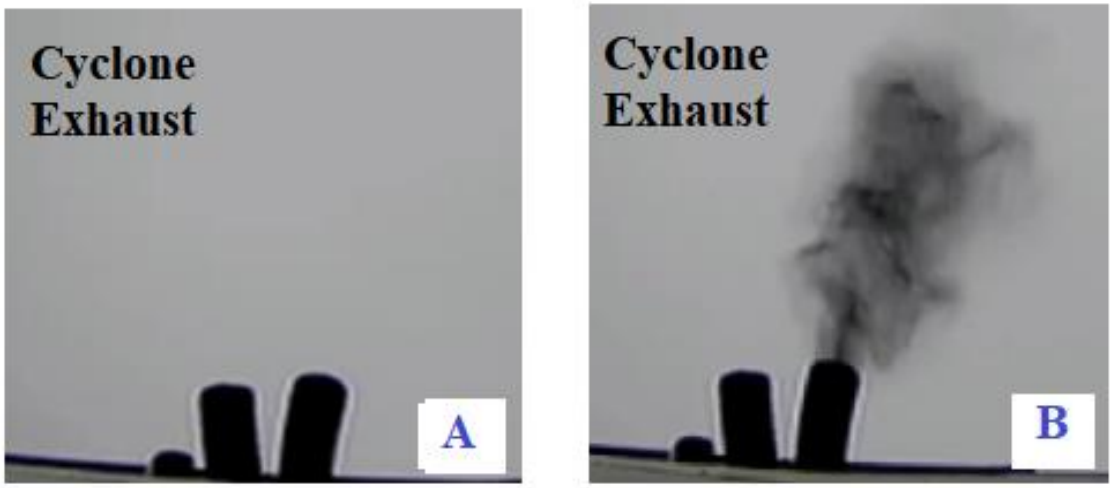

Figure 4-1. Solids losses from cyclone exhaust monitoring during A) regular operation B) during periods of unacceptable solids losses.

The dust emissions resulted from fine coke particles entering the cyclone from the reactor freeboard and escaping through the exhaust rather than being returned to the fluidized bed by the

cyclone dipleg. Over time, as the entrained solids are not returned to the fluidized bed, the bed mass decreases, impacting the hydrodynamics of the system.

Monitoring the cyclone exhaust with a camera identified three distinct solids loss regimes:

- Safe operation (Solids losses < 0.01 kg/min)
- Heavy Pulses: intermittent at low gas velocities (Solids losses ≈ 1 kg/min)
- Continuous Dipleg Backup: a continuous flow of solids escaping cyclone at high gas velocities (Solids losses ≈ 10 kg/min)

In the safe operation regime, dust emissions were not visible from the cyclone exhaust, and the cyclone and dipleg functioned as designed. However, the straight termination to the cyclone dipleg allowed for gas to flow back up the dipleg and into the cyclone, causing slugs to rise and explode at the bottom of the cyclone. Solids thus entered the exiting inner gas spiral of the cyclone, decreasing the cyclone efficiency and resulting in high dust emissions from the cyclone exhaust seen in the heavy pulses regime (Huang et al., 2018a; Huang, et al., 2018b; Yan et al., 2020).

At solids fluxes higher than the dipleg capacity, entrained solids from the freeboard enter the cyclone faster than the solids could exit the dipleg in the fluidized bed. Solids accumulated in the dipleg, causing dense solids to reach the bottom of the cyclone cone. High dust emissions, seen in the continuous dipleg backup regime, were caused as the cyclone pressure drop created a vacuum that sucked solids up the dipleg. Solids bridging in the dipleg could also result in flow restrictions and reduce the dipleg capacity, resulting in dipleg backup (Issangya et al., 2011).

The relative magnitude of solids losses for each regime is illustrated in Figure 4-2. Solids losses were estimated from the change in bed mass over 2-60 minutes, depending on the magnitude. Operation at conditions where solids losses from the system are higher than 0.01 kg/min is not desirable; thus, a definition of the limits around the safe operation regime is required.

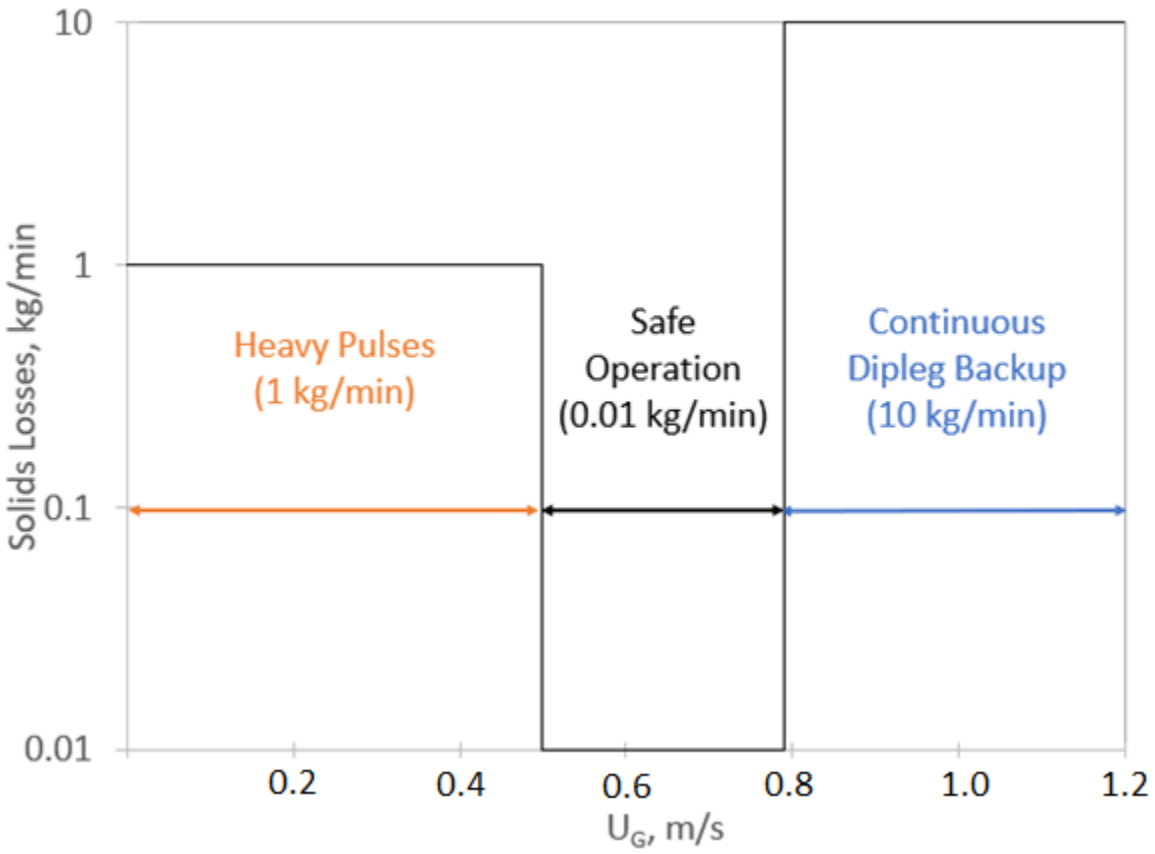

Figure 4-2. Example of magnitude of solids losses for each regime for a $H_{Defluidized}$ = 2.12 m.

The reactor vessel was operated at a range of bed masses and superficial gas velocities while monitoring the cyclone exhaust with a camera to determine the transition velocity between regimes. Figure 4-3 shows the safe operating velocities for the reactor as a function of bed mass.

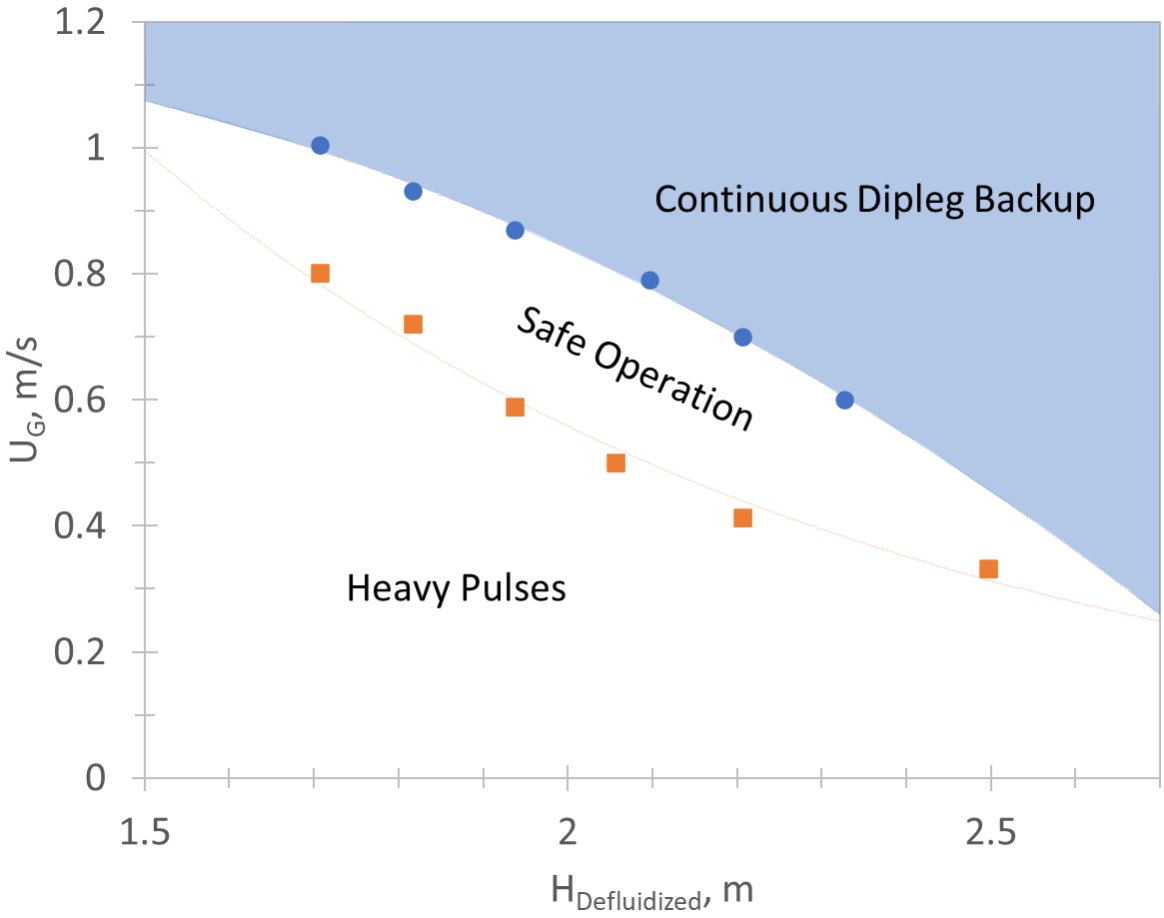

Figure 4-3. Reactor safe operating envelope with original Cold Model configuration and All Spargers gas distribution.

The velocity associated with a regime transition is a function of defluidized bed height, limiting the reactor operation to moderate gas velocities or low bed masses. The heavy pulse regime is shown as the boundary at the safe operation zone, and is the maximum superficial gas velocity where heavy pulses were observed. Heavy pulses were observed at lower superficial gas velocities than the boundary and above the minimum fluidization velocity, however it was not feasible and deemed unnecessary to define a lower limit to the heavy pulse regime as typical operation was not planned in that regime with high solids losses. At the nominal operating condition of U_G = 0.6 m/s, the reactor could be operated at a defluidized bed height between 1.86

and 2.37 m. Therefore, it was determined that modifications to the unit were required to extend the safe operation regime, discussed in the following section.

4.2.2 Phase 1 Modifications

The modifications made to the Cold Model Fluid Coker were detailed in Chapter 2.1.3. Refer to Table 2-1 and Figure 2-12 for more details.

To summarize, modifications made to both the heater and reactor vessels were to:

- Extend the column and dipleg by 0.91 m.
- Increase the dipleg diameter by 0.025 m (1 inch) to a diameter of 0.076 m (3 inches).
- Add an elbow termination to the dipleg.
- Add an aeration tap 0.025 m (1 inch) above the elbow termination.

4.2.2.1 Continuous Dipleg Backup

The impact of the Phase 1 modifications on the safe operating regime was determined by operating the reactor vessel over a range of bed masses fluidized using compressed air at room temperature in the All Spargers gas distribution configuration, described in Chapter 2.1.4 (Figure 2-3). The unit was initially fluidized at 0.1 m/s, and the fluidization velocity was gradually increased while monitoring the cyclone exhaust with a camera to identify high dust emissions. Figure 4-4illustrates the transition from the safe operation regime to the continuous dipleg backup regime for different reactor bed masses.

The continuous dipleg backup regime was not eliminated; however, the transition velocity increased to close to 1 m/s for all bed masses tested. Extending the column height and increasing the dipleg diameter resulted in a lower flux of solids down the cyclone dipleg and reduced the risk of solids bridging in the dipleg. The modifications allow for safe operation at the nominal operating condition of U_G = 0.6 m/s, at defluidized bed heights higher than 2.37 m.

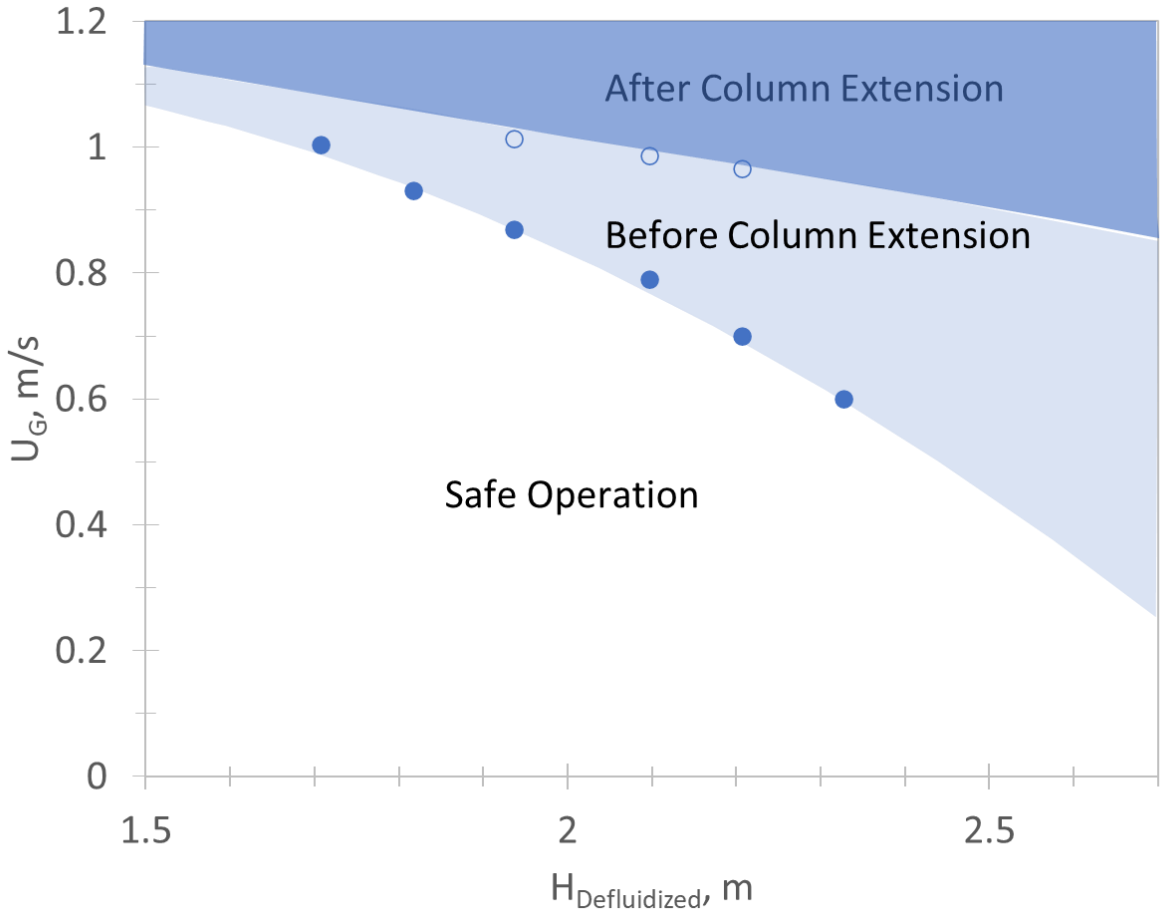

Figure 4-4. Impact of modifications on continuous dipleg backup and heavy pulses and All Spargers gas distribution.

4.2.2.2 Heavy Pulses

While gradually increasing the reactor gas velocity to define the safe operation regime, no heavy pulses were observed from the cyclone exhaust with the Phase 1 modifications. The elbow termination limits gas bubbles from flowing up the dipleg and eliminates the lower limit from the safe operation regime. While the risk of heavy pulses was eliminated, a new solids loss regime was identified. As the superficial gas velocity approaches the transition to the continuous dipleg backup regime, light pulses appear out of the cyclone exhaust. Figure 4-5. Solids losses from

reactor cyclone exhaust during A) Heavy pulse, B) Light pulse shows the difference in appearance between heavy pulses and the newly identified light pulses.

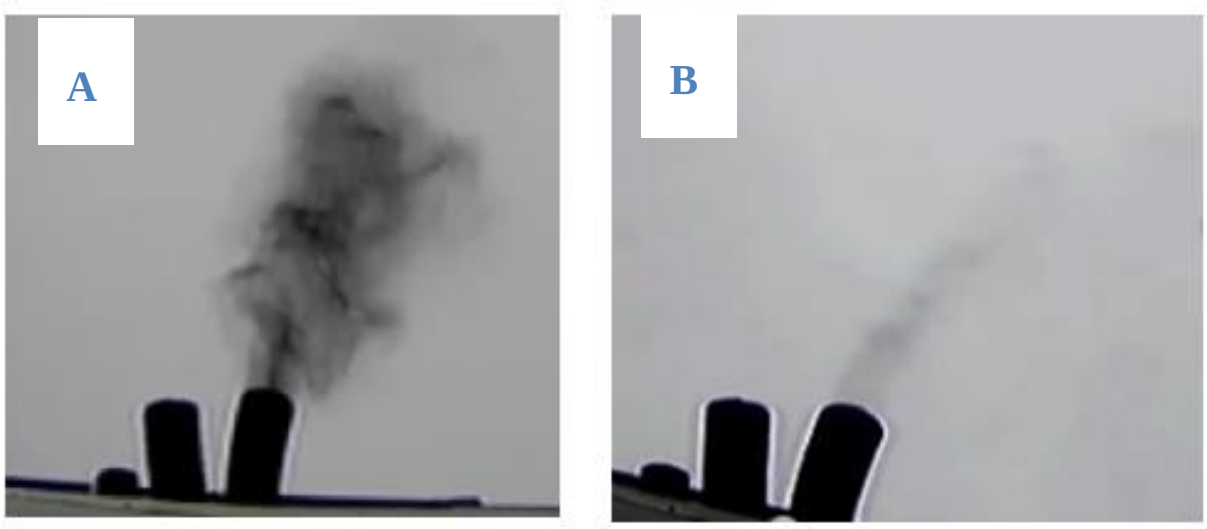

Figure 4-5. Solids losses from reactor cyclone exhaust during A) Heavy pulse, B) Light pulse.

The solids losses are lower in the light pulses regime (≈ 0.1 kg/min) than in the previous heavy pulses regime (≈ 1 kg/min). Figure 4-6 shows the magnitude of solids losses associated with each regime after the Phase 1 modifications to the Cold Model Pilot Plant. Solids losses in the light pulse regime were estimated from the change in bed mass over 60 minutes.

Operating at conditions where solids losses from the system are higher than 0.01 kg/min is not desirable; thus, a definition of the light pulse regime was required. The reactor superficial gas velocity was again gradually increased and allowed to stabilize for 5 minutes at each incremental velocity, until intermittent pulses were observed by the camera. Figure 4-7 shows the transition velocity between the safe operation and light pulses regimes for several defluidized bed heights. While the addition of an elbow termination removed the risk of heavy pulses and increased the safe operation regime, the appearance of light pulses indicates there remains an issue with the flow of solids in the dipleg.

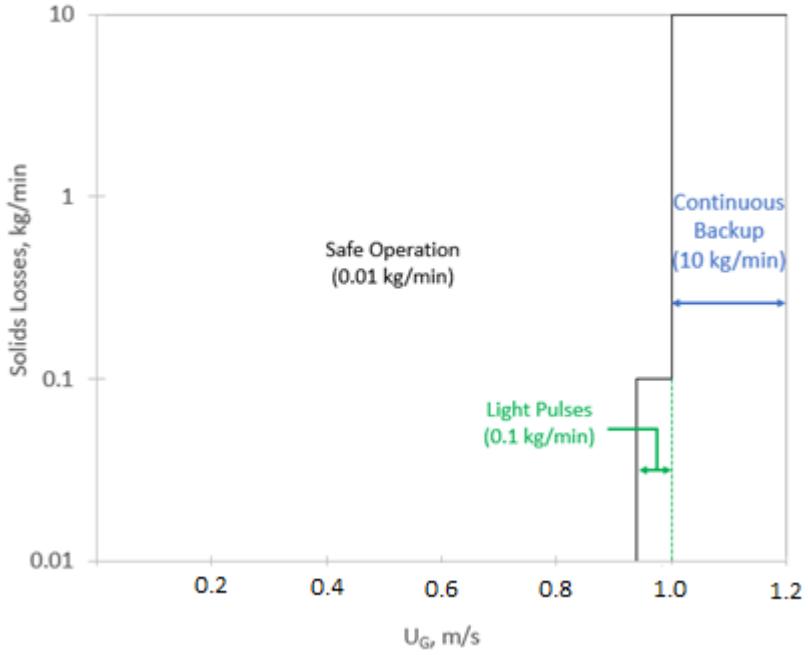

Figure 4-6. Example of the magnitude of solids losses for each regime after Phase 1 modifications for $H_{Defluidized}$ = 1.86 m.

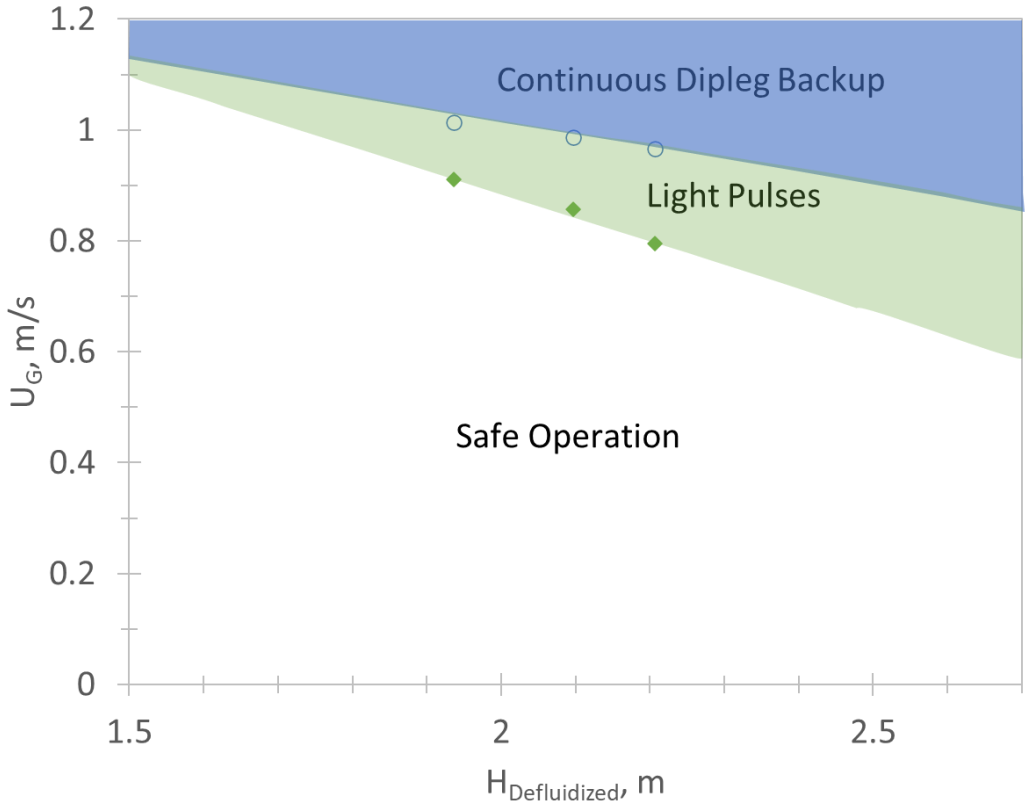

Figure 4-7. Reactor safe operating envelope after modifications with All Spargers gas distribution.

4.2.2.3 Impact of Dipleg Aeration

In addition to increasing the diameter and adding a termination to the dipleg, an aeration tap was installed 0.025 m (1 inch) above the elbow termination. As mentioned in Chapter 2, the fluid coke used in these experiments is near the transition between powder Group A and powder Group B. The entrained solids entering the cyclone are smaller than in the bed and behave as a Group A powder in the dipleg. Aerating such powders can help facilitate their flow and improve the dipleg capacity from the limit of gravity flow (Li et al., 1997; Mountziaris and Jackson, 1991; Reddy Karri and Knowlton, 2004). The dipleg was aerated at $U_{G,AERATION}$ = 0.05 m/s to see if the light pulses regime could be eliminated. Figure 4-8 demonstrates the impact of dipleg aeration on

the safe operation and light pulses regimes. Aerating the dipleg at $U_{G,AERATION}$ = 0.05 m/s increased the velocity where the solids losses transition from the safe operation regime to the light pulses closer to the continuous dipleg backup regime.

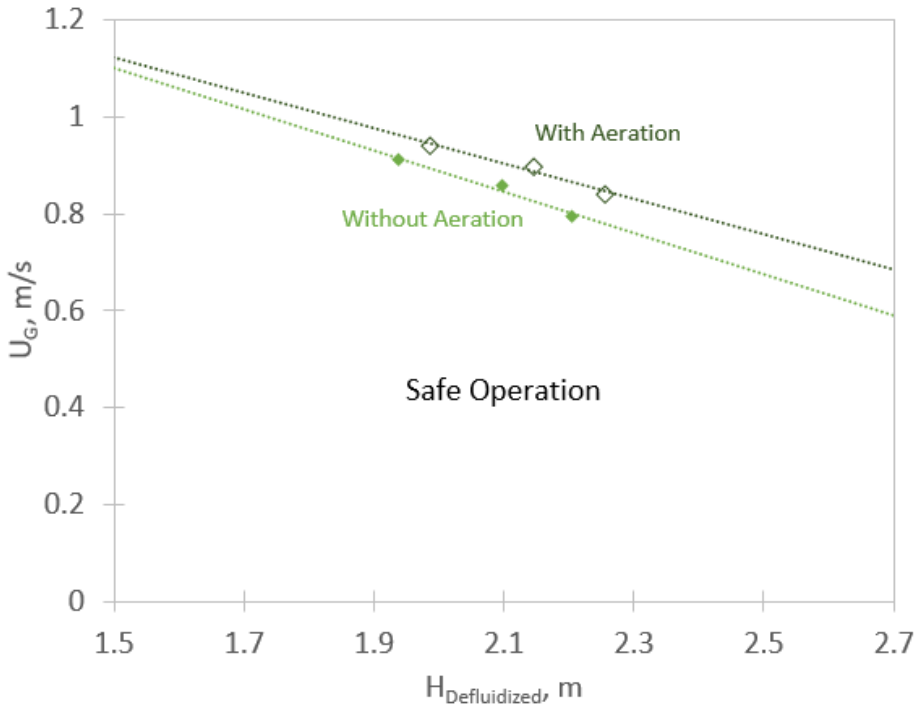

Figure 4-8. Change in light pulse regime with and without dipleg aeration ($U_{G,AERATION}$ = 0.05 m/s) with All Spargers gas distribution.

It should be noted that in this case, the linear regression fit model is a loose approximation based on three points of data. The extrapolation should not be used for predictions, as three data points are not sufficient to indicate a trend. The data collected indicated a sufficient improvement to the original design safe operating zone (Figure 4-3). A deeper examination was deemed unnecessary at this stage, as significant changes to the continuous dipleg backup regime were not expected. Further investigation across a more extensive range of conditions was completed following the Phase 2 modifications (Figure 4-10).

As the light pulses regime could not be eliminated, the impact of $U_{G,AERATION}$ on solids losses from the reactor was required to determine if an aeration flowrate existed that would further extend the range of conditions where solids losses were tolerable (< 0.01 kg/min). For simple operation of the Cold Model Pilot Plant, one aeration flowrate that can be used across all Reactor superficial gas velocities is desired. The solids losses from the reactor were measured using the change in bed mass over 60 minutes (method described in Appendix I). Figure 4-9 summarizes the measured solids losses as a function of $U_{G,AERATION}$ for the nominal operating gas velocity (U_G = 0.6 m/s) and the gas velocity at the transition to the light pulses regime (U_G = 0.9 m/s).

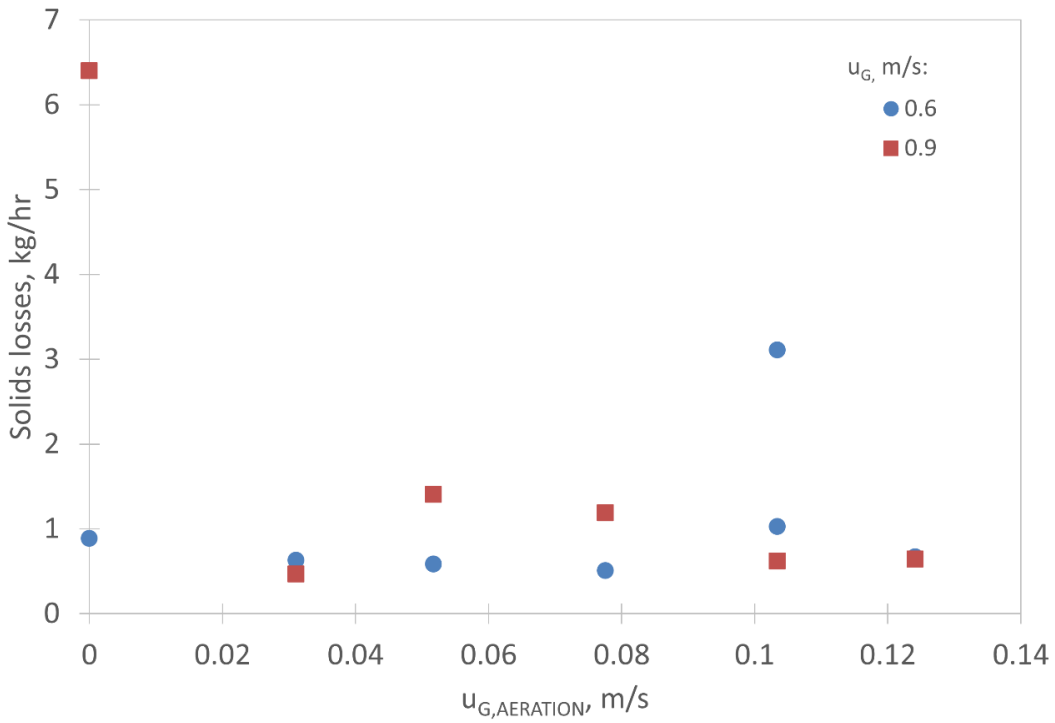

Figure 4-9. Impact of dipleg aeration velocity on solids losses at $H_{Defluidized}$ = 1.94 with All Spargers gas distribution.

When the dipleg was not aerated, the reactor vessel lost 0.89 to 6.40 kg/hr (0.015 to 0.107 kg/min) of fluid coke. When the dipleg was aerated at $U_{G,AERATION}$ = 0.03 m/s, the losses were reduced to less than 0.63 kg/hr (0.011 kg/min), which are acceptable solids losses. Aeration flowrates above $U_{G,AERATION}$ = 0.03 m/s increased the solids losses at U_G = 0.9 m/s and had little

impact at U_G = 0.6 m/s, until a flowrate of $U_{G,AERATION}$ = 0.1 m/s where the solids losses increased. As such, operation at high aeration flowrates can cause the formation of rising slugs in the dipleg that eject solids into the cyclone. Thus, an investigation into the cause of light pulses is required to fully understand the operational limits of the Cold Model Pilot Plant.

4.2.3 Phase 2 Modifications

The Phase 2 modifications made to the Cold Model Fluid Coker were detailed in Chapter 2.1.3. Refer to Table 2-1 and Figure 2-12 for more details.

To summarize, modifications made were to:

- Increase stripper sheds diameter from 0.3 m (12 in) to 0.6 m (24 in).
- Replace Reactor to Heater transfer line (U-bend) with a 45° angled transfer line.
- Increase the Heater to Reactor transfer line (loop seal) from 0.05 m (2 in) to 0.08 m (3 in).

The increased diameter of the stripper sheds would change the distribution of gas in the lower region of the Reactor, and could impact the transition velocities for the solids losses regimes. The same procedure to test the transition velocities between the solids losses regimes was repeated at the same defluidized bed heights to offer a comparison. Figure 4-10 summarizes the superficial gas velocities where light pulses were observed from the cyclone exhaust and when the dipleg entered the continuous dipleg backup regime for different defluidized bed heights.

No significant change to the continuous dipleg backup limit was observed, however, the region where light pulses occur shifted closer to transition to continuous dipleg backup. This allows operation at higher velocities with tolerable solids losses, and could be improved further with aeration, as shown in Chapter 4.2.2.3. Dipleg aeration could not eliminate or shift the continuous dipleg backup zone, however, so caution is required when operating close to the transition to avoid catastrophic solids losses. While the unit modifications improved the safe operating zone, further investigation is required into the cause of the light pulses to implement a solution.

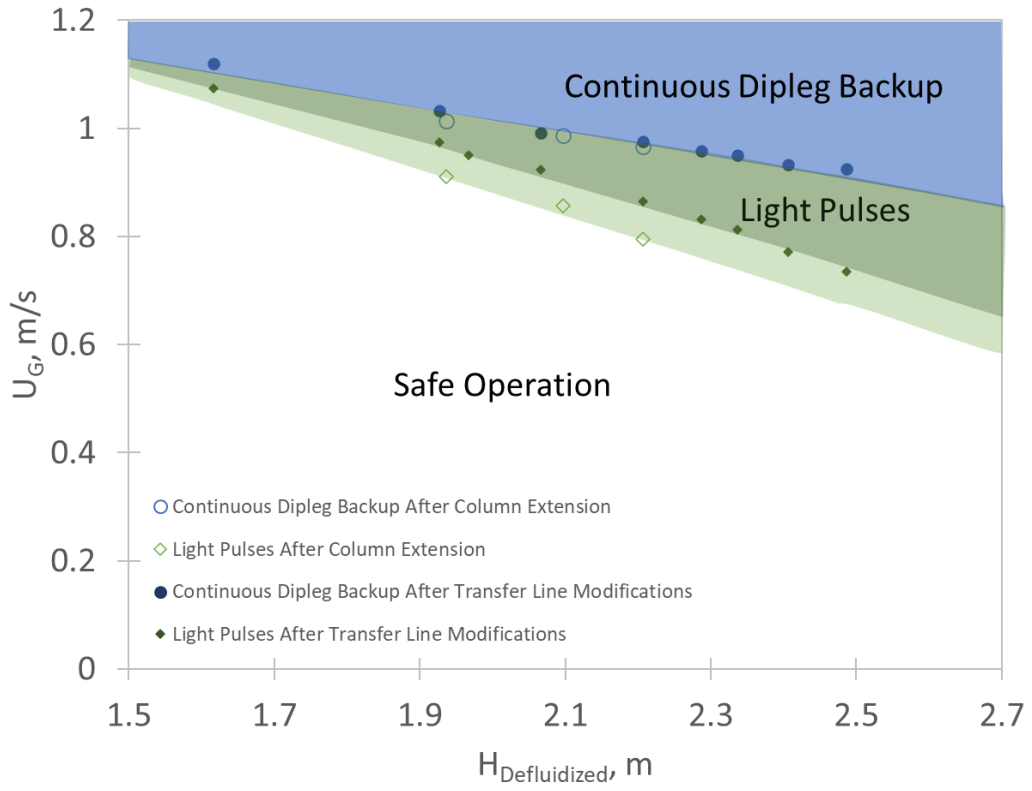

Figure 4-10. Reactor safe operating envelope after Phase 2 of Modifications with All Spargers gas distribution.

4.3 Investigation into Causes of Light Pulses

The previous section observed intermittent light pulses of solids escaping from the cyclone exhaust. There are several potential causes of the pulses, including:

1. Pulses in entrained solids as they enter the cyclone.
2. Re-entrainment of solids from the dipleg into the bottom of the cyclone.
3. Re-entrainment of solids from the cyclone vortex.

4.3.1 Pulses in Entrained Solids

Entrained solids result from gas bubbles exploding at the bed surface, which project solids into the vessel freeboard. Pulses were primarily observed during operation at high gas velocities and thus high solids loadings. Pulses might result from slugging, which is unlikely given the large column diameter, the observed pressure fluctuations, and past studies with coke particles fluidized with air at ambient conditions (Cochet, 2021).

An isokinetic probe was installed in the cyclone inlet to identify pulses in the flux of entrained solids entering the cyclone, where the mass of collected solids was measured online using a balance (readability = ± 0.5 g). A detailed description of the experimental setup and sampling procedure can be found in Chapter 2.3. The collected mass was recorded at various superficial gas velocities for 1 hour with an initial defluidized bed height of 1.94 m. Figure 4-11 presents the change in the mass of collected solids from the cyclone inlet with time over a range of superficial gas velocities, including one (U_G = 0.9 m/s) at the transition to the light pulse regime. No pulses in entrained solids flowrate were correlated with light pulses observed from the cyclone exhaust. However, slight variations in the flowrate of entrained solids may contribute to the light pulses.

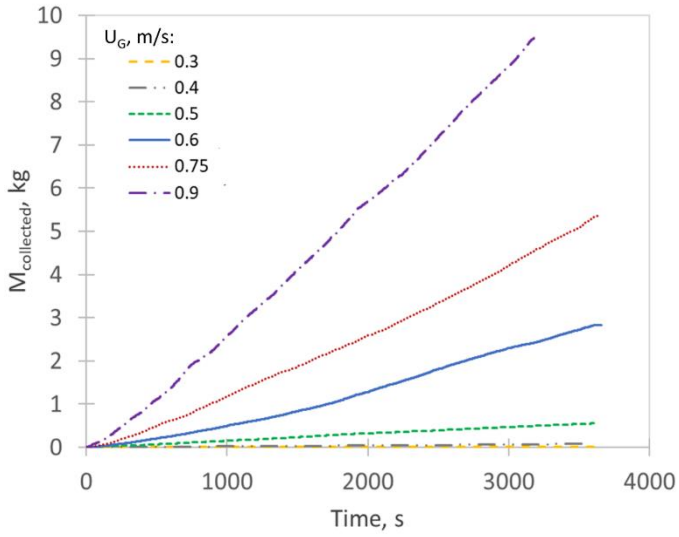

Figure 4-11. Mass of solids collected from the cyclone inlet with time, at $H_{Defluidized}$ = 1.94 m with All Spargers gas distribution.

4.3.2 Re-entrainment from dipleg

Several mechanisms exist by which solids in the cyclone dipleg may be re-entrained into the cyclone vortex, increasing dust emissions, primarily:

- Gas flow up from the dipleg into the cyclone cone (Huang et al., 2018a; Huang, et al., 2018b; Yan et al., 2020).
- High solids flux overwhelming the dipleg capacity, either from entrained particles or small dipleg diameter (Bristow and Shingles, 1989; Dries and Bouma, 1997; Issangya et al., 2011). The dipleg capacity may also be limited by the dipleg termination (Knowlton, Mountziaris and Jackson, 1986; Reddy Karri and Knowlton, 2004).

A pulley and weighted float were installed in the cyclone dipleg to determine if the level of dense solids approaches the cyclone cone, causing solids to be re-entrained. A detailed description of the experimental setup is provided in Chapter 2.4.

4.3.2.1 Original Cold Model Configuration

Preliminary tests were performed on the original Cold Model design (refer to Figure 2-6) to determine the general behaviour of solids in the dipleg during each of the solids losses regimes discussed in Chapter 4.2.1 (i.e., safe operation, heavy pulsing and continuous dipleg backup). After reaching the operating conditions for each regime, the fluidization gas was shut down rapidly, and the pulley lowered to measure the solids level in the dipleg. Figure 4-12 presents the measured solids level in the cyclone dipleg during each of the operating regimes.

During safe operation, solids were measured close to the bed surface, and never approached the cyclone cone. When the unit was defluidized during a heavy pulse (before the pulse had completely stopped), solids were measured at the top of the dipleg or bottom of the cyclone. After entering the continuous dipleg backup regime, the solids were measured near the top of the cyclone. This confirmed that solids were re-entrained from the dipleg into the cyclone cone

during periods of heavy solids losses. As modifications to the unit were planned to improve overall performance, a detailed study was not completed for this configuration.

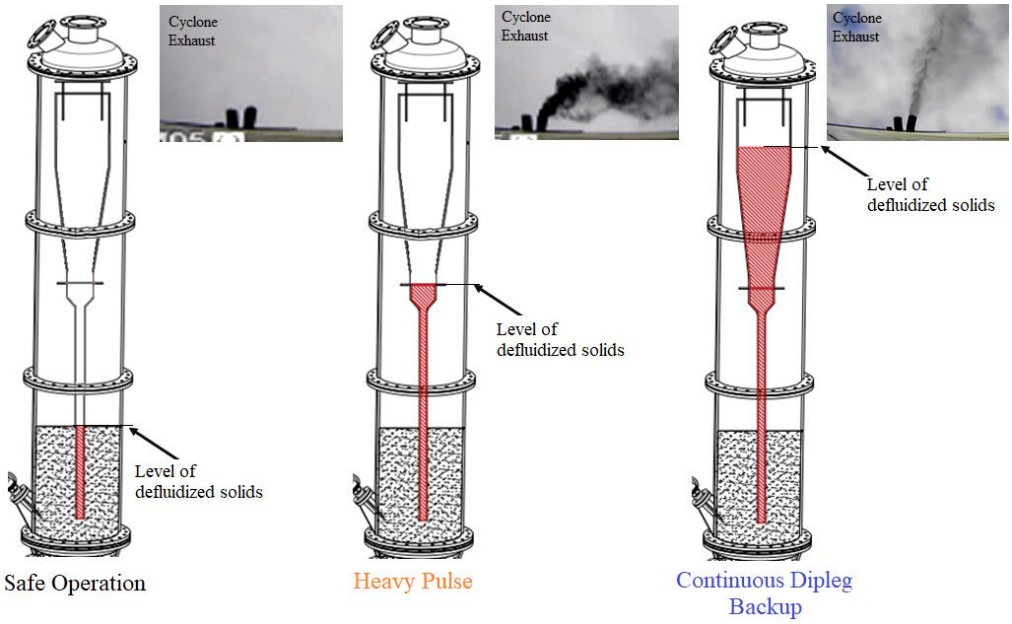

Figure 4-12. Examples of measured level of defluidized solids in the reactor dipleg in the different solids losses regimes.

4.3.2.2 Phase 1 Modifications

As detailed in Chapter 4.2.2, the Phase 1 modifications (Refer to Table 2-1 and Figure 2-12 for summary of modifications) eliminated the heavy pulses and increased the safe operating range, however, light pulses appeared approaching the continuous dipleg backup limit. To study the behaviour of the solids in the dipleg in the light pulse regime, the level of defluidized solids in dipleg was measured (see Chapter 2.4) to determine if light pulses were also a result of solids reaching the bottom of the cyclone cone.

Level measurements were taken 20 times for a combined 100 minutes of fluidization. Theoretically, the level of solids in the dipleg above the bed height can be predicted using a pressure balance around the dipleg, shown in Equation (4.4):

$$z_D = \frac{\rho_{Bed} H_S + \frac{\Delta Pc}{g}}{\rho_D} \quad (4.4)$$

The local density of solids in the dipleg, ρ_D, is higher than the bed density, so the density at minimum fluidization (ρ_{mf}) was used for predictions. Figure 4-13 presents the cumulative probability of measured defluidized solids in the dipleg at a constant gas velocity, and different defluidized bed heights. The level of defluidized solids is presented as Z_C, the distance from the dense solids to the bottom of the cyclone cone.

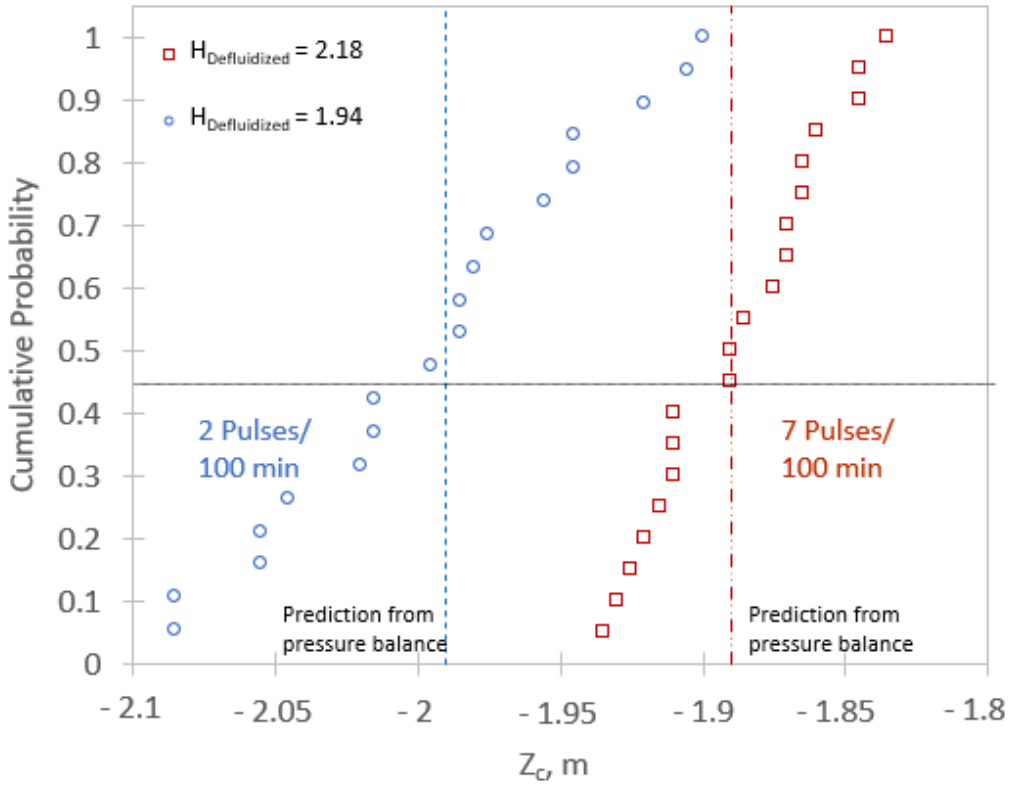

Figure 4-13. Impact of defluidized bed height on the distribution of measured distance to the bottom of the cyclone cone (Z_c) from defluidized solids in the dipleg using All Spargers gas distribution when U_G = 0.6 m/s and the dipleg was not aerated.

The prediction of solids level from the pressure balance agreed well with the median level measured in both cases. Over 100 minutes of fluidization, two light pulses were observed from

the cyclone exhaust at $H_{Defluidized}$ = 1.94 m, while seven pulses were observed at $H_{Defluidized}$ = 2.18 m. The median solids level in the dipleg was closer to the bottom of the cyclone cone (Z_c = 0) at $H_{Defluidized}$ = 2.18 m and correlated with a higher instance of light pulses. If the flow of solids down the dipleg is restricted, or if gas travels up the dipleg to create a slug, the solids have a shorter distance to travel to reach the cyclone cone and become re-entrained at higher defluidized bed heights; this corresponds to the operational limits defined in Chapter 4.2, in which high dust emissions were seen at high defluidized bed heights.

It was shown previously that dipleg aeration could reduce solids losses from the bed. Thus, dipleg aeration was investigated to reduce the solids level in the dipleg, and the frequency of observed pulses was investigated. Figure 4-14 shows the cumulative probability of measured defluidized solids in the dipleg at U_G = 0.6 m/s with and without aeration for a defluidized bed height of 1.94 m.

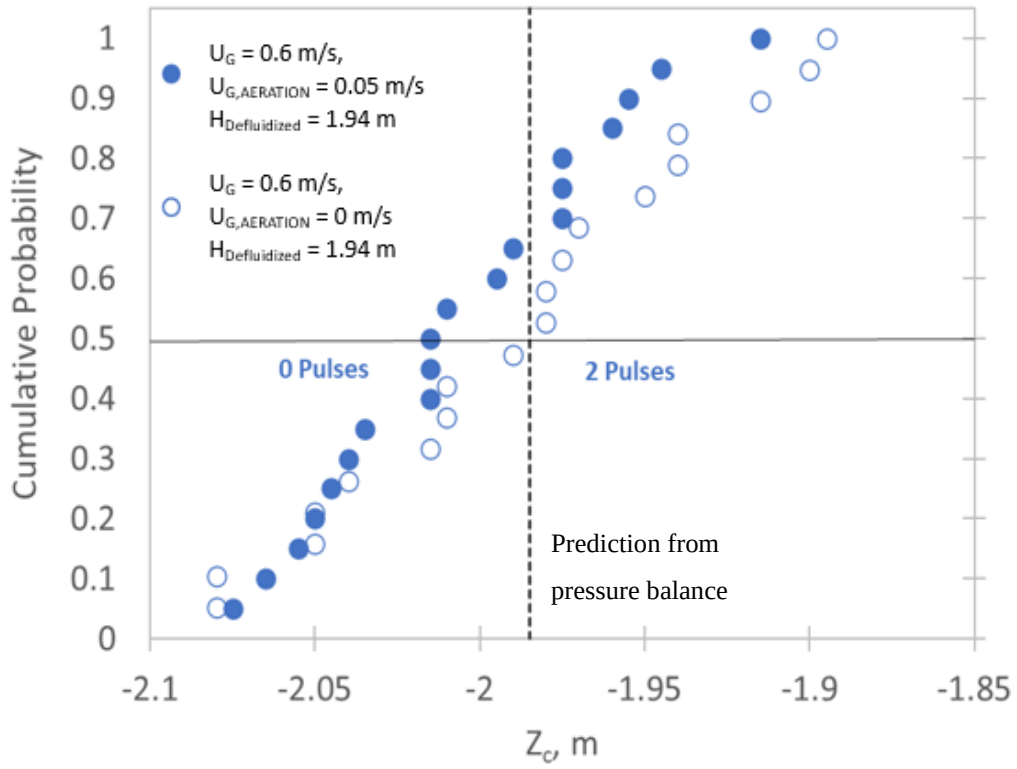

Figure 4-14. Impact of aeration on the distribution of defluidized distance of solids in the dipleg from the bottom of the cyclone (Z_c) with All Spargers gas distribution.

Over 100 minutes of fluidization, 2 light pulses were observed from the cyclone exhaust at $U_{G,AERATION}$ = 0 m/s, while no pulses were observed at $U_{G,AERATION}$ = 0.05 m/s. The prediction of solids level from the pressure balance was higher than the median measured level when $U_{G,AERATION}$ = 0.05 m/s. Aerating the dipleg reduced the median defluidized solids level, corresponding to fewer light pulses and solids losses from the cyclone exhaust. The aerated solids had a longer distance to travel to reach the bottom of the cyclone cone and become re-entrained; therefore, the probability of a pulse occurring was reduced.

To increase the probability of observing a light pulse and shutting off the gas when the solids were in the cyclone, 20 measurements were taken when U_G = 0.9 m/s at a defluidized bed height of 1.86 m, conditions which approach the continuous dipleg backup regime of solids losses. The same procedure was used; however, the fluidization gas was cut off immediately if a pulse was observed in the cyclone exhaust. Figure 4-15 presents the cumulative probability of measured defluidized solids in the dipleg at U_G = 0.9 m/s. Over 100 minutes of fluidization, nine pulses were observed from the cyclone exhaust.

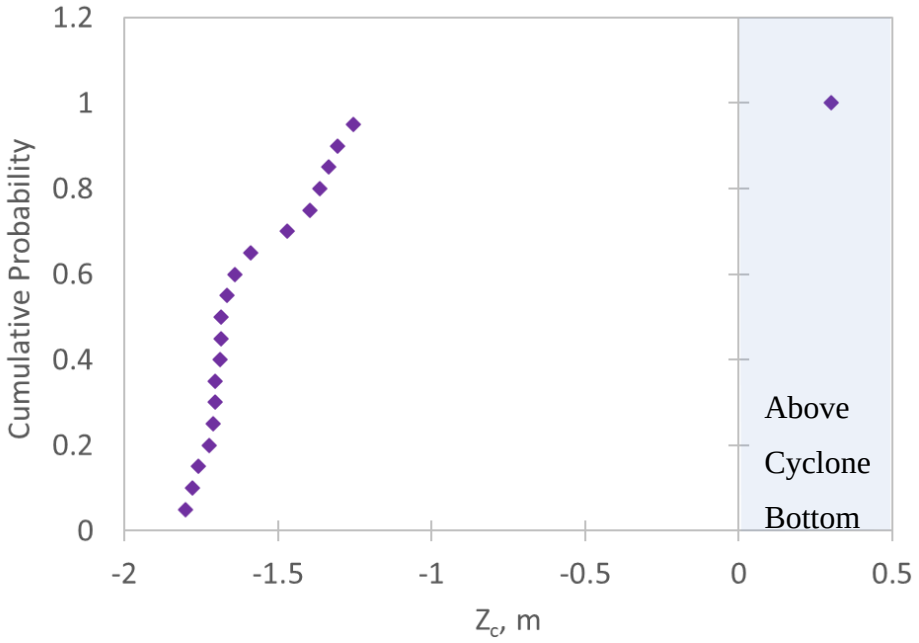

Figure 4-15. Distribution of measured defluidized solids levels as measured distance to the bottom of the cyclone cone (Z_c) at U_G = 0.9 m/s and $H_{Defluidized}$ = 1.94 m (close to continuous dipleg backup regime) using All Spargers gas distribution.

4.3.2.3 Phase 2 Modifications

The increased stripper shed diameter after Phase 2 modification (Refer to Table 2-1 and Figure 2-12 for more) was shown to increase the transition velocity where light pulses occur in Chapter 4.2.3. The dipleg solids level measurements performed in the previous section were completed at the same operating conditions, shown in Figure 4-16.

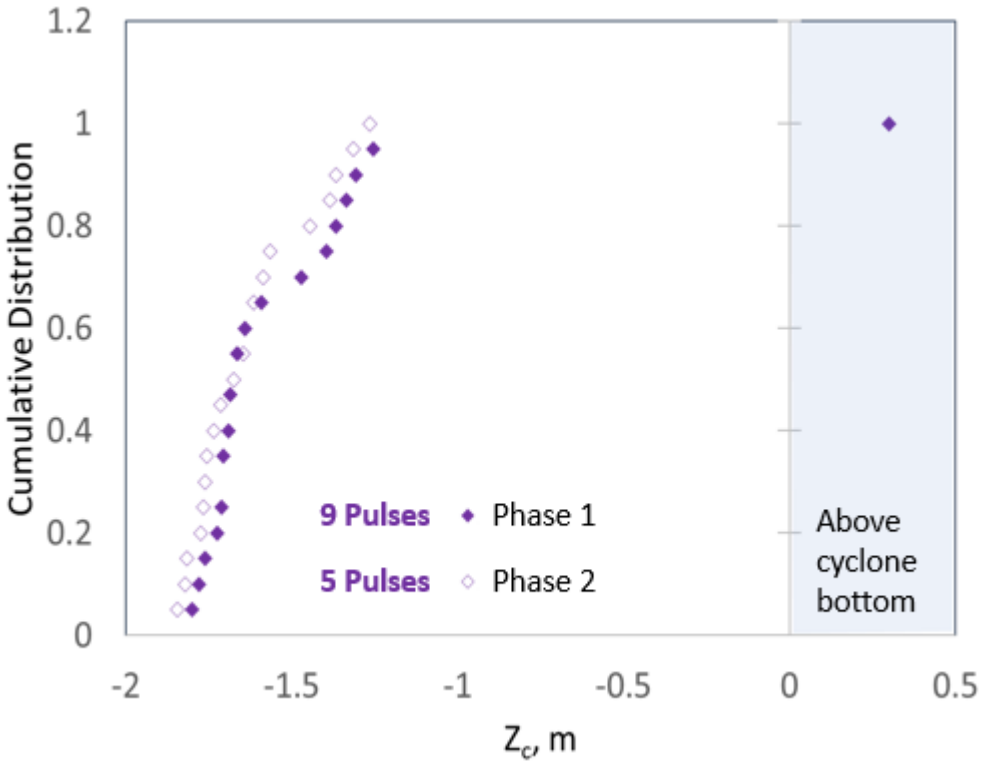

Figure 4-16. Comparison of distribution of measured defluidized solids levels after the column extension and after the transfer line modifications at U_G = 0.9 m/s and $H_{Defluidized}$ = 1.94 m.

There was no significant change in the distribution of solids levels measured below the bottom of the cyclone. Fewer pulses were observed after the change to the stripper section, and no solids were measured above the bottom of the cyclone due to the short duration of individual pulses.

To determine whether the light pulses were still a result of the solids level in the dipleg after the change to the stripper shed, measurements were repeated at a higher gas velocity, U_G = 0.95 m/s. Figure 4-17 shows an increase in the frequency of pulses and probability of catching a pulse by increasing the gas velocity, as the solids level was measured at the bottom or above the bottom of the cyclone 3 times. While re-entrainment of solids from the dipleg explains the light pulses observed in certain operational conditions, it is unclear if they result from flow restriction down the dipleg or gas bypassing in the dipleg. Therefore, further investigation was required to explain and predict the light pulses phenomenon.

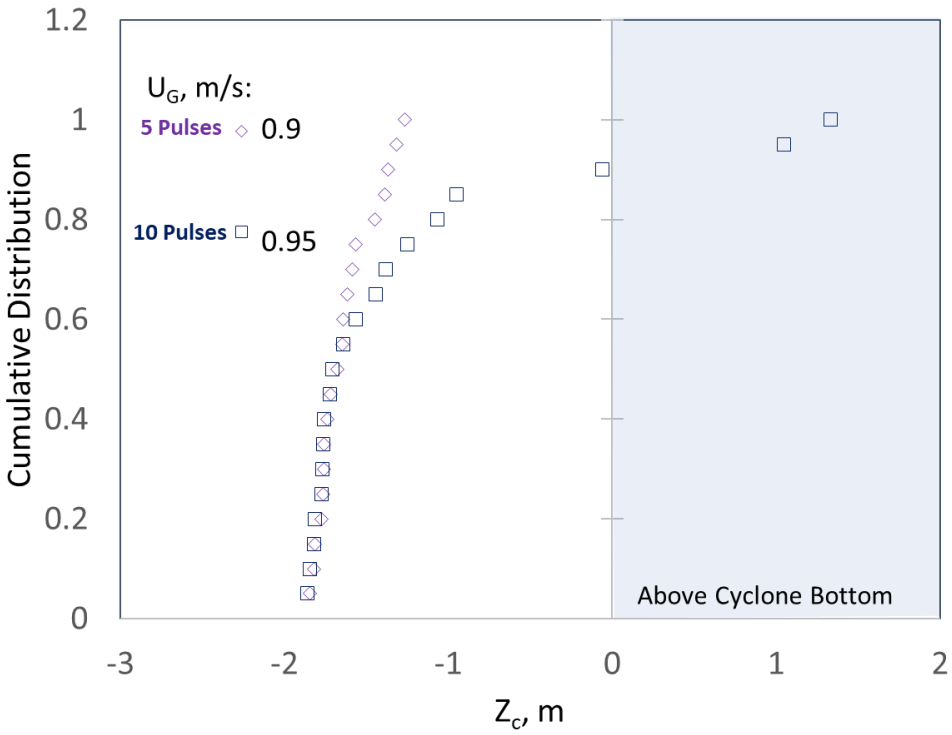

Figure 4-17. Impact of higher gas velocity on the distribution of measured defluidized solids levels after Phase 2 modifications at $H_{Defluidized}$ = 1.94 m.

4.3.3 Re-entrainment from cyclone vortex

As previously mentioned, instabilities in the cyclone vortex can decrease the cyclone efficiency when the vortex intermittently extends down into the cyclone cone, re-entraining solids and causing high dust emissions (Gao, et al., 2020; Grimble, Agarwal, and Juniper, 2017; Peng et al., 2005; Pisarev, et al., 2012; Sun, et al., 2020), which may be enhanced by gas flowing up from the cyclone dipleg into the cyclone cone (Sun et al., 2020). Re-entrainment from the cyclone cone increases with inlet gas velocity (Avci and Karagoz, 2003; Gimbun and Fakhru, 2004). As re-entrainment from the vortex is a function of gas velocity, increasing the bed mass will not increase re-entrainment from the cyclone cone. Increasing the concentration of solids entering the cyclone for the same gas velocity should improve cyclone efficiency (Zenz, 1982). Additionally, changing the gas distribution will not impact the cyclone inlet gas velocity, or re-entrainment from the cone, as the amount of gas being supplied does not change.

As the light pulses correlated with the level of solids in the dipleg, the cyclone vortex was not investigated. Future work may use a camera in the cyclone barrel and internals to stabilize the vortex and reduce solids re-entrainment from the cyclone cone (Masoud and Marghzar, 2011).

4.4 Solids Entrainment into Primary Cyclone

The importance of solids entrainment from fluidized beds was reviewed in Chapter 4.1.2. While no strong pulses in entrained solids were seen using an isokinetic probe in the cyclone inlet in Chapter 4.3.1, the flux of solids in the dipleg will affect the solids level in the dipleg. It is thus essential to know the flux of entrained solids in the reactor across various conditions. Additionally, determining whether the cyclone inlet is above the TDH is required to characterize the unit thoroughly. Predictions of the TDH were completed in Chapter 3.5, specifying conditions where the cyclone inlet is below the TDH, especially before the column extension was completed in Phase 1 of modifications (See Table 2-1 and Figure 2-12). The flux of solids entering the cyclone at each modification phase was therefore measured, and the cyclone efficiency was calculated.

4.4.1 Original Design

The flux of entrained solids entering the cyclone was measured using an isokinetic probe located in the cyclone inlet. A detailed description of the experimental setup and sampling procedure can be found in Chapter 2.3. Using the All Spargers gas distribution, solids were collected at various superficial gas velocities and defluidized bed heights for between 3 and 30 minutes, depending on the solids flux. The bed height was determined using the vertical pressure profile in the bed, as described in Chapter 3.1 (see Figure 3-2).

Figure 4-18 presents the flux of entrained solids entering the cyclone as a function of bed height. It shows that the flux of particles increased with bed height for each gas velocity.

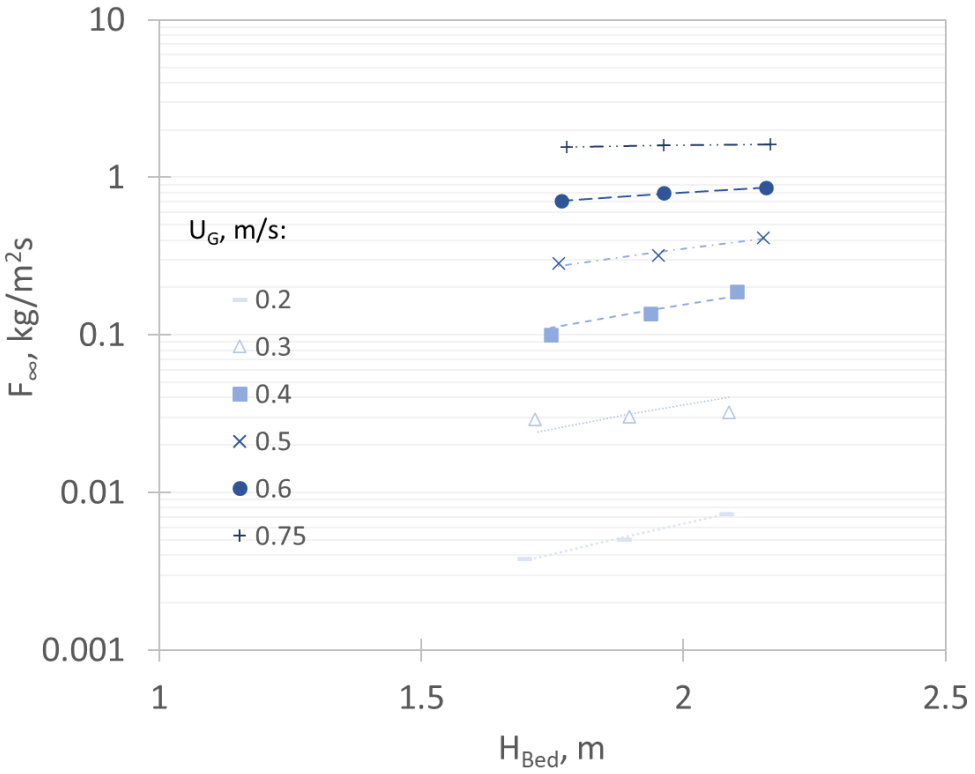

Figure 4-18. Flux (F_∞) in the freeboard cross-section at the top of the cyclone of entrained solids collected from the cyclone inlet as a function of bed height (H_{bed}) using All Spargers gas distribution.

The flux was fitted as a function of bed height using the following Equation (4.5):

$$F = a \cdot H_{Bed}^{b} \tag{4.5}$$

The coefficients used to fit the data were summarized in Table 4-1. Using a linear regression on the flux as a function of bed height, the probability that the slope, b, is negative was calculated and summarized below in Table 4-1. It should be noted in this case, the linear regression fit model is a loose approximation based on three points of data. The extrapolation should not be used for predictions, as three data points are not sufficient to indicate a trend. However, this was considered acceptable as the unit was to be modified, and entrainment values were expected to change.

Table 4-1. Summary of coefficients for $F_\infty = a \cdot H_{Bed}^{b}$ for flux measured with Original Cold Model design.

U_G, m/s	a	b	Probability b is Negative, %
0.2	0.0006	3.338	9.7
0.3	0.0059	2.604	4.85
0.4	0.0278	2.485	8.9
0.5	0.0918	1.941	17.8
0.6	0.4197	0.937	45.2
0.75	1.4031	0.191	99.9

The flux sensitivity to bed height increased with increasing gas velocity, indicating the cyclone inlet was below the TDH at superficial gas velocities above 0.5 m/s and below the intermediate cyclone zone. As reviewed previously, Benoni et al. (1994) developed a model to predict the flux of particles entrained above the TDH, accounting for the agglomeration of smaller particles onto larger particles. Figure 4-19 compares the fluxes measured and predictions with the Benoni model. The fluxes shown are the average value across the bed heights presented in Figure 4-18.

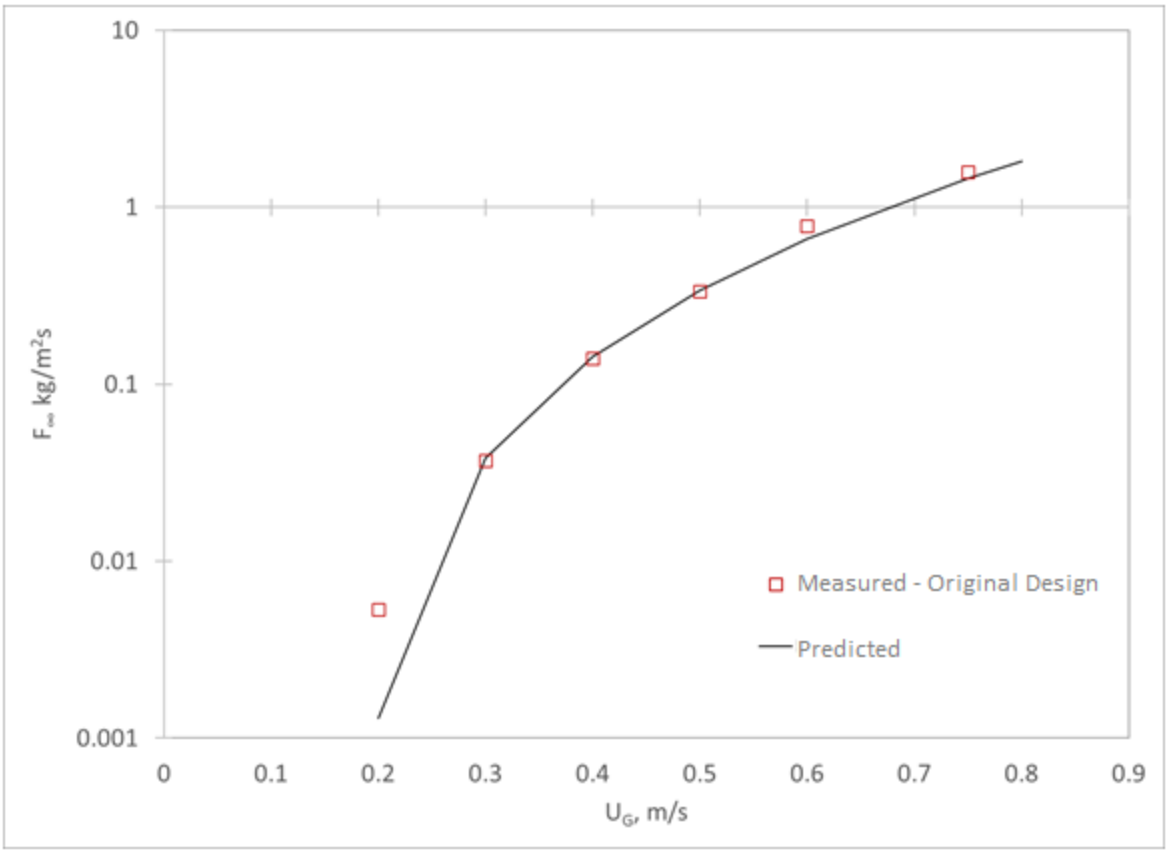

Figure 4-19. Flux of particles entrained above the TDH with Benoni model.

It shows good agreement between the measured and predicted flux; however, the measured flux was higher than the predicted flux in all cases. The agreement between measured and predicted flux above the TDH suggests that the cyclone inlet is above the TDH at all conditions before the column extension.

Another method to confirm the location of the cyclone inlet to the TDH is to analyze the size of entrained particles. The particle size distribution for each sample was measured using a HELOS (H2316) particle size analyzer (see Appendix B). Particle size distributions are available in Appendix I. The change in Sauter-mean diameter with gas velocity is shown in Figure 4-20. The Sauter-mean diameter increased with U_G, as higher velocities allow larger particles to be carried without inertial effects (Do and Grace, 1972). Increasing the defluidized bed height had little

impact on the Sauter mean diameter at each gas velocity; however, differences above U_G = 0.6 m/s indicate some impact.

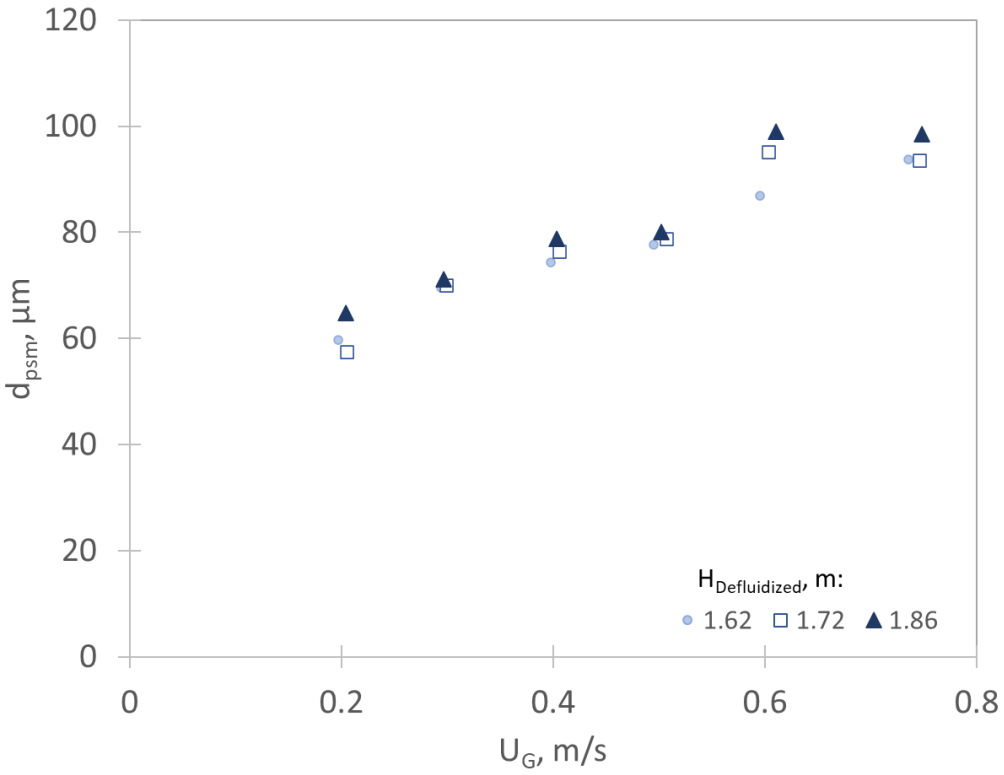

Figure 4-20. Change in Sauter mean diameter of entrained particles at cyclone inlet with U_G with All Spargers gas distribution.

It has been shown that the average size of entrained particles decreases with distance from the bed surface until the TDH, above which the average particle size no longer decreases and becomes nearly constant (Baron et al., 1988a; Wen and Chen, 1982; Yoon et al., 1986). Consequently, the cyclone inlet was likely below the TDH at gas velocities higher than 0.5 m/s and defluidized bed heights above 1.72 m.

4.4.2 Phase 1 Modifications (After Column Extension)

As detailed in Chapter 2.1.3, the column and cyclone dipleg were extended by 0.91 m (3 ft) (Refer to Table 2-1 and Figure 2-12 for more details). The updated flux of solids into the cyclone (and dipleg) was required to characterize the new system properly. The flux of entrained solids entering the cyclone was measured using the same isokinetic probe in the cyclone inlet. Replicate measurements were made at every defluidized bed height tested for U_G = 0.4 m/s and U_G = 0.6 m/s to provide confidence in the measurements made at nominal operating conditions. Several replicates were also completed at U_G = 0.3 m/s and U_G = 0.8 m/s at a lower and higher superficial gas velocity to demonstrate the repeatability outside the nominal operating range. Due to the extension, higher defluidized bed heights could be explored in this section; however, at U_G = 0.9 m/s, the operation was limited to defluidized bed heights below 2.18 m. Figure 4-21 presents the change in the flux of entrained solids entering the cyclone with bed height. It shows that the flux of particles increased with bed height for each gas velocity.

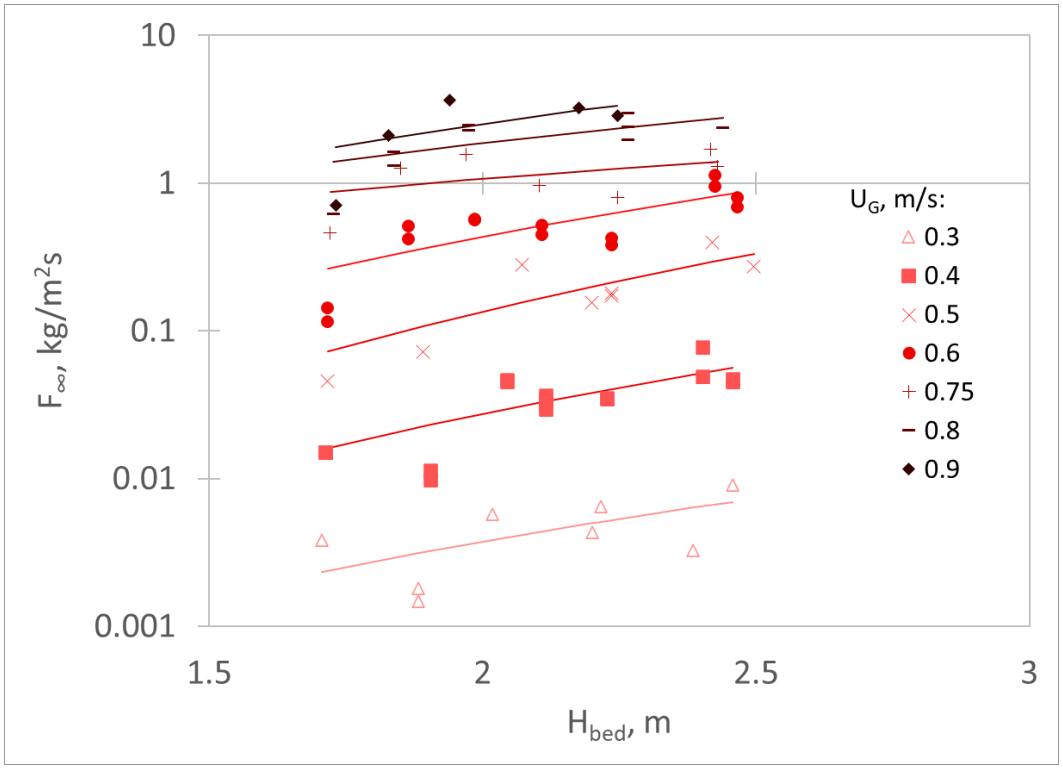

Figure 4-21. Change in entrained particle flux (F_∞) in freeboard cross-section at the top of the cyclone with bed height after phase 1 modifications with All Sparger gas distribution.

The flux was fit as a function of bed height using Equation (4.5). The coefficients for each gas velocity are summarized in **Error! Not a valid bookmark self-reference.** Additionally, the flux as a function of bed height was fit using a linear regression model. Finally, the probability that b was negative was calculated across the gas velocities and summarized in Table 4-2.

Table 4-2. Summary of coefficients for Equation (4.5) for flux measured after Phase 1 of Cold Model modifications

U_G, m/s	a	b	Probability b is Negative, %
0.3	0.0005	2.985	9.2
0.4	0.0025	3.482	6.6
0.5	0.0081	4.051	5.5
0.6	0.0446	3.276	7.5
0.75	0.4138	1.367	27.5
0.8	0.4719	1.977	13.4
0.9	0.4530	2.474	9.9

The flux was not very sensitive to changes in the bed height, indicating the cyclone inlet was likely above or near the TDH. However, the flux appeared to have reached a plateau in the middle range of bed heights tested. This plateau is likely due to the geometry of the internal cyclone (See Chapter 2.1.3 and Figure 2-12), where above the cyclone cone, there was a cylindrical section with a constant cross-section. The distance from the top of the cone to the bottom of the cyclone inlet was 36 cm. Using the fluidized bed heights where the fluxes plateau

at U_G = 0.6 m/s as an example, the range was estimated to be 36 cm. The flux increases above the subsequent measurement at H_{Bed} = 2.42 m, indicating that in this configuration the cyclone inlet was below the TDH. Below a bed height of H_{Bed} = 1.86 m, the TDH was in the cyclone cone, where the fraction of freeboard occupied by the cyclone decreased, decreasing the local superficial gas velocity and flux.

Since the cyclone inlet was below the TDH except for the highest defluidized bed height, the measured fluxes were predicted using the model from Benoni et al. (1994), using the average flux across all bed heights below the TDH. Figure 4-22 compares the measured fluxes, both before and after the column extension to the fluxes predicted with the Benoni model.

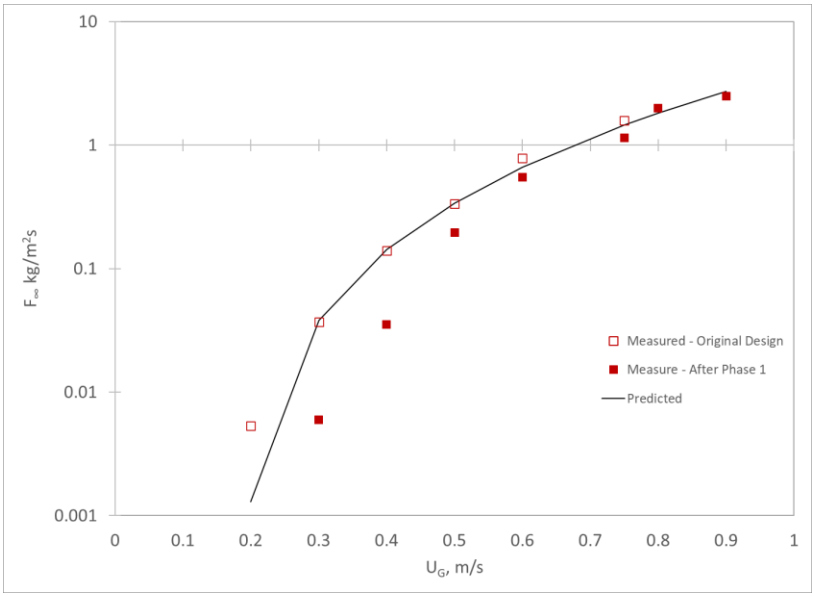

Figure 4-22. Predicted flux of particles entrained above the TDH with Benoni model compared to measured fluxes from the original design and after Phase 1 modifications.

The fluxes were lower after Phase 1 modifications when compared to the original design across all measured gas velocities, demonstrating the impact of the column extension. The Benoni

model assumes a diameter below which particles are 100% agglomerated and above which 100% are not agglomerated. A particle diameter of 50 µm was used for these predictions.

Figure 4-23 shows the weight fraction ratio in solids measured in the cyclone inlet to the weight fraction in the bed as a function of d_{pi}, for each size cut. The results are shown for a defluidized bed height of 1.62 m with the original Cold Model design and after Phase 1 of modifications.

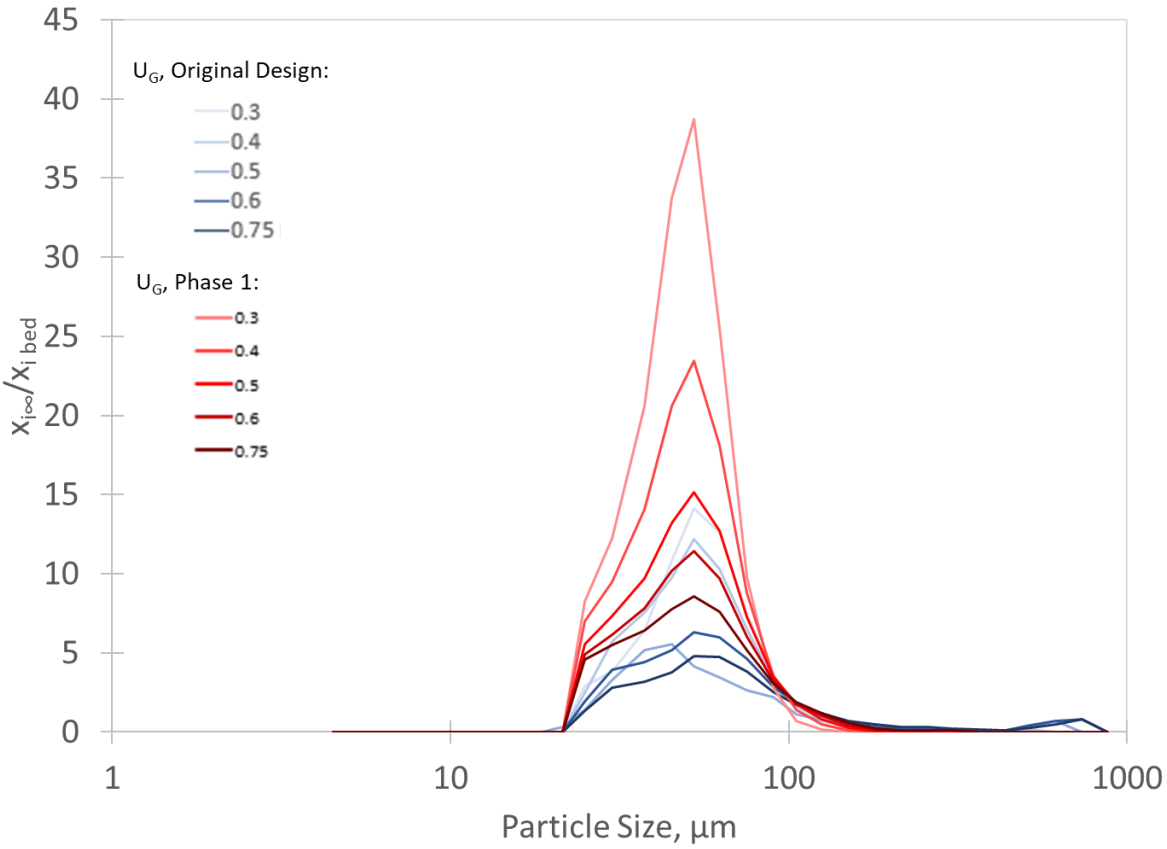

Figure 4-23. Weight fraction of entrained particles to weight fraction of bed particles in each size cut for the measured flux in the original design, and after Phase 1 modifications for a defluidized bed height of 1.62 m.

The peak appeared at the same particle size, 52 µm, across most conditions shown; however, after the Phase 1 modifications, the peak was much more substantial, especially at lower gas velocities. This more substantial peak indicates more agglomeration for the measurements made after Phase 1 modifications, which would explain the lower fluxes seen in Figure 4-22.

Final confirmation on the location of the cyclone inlet in relation to the TDH is to look at the size of entrained particles. The change in Sauter-mean diameter with gas velocity is presented in

Figure **4-24**. The Sauter-mean diameter increased with U_G, as higher velocities allow larger particles to be carried to farther levels above the bed surface (Chew et al., 2015; Do and Grace, 1972). Although there is scatter in the Sauter mean diameter, increasing the defluidized bed height had minimal impact at each gas velocity, and there is no definite trend. Based on the flux and size distributions discussed, there is significant agglomeration in the bed, and operating at fluidized bed heights below 2.24 m will ensure the cyclone inlet is above the TDH.

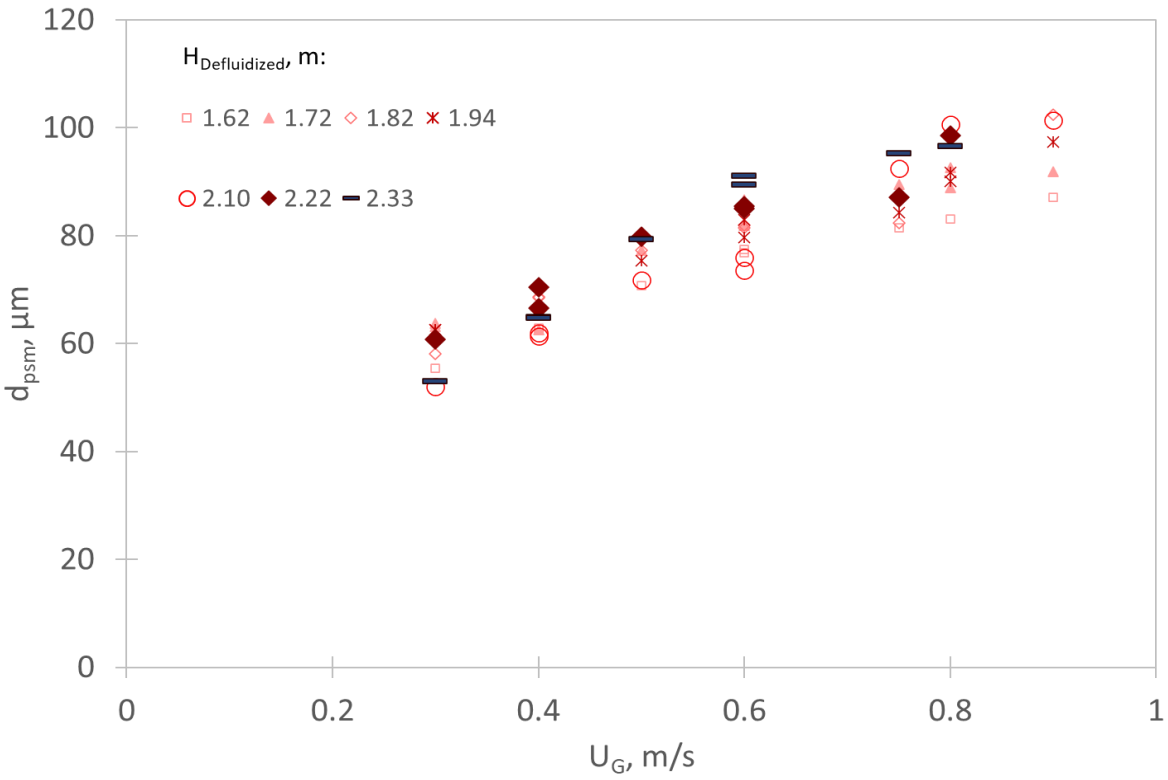

Figure 4-24. Change in Sauter-mean diameter of entrained solids after column extension.

4.4.3 After Phase 2 Modifications

The solids fluxes entering the cyclone for the final configuration of the Cold Model (Refer to Table 2-1 and Figure 2-12 for more details) were measured using an isokinetic probe in the cyclone (detailed in Chapter 2.3). Due to the improved safe operating envelope after Phase 2 of Modifications (see Figure 4-10), samples were taken at U_G = 1 m/s and 1.15 m/s for defluidized bed heights below 1.72 m. In addition, samples for U_G = 0.9 m/s could also be taken at higher defluidized bed heights than in the previous section. Replicate measurements were made at every defluidized bed height tested for U_G = 0.4 m/s and U_G = 0.6 m/s to provide confidence in the measurements made at nominal operating conditions. Additionally, replicates were made at both defluidized bed height tested at U_G = 1.0 m/s and U_G = 1.15 m/s to ensure accurate measurements at the operational limit of the system. Several replicates were also completed at U_G = 0.3 m/s, U_G = 0.8 m/s and U_G = 0.9 m/s at a lower and higher superficial gas velocity to demonstrate the repeatability outside the nominal operating range.

Figure 4-25 shows the change in the flux of entrained solids entering the cyclone with bed height. It shows that the flux of particles increased with bed height for each gas velocity.

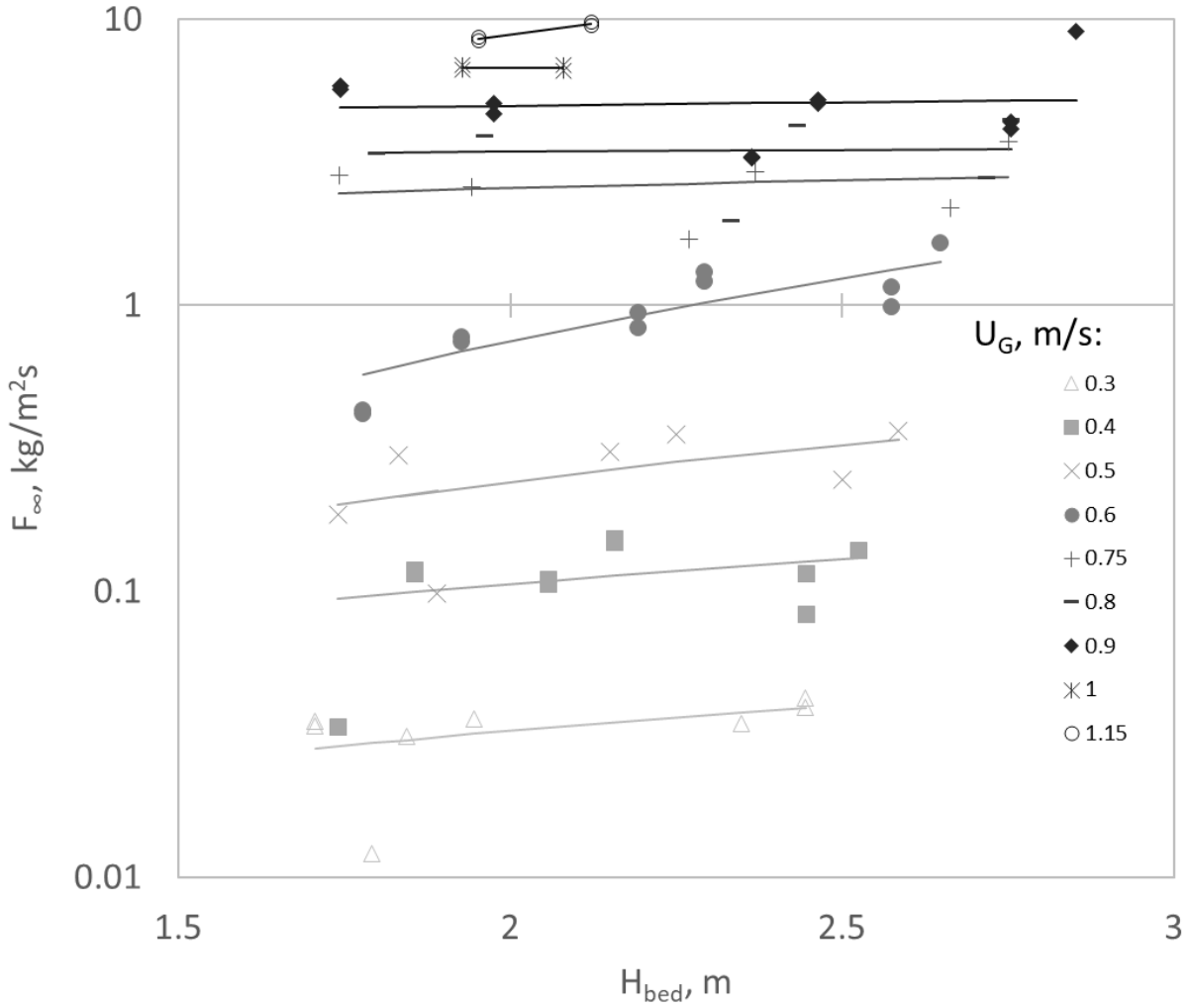

Figure 4-25. Change in entrained particle flux (F_∞) in freeboard cross-section at the top of the cyclone with bed height after Phase 2 modifications with All Sparger gas distribution.

The flux was again fitted as a function of bed height using Equation (4.5). The coefficients for each gas velocity are summarized in Table 4-3. Additionally, the flux as a function of bed height was fit using a linear regression model. Finally, the probability that b was negative was calculated across the gas velocities and summarized in Table 4-3.

Table 4-3. Summary of coefficients for $F_\infty = a*H_{Bed}^{b}$ flux measured after Phase 2 of Cold Model modifications.

U_G, m/s	a	b	Probability b is Negative, %
0.3	0.017	0.922	57.9
0.4	0.057	0.888	54.8
0.5	0.097	1.322	28.8
0.6	0.156	2.27	10.6
0.75	2.115	0.281	27.5
0.8	3.305	0.056	99.9
0.9	4.581	0.121	99.9

The probability that b was negative was much higher in this case than previously; the slope of flux with bed height was also smaller, and the flux was less sensitive to changes in the bed height. As in the previous section, the flux appeared to plateau in the middle range of bed heights tested, where the TDH was in the cylindrical section of the cyclone with a constant cross-section.

Figure 4-26 compares all the measured fluxes above the TDH at each stage of modifications and fluxes predicted with the Benoni model. It shows that the flux was much higher after Phase 2 of the modifications across all measured gas velocities when compared to Phase 1. It also shows the Benoni model agrees with the measured entrainment fluxes across the phases of modifications, indicating it can be used to extrapolate to the conditions used in the Hot Pilot Plant.

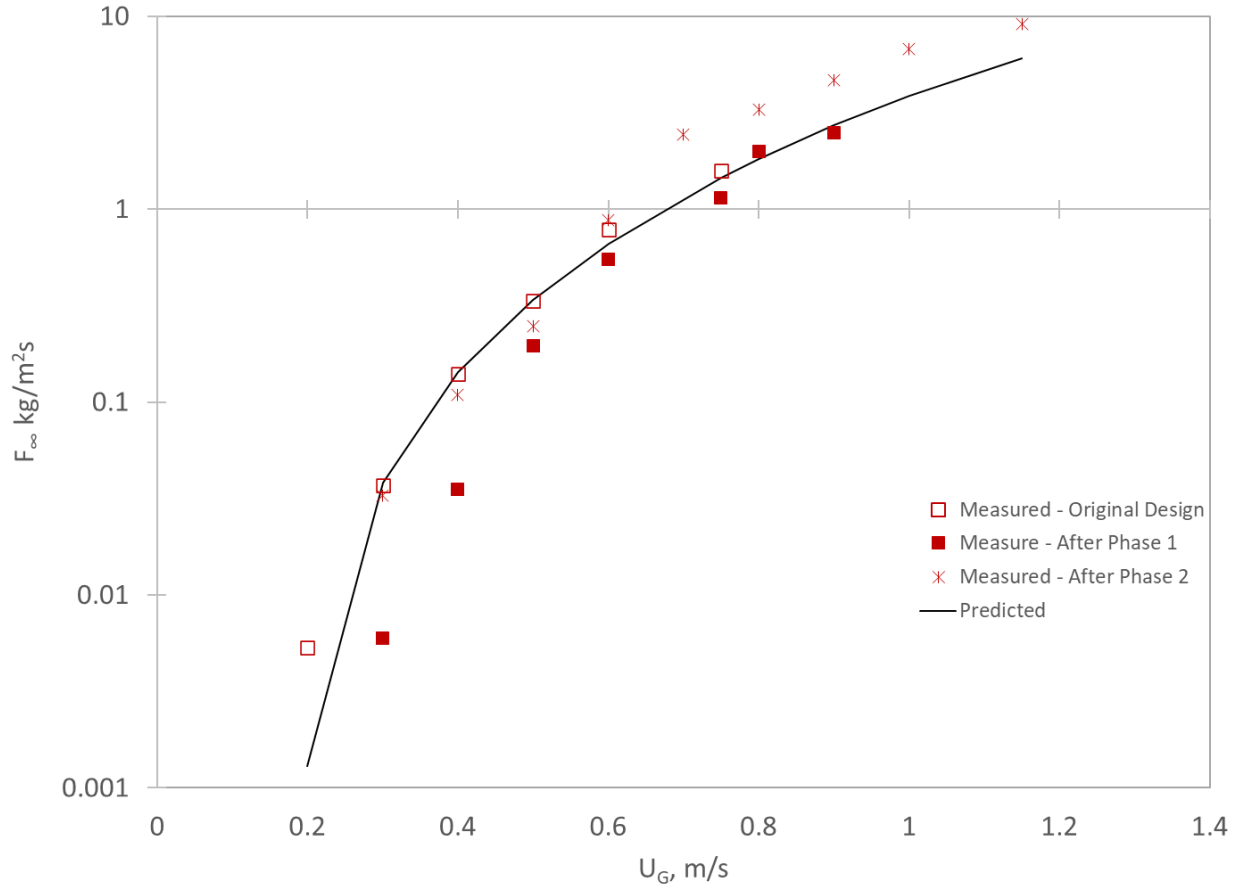

Figure 4-26. Predicted flux of particles entrained above the TDH with Benoni model compared to measured fluxes from the original design and after Phase 1 modifications.

The gas density and viscosity in the reactor is higher in the Hot Pilot Plant (ρ_g = 2.05 kg/m^3; μ_g = 0.02 cp). When these conditions are applied in the Benoni model, the entrainment rate is expected to be roughly 20% higher than the Cold Model at U_G = 1 m/s. The Cold Model was tested at a solids flowrate of 1.55 kg/s entering the cyclone, which would allow safe operation at the Hot Pilot conditions up to U_G = 1 m/s based on the prediction from Benoni.

Figure 4-27 directly compares the change in measured flux with bed height after Phase 1 and Phase 2 of modifications at U_G = 0.3 m/s. The comparisons for the remaining velocities are available in Appendix J. It shows the entrainment flux was higher after Phase 2 of modifications, even when the cyclone inlet was above the TDH (for example, H_{Bed} = 1.7).

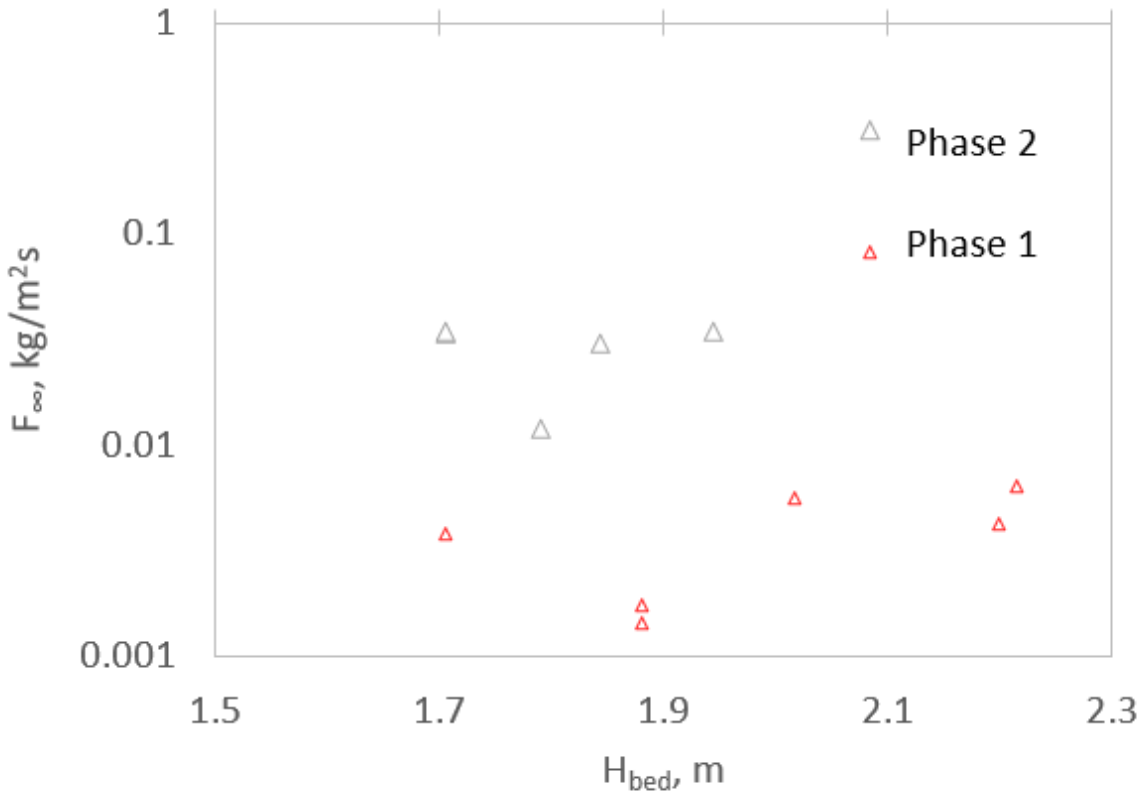

Figure 4-27. Measured flux of particles above the TDH at U_G = 0.3 m/s with All Spargers gas distribution after Phase 1 and Phase 2 of modifications.

It was previously shown that there was significant agglomeration, with the impact more pronounced at lower gas velocities. The solids were sprayed with an anti-static solution while loaded into the reactor for Phase 2 measurements due to issues related to electrostatics. Agglomeration is often a result of electrostatic effects, which cause smaller particles to preferentially adhere to larger particles or the column wall (Baron et al, 1992; Benoni et al, 1994; Nakazato and Kato, 2008), and eliminating electrostatic effects by neutralizing particle charges can increase the entrainment flux above the TDH by up to two orders of magnitude (Baron et al., 1987; Baron et al, 1992). It is assumed that the effect of the anti-static solution dissipated with time; however, it may not have wholly dissipated during testing. Therefore, samples were taken immediately after spraying the anti-static solution while loading the solids and after 6 hours of fluidization to re-charge the particles to confirm whether the anti-static solution affected the flux.

Figure 4-28 summarizes the difference in flux with the anti-static solution. Immediately after spraying the anti-static solution, the flux was higher than after 6 hours of fluidization, especially at lower gas velocities. The impact of the anti-static solution could thus explain the higher flux after Phase 2 of modifications compared to Phase 1.

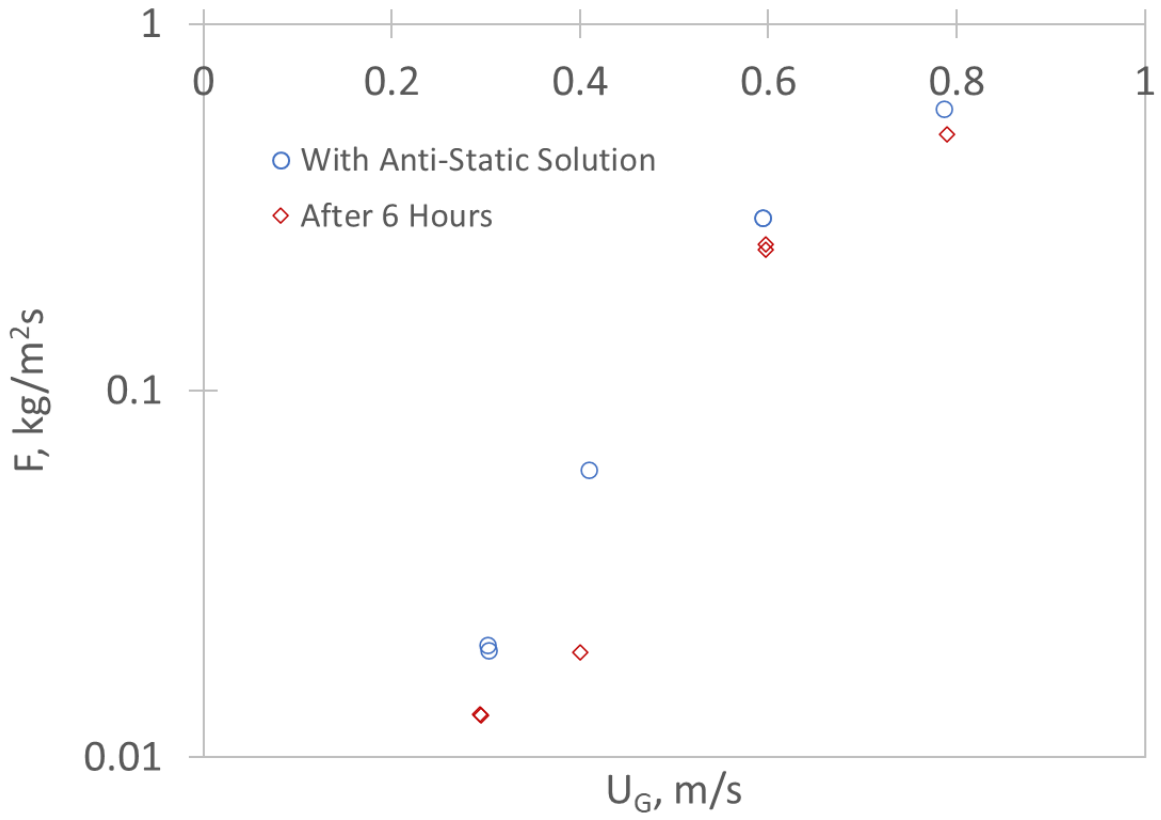

Figure 4-28. Difference in measured flux with anti-static solution, and after 6 hours of fluidization at different gas velocities with All Spargers gas distribution and $H_{Defluidized}$ = 1.6 m.

A particle size analysis was performed to confirm the effect of the anti-static solution (see Appendix B). Figure 4-33 shows the impact of the anti-static solution on the ratio of the weight fraction in solids measured in the cyclone inlet to the weight fraction in the bed as a function of particle size. The distribution with the anti-static solution was wider than after 6 hours of fluidization, indicating more fines with the anti-static solution, especially at lower gas velocities. This increase in fines explains the increased entrainment flux observed after Phase 2 of

modifications. Therefore, if it is desired to reduce the flux of solids above the TDH, the solids should be fluidized for a more extended period to dissipate the anti-static solution.

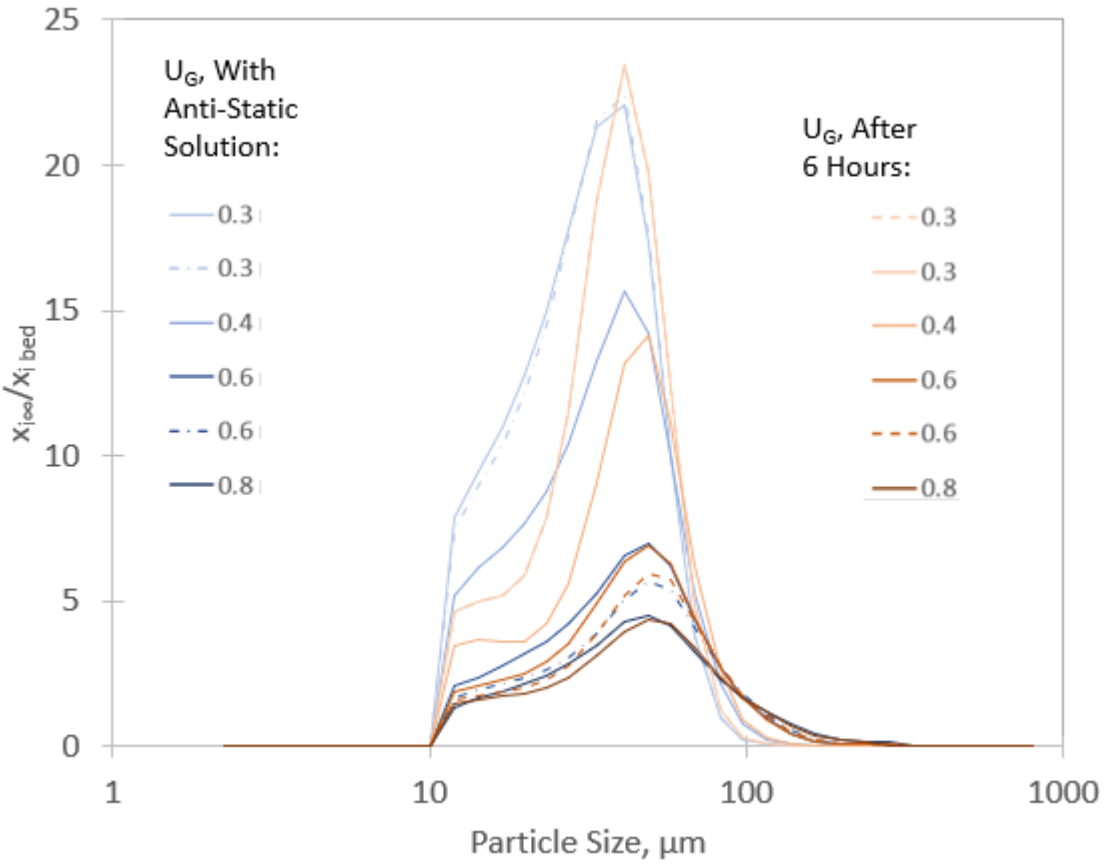

Figure 4-29. Weight fraction of entrained particles to weight fraction of bed particles in each size cut for the measured flux in the original design, with the anti-static solution and after 6 hours of fluidization for a defluidized bed height of 1.62 m.

In a hot pilot plant, an anti-static additive will evaporate as the bed temperature increases. On the other hand, electrostatic effects may be much reduced at high temperatures. Therefore, it might be helpful to characterize particle agglomeration in a high-temperature bed of coke particles.

4.4.4 Discussion on TDH

The internal cyclone takes up a significant cross-sectional area in the reactor freeboard. Reducing the freeboard cross-sectional area accelerates the gas in that area, carrying entrained particles farther before they fall back towards the bed surface. The freeboard has three main zones: 1) Below cyclone zone; 2) Intermediate zone; 3) Cyclone zone.

The local gas velocity above the bottom of the cyclone increases as the cross-section occupied by the cyclone increases. Therefore, the higher superficial gas velocity increases the maximum entrainable particle size above the TDH. Figure 4-38 demonstrates how the maximum entrainable particle size increases with gas velocity.

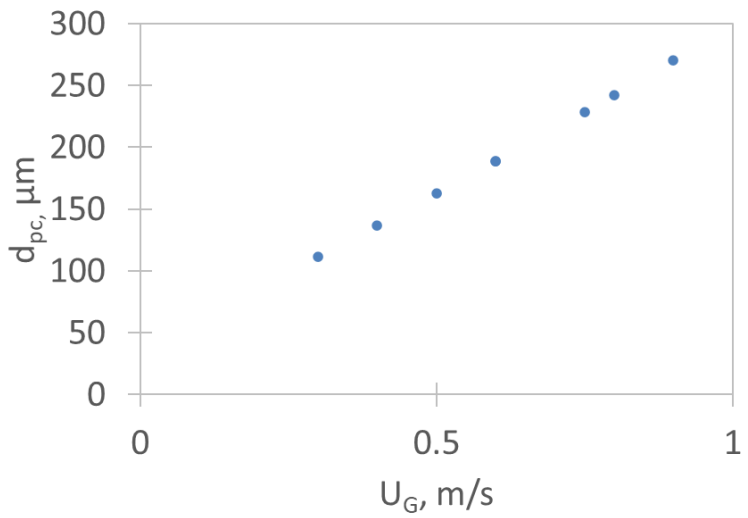

Figure 4-30. Maximum entrainable particle size (d_{pc}) using Ganser's (1993) approximation for the terminal free-falling velocity as a function of gas velocity (U_G).

The maximum entrainable particle size was calculated in the different freeboard zones to determine the impact of the cross-sectional cyclone area on the TDH, using the approximation of the correlation from Ganser (1993), correcting for the cross-sectional area occupied by the dipleg. An example of the change in local gas velocity, with the equivalent change in d_{pc} in the three different cyclone zones for U_G = 0.3 m/s, is shown in Figure 4-31.

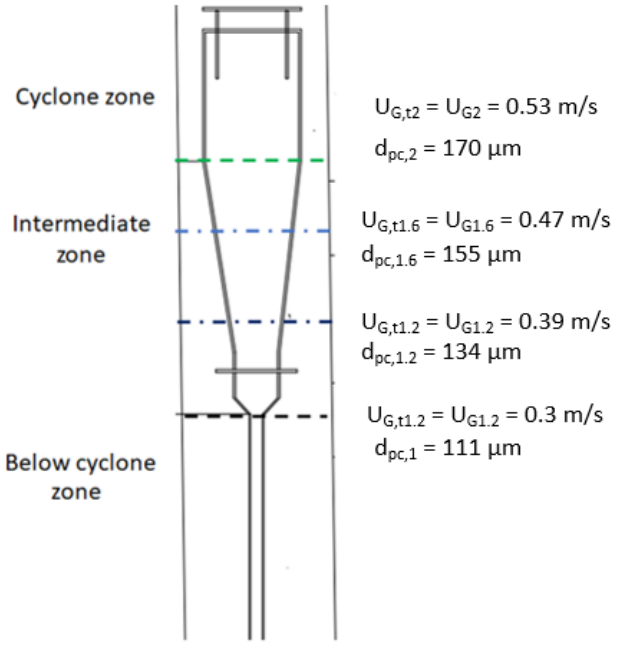

Figure 4-31. Example of the impact gas velocity in different cyclone zones at U_G = 0.3 m/s before freeboard extension.

The weight percent of particles in the bed and solids collected from the cyclone inlet below the maximum entrainable particle size was then calculated. Finally, in each of the different freeboard zones, the weight percent of solids entering the cyclone that would belong to clusters if the TDH were in that zone was calculated using Equation (4.6):

$$\%\ Clusters\ in\ cyclone\ inlet = 100 * \frac{(100 - Fraction\ of\ bed\ solids\ below\ d_{pc})}{(100 - Fraction\ of\ cyclone\ solids\ below\ d_{pc})} \quad (4.6)$$

Baron et al. (1988a) showed that the flux of clusters decreases exponentially with distance from the freeboard. Therefore, the percentage of clusters entering the cyclone should be nearly constant and close to zero if the cyclone inlet is above the TDH.

4.4.4.1 Original Cold Model Design

The cyclone inlet was predicted to be below the TDH above superficial gas velocities of 0.5 m/s and defluidized bed heights of 1.72 and above. The fraction of clusters that would be entering the

cyclone if the TDH were in the different cyclone zones was calculated. Figure 4-32 presents an example of the change in the predicted % of clusters entering the cyclone inlet at U_G = 0.3 m/s (different velocities are shown in Appendix K). The fraction of clusters decreases if the TDH is in the intermediate and cyclone zone; however, it does not reach a constant value, indicating the cyclone inlet was below the TDH at all conditions with the Original Cold Model design.

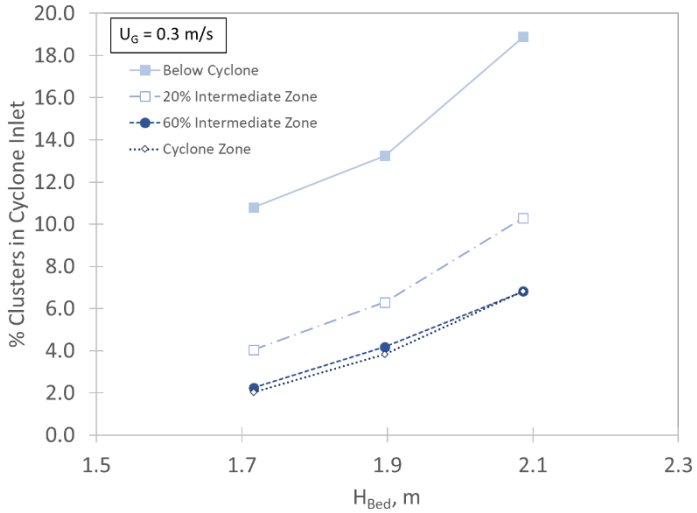

Figure 4-32. Change in the fraction of clusters ejected from the bed in cyclone inlet with bed height at U_G = 0.3 m/s before the column extension.

4.4.4.2 After Phase 1 of Modifications

After Phase 1 of Modifications (Refer to Table 2-1 and Figure 2-12 for more details), the cyclone inlet was predicted to be above the TDH up to a defluidized bed height of 2.24 m. Figure 4-33 summarizes the heights of the various cyclone zones after the column extension.

The fraction of clusters in the cyclone inlet was calculated with Equation (4.6) to confirm these results. Figure 4-34 shows an example of the change in the fraction of clusters entering the cyclone inlet with bed height, for example, at U_G = 0.3 m/s. Results for other velocities are shown in Appendix K.

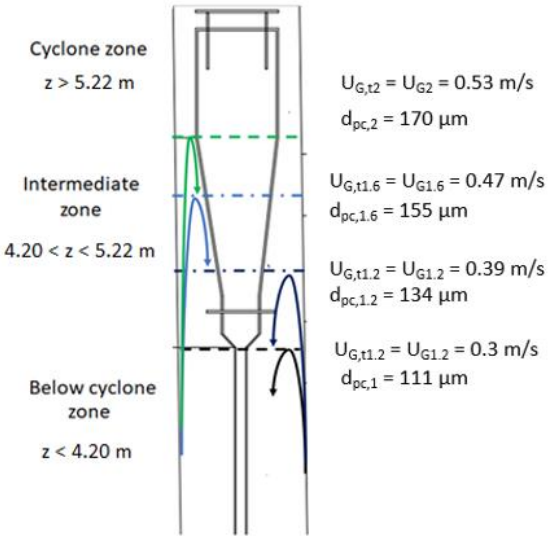

Figure 4-33. Heights of cyclone zones after column extension.

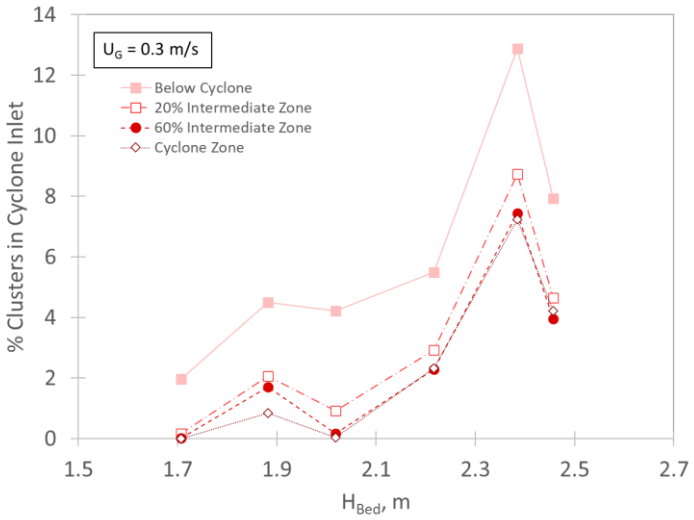

Figure 4-34. Change in the fraction of clusters ejected from the bed in cyclone inlet with fluidized bed height at U_G = 0.3 m/s after Phase 1 of modifications.

In this example, the fraction of clusters reaches a constant value near zero at bed heights below 2.12 m in the intermediate cyclone zone and above: the TDH is in the intermediate zone at defluidized bed heights below 1.82 m and above the cyclone inlet defluidized bed heights larger than 2.38 m for U_G = 0.3 m/s. These results agree with predictions from the previous section. The

TDH predicted from this method at various gas velocities is shown in Figure 4-35. This method predicted a nearly constant TDH, which agrees with predictions in Chapter 3.5. This TDH indicates the cyclone inlet is below the TDH when the defluidized bed height is 2.3 m or higher.

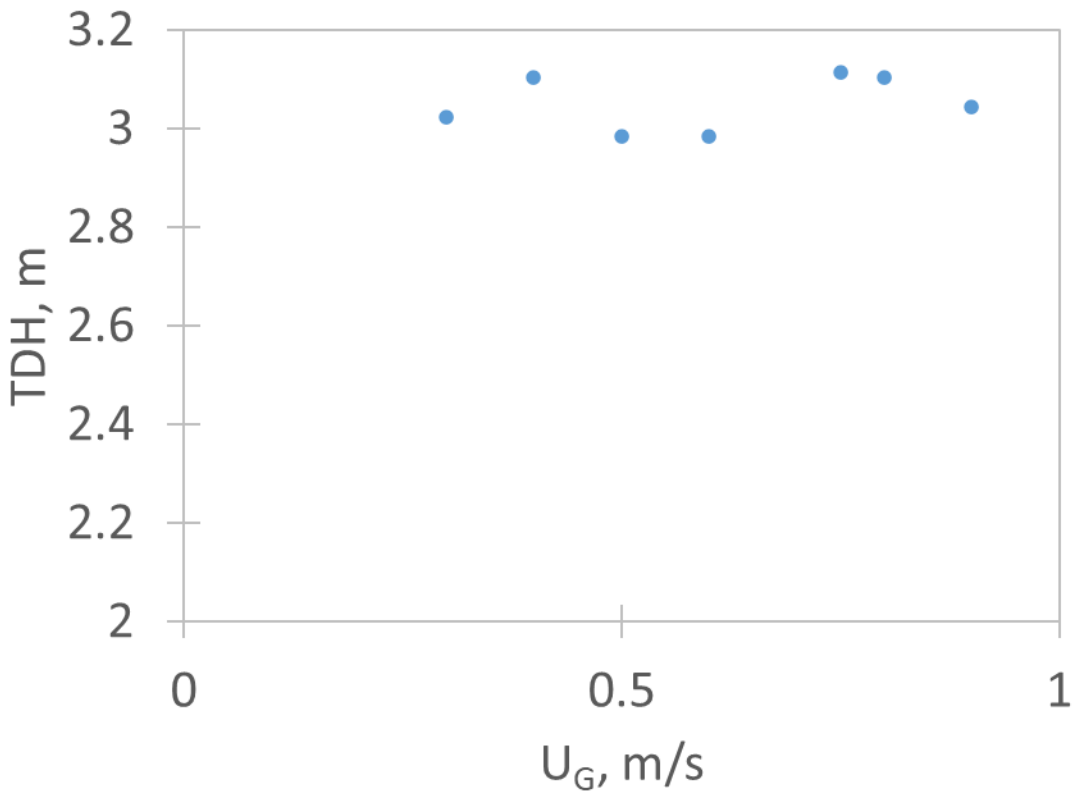

Figure 4-35. TDH predicted from the predicted fraction of clusters entering cyclone inlet After Phase 1 of Modifications.

4.4.4.3 After Phase 2 of Modifications

After Phase 2 of Modifications (Refer to Table 2-1 and Figure 2-12 for more details), the cyclone inlet was predicted to be above the TDH up to a defluidized bed height of 2.24 m. Therefore, the fraction of clusters in the cyclone inlet was calculated with Equation (4.6) to confirm these results, and Figure 4-36 shows an example of the change in the fraction of clusters entering the cyclone inlet with bed height at U_G = 0.3 m/s (results for other velocities are shown in Appendix K).

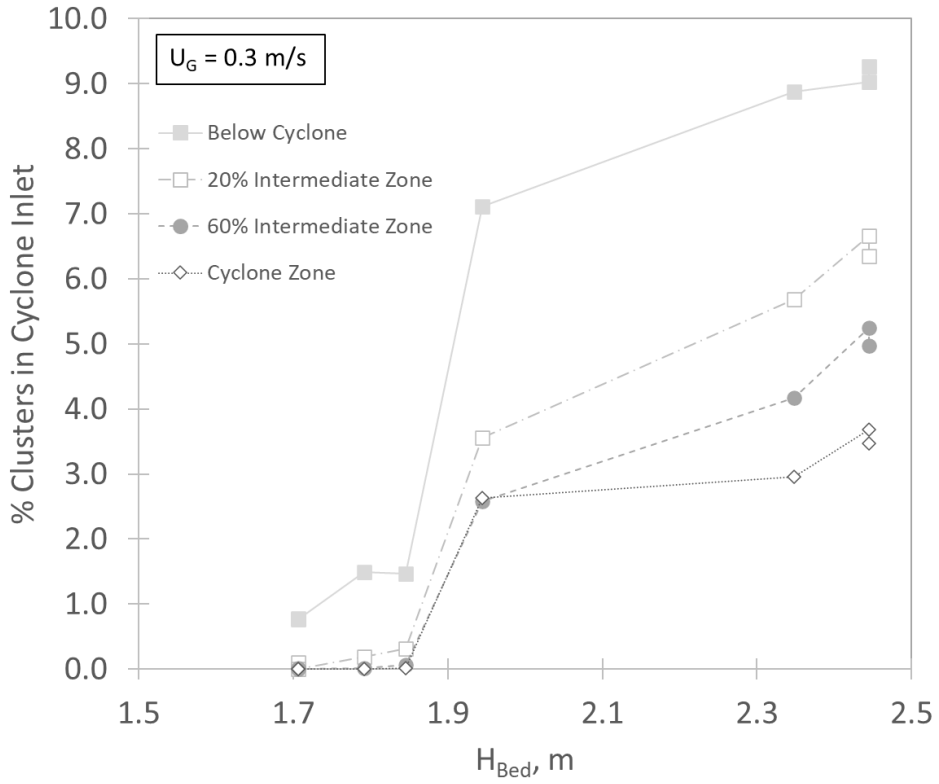

Figure 4-36. Change in the fraction of clusters ejected from the bed in cyclone inlet with bed height at U_G = 0.3 m/s after the transfer line modifications.

In this example, the fraction of clusters reaches a constant value near zero at bed heights below 2.12 m (reaches zero at H_{bed} = 1.85 m) in the intermediate cyclone zone and above: the TDH is in the intermediate zone at defluidized bed heights below 1.85 m and above the cyclone inlet defluidized bed heights larger than 2.36 m for U_G = 0.3 m/s. These results agree with predictions from the flux in the previous section. The TDH predicted from this method at various gas velocities is shown in Figure 4-37. This method predicted a nearly constant TDH, which agrees predictions made in Chapter 3.5. This TDH indicates the cyclone inlet is below the TDH when the defluidized bed height is 2.2 m or higher.

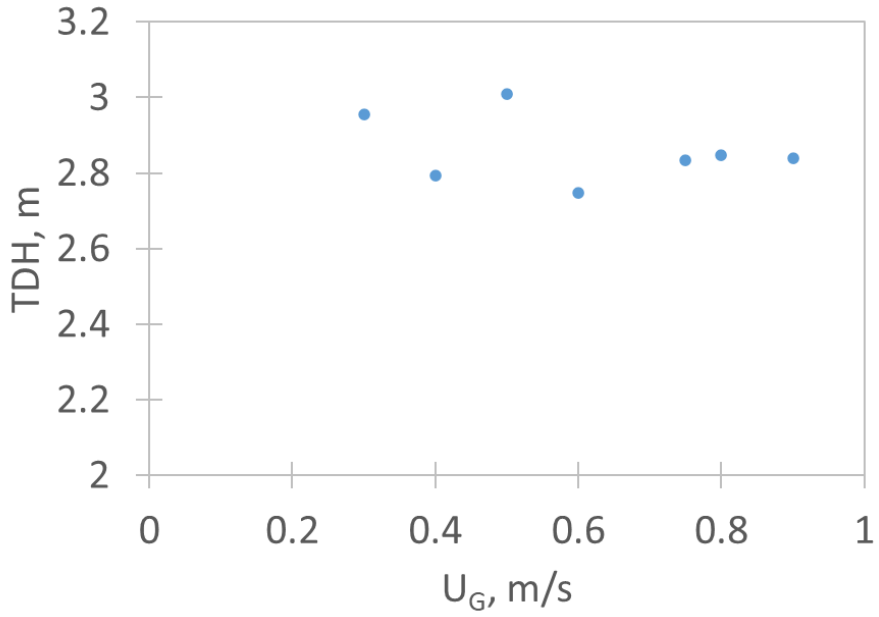

Figure 4-37. TDH predicted from the predicted fraction of clusters entering cyclone inlet After Phase 2 of Modifications.

4.4.5 Cyclone Efficiency

Primary cyclones are typically designed to capture and return 99% of entrained solids to the fluidized bed. The following section investigated the baseline cyclone efficiency to establish whether the cyclone was adequate for solids recovery during regular operation, in the absence of pulses, or if modifications were required.

To determine the reactor cyclone efficiency during regular operation (when solids losses < 0.01 kg/min), an isokinetic probe was installed in the cyclone exhaust, and the mass of solids escaping the cyclone was collected and weighed off-line. A detailed description of the experimental setup and sampling procedure can be found in Chapter 2.3. The cyclone efficiency was determined from solids flowrates before modifications were made to the unit, as extending the column should not significantly affect the efficiency under regular operation.

The reactor cyclone efficiency is calculated from the ratio of the flowrate of particles escaping the cyclone, and the flowrate of particles entering the cyclone, calculated using Equation (4.7):

$$\eta_{cyclone} = 1 - \frac{F_{Exhaust}}{F_{Inlet}} \quad (4.7)$$

Figure 4-38 displays the cyclone efficiency ($\eta_{cyclone}$) before modifications as a function of gas velocity at a bed mass of 280 kg. The efficiency was greater than 99% for all velocities measured and increased with increasing superficial gas velocity.

It has been shown that cyclone efficiency increases with increasing solids concentration until reaching a concentration that causes saltation in the cyclone inlet (Fassani and Goldstein, 2000; Mothes and Loeffler, 1985; Trefz and Muschelknautz, 1993; Zenz, 1982). Two explanations have been proposed to account for the increase in collection efficiency:

1. Mothes and Loeffler (1985) proposed a "piggy-back" collection mechanism when a mix of particles of different sizes in the solids enter the cyclone. The large particles move towards the cyclone wall faster than small particles and capture them by impaction.

2. Trefz and Muschelknautz (1993) proposed the critical load concept, where at high solids loadings, most of the solids entering the cyclone are collected near the inlet and flow down the walls as strands. The cyclone typically separates the remaining solids. This phenomenon is similar to saltation in horizontal pneumatic transport lines, where centrifugal forces replace gravity.

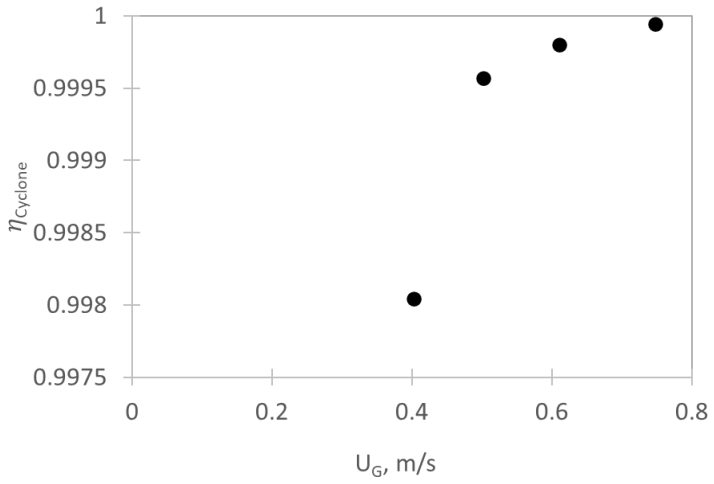

Figure 4-38. Cyclone efficiency as a function of gas velocity at $H_{Defluidized}$ = 1.86 m.

The measured cyclone efficiency indicated that more than 99% of solids entering the cyclone were captured and returned to the bed during regular operation (i.e., when no light pulses are present). Thus, the original cyclone design was acceptable, and modification was not required.

4.5 Cyclone Dipleg Flow Issue

The measured level of defluidized solids in the dipleg was correlated with the occurrence of light pulses, as shown in section 4.3.2. In addition, defluidized bed height, aeration, and superficial gas velocity were shown to impact the occurrence of light pulses. Therefore, the following section aims to develop a model to predict the fluctuations in the dipleg solids level.

4.5.1 Measured Defluidized Solids Levels in Dipleg

The following experiments were performed using the Cold Model after Phase 1 of modifications, detailed in Chapter 2.1.3 (Refer to Table 2-1 and Figure 2-12 for more details). Defluidized solids level in the dipleg was previously measured at two superficial gas velocities (see Chapter 4.3.2.2). In this section, the fluctuations in defluidized solids level in the dipleg were measured across a more extensive range of gas velocities at the same defluidized bed height of 1.94 m. In addition, the same measurement procedure used in section 4.3.2.2 was performed, taking ten measurements over 50 minutes of fluidization. Table 4-4 summarizes the frequency of pulses observed during the experiments.

Table 4-4. Frequency of observed pulses during defluidized solids level measurements in the dipleg with All Spargers gas distribution configuration

U_G, m/s	**Number of pulses in 50 minutes**
0.3	0
0.4	0
0.5	0

0.6	2
0.75	2
0.8	3
0.9	9

The first series of experiments focused on the highest velocity (U_G = 0.9 m/s), for which the pulse frequency was highest. Figure 4-39 shows that one of the ten measured solids levels was in the cyclone cone, above the top of the dipleg ($Z_c > 0$), confirming that the dipleg solids level could reach the cyclone cone. Figure 4-39 also shows that the measured solids level in the dipleg spanned about 2 m.

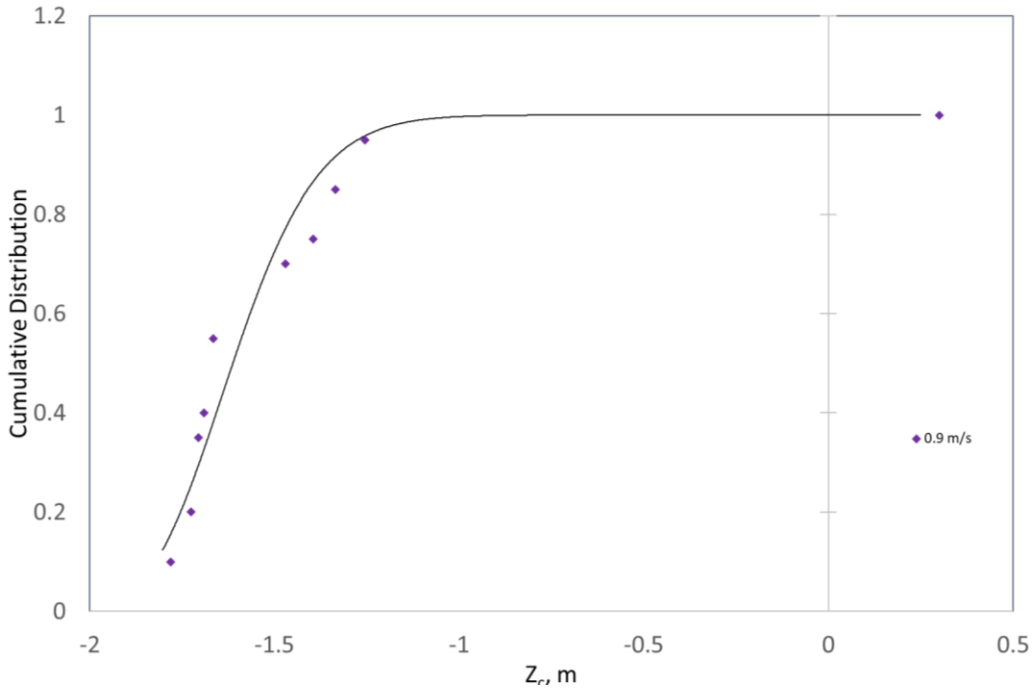

Figure 4-39. Probability distributions of measured level of defluidized solids in dipleg at 0.9 m/s with All Spargers gas distribution.

Figure 4-40 presents the cumulative probability distributions of the measured level of defluidized solids in the dipleg at lower fluidization velocities, using the All Spargers gas distribution configuration (refer to Figure 2-3).

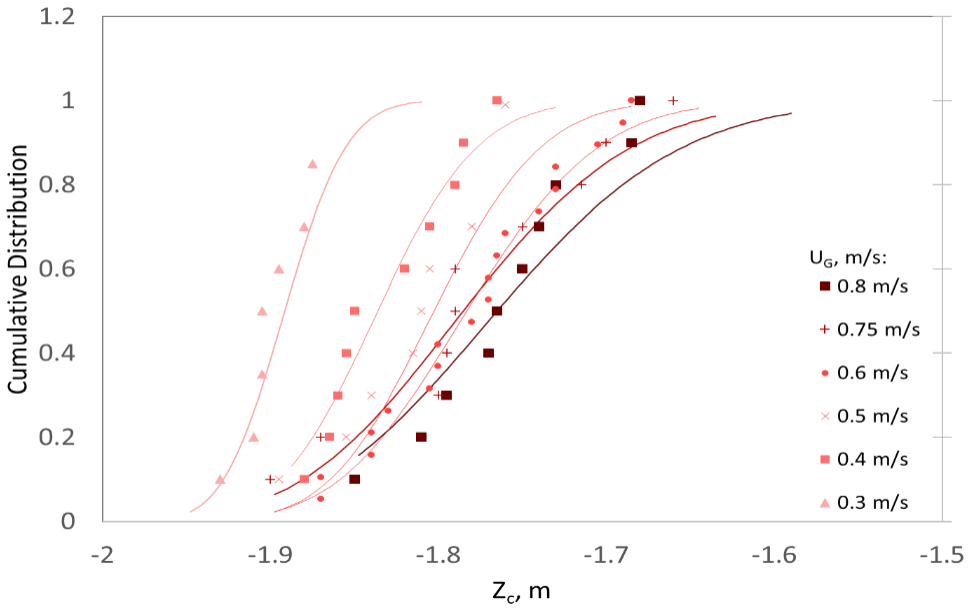

Figure 4-40. Probability distributions of measured level of defluidized solids in dipleg with All Spargers gas distribution.

The measurements showed that the average level and amplitude of fluctuations in the solids level in the dipleg increased with gas velocity. The probability of the level of defluidized solids in the dipleg reaching the bottom of the cyclone ($Z_c = 0$) decreases sharply as the velocity U_G is decreased below 0.8 m/s.

The distributions of measured defluidized solids levels were fitted with a cumulative log-normal function, described by Equation (4.8):

$$\boldsymbol{y} = \frac{\boldsymbol{ln(x) - ln(\mu)}}{\boldsymbol{\sigma}} \tag{4.8}$$

where,

x is the distance of the solids from the bottom of the cyclone, m;

μ is the mean of the distances from the bottom of the cyclone, m; and

σ is the standard deviation of the distances from the bottom of the cyclone, m.

By extrapolating the cumulative log-normal function for each set of conditions, the probability of the solids level reaching the bottom of the cyclone ($Z_c = 0$) was estimated. The results are summarized in Table 4-5.

Table 4-5. Probability of solids reaching the critical level in dipleg for different gas velocities.

U_G, m/s	**Probability Where $Z_c = 0$**	**Predicted Z_c where P = 1, m**
0.3	1	-1.6575
0.4	1	-1.4975
0.5	1	-1.4375
0.6	1	-1.32
0.75	1	-1.165
0.8	1	-1.3275
0.9	0.999999987	0.2475

The extrapolated probability of the dipleg solids reaching the bottom of the cyclone ($Z_c = 0$) was 0 for all U_G velocities 0.8 m/s and below. However, light pulses were observed at gas velocities above $U_G = 0.6$ m/s, which indicates that the solids level reached the bottom of the cyclone several times over the 50-minute measurement period. At velocities below 0.9 m/s, the observed pulses, although they have a significant impact on solids losses, are infrequent events that are difficult to capture from a few measurements of the solids level in the dipleg.

In this case, the log-normal fit model did not fit the data with a high degree of accuracy and decreased with increasing gas velocity. While the prediction helps predict the behaviour of the solids in the dipleg at lower gas velocities, it should not be used for predictions across all conditions, indicating a more detailed model should be developed.

All the measurements discussed previously used the All Spargers gas distribution. Figure 4-41 and Figure 4-42 demonstrate the impact of using the Bottom Sparger Only gas distribution (refer to Figure 2-3) on the cumulative probability distribution of measured solids levels for different gas velocities. At the lower gas velocities of U_G = 0.3 m/s and U_G = 0.6 m/s, the median level of solids measured in the dipleg was lower when using the Bottom Sparger gas configuration; the local gas velocity at the diplegwas likely lower when using the Bottom Sparger only, resulting in a higher density (and thus lower level) of solids in the dipleg.

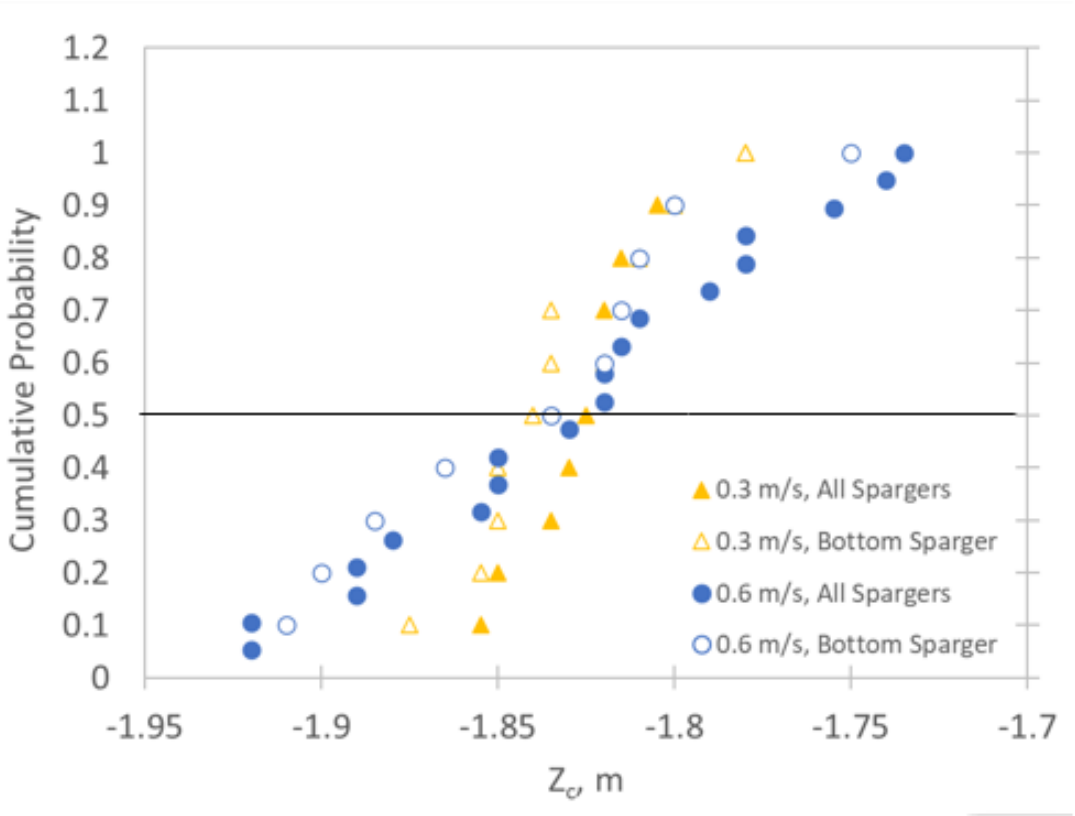

Figure 4-41. Probability distribution of measured level of defluidized solids in dipleg for different gas distributions when U_G = 0.3 m/s and U_G = 0.6 m/s.

The gas distribution had a much more substantial impact at U_G = 0.8 m/s, shown in Figure 4-42. With the All Spargers configuration, none of the ten solids level measurements was near the bottom of the cyclone. In contrast, when using the Bottom Sparger only gas distribution, four of the ten measurements showed that the dipleg solids reached the cyclone. This corresponded to a greater number of pulses with the Bottom Sparger only gas distribution: five pulses were observed in the cyclone exhaust over 50 minutes of fluidization, compared with only three pulses with the All Spargers configuration. Figure 4-42 also shows that for the Bottom Sparger only gas distribution, the cumulative log-normal function does not agree with measured level distribution, confirming that it cannot be reliably used to estimate the probability of the solids level reaching the bottom of the cyclone. A reliable model is thus required to predict the solids level in the dipleg.

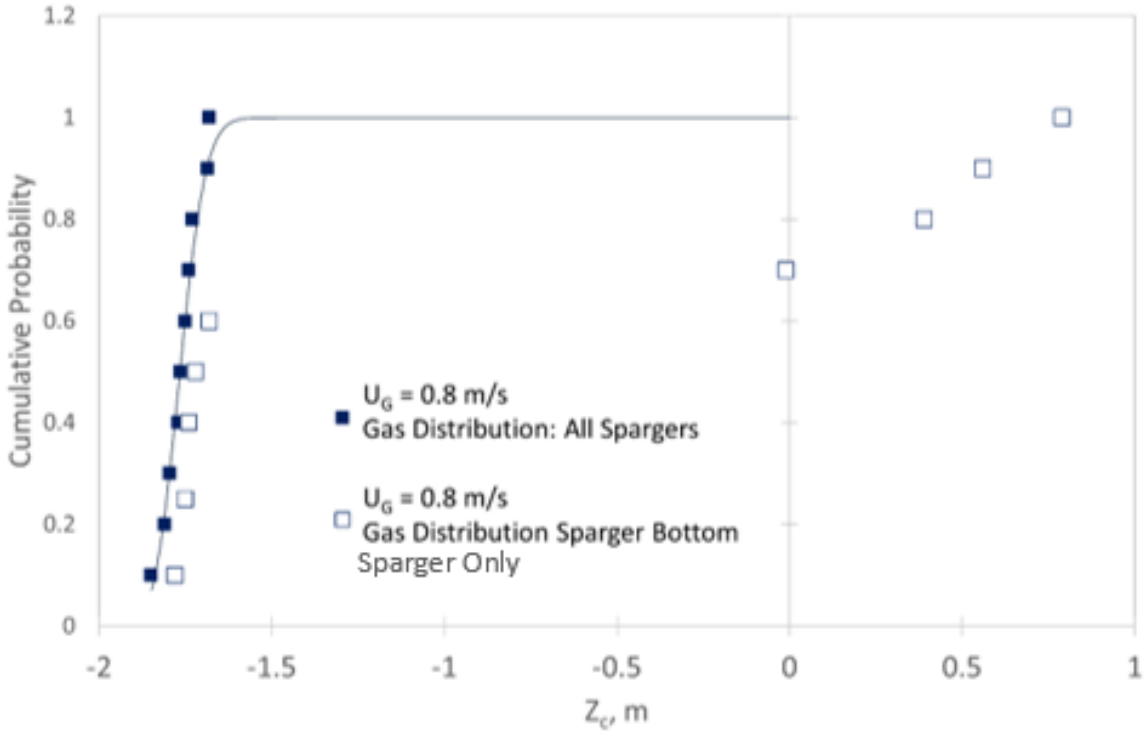

Figure 4-42. Probability distribution of measured distance from primary cyclone bottom of defluidized solids in dipleg for different gas distributions at U_G = 0.8 m/s.

4.5.2 Dipleg Solids Level Model

This section aims to develop a model to predict when the solids reach the bottom of the cyclone.

4.5.2.1 Model Development

The model assumes that the dipleg solids flow is driven by the pressure difference between the dipleg bottom and the fluidized bed near the dipleg termination. Although the pressure inside the dipleg is usually higher than the pressure in the bed, driving solids from the dipleg to the bed, the pressure fluctuations encountered in large, high-velocity fluidized beds are such that the pressure in the bed may momentarily become higher than the dipleg pressure, driving solids from the bed into the dipleg.

The level of solids in the dipleg is related to the total mass of solids in the dipleg. In previous sections, the defluidized level of solids was measured. In practice, when the bed is fluidized, the solids in the dipleg remain fluidized.

Therefore, it is assumed that:

(1) The dipleg is fully fluidized;

(2) The density in the dipleg (ρ_D) is equal to the density in the bed (ρ_{Bed}); and

(3) The model calculations have an initial condition that assumes that the solids level in the dipleg, z_d, is equal to the bed height, H_{bed}, at t = 0. Typically the solids level in the dipleg is higher than in the bed, however during development of the model it was determined the impact of the assumed initial H_{bed} is negligible and no matter the initial assumption after approximately 300 ms the pressure fluctuations dictate the solids level in the dipleg.

The initial mass of solids in the dipleg when $z_d = H_{bed}$ is calculated using the density of fluidized solids and the cross-sectional area of the dipleg, as shown in Equations (4.9) and (4.10):

$$M_s = \beta \cdot z_d \tag{4.9}$$

Where,

$$\beta = \rho_D \cdot \frac{\pi}{4} \cdot D_d^2 \quad (4.10)$$

It has been shown that taking a pressure balance around the cyclone can predict the solids level in the dipleg for a net-zero solids flow. Consequently, the pressure inside the dipleg termination (or orifice), P_i, can be calculated using Equation (4.11):

$$P_i = -\Delta P_c + (\rho_D \cdot g \cdot z_d) \quad (4.11)$$

The flowrate of fluidized particles through an orifice has been found experimentally proportional to the square root of the pressure drop above the orifice (Martin and Davidson, 1983; Tallon and Davies, 2005). A constant, α , is applied to the flow as an empirical orifice parameter, which depends on the geometry of the dipleg termination. The flow of solids in the dipleg, F_o, is negative when the pressure in the dipleg outlet, P_o, is higher than the pressure in the dipleg, P_i. A negative value for F_o means solids flow up the dipleg, increasing the level of solids in the dipleg. Conversely, when P_o is smaller than P_i, F_o is positive, and solids flow out of the dipleg and into the bed. F_o can be calculated from Equation (4.12a) or (4.12b) depending on the flow direction:

$$If: P_i - P_o > 0,\ F_o = \alpha\sqrt{P_i - P_o} \quad (4.12a)$$

$$If: P_i - P_o < 0,\ F_o = -\alpha\sqrt{|P_i - P_o|} \quad (4.12b)$$

The new mass of solids in the dipleg at time $t = t_i$ can be calculated by combining the flow of solids in the dipleg, F_o, with the flow of solids entering the cyclone, F_e (from Chapter 4.4), using Equation (4.12), where Δt is the time interval between t_{i-1} and t_i:

$$M_{s,i} = M_{s,i-1} + F_e\Delta t - F_o\Delta t \quad (4.13)$$

Finally, the new level of solids in the dipleg, $z_{d,i}$, at $t = t_i$ is calculated using Equation (4.14):

$$z_{d,i} = \frac{M_{s,i}}{\beta} \quad (4.14)$$

In the following discussion, the results are presented as the distance from the bottom of the cyclone cone. As the apex of the cyclone cone is actually several centimeters into the dipleg, and

the vortex intermittently extends below the cyclone cone, the solids level is considered “in the cyclone” 10 cm below the bottom of the cyclone. The total dipleg length from the cyclone bottom to the elbow termination is 2.8 m (see Figure 2-12). Consequently, the solids level is converted to distance from the cyclone bottom using Equation (4.15):

$$z_{c,i} = z_{d,i} - 2.7\ m \tag{4.15}$$

When $z_{c,i} \geq 0$, the dipleg is full, and solids are in the cyclone, decreasing cyclone efficiency and resulting in a pulse in dust emissions. The empirical parameter α_A was adjusted to match the number of pulses predicted to the number of observed pulses from cyclone exhaust. α_A was found to be 0.3 by fitting the data. The parameter α was also calculated using the correlation from Martin and Davidson (1983) for a regular orifice shown below in Equation (4.16):

$$\alpha_A = 0.25 C_D * D^2 * \sqrt{2\rho_D} = 0.027 \tag{4.16}$$

The empirical parameter determined from fitting the data is one order of magnitude higher than predicted from the correlation. This difference is likely a result of the bend at the dipleg termination, which was designed to minimize the risk of gas bubbles entering the dipleg. The following section explores the model results using pressure measurements made at the dipleg level in the bed.

4.5.2.2 Model Validation

The pressure fluctuations near the dipleg outlet were measured in the dipleg after Phase 2 of modifications (Refer to Table 2-1 and Figure 2-12 for more details) for 1 hour while recording the frequency of light pulses observed from cyclone exhaust. Figure 4-43 shows the position of pressure taps used to predict the solids level fluctuations in the dipleg. In addition to the frequency of pulses, the solids losses were measured using the change in pressure measured with a U-tube manometer before and after each 1-hour experiment (see Appendix I). After each experiment, solids were added to the bed to compensate for solids losses and maintain a constant defluidized bed height.

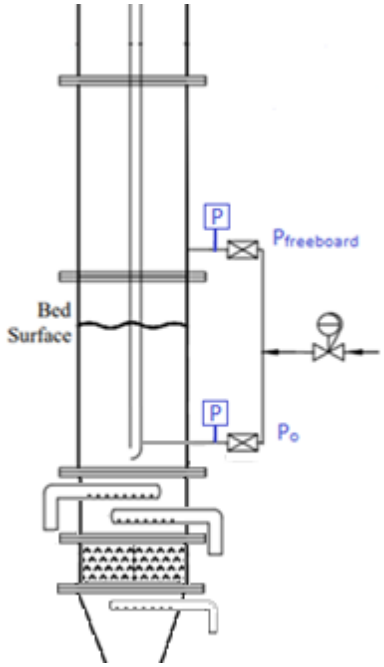

Figure 4-43. Position of pressure taps used to model dipleg level fluctuations.

Measurements were made with the All Spargers and Bottom Sparger only gas distribution (see Figure 2-3) at defluidized bed heights of 2.26 and 2.40 m. One replicate measurement was made at U_G = 0.9 m/s, $H_{Defluidized}$ = 2.40 with the All Spargers gas distribution. It should be noted that under these conditions, the cyclone inlet is below the TDH (see Figure 3-13); however, the cyclone functioned well when pulses did not occur.

Individual pulses were counted when the time interval between dust emissions from the cyclone inlet was greater than 20 seconds. If emissions were seen from the exhaust at a shorter interval, only one pulse was counted, as time is required for the solids level to build back up in the dipleg. Multiple pulses seen in a short period can result from solids settled in the flexible exhaust being carried by gas escaping the cyclone. For the same defluidized bed height and superficial gas velocity, the pulses and solids losses were higher using the Bottom Sparger Only. As expected, reducing the defluidized bed height and superficial gas velocity reduced the frequency of pulses and the magnitude of solids losses.

As pulses were only counted if the time interval was larger than 20 seconds, a similar approach was applied to the model predictions. Figure 4-44 illustrates the method used to count the number of times the level of solids in the dipleg is predicted to reach the bottom of the cyclone. The pressure fluctuations at the dipleg level and entrainment flowrate were used to predict the flowrate of dipleg solids; the distance of the dipleg solids level from the cyclone bottom was then predicted per Equations (4.8) to (4.14). The maximum predicted distance from the cyclone bottom, z_c, was taken every 20 seconds of the signal. If $z_c \leq 0$, no pulse was predicted, while if $z_c \geq 0$, one pulse was predicted.

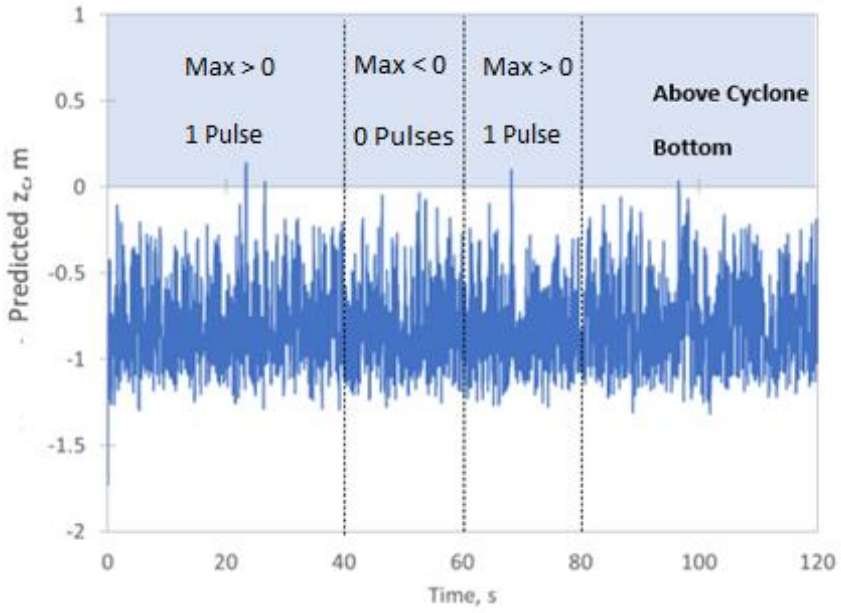

Figure 4-44. Example of method to count frequency of pulses predicted by model at $H_{Defluidized}$ = 2.26 and U_G = 0.9 m/s.

The comparison between observed and predicted pulses per hour is shown in Figure 4-45. It shows good agreement between the observed and predicted pulses, with an R^2 value of 0.947.

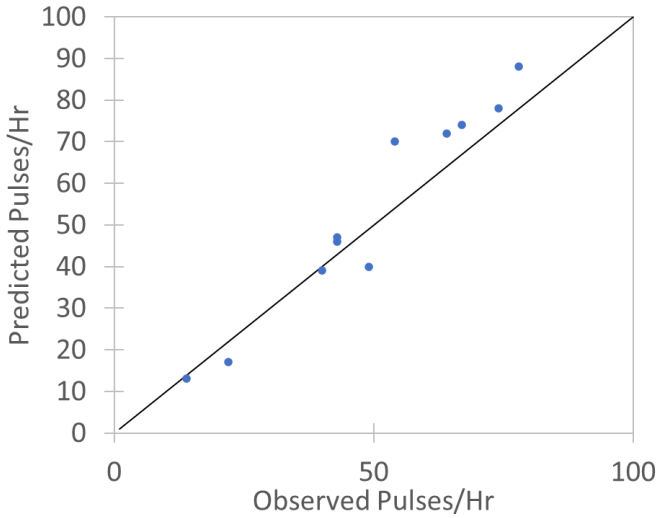

Figure 4-45. Comparison of the observed and predicted pulses per hour predicted from the model.

The predictions from the model are summarized in Table 4-6, and compared to observations. The results align well with the observed pulses for the All Spargers configuration and predicted slightly more pulses than observed in the Bottom Sparger only case. The model correctly predicts that pulses were more frequent with the Bottom Sparger only configuration.

Table 4-6. Frequency of pulses predicted by model.

U_G, m/s	**Defluidized Bed Height, m**	**Pulses/hr All Spargers**		**Pulses/hr Bottom Sparger Only**	
		Observed	**Predicted**	**Observed**	**Predicted**
0.8	2.40	49	40	67	74
0.85	2.40	64	72	78	88
0.9	2.40	74	78	NA	NA

0.8	2.26	14	13	43	47
0.85	2.26	28	17	54	70
0.9	2.26	40	39	NA	NA
0.9	2.26	43	46	NA	NA

The model assumes the density of solids in the dipleg is equal to the bed density calculated from the pressures at the reactor wall. The density may vary with local fluidization velocity as gas enters the dipleg from the bed when the solids flow reverses. Future studies may improve the predictions from the model by measuring the density of solids in the dipleg.

4.5.2.3 Sensitivity Analysis

A sensitivity analysis was performed on the various model inputs to determine their contribution to model predictions: the model can predict the change in the number of pulses resulting from a change in each input. Table 4-7 shows how the predicted number of pulses changes when the input was adjusted for the cases with a defluidized bed height of 2.40 m, and the All Spargers distribution.

Table 4-7. Sensitivity of model inputs with All Spargers distribution, and a defluidized bed height of 2.40 m.

U_G, m/s	**Model Input**	**Factor Increase to Model Input**	**Predicted Pulses in 60 min**	**Change factor of predicted pulses**
0.9	ρ_d	0.95x	154	1.98
	P_o	1.05x	95	1.22
	α	1.05x	86	1.10

	F_o	2.00x	101	1.30
0.85	ρ_d	0.95x	128	1.78
	P_o	1.05x	85	1.18
	α	1.05x	79	1.10
	F_o	2.00x	88	1.22
0.8	ρ_d	0.95x	61	1.56
	P_o	1.05x	43	1.10
	α	1.05x	41	1.05
	F_o	2.00x	43	1.10

The results indicate that the model is highly sensitive to the density of solids in the dipleg (ρ_d). For example, decreasing the density by 5% increased the number of pulses by 156-198%, depending on the conditions. The model is moderately sensitive to the amplitude of pressure fluctuations. Therefore, the pressure signal at the dipleg level (P_o) was amplified using Equation (4.16):

$$\overline{\boldsymbol{P_o}} + \boldsymbol{A}(\boldsymbol{P_{o,i}} - \overline{\boldsymbol{P_o}}) \tag{4.16}$$

where A is a constant used to amplify the signal.

A 5% increase in P_o (A = 1.05) resulted in a 10-22% increase in pulses. Additionally, the model is moderately sensitive to the flowrate of entrained solids (F_o). Doubling F_o resulted in a 10-30% increase in predicted pulses. Finally, the model is somewhat sensitive to changing the empirical parameter (α), where a 5% increase caused a 5-10% increase in predicted pulses.

The sensitivity analysis demonstrates the importance of accurate measurements for the model inputs. For example, predictions could be improved by directly measuring the pressure fluctuations and density in the dipleg.

Pressure fluctuations are expected to be higher in the hot model pilot plant conditions, especially with the introduction of liquid injection from the feed nozzle. As such, it is expected that the frequency of pulses would be higher in the hot model compared to the cold model, as indicated by the high sensitivity of the pulses to pressure fluctuations at the dipleg level.

Two recommendations can be made based on this analysis:

- The frequency of pulses, and thus solids losses, could be reduced by locating the dipleg termination in a bed region with moderate pressure fluctuations. Using baffles to moderate pressure fluctuations near the dipleg termination may even be beneficial.
- The current dipleg has an elbow termination to reduce the risk of gas bubbles entering the dipleg. This analysis shows that the resulting increase in the α parameter, compared to a straight tube termination, has an additional beneficial impact on dipleg and cyclone operation.

4.6 Summary

The Cold Model was tested to define a safe operating zone where solids losses were less than 0.01 kg/min, and no pulses in entrained solids were observed. Unit modifications were implemented to improve the operation and extend the safe operating zone. Extending the reactor vessel by 0.9 m extended the transition to the continuous backup regime to close to 1 m/s for all defluidized bed heights tested, while the addition of a 90° elbow eliminated the heavy pulses regime. Light pulses appeared at conditions approaching the transition to the continuous dipleg backup regime, and further investigation indicated the light pulses were a result of re-entrainment from the cyclone dipleg. The entrainment rate of solids entering the primary cyclone was investigated through the various phases of modifications. It showed that the Benoni model (1994) could be used to predict the entrainment rate for the Cold Model and therefore extrapolated to the Hot Pilot Conditions. Using the measured entrainment rate and pressure fluctuations in the cyclone dipleg, a model was developed to predict the frequency of pulses escaping the Cold Model primary cyclone. Sensitivity analysis highlighted the importance of rapid and accurate pressure measurement for both the Cold Model, and Hot Pilot Plant.

4.7 References

Avci, A., & Karagoz, I. (2003). Effects of flow and geometrical parameters on the collection efficiency in cyclone separators. *Journal of Aerosol Science*, *34*(7), 937–955. https://doi.org/10.1016/S0021-8502(03)00054-5

Baron, T., Briens, C. L., Bergougnou, M. A., & Hazlett, J. D. (1987). Electrostatic Effects on Entrainment from a Fluidized-Bed. *Powder Technology*, 53, 55-67.

Baron, T., Briens, C. L., & Bergougnou, M. A. (1988a). Measurement of the flux of clusters ejected from a fluidized bed. *Powder Technology*, *55*(2), 115–125. https://doi.org/10.1016/0032-5910(88)80094-9

Baron, T., Briens, C. L., & Bergougnou, M. A. (1988b). Study of the transport disengaging height. *The Canadian Journal of Chemical Engineering*, *66*(5), 749–760. https://doi.org/10.1002/cjce.5450660508

Baron, T., Briens, C. L., Galtier, P., & Bergougnou, M. A. (1990). Effect of bed height on particle entrainment from gas-fluidized beds. *Powder Technology*, *63*(2), 149–156. https://doi.org/10.1016/0032-5910(90)80037-Y

Baron, T., Briens, C. L., Hazlett, J. D., Bergougnou, M. A., & Galtier, P. (1992). Size Distribution of the Particles Entrained from Fluidized-Beds - Gas Humidity Effects. *Canadian Journal of Chemical Engineering*, 70, 631-635.

Bi, H. T. (2007). A critical review of the complex pressure fluctuation phenomenon in gas-solids fluidized beds. *Chemical Engineering Science*, *62*(13), 3473–3493. https://doi.org/10.1016/j.ces.2006.12.092

Briens, C.L. (2021). Advanced Particles and Fluidization Technology Course notes. University of Western Ontario.

Briens, C., & McMillan, J. (2021). Review of Research Related to Fluid Cokers. *Energy and Fuels*, *35*(12), 9747–9774. https://doi.org/10.1021/acs.energyfuels.1c00764

Briggs, L. W. (1946). Effect of dust concentration on cyclone performance. *Trans. Am. Inst. Chem. Eng.*, *42*, 511-526.

Bryant, H. S., Silverman, R. W., & Zenz, F. A. (1983). How dust in gas affects cyclone pressure drop. *Hydrocarbon Process.*, *62:6*. https://www.osti.gov/biblio/5674674

Cahyadi, A., Neumayer, A. H., Hrenya, C. M., Cocco, R. A., & Chew, J. W. (2015). Comparative study of Transport Disengaging Height (TDH) correlations in gas-solid

fluidization. *Powder Technology*, *275*, 220–238. https://doi.org/10.1016/j.powtec.2015.02.010

Chew, J. W., Cahyadi, A., Hrenya, C. M., Karri, R., & Cocco, R. A. (2015). Review of entrainment correlations in gas-solid fluidization. *Chemical Engineering Journal*, *260*, 152–171. https://doi.org/10.1016/j.cej.2014.08.086

Cochet, Y. (2021). *Mitigation of fouling and liquid losses in a Fluid Coker™: Influence of operating conditions and internals on wet-agglomerates contribution to liquid carry-under*. The University of Western Ontario.

Dehdarinejad, E., & Bayareh, M. (2021). An Overview of Numerical Simulations on Gas-Solid Cyclone Separators with Tangential Inlet. *ChemBioEng Reviews*, *8*(4), 375–391. https://doi.org/10.1002/cben.202000034

Do, H. T., Grace, J. R., & Clift, R. (1972). Particle ejection and entrainment from fluidised beds. *Powder Technology*, *6*(4), 195–200. https://doi.org/10.1016/0032-5910(72)83013-4

Fassani, F. L., & Goldstein, L. (2000). A study of the effect of high inlet solids loading on a cyclone separator pressure drop and collection efficiency. *Powder Technology*, *107*(1–2), 60–65. https://doi.org/10.1016/S0032-5910(99)00091-1

Fung, A. S., & Hamdullahpur, F. (1993). A gas and particle flow model in the freeboard of a fluidized bed based on bubble coalescence. *Powder Technology*, *74*(2), 121–133. https://doi.org/10.1016/0032-5910(93)87004-8

Ganser, G. H. (1993). A rational approach to drag prediction of spherical and nonspherical particles. *Powder Technology*, *77*(2), 143–152. https://doi.org/10.1016/0032-5910(93)80051-B

Gao, Z., Wang, J., Liu, Z., Wei, Y., Wang, J., & Mao, Y. (2020). Effects of different inlet structures on the flow field of cyclone separators. *Powder Technology*, *372*, 519–531. https://doi.org/10.1016/j.powtec.2020.06.014

Gao, Z., Wang, J., Wang, J., & Mao, Y. (2019). Time-frequency analysis of the vortex motion in a cylindrical cyclone separator. *Chemical Engineering Journal*, *373*(November 2018), 1120–1131. https://doi.org/10.1016/j.cej.2019.05.054

Geldart, D., Broodryk, N., Kerdoncuff, A. (1993). Studies on the flow of solids down cyclone diplegs. *Powder Technology*, *76*, 175–183.

Geldart, D., Xue, Y., & Xie, H. (1995). Measurement of bottom bed and transport disengagement heights in beds of fresh FCC catalyst. In AIChE Symposium Series (Vol. 91, pp. 93-102): New York, NY: *American Institute of Chemical Engineers*, 1971-c2002.

Gimbun, J., & Fakhru, A. (2004). Prediction of the Effect of Dimension , Particle Density , Temperature , and Inlet Velocity on Cyclone Collection Efficiency. *Journal Teknologic*, *40*(F), 37–50. https://doi.org/10.11113/jt.v40.421

Grimble, T. A., Agarwal, A., & Juniper, M. P. (2017). Local linear stability analysis of cyclone separators. *Journal of Fluid Mechanics*, *816*, 507–538. https://doi.org/10.1017/jfm.2017.89

Hilligardt, K., & Werther, J. (1986). *Local bubble gas hold-up and expansion of gas/solid fluidized beds*. 215–221.

Hoffmann, A. C., De Groot, M., Peng, W., Dries, H. W. A., & Kater, J. (2001). Advantages and risks in increasing cyclone separator length. *AIChE Journal*, *47*(11), 2452–2460. https://doi.org/10.1002/aic.690471109

Hoffmann, A. C., de Jonge, R., Arends, H., & Hanrats, C. (1995). Evidence of the "natural vortex length" and its effect on the separation efficiency of gas cyclones. *Filtration and Separation*, *32*(8), 799–804. https://doi.org/10.1016/S0015-1882(97)84131-6

Huang, Y., Zhang, M., Lyu, J., Liu, Z., & Yang, H. (2018a). Effects of gas leakage on the separation performance of a cyclone. Part 1: Experimental investigation. *Chemical Engineering Research and Design*, *136*, 900–905. https://doi.org/10.1016/j.cherd.2018.03.047

Huang, Y., Zhang, M., Lyu, J., Liu, Z., & Yang, H. (2018b). Effects of gas leakage on the separation performance of a cyclone. Part 2: Simulation. *Chemical Engineering Research and Design*, *136*, 906–915. https://doi.org/10.1016/j.cherd.2018.06.002

Huard, M., Briens, C., Berruti, F., & Gauthier, T. A. (2010). A review of rapid gas-solid separation techniques. *International Journal of Chemical Reactor Engineering*, *8*(1). https://doi.org/10.2202/1542-6580.2069/MACHINEREADABLECITATION/RIS

Issangya, a S., Karri, S. B. R., Knowlton, T. M., & Cocco, R. (2011). Effect of Gas Bypassing in Deep Beds on Cyclone Dipleg Operation. *Splash*, *1*.

Knowlton, T. M., Mountziaris, T. J., & Jackson, R. (1986). The effect of pipe length on the gravity flow of granular materials in vertical standpipes. *Powder Technology*, *47*(2), 115–128. https://doi.org/10.1016/0032-5910(86)80107-3

Knowlton, T. M., Mountziaris, T. J., & Jackson, R. (1986). The effect of pipe length on the gravity flow of granular materials in vertical standpipes. *Powder Technology*, *47*(2), 115–128. https://doi.org/10.1016/0032-5910(86)80107-3

Kunii, D., & Levenspiel, O. (1991). Industrial Applications of Fluidized Beds. In *Fluidization Engineering* (pp. 15–59). Elsevier. https://doi.org/10.1016/b97808-050664-7.50008-1

Large, J. F., Martinie, Y., & Bergougnou, M. A. (1977). Interpretive model for entrainment in a large gas-fluidized bed. *J. Powders Bulk Solids Technol.; (United States)*, *1*(13). https://www.osti.gov/biblio/6844065

Li, X., Song, J., Sun, G., Jia, M., Yan, C., Yang, Z., & Wei, Y. (2016). Experimental study on natural vortex length in a cyclone separator. *Canadian Journal of Chemical Engineering*, *94*(12), 2373–2379. https://doi.org/10.1002/cjce.22598

Li, Y., Lu, Y., Wang, F., Han, K., Mi, W., Chen, X., & Wang, P. (1997). Behavior of gas-solid flow in the downcomer of a circulating fluidized bed reactor with a V-valve. *Powder Technology*, *91*(1), 11–16. https://doi.org/10.1016/S0032-5910(96)03226-3

Martinie, Y. (1975). *Entrainment and de-entrainment above a large gas fluidized bed*. ME Sc. Thesis, The University of Western Ontario.

Mothes, H., & Löffler, F. (1985). Motion and deposition of particles in cyclones. *German Chemical Engineering, 8*, 223-233.

Mountziaris, T. J., & Jackson, R. (1991). The effects of aeration on the gravity flow of particles and gas in vertical standpipes. *Chemical Engineering Science*, *46*(2), 381–407. https://doi.org/10.1016/0009-2509(91)80001-F

Peng, W., Hoffmann, A. C., Dries, H. W. A., Regelink, M. A., & Stein, L. E. (2005). Experimental study of the vortex end in centrifugal separators: The nature of the vortex end. *Chemical Engineering Science*, *60*(24), 6919–6928. https://doi.org/10.1016/j.ces.2005.06.009

Pisarev, G. I., Gjerde, V., Balakin, B. V., Hoffmann, A. C., Dijkstra, H. A., & Peng, W. (2012). Experimental and computational study of the “end of the vortex” phenomenon in reverse-flow centrifugal separators. *AIChE Journal*, *58*(5), 1371–1380. https://doi.org/10.1002/AIC.12695

Reddy Karri, S. B., & Knowlton, T. M. (2004). *Effect of Aeration on the Operation of Cyclone Diplegs Fitted with Trickle Valves*. https://doi.org/10.1021/ie034213j

Stewart, P. S. ., & Davidson, J. F. (1967). Slug Flow in Fluidised Beds. *Powder Technology*, *1*, 61–80.

Sun, J. G., Chen, M. M., & Chao, B. T. (1988). *On fluctuating motions due to surface waves in gas fluidized beds*. https://www.osti.gov/biblio/7001703

Sun, L., Wang, D., Song, J., Liu, J., Wang, J., & Wei, Y. (2020). Experimental study of gas swirling flow instability characteristics in a cyclone using the hot-wire anemometry technique. *AIChE Journal*, *66*(1). https://doi.org/10.1002/aic.16759

Tallon, S., & Davies, C. E. (2005). Discharge of a fluidised bed of particles through an orifice. *Powder Technology*, *160*, 45–53. https://doi.org/10.1016/j.powtec.2005.04.050

Trefz, M., & Muschelknautz, E. (1993). Extended cyclone theory for gas flows with high solids concentrations. *Chemical Engineering & Technology*, *16*(3), 153–160. https://doi.org/10.1002/ceat.270160303

Wang, J., Bouma, J. H., & Dries, H. (2000). An experimental study of cyclone dipleg flow in fluidized catalytic cracking. *Powder Technology*, *112*, 221–228.

Wen, C. Y., & Chen, L. H. (1982). Fluidized bed freeboard phenomena: Entrainment and elutriation. *AIChE Journal*, *28*(1), 117–128. https://doi.org/10.1002/AIC.690280117

Yan, C.-Y., Sun, G.-G., Chen, J.-Y., Wei, Y.-D., & Lu, C.-X. (2020). Experimental study on the particle flow patterns in a cyclone dipleg with a trickle valve. *Petroleum Science*, *17*. https://doi.org/10.1007/s12182-020-00449-7

Yang, J., Sun, G., & Gao, C. (2013). Effect of the inlet dimensions on the maximum-efficiency cyclone height. *Separation and Purification Technology*, *105*, 15–23. https://doi.org/10.1016/j.seppur.2012.12.020

Yoon, Y. S., Kim, S. D., & Park, W. H. (1986). Entrainment of coal particles in a gas fluidized bed. *Korean Journal of Chemical Engineering*, *3*(2), 121–125. https://doi.org/10.1007/BF02705023

Z., J., X., W., & M., S. (1991). Experimental research on the natural turning length in the cyclone. *Proceedings of Filtech Europa 91 Conference*, *2*, 583 – 589. https://www.scopus.com/inward/record.uri?eid=2-s2.0-25844489915&partnerID=40&md5=0f3624be416102cae28a89c5ce7011ab

Zenz, F. A. (1982). *State-of-the-art review and report on critical aspects and scale-up considerations in the design of fluidized-bed reactors. Final report on Phase II*. https://www.osti.gov/biblio/6612476

Chapter 5

5 Solids Recirculation Between Dense Fluidized Beds

5.1 Introduction

The solids recirculation rate between the reactor and burner is crucial for the fluid coking process. Stable recirculation rates are required to provide the energy required to thermally crack bitumen and maintain the optimal reactor temperature to avoid rapid agglomeration and defluidization (Briens and McMillan, 2021). Unstable recirculation rates can cause an accumulation of coke in either vessel, increasing entrainment and risking significant solids losses if either cyclone dipleg is uncovered. When operability issues restrict recirculation rates, the reactor feed rate must be reduced. Therefore, good transfer line operation is critical to the fluid coking process. The following section investigates the recirculation rate between the Reactor and Heater in the Cold Model pilot plant.

5.1.1 Requirements for Operation

The requirements for the operation of the Cold Model are:

1. Stable solids recirculation rates between 3000 and 4000 kg/hr
2. Stable fluidized bed levels in both Reactor and Heater
3. No gas flow from the Reactor to the Heater

5.1.2 Literature Review

A pressure-balanced system of standpipes and risers is used to transfer solids between vessels during solids recirculation. Particles flow downwards from a vessel and enter a standpipe, which generates the pressure needed to transfer the solids from low pressure to a higher pressure by extending below the vessel. In addition to providing pressure, the standpipe must provide a stable flow of solids and provide a seal to prevent gas flow back into the initial vessel. Keeping the solids fluidized by introducing a small amount of gas to the standpipe will help meet those

requirements while avoiding the formation of large gas bubbles that could hamper solids flow if excess gas is introduced. Bodin et al. (2002a) developed a model to determine the optimal aeration flowrate in the standpipe and the maximum vertical spacing between the aeration taps. The difference in density between the standpipe and riser creates a pressure difference that drives the recirculation (Knowlton & Reddy, 2020; Masten. 1973). Several researchers have studied solids flow in standpipes and risers to estimate solids flow rates (Fan and Zhu, 1998; Grace and Knowlton, 1997; Leung and Jones, 1976).

Three flow regimes have been identified in standpipes (Bodin et al., 2002b; Knowlton, 2003):

1) Fluidized flow is where solids flow down the standpipe as a dense, fluidized phase. This ideal regime provides stable flow and a pressure seal.

2) Packed bed flow is where particles are not fluidized. The solids flow is often intermittent and unstable. Packed bed flow does not provide a good seal.

3) Streaming flow is where the solids have a low voidage and a large gas flowrate. This flow regime is often encountered in cyclone diplegs and can be improved by increasing the dipleg immersion.

The solids flowrate through a standpipe connecting two fluidized beds can be controlled with either mechanical valves, such as slide valves, or non-mechanical valves, which can reduce gas flow between the two units connected by the standpipe and control the solids flowrate between the two units using aeration. Several non-mechanical valves have been proposed, including V-valves (Leung et al., 1987), J-valves (Terasaka, Akashi, and Tsuge, 2002), L-valves (Chovichien, et al., 2013; Monazam, Breault, and Shadle, 2019; Monazam, Breault, Shadle, and Weber, 2018; Smolders & Baeyens, 1995; Yazdanpanah, Forret, Gauthier, & Delebarre, 2012) and loop seals (Prabir Basu and Butler, 2009; Prabir Basu and Cheng, 2000; Kim and Kim, 2002; Knowlton and Reddy Karri, 2020; Li, Li, and Zhu, 2014; Stollhof, et al., 2019). This work focuses on the loop seals.

When using loop seals, the downstream leg is connected to the downstream fluidized bed with an overflow pipe, and the flowrate of solids into the standpipe automatically adjusts to keep the mass of solids in the downstream bed constant (Kim et al., 2000). As a result, there may be an overflow on the supply side or an underflow connection to the downstream fluidized bed (Stollhof, et al., 2019). Figure 5-1 depicts a simplified diagram of a loop seal downleg and upleg. The loop seal is usually operated between minimum fluidization (U_{mf}) up to approximately 3 U_{mf}. Within this range, increasing the superficial gas velocity increases the solids flowrate (Prabir Basu & Butler, 2009; Stollhof, et al., 2019); however, gas flow from the upstream unit was increased to the downstream unit (Bareschino, Solimene, Chirone, & Salatino, 2014; Stollhof, et al., 2019). The length of the horizontal section between the supply and downleg also has some impact: a longer horizontal section is associated with a lower solids flowrate (Prabir Basu & Butler, 2009) and lower gas leakage. Several studies have used tracer gas to study the flow of gas and solids in loop seals (Yao et al., 2011; Stollhof et al., 2019; Lindmüller et al., 2021; Saayman et al., 2014). Models have been developed to predict the loop seal pressure drop and the gas and solids flowrates through the loop seal (Cheng & Basu, 1999; Kim & Kim, 2002; Li, et al., 2014; Li, Zou, Li, & Zhu, 2018). However, these models have yet to be validated over various conditions.

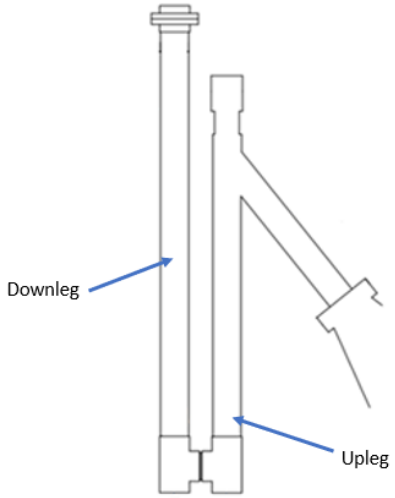

Figure 5-1. Simplified diagram of a loop seal.

5.1.3 Study Objectives

The objectives pursued in this section of the thesis are:

- Defining the operational limits of the Cold Model Fluid Coker, where solids recirculation rates are stable (i.e., minimal changes to bed levels in Reactor or Heater).
- Achieving solids recirculation rates between 3000 and 4000 kg/hr.
- Identifying operational limits to prevent gas flow from Reactor to Heater.

5.2 Original Cold Model Design

Preliminary tests of the solids transfer lines with the original Cold Model design (see Figure 2-6) used one-way transfers of solids to identify limitations prior to recirculating solids between both units.

5.2.1 Impact of Aeration on One-Way Flow Capacity in U-Bend

One way transfer of solids from the Reactor to the Heater was used to see the impact of aeration velocity on the solids flow rate. The reactor was overfilled to a constant height, and the gate valve opened fully for each run while the aeration flow was adjusted with the U-Bend rotameters (see Chapter 2.1.2). As the mass of solids in the Reactor is limited, each transfer could only operate for 60 to 120 s. Therefore, the one-way transfer could not be used to determine possible recirculation rates as the level of solids in the reactor was higher than it would be during recirculation, artificially increasing potential flowrates. Figure 5-2 presents the change in solids flowrate, F_s, when varying the U-Bend aeration velocity. The solids flowrate was obtained using the riser pressure drop (refer to Appendix C: Solids Flowrate Calibration). An optimal aeration velocity of 0.66 m/s can be observed for this configuration.

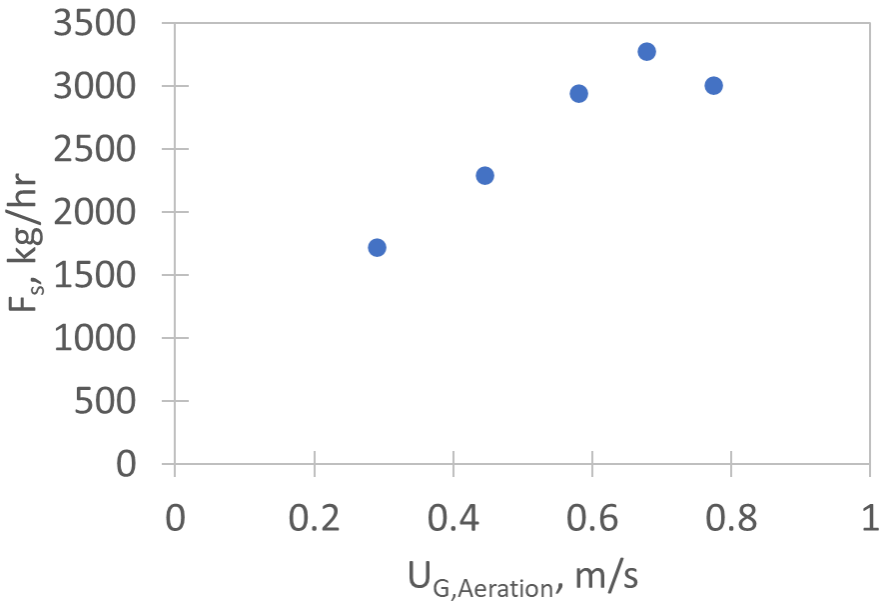

Figure 5-2. Impact of aeration on one-way transfer rate in U-Bend with $U_{G,Reactor}$ = 0.6 m/s with All Spargers gas distributions and $U_{G,Heater}$ = 0 m/s.

5.2.2 Impact of Aeration on One-Way Flow Capacity in Loop Seal

The one-way transfer of solids from the Heater to the Reactor was used to see the impact of aeration velocity on potential solids flowrate. The heater was overfilled to the same level for each run, while aeration flow was adjusted with the loop seal rotameters (refer to Figure 2-5 for aeration locations).

The solids level in the Heater was again higher for the one-way transfer than it would be during recirculation, so the transfer rate was artificially inflated. The solids flowrate from the Heater to the Reactor was determined by measuring the change in pressure with time in the Reactor at tap P_4 (Figure 2-18). The one-way solids transfer rates from Heater to Reactor were much lower than the other transfer line, so transfers were operated for 100 to 200 s. Figure 5-3 shows how the reactor pressure evolved as solids are transferred from the Heater to the Reactor.

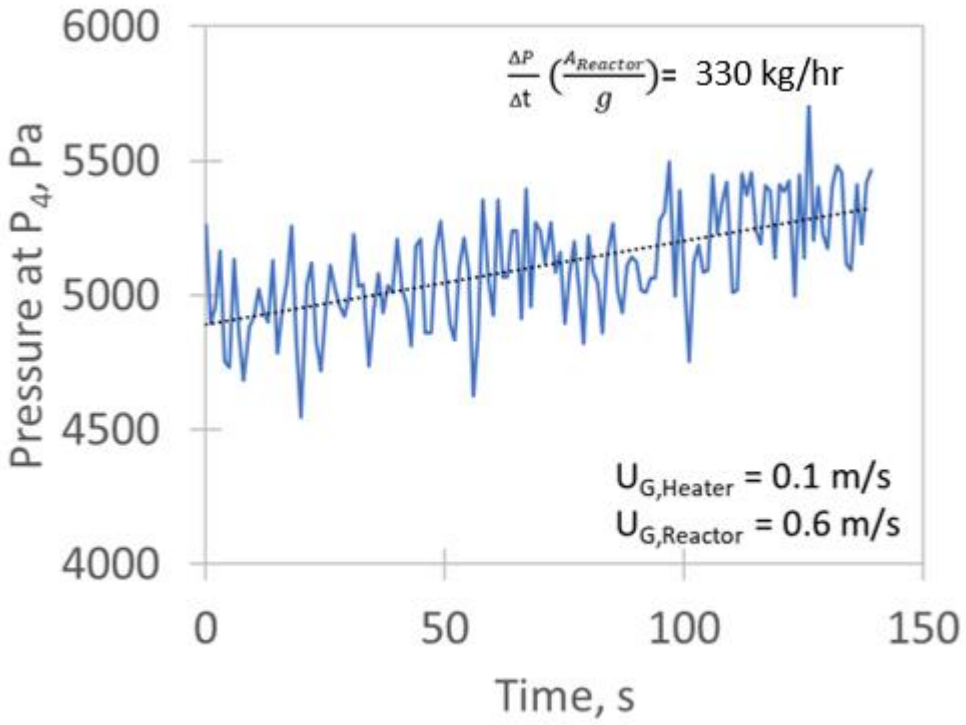

Figure 5-3. Example of change in pressure with time at tap P_4 as solids transfer from Heater to Reactor with $U_{G,Heater}$ = 0.1m/s, $U_{G,Reactor}$ = 0.6 m/s using All Spargers gas distribution, $U_{G,Upleg}$ = 0.2 m/s and $U_{G,Downleg}$ = 0.09 m/s.

Figure 5-4 shows the impact of the upleg and downleg aeration flow rates on the one-way transfer rate while maintaining the other flow constant. While increasing the upleg aeration flowrate to 0.2 m/s improved the solids flowrate from 144 kg/hr to 300 kg/hr, and increasing the downleg aeration to 0.09 m/s improved the solids flowrate from 120 kg/hr to 330 kg/hr, the transfer rate was roughly 10% of the desired recirculation rate. Therefore, while further optimization may have helped increase solids transfer rates, the Cold Model was modified to provide a much larger solids flowrate.

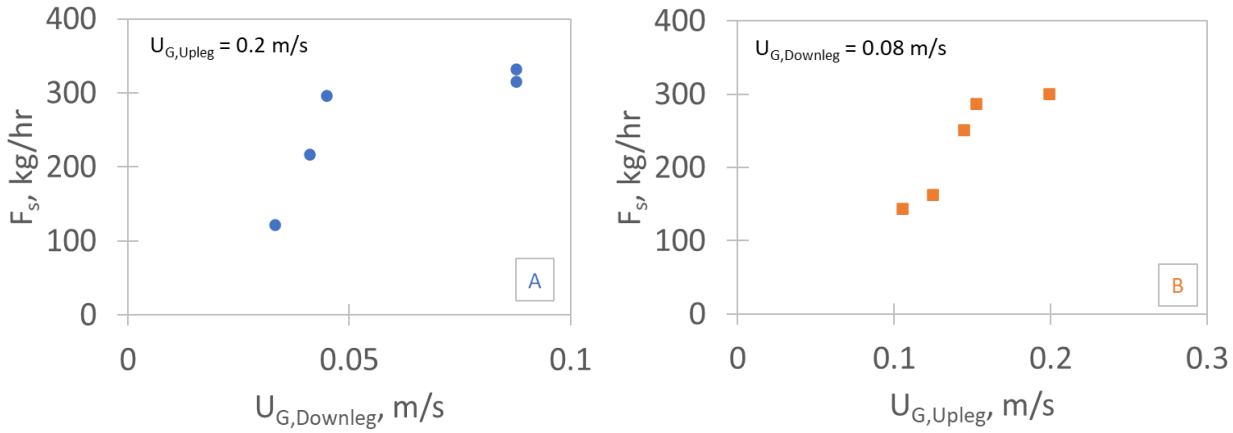

Figure 5-4. Impact of loop seal aeration on one-way solids transfer from Heater to Reactor when A) Total upleg aeration was constant, and downleg aeration was varied B) Total downleg aeration was constant, and upleg aeration was varied.

5.3 Phase 1 of Cold Model Modifications

The changes made to the transfer lines during Phase 1 Modifications included removing the venturi at the top of the riser and replacing the 0.05 m (2 in) loop seal with a 45° angled line of the same diameter (Refer to Figure 2-10 for details).

5.3.1 Impact of Aeration on One-Way Flow Capacity in 0.05 m (2 in) 45° Angled Line

As detailed in the previous section, the heater to reactor solids transfer rate can only be optimized using the aeration flow velocity, as the Heater is filled above the typical level used during recirculation. Figure 5-5 shows that increasing the aeration flowrate in the downleg of the transfer line improved the transfer rate from the Heater to the Reactor. However, the slug velocity in the transfer line is $U_{G,Slug}$ = 0.25 m/s, so aeration rates above that velocity were not investigated (Stewart and Davidson, 1967).

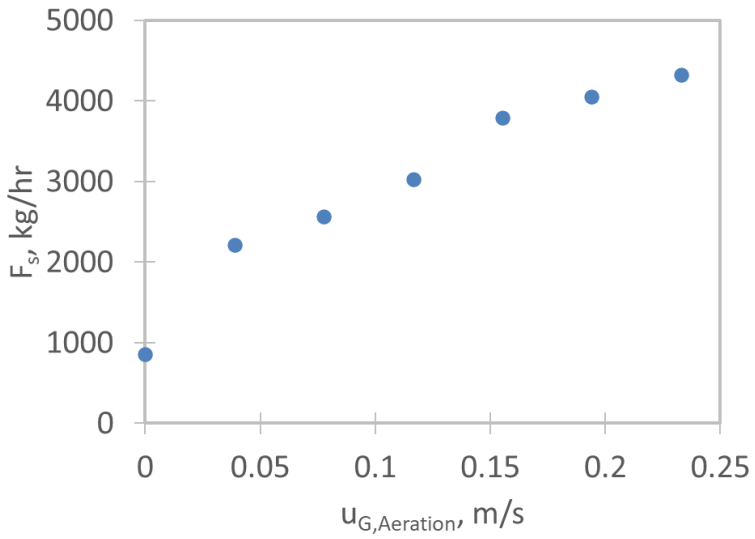

Figure 5-5. Impact of aeration flowrate in downleg of 45° angled Heater to Reactor transfer line with $U_{G,Heater}$ = 0.1 m/s, $U_{G,Reactor}$ = 0.6 m/s in All Spargers gas distribution.

5.3.2 Stable Recirculation Rate

The angled line was aerated at $U_{G,AERATION}$ = 0.24 m/s to determine the maximum stable recirculation rate, and the gate valve at the bottom of the Reactor was gradually opened to allow the system to stabilize. Once the valve was 100% open and the bed heights in the Heater and Reactor were stable, the pressure in the Reactor and the pressure drop in the riser were measured for 30 minutes. Figure 5-6 shows the pressure signal in tap P_4 and the solids flowrate through the riser over 30 minutes (See Appendix C: Solids Flowrate Calibration). The time average of the solids flowrate at these conditions was F_s = 3400 kg/hr. Simplifying the transfer line from a loop seal to a 45° angled line allows for a 3400 kg/hr recirculation rate without increasing the transfer line diameter. A stable pressure signal at P_4 in the Reactor and in the riser means the fluidized bed level is not changing in the Reactor, and the overflow pipe in the Heater is operating as intended.

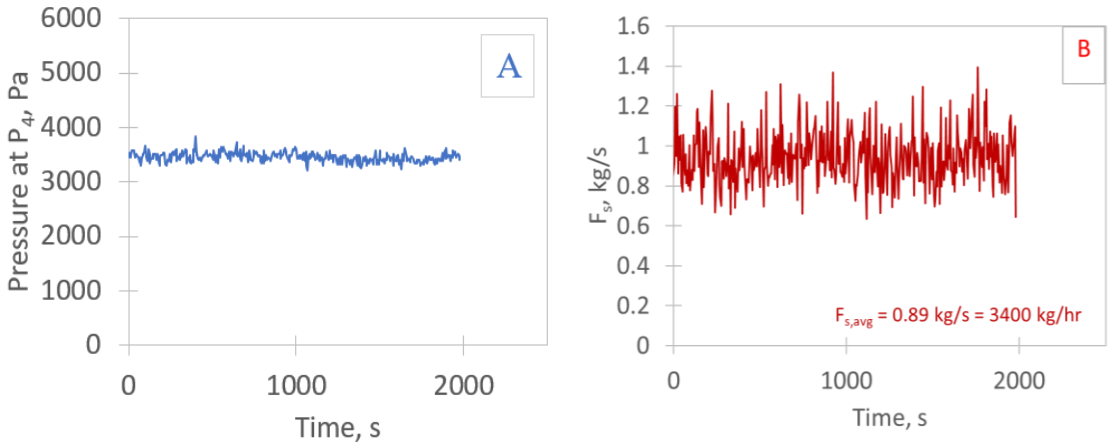

Figure 5-6. Example of stable recirculation rate over 30 min (time averaged every 5 seconds) A) Pressure signal at tap P_4 in the Reactor at $U_{G,Reactor}$ = 0.6 m/s in All Spargers gas distribution B) Solids flowrate, $F_{s,avg}$ = 3400 kg/hr, from riser pressure drop calibration.

5.3.3 Gas Flow from Reactor to Heater

While the 45° angled line improved the stable recirculation rate into the target recirculation range, it is difficult to maintain in the transfer line the dense solids phase needed to seal the line and prevent gas from flowing from the Reactor to the Heater. In the Hot Model pilot plant, this would result in losses of the product vapours and impact the mass balance around the unit.

Nitrogen was injected to aerate the transfer line to define the operating limit where the 45° angled line would be adequate to stop gas flow from the Reactor to the Heater. Then, gas was sampled and tested in the transfer line per the procedure outlined in Chapter 2.5 Figure 5-7 shows the percentage of oxygen detected with an oxygen probe for gas sampled across several solids flowrates (recirculation rates).

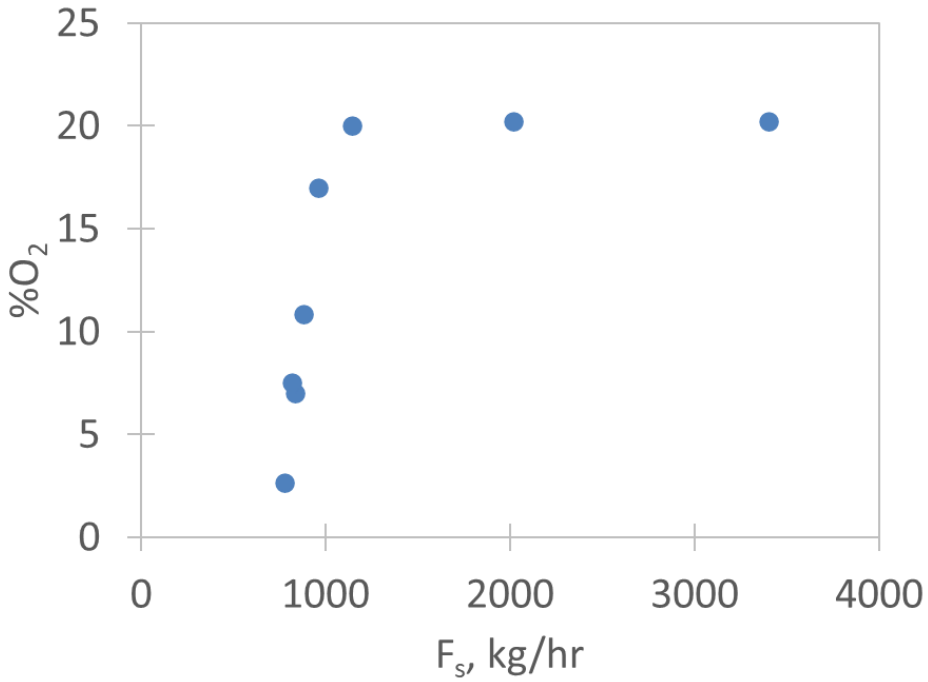

Figure 5-7. Percent O_2 measured with oxygen probe from gas sampled at recirculation rate (F_s).

Percentages of oxygen below 21% indicate contamination with additional nitrogen in the gas sample. Figure 5-7 indicates operation at solids flowrates below 1100 kg/hr allowed gas to flow back up towards the heater. At this solids flowrate and lower, the downward velocity of solids and gas cannot force the gas back to the Reactor. Therefore, gas did not flow from the Reactor to the Heater at solids flowrates above 1100 kg/hr, including the target solids recirculation rate of 3000 to 4000 kg/hr. If low recirculation rates are not required in the Hot Model pilot plant, the angled line could be used for a more straightforward operation.

5.4 Phase 2 of Cold Model Modifications

Refer to Chapter 2.1.3. Refer to Table 2-1 and Figure 2-12 for more details on the modifications made in Phase 2.

5.4.1 Impact of Aeration on Loop Seal Operation During Recirculation

This section aimed to achieve a solids recirculation rate greater than 4000 kg/hr to show a clear improvement over the 0.05 m (2 in) 45° angled line (refer to Figure 2-10).

Table 5-1 summarizes the aeration flowrates used to test the recirculation rate.

Table 5-1. Summary of loop seal aeration flowrates used for recirculation tests

Injection Location	$U_{G,AERATION}$ With Lateral Injection, m/s	$U_{G,AERATION}$ Without Lateral Injection, m/s
A1	0.05	0
A2	0.05	0
A3	0.05	0
A4	0.05 – 0.13	0.02 – 0.08
A5	0.17	0.17

The change in recirculation rate with aeration flowrate is shown in Figure 5-8. Initial experiments used aeration in the lateral taps A_1 to A_3, and the recirculation achieved was between 3650 and 3920 kg/hr. The lateral injections were then removed to reduce the overall gas in the downleg of the transfer line. Removing the lateral injections improved the solids flowrate from 3950 kg/hr to 4260 kg/hr for $U_{G,A4}$ = 0.05 m/s for the three replicates completed at these conditions. Increasing or decreasing the aeration flowrate in A_4 decreased the recirculation rate, indicating a flowrate of $U_{G,A4}$ = 0.05 m/s is close to the optimum flowrate. Further optimization is recommended to achieve stable flowrates higher than 4260 kg/hr; however, the objectives of this thesis were met.

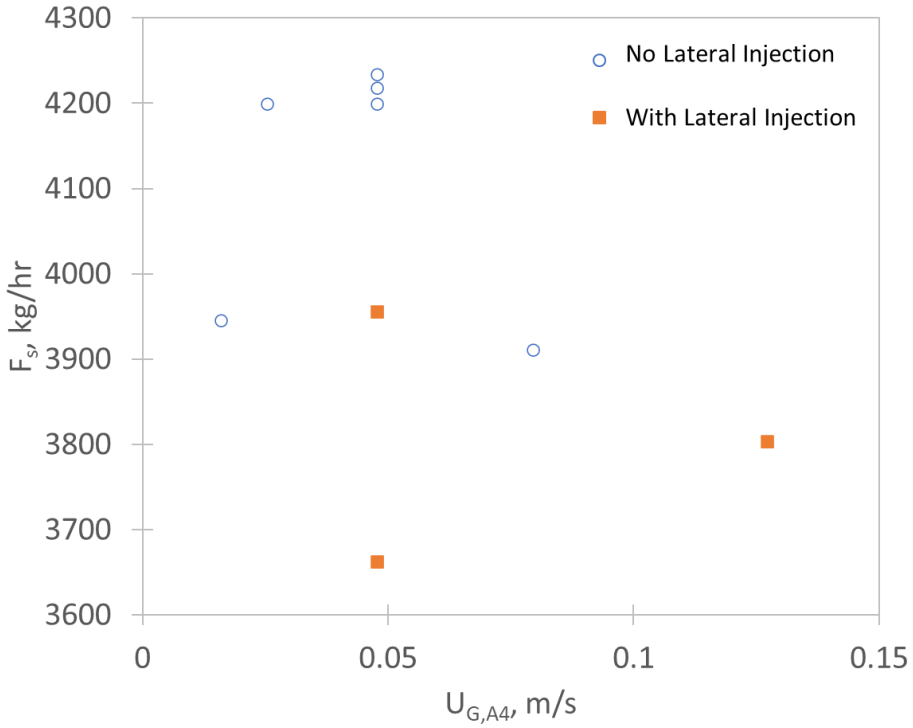

Figure 5-8. Impact of aeration in loop seal tap A_4, with and without lateral injection, on the stable recirculation rate (F_s) with $U_{G,Heater}$ = 0.1 m/s and $U_{G,Reactor}$ = 0.6 m/s with All Spargers gas distribution.

5.4.2 Maximum Stable Recirculation Rate

Maintaining a stable recirculation rate over long periods is essential to minimize operational disruption. To determine the maximum stable recirculation rate, the loop seal was aerated at $U_{G,A4}$ = 0.05 m/s and $UG_{A,5}$ = 0.17 m/s and the gate valve at the bottom of the Reactor was gradually opened to allow the system to stabilize. Once the valve was open 100% and the bed heights in the Heater and Reactor were stable, the pressure in the Reactor and the pressure drop in the riser were measured for 30 minutes. Figure 5-9 shows the pressure signal in tap P_4 and the solids flowrate through the riser over 30 minutes (see Appendix C: Solids Flowrate Calibration). The time average of the solids flowrate at these conditions was F_s = 4260 kg/hr.

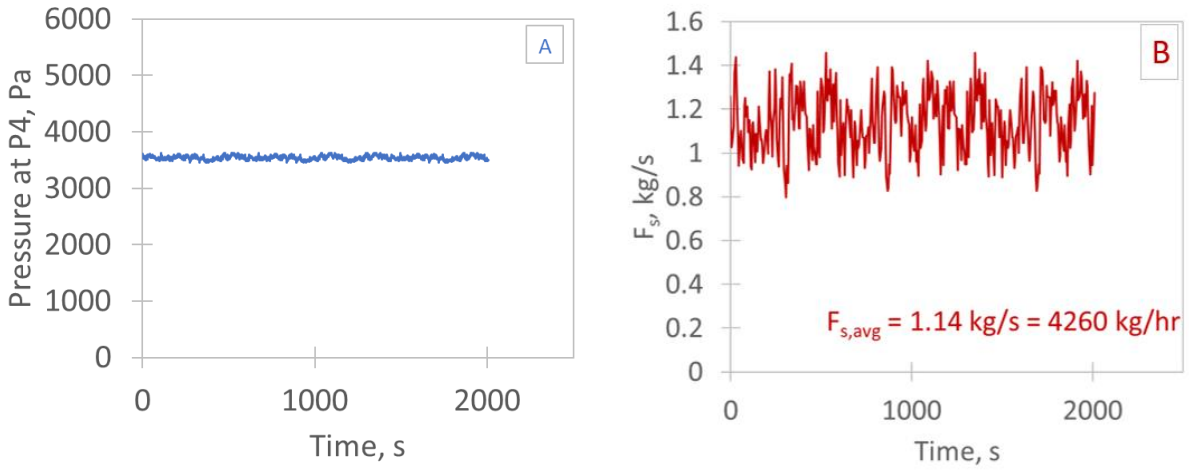

Figure 5-9. Example of stable recirculation rate over 30 min (time averaged over 5 seconds) A) Pressure signal at tap P_4 in the Reactor at $U_{G,Reactor}$ = 0.6 m/s in All Spargers gas distribution and $U_{G,Heater}$ = 0.1 m/s B) Solids flowrate, $F_{s,avg}$ = 4260 kg/hr, from riser pressure drop calibration.

Increasing the loop seal diameter to 0.08 m (3 in) improved the stable recirculation rate to 4260 kg/hr, as the pressure signal in the Reactor and solids flowrate measured in the riser did not change significantly with time. Gravity flow through the pipe is estimated at 8800 kg/hr (Zenz, 1975), suggesting a factor limiting flow through the loop seal. The slug velocity in the pipe at the aeration conditions of interest is estimated at $U_{G,Slug}$ = 0.34 m/s (Stewart and Davidson, 1967). The velocity of the emulsion at F_s = 4200 kg/hr is 0.3 m/s. The conditions indicate that slugs could form and stagnate when flowing towards the heater, as illustrated in Figure 5-10. These slugs could limit the maximum recirculation rate. Gas tracer experiments described in the next section were conducted to determine whether slugs were flowing up towards the heater.

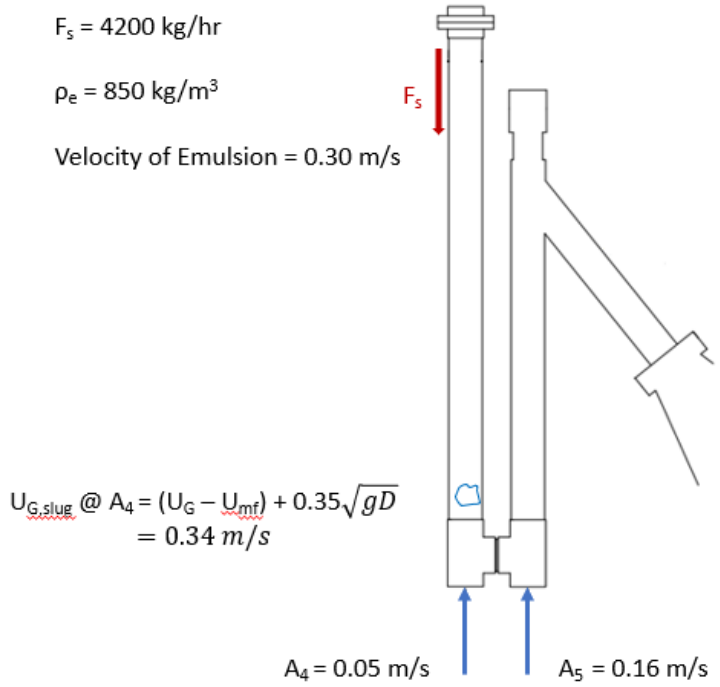

Figure 5-10. Illustration of slug flow up transfer line downleg.

5.4.3 Gas Flow from Reactor to Heater

Nitrogen was injected in aeration tap A_4 at the same conditions in the previous section, summarized below in Figure 5-11 shows no change in the oxygen probe reading for these conditions after injecting the sample at t = 10 s, indicating no gas flowing up the transfer line downleg. The percentages of oxygen detected with the oxygen probe for gas sampled at the conditions outlined above are summarized in Table 5-3. No contamination with excess nitrogen was detected at any of the solids flow rates tested, indicating that the solids flowrate is large enough to push any gas slug horizontally through the loop seal, and towards the reactor.

Table 5-2. Gas was sampled from the transfer line, in the downleg, and tested per the procedure outlined in Chapter 2.5 (refer to Figure 2-27, sample line A, for injection and sampling locations). Figure 5-11 shows no change in the oxygen probe reading for these conditions after injecting the sample at t = 10 s, indicating no gas flowing up the transfer line downleg. The percentages of oxygen detected with the oxygen probe for gas sampled at the conditions outlined above are summarized in Table 5-3. No contamination with excess nitrogen was detected at any of the solids flow rates tested, indicating that the solids flowrate is large enough to push any gas slug horizontally through the loop seal, and towards the reactor.

Table 5-2. Summary of nitrogen, air and solids flowrates used to test for gas flow up downleg

$U_{G,Aeration}$, N_2, m/s	$U_{G,Aeration}$, Air, m/s		Recirculation Rate, F_s, kg/hr
A4	**A1 – A3**	**A5**	
0.5	0.05	0.17	3955
0.13			3804
0.02	0		3945
0.03			4200
0.05			4260
0.08			3910

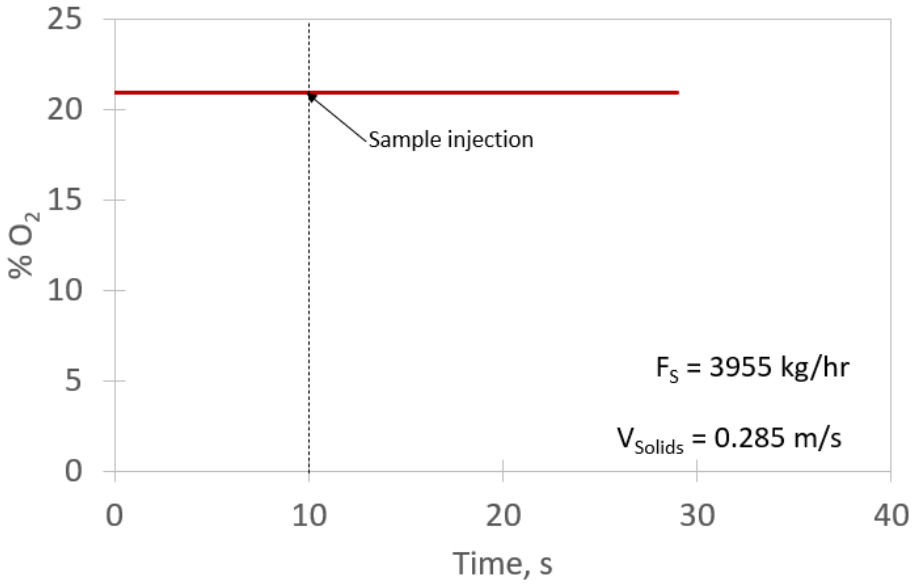

Figure 5-11. Example of the oxygen probe signal before and after sample injection in the testing cell for $U_{G,Aeration\ at\ A4}$ = 0.05 with lateral gas injection and a solids flowrate of 3955 kg/hr.

Table 5-3. Summary of oxygen probe readings for different solids flowrates

$U_{G,Aeration}$, N_2, m/s	$U_{G,Aeration}$, Air, m/s		F_s, kg/hr	%O2
A4	A1 – A3	A5		
0.5	0.05	0.17	3955	20.95
0.13	0.05	0.17	3804	20.95
0.02	0	0.17	3945	20.95
0.03	0	0.17	4200	20.95
0.05	0	0.17	4260	20.95
0.08	0	0.17	3910	20.95

To confirm this behaviour at operating conditions used for the maximum stable recirculation rate (F_s = 4260 kg/hr, No lateral injection, $U_{G,A4}$ = 0.05 m/s, $U_{G,A5}$ = 0.17 m/s), nitrogen was injected at tap A_4, and gas was sampled in the upleg above tap A_5 (refer to Figure 2-27, sample line B). Figure 5-12 shows the oxygen probe signal before and after sample injection for the sample taken above tap A_5. The percentage of oxygen was 16 % for the sample and replicate, indicating excess nitrogen was present. As the air was injected at A_5, the nitrogen would be diluted with air. A mass balance shows that this sample represented 100% of the nitrogen injected at A_4. Therefore, at the target solids flowrates, the velocity of solids is large enough to push the gas slugs formed in the loop seal downleg horizontally to the Reactor.

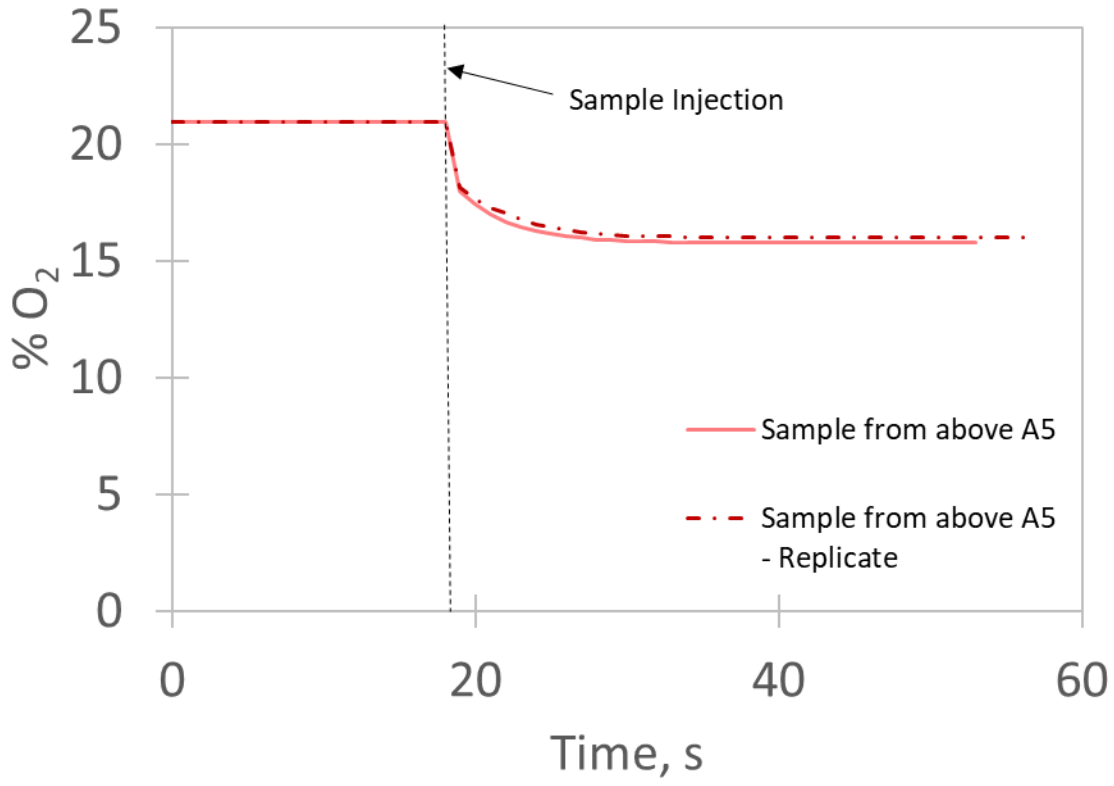

Figure 5-12. Oxygen probe signal before and after sample injection in the testing cell for sample taken at tap A_5 for F_s = 4260 kg/hr, No lateral injection, $U_{G,A4}$ = 0.05 m/s, $U_{G,A5}$ = 0.17 m/s.

A final confirmation that the loop seal works as intended to seal the Reactor product gas from flowing to the Heater was to inject nitrogen in the angled section of the loop seal (directly

upstream from the Reactor fluidized bed) and sample in the down leg (Figure 2-27, sample line C). Figure 5-13 shows that no excess nitrogen was detected in the downleg, indicating the loop seal functions as intended at the target recirculation rates.

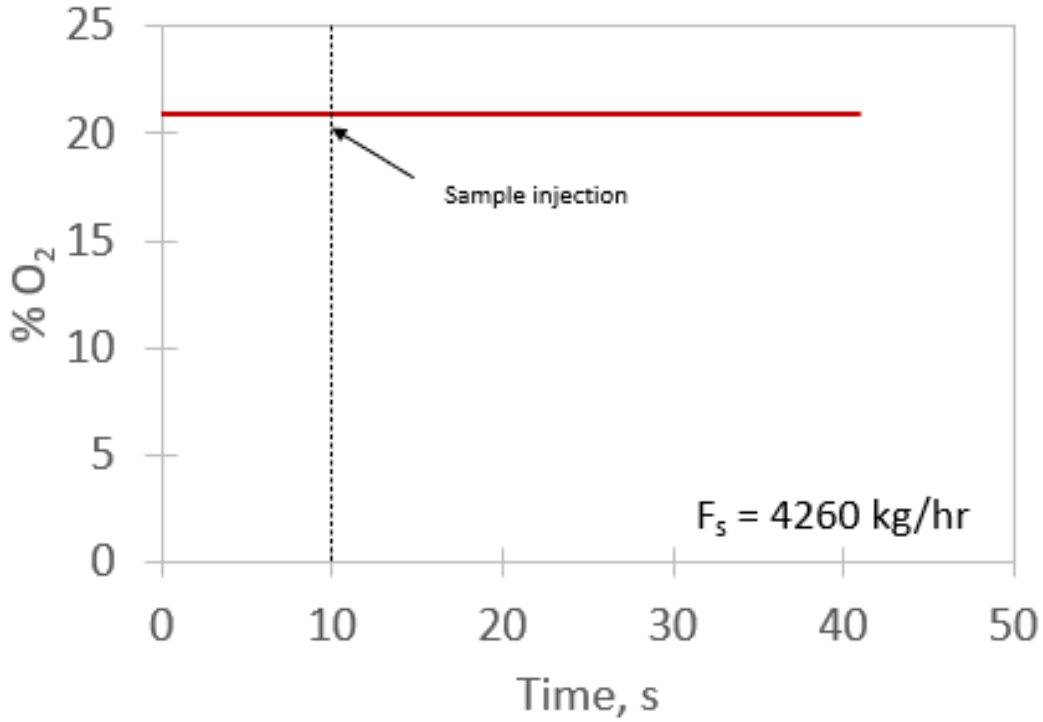

Figure 5-13. Oxygen probe signal before and after sample injection in the testing cell when nitrogen was injected in the angled portion of the loop seal for F_s = 4260 kg/hr, No lateral injection, $U_{G,A4}$ = 0.05 m/s, $U_{G,A5}$ = 0.17 m/s.

The completed modifications to the Cold Model allow stable recirculation rates up to 4260 kg/hr, which exceeds the target range of 3000 to 4000 kg/hr. At these recirculation rates, no gas flows from the Reactor to the Heater, meeting all requirements for ideal operation. Further studies should be conducted to optimize the aeration flowrate in the loop seal and start-up procedure to minimize downtime and operational issues.

5.5 Summary

The operation of the Cold Model required a stable recirculation rate of 3000 to 4000 kg/hr. Initial testing of the original Cold Model design indicated that the loop seal limited the overall recirculation rate to less than 350 kg/hr. Therefore, two phases of unit modifications were implemented and studied to improve the stable recirculation rate. Concurrently, gas flow from the reactor to the heater through the solids return line was measured using nitrogen as a gas tracer and an oxygen probe at both phases of unit modifications. It was shown that if operated at a sufficient recirculation rate (F_s > 1100 kg/hr), an angled line can be used in the place of a loop seal to return solids to the reactor during recirculation with no gas flow from the reactor to the heater. Following Phase 2 of unit modifications, a stable recirculation rate of 4200 kg/hr was achieved through the 0.08 m (3 inch) loop seal, meeting the target requirements of 3000 to 4000 kg/hr. Finally, a nitrogen gas tracer testing indicated the solids circulation rate was sufficient to prevent gas flow from the reactor to the heater, satisfying the operating requirements defined in Section 1.4 and Section 5.1.1.

5.6 References

Bareschino, P., Solimene, R., Chirone, R., & Salatino, P. (2014). Gas and solid flow patterns in the loop-seal of a circulating fluidized bed. *Powder Technology, 264*, 197–202. https://doi.org/10.1016/j.powtec.2014.05.036

Basu, P., & Cheng, L. (2000). An analysis of loop seal operations in a circulating fluidized bed. *Chemical Engineering Research and Design*, *78*(7), 991–998. https://doi.org/10.1205/026387600528102

Bodin, S., Briens, C., Bergougnou, M. A., & Patureaux, T. (2002a). Modeling of withdrawal wells and conical transitions in standpipe systems. Experimental validation. *Powder Technology*, 124, 85-93.

Bodin, S., Briens, C., Bergougnou, M. A., & Patureaux, T. (2002b). Standpipe flow modeling, experimental validation and design recommendations. *Powder Technology*, *124*(1–2), 8–17. https://doi.org/10.1016/S0032-5910(01)00473-9

Chinsuwan, A. (2021). A mathematical model for predicting the flow behavior through a CFB reactor U type loop-seal. *International Journal of Heat and Mass Transfer*, *177*, 121541. https://doi.org/10.1016/j.ijheatmasstransfer.2021.121541

Chovichien, N., Pipatmanomai, S., & Chungpaibulpatana, S. (2013). Estimate of solids circulation rate through an L-valve in a CFB operating at elevated temperature. *Powder Technology*, 235, 886-900.

Daous, M. A., & Al-Zahrani, A. A. (1998). Modeling solids and gas flow through an L-valve. *Powder Technology*, 99, 86-89.

Fan, L. S., & Zhu, C. (1999). Principles of gas-solid flows.

Kim, J. M., Han, G. Y., & Yi, C. K. (2000). The Characteristics of Particle Flow in the Overflow and Underflow Standpipe of Fluidized Beds. *Korean Journal of Chemical Engineering*, *17*(3), 273–279. https://doi.org/10.1007/BF02699039

Kim, S. W., Namkung, W., & Kim, S. D. (1999). Solids flow characteristics in loop-seal of a circulating fluidized bed. *Korean Journal of Chemical Engineering*, *16*(1), 82–88. https://doi.org/10.1007/BF02699009

Knowlton, T. (2003). Standpipes and nonmechanical valves. HANDBOOK of FLUIDIZATION and FLUID-PARTICLE SYSTEMS.

Knowlton, T. M., & Reddy Karry, S. B. (2020). Essentials of fluidization technology. In *Essentials of Fluidization Technology*. https://doi.org/10.1002/9783527699483

Knowlton, T. M., Grace, J. R., & Avidan, A. A. (Eds.). (1997). *Circulating fluidized beds*. Blackie Academic & Professional.

L.S Leung L.S., Jones, P.J. (1976), *Powder Technol*., 20, p. 145

Leung, L. S., Chong, Y. O., & Lottes, J. (1987). Operation of V valves for gas—solid flow. Powder Technology, 49, 271-276.

Lindmüller, L., Haus, J., Ramesh, A., Nair, K., & Heinrich, S. (2021). *Minimizing gas leakages in a system of coupled fluidized bed reactors for chemical looping combustion*. https://doi.org/10.1016/j.ces.2021.117366

Matsen, J. M. (1973). Flow of fluidized solids and bubbles in standpipes and risers. *Powder Technology*, *7*(2), 93–96. https://doi.org/10.1016/0032-5910(73)80011-7

Saayman, J., Xu, M., Lim, J. C., & Ellis, N. (2014). Gas leakage between reactors in a dual fluidized bed system. *Powder Technology*, *266*, 196–202. https://doi.org/10.1016/j.powtec.2014.06.012

Stewart, P. S. ., & Davidson, J. F. (1967). Slug Flow in Fluidised Beds. *Powder Technology*, *1*, 61–80.

Stollhof, M., Penthor, S., Mayer, K., & Hofbauer, H. (2019). Influence of the loop seal fluidization on the operation of a fluidized bed reactor system. *Powder Technology*, *352*, 422–435. https://doi.org/10.1016/j.powtec.2019.04.081

Terasaka, K., Akashi, S., & Tsuge, H. (2002). Development of a J-shaped pneumatic valve to control the solid particle circulation rate in a circulating fluidized bed. *Powder Technology*, 126, 13-21.

Yao, X., Yang, H., Zhang, H., Zhou, C., Liu, Q., & Yue, G. (2011). Gas-Solid Flow Behavior in the Standpipe of a Circulating Fluidized Bed with a Loop Seal. *Energy Fuels*, *25*, 246–250. https://doi.org/10.1021/ef1011897

Yazdanpanah, M. M., Forret, A., Gauthier, T., & Delebarre, A. (2012). *An experimental investigation of loop-seal operation in an interconnected circulating fluidized bed system*. https://doi.org/10.1016/j.powtec.2012.11.033

Zenz F.A., Hydrocarbon Processing, May (1975) 125-128

Chapter 6

6 Conclusions and Recommendations

This chapter summarizes the results, highlights the most critical findings and draws conclusions from this thesis. In addition, several actions are proposed for the Hot Model Pilot Plant.

6.1 Conclusions

1) The cyclone efficiency was greater than 99% and functioned well to return entrained solids to the bed during regular operation, even when the cyclone inlet is below the TDH.

2) The completed unit modifications extended the safe operating zone in the Reactor. The Reactor can operate with less than 0.01 kg/hr solids losses at the nominal operation fluidization velocity of 0.6 m/s at all defluidized bed heights tested (1.6 to 2.5 m). The Reactor could be safely operated to 1.0 m/s, but the operation was still limited to defluidized bed heights below 1.7 m due to pulses of re-entrained solids from the cyclone dipleg.

3) Following the unit modifications, a stable recirculation rate of 4200 kg/hr was achieved with no gas flow from the Reactor to the Heater. This stable recirculation rate met the target requirements of 3000 to 4000 kg/hr.

4) Pressure measurements using backflushing gas can monitor the fluidized bed heights and solids flowrates, providing rapid feedback on issues that may arise during operation due to their improved response time ($\tau. = 0.016$ s)

5) Two-phase theory can be used to model the bed expansion. The model predicts a constant bubble velocity at the superficial gas velocities of interest. The bubble velocity was used to predict the TDH, which was also constant at the superficial gas velocities of interest. The model predicted TDH cyclone cone at most defluidized bed heights and superficial gas velocities tested.

6) The entrainment flux was not very sensitive to increasing bed height, as the cyclone inlet was above the TDH for most conditions. The experimental entrainment data agreed with predictions from the model proposed by Benoni et al. (1994), which can be used in the design stage or to estimate the entrainment rate under other operating conditions.

7) The level of solids reaching the bottom of the cyclone cone was determined to cause the pulses of solids escaping the cyclone exhaust. A model was developed to predict the frequency of pulses in solids re-entrained from the dipleg using the pressure fluctuations in the dipleg. The magnitude of solids losses increased with pulse frequency, so higher predicted pulses will result in higher solids losses from the system.

6.2 Recommendations

1) The system can be operated with the cyclone inlet below the TDH; however it is recommended to operate with the cyclone inlet above the TDH to reduce the solids entering the dipleg. While the dipleg capacity is large enough that higher solids fluxes can be accommodated, this increases the probability of the dipleg solids level reaching the bottom of the cyclone cone, leading to re-entrainment during large pressure fluctuations.

2) Pressure fluctuations in the Hot Model Pilot Plant are unlikely to be lower than in the Cold Model and may be higher due to bitumen injection. It is therefore recommended that the pressure fluctuations are monitored closely to avoid elevated solids losses through the primary cyclone.

3) When building the Hot Model Pilot Plant, the dipleg should be extended to minimize the frequency of pulses and magnitude of solids losses. For example, increasing the dipleg length by 0.3 m in the model reduced the frequency of predicted pulses to 0-10 per hour, depending on bed mass and gas distribution. This extension could be accomplished by:

    a. Extending the freeboard height if there is sufficient height in the facility.

b. Modifying the angle of the cyclone cone to shorten the overall cyclone length; however, this modification could cause issues with the cyclone vortex or solids flow (e.g., may lead to excessive erosion of the cone).

c. Increasing dipleg immersion. This increased immersion is also recommended to ensure that the dipleg termination is well below the liquid injection nozzle to minimize the impact of fluctuations when liquid is injected.

4) Unit modifications allowed for stable recirculation at the target recirculation rate; however, the increased cross-sectional area of the loop seal should allow higher flowrates (gravity flow > 8000 kg/hr). A study on the gas/solids flows in the loop seal is thus recommended to optimize the solids recirculation rate in the Cold Model.

5) Reaching stable recirculation rates required a gradual increase in the flow rate of solids from the Reactor to the Heater by opening the gate valve. Therefore, studying the impact of start-up procedure on the recirculation rate is recommended to optimize the flowrate and minimize downtime in the Hot Model Pilot Plant.

6) Pressure measurements in the riser provide a fast and stable measurement of the solids flowrate from Reactor to Heater; however, the bed heights in the Heater and Reactor must be monitored to detect issues with recirculation. It is hence recommended to develop a method to directly measure the return solids flowrate through the loop seal to improve monitoring and identify potential issues with solids flow.

7) The Reactor is well fluidized at the nominal superficial gas velocity of 0.6 m/s and above; however, if testing at lower superficial gas velocities is desired, it is recommended to provide an independent gas line to the bottom sparger in the All Spargers gas distribution or operate with the Bottom Sparger Only gas distribution.

Appendices

Appendix A: Fluid coke particle size distribution

A HELOS (H2316) particle size analyzer from Sympatec Gmbh (see Appendix B) was used to perform a particle size distribution on coke used by Syncrude Canada Ltd. in their commercial Fluid Coker (Fort McMurry, Alberta, Canada) and used in this research.

Solids were sieved using a 1 mm screen to remove agglomerates and added to the Cold Model Pilot Plant. Solids were then sampled directly from the experimental bed.

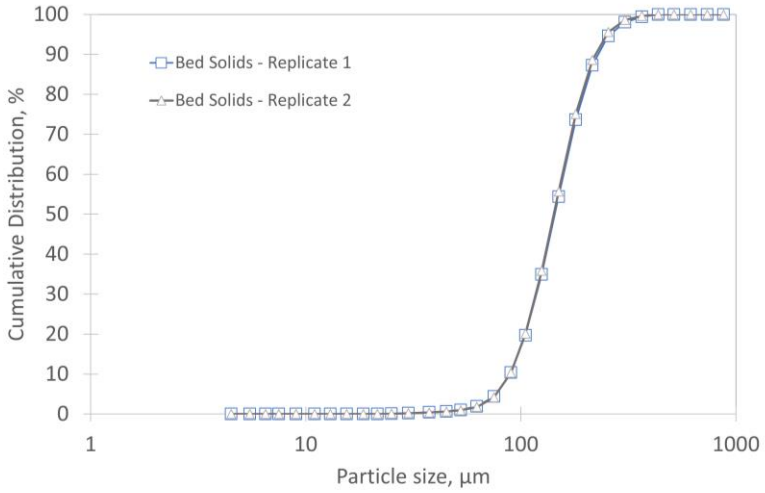

Figure A-1. Coke particle size distribution measured with HELOS (H2316) particle size analyzer (Sympatec Gmbh).

Appendix B: Particle Size Analysis Procedure

The Particle Size Analyzer measures changes in scattered light intensity caused by diffusing particles. Sample is gradually added to a quartz cuvette containing deionized water and a dispersing additive. In the bottom of the quartz cuvette a stir bar rotates at 1500 rpm, evenly dispersing the particulate within the cuvette. Once the target concentration of sample is achieved, a laser passes through the cuvette, determining the size and ratio of particulate within the sample.

Apparatus

The Particle Size Analyzer consists of the Main Machine (Sympa Tec Helos/BF Particle Size Analyzer), 50 mL Quartz Cuvette , Magnetic Stir Bar and Operating Computer.

Figure B-1. Sympa Tec Helos/BF Particle Size Analyzer.

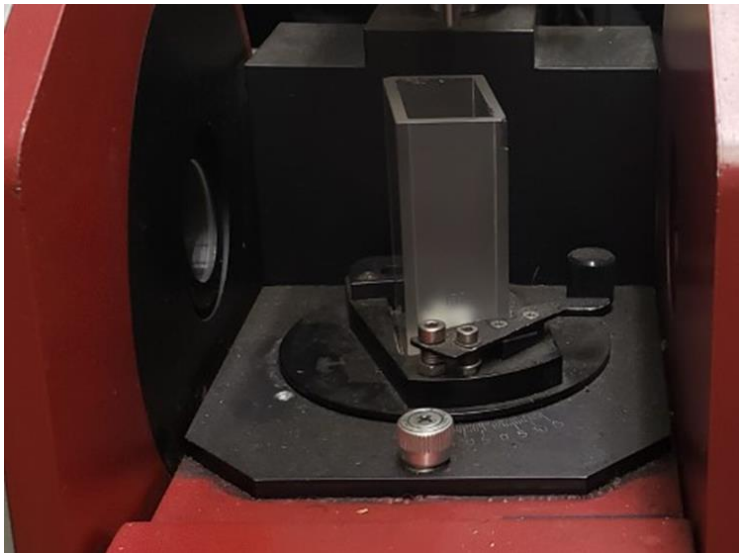

Figure B-2. 50 mL quartz cuvette.

Step-By-Step Procedure

1) Unlock Computer and Lock Box. Plug in instrument.
2) Turn on Main Machine by inserting key into lock and turning right 2 times (2 green lights should be on.)
3) Prepare 500ml of deionized water and add 5 drops of dispersing additive.
4) Open "Helos Sensor Control" program on the desktop of the Operating Computer.
5) In "Product" dropdown menu, select the most appropriate option to match sample ("Hot Coke" was selected for these experiments).
6) Click "User Parameter" icon and enter sample name.
7) Rinse quartz cuvette and stir bar with deionized water, and dry gently with Kim wipe.
8) Fill quartz cuvette with deionized water and dispersant additive mixture, leaving roughly 1 cm space at the top. Wipe down exterior of cuvette with Kim wipe to eliminate any water stains or finger prints.
9) Place cuvette back on PSA holder and insert cleaned stir bar.
10) Click "Signal Test" icon to open a second window.
11) Select "Show Optical Concentration" icon.
12) Click "Reference Measurement" in first window. This will obtain a blank reading o deionized water and dispersant agent mixture.
13) Prepare sample:
    i. Pour entire sample into appropriately sized beaker (should be adequate space to mix sample thoroughly and clean spatula on rim).
    ii. While mixing, add deionized water until sample is the consistency of a paste.
14) Carefully add sample to cuvette using a narrow spatula. Gradually add sample until the "Optical Concentration" reading is between 20-30% -OR- the stir bar begins to be unstable (whichever comes first). Note: Mix sample throughout process.
15) Click "Normal Measurement" icon to being analysis.
16) Once the results file opens, save as an RTF file.
17) Repeat STEPS 6-17 for all remaining samples.
18) Once finished:

i. Close “Helos Sensor Control” software and turn key to OFF position (all the way to the left - no green lights should be on).
ii. Lock out both the PSA and the Controlling Computer.

Procedure Repeatability

To test the repeatability of the procedure outlined above, two separate samples were prepared. Each prepared sample was added to the cuvette and analyzed four times, cleaning the cuvette thoroughly between each analysis. Figure B-0-4 shows the repeat particle size distributions for Sample 1 ($H_{Defluidized}$ = 1.94 m; U_G = 0.5 m/s). Figure B-0-5 shows the repeat particle size distributions for Sample 2 ($H_{Defluidized}$ = 1.94 m; u_G = 0.8 m/s). The procedure provides good repeatability across the same sample.

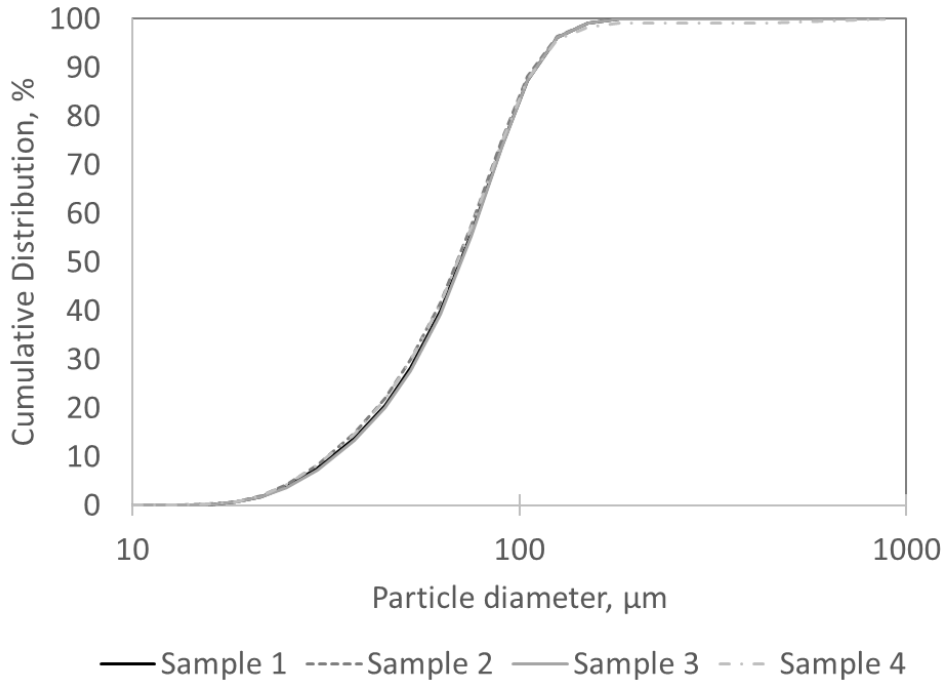

Figure B-3. Size distribution replicates for sample from $H_{Defluidized}$ = 1.94 m and U_G = 0.5 m/s.

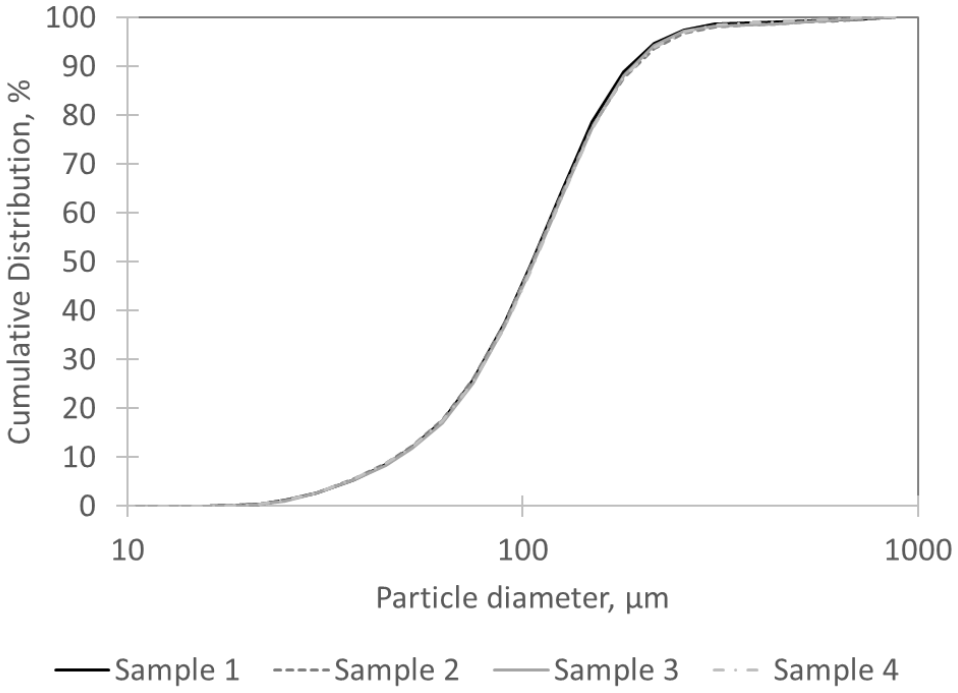

Figure B-4. Size distribution replicates for sample taken at $H_{Defluidized}$ = 1.94 m; U_G = 0.8 m/s.

Impact of Sample Concentration

The recommended range of optical concentrations is 20-30%. A sample was prepared per the procedure outlined above and tested at a lower optical concentration to test for sensitivity to fines or larger particles. Reducing the concentration to 12% had no impact on the size distribution reading.

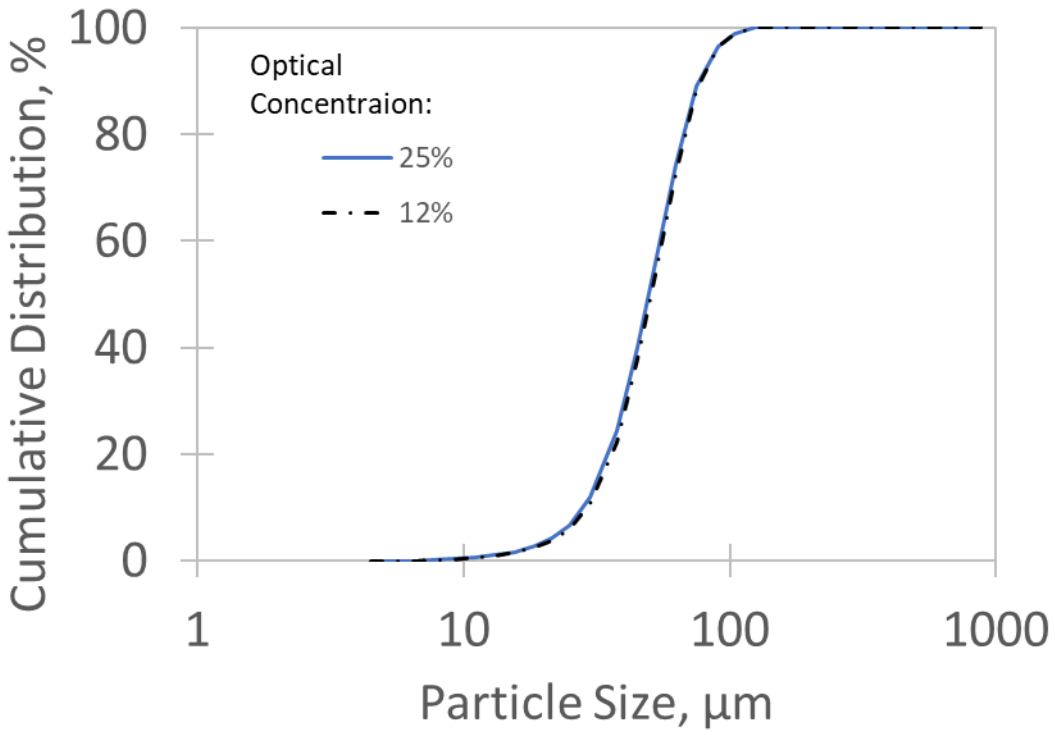

Figure B-5. Impact of optical concentration on particle size distribution for sample taken at $H_{Defluidized}$ = 1.62 m; U_G = 0.3 m/s.

Impact of Dispersant

A dispersing agent is typically used to prevent agglomeration in the sample. Two samples were prepared per the procedure outlined above, one with and one without the dispersing agent. The dispersant had no impact on the size distribution reading.

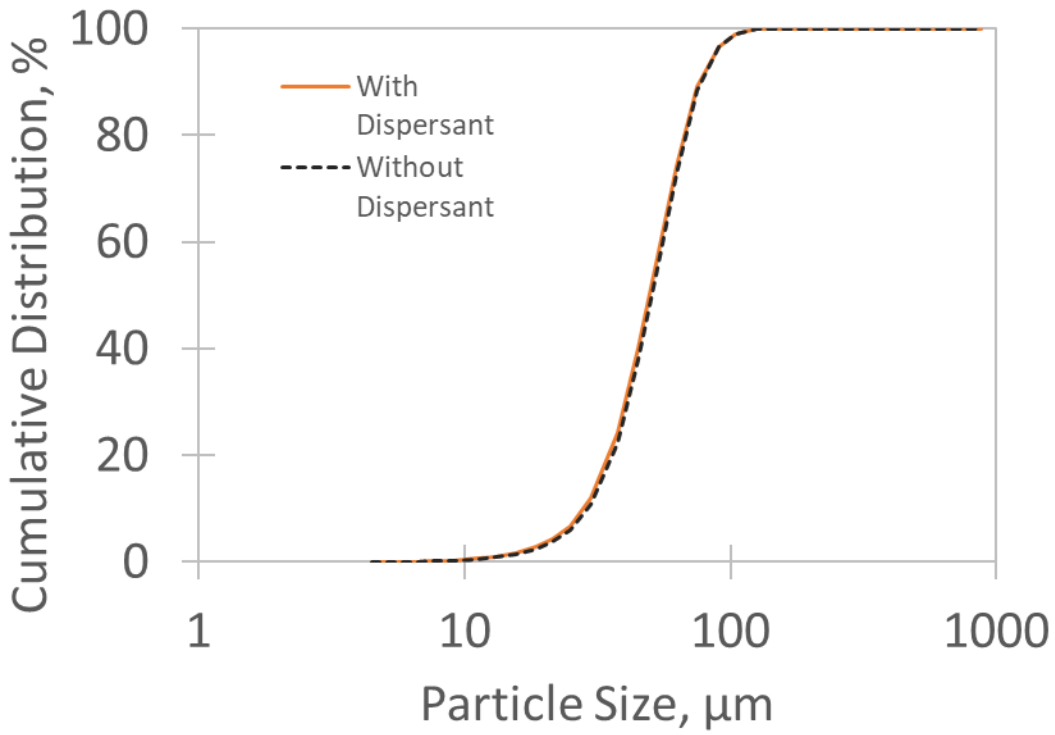

Figure B-6. Impact of dispersant on particle size distribution for sample taken at $H_{Defluidized}$ = 1.62 m; U_G = 0.3 m/s.

Impact of Ultrasound

Two samples were prepared per the procedure outlined above. One was tested normally, while the other was placed in an ultrasonic bath for 10 minutes to break up potential agglomerates. The ultrasonic bath had no impact on the particle size distribution reading.

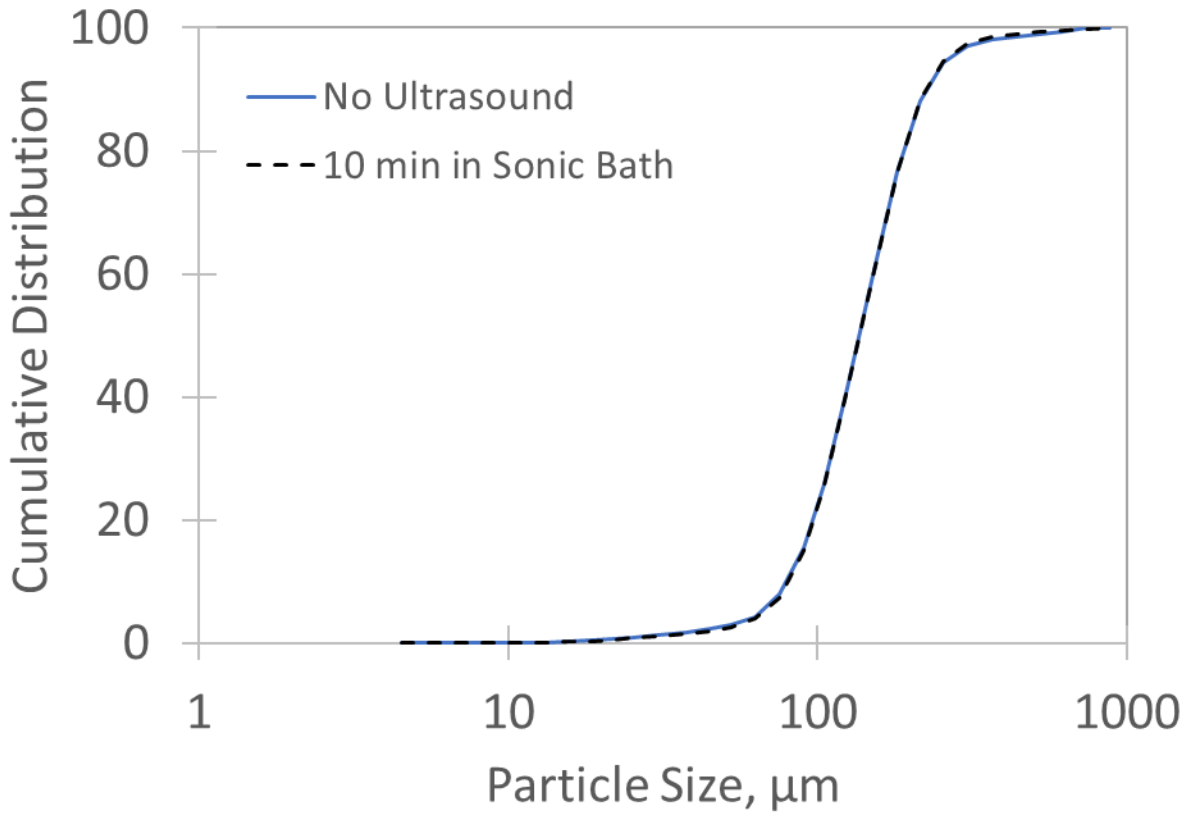

Figure B-7. Impact of ultrasound on particle size distribution for Bed Solids sampled at $H_{Defluidized}$ = 1.62 m.

Appendix C: Solids Flowrate Calibration

The flowrate of solids was calibrated with the riser pressure drop using backflushing pressure measurements. The location of the pressure measurements is shown below in Figure C-1. Location of pressure measurements used for solids flowrate calibration.

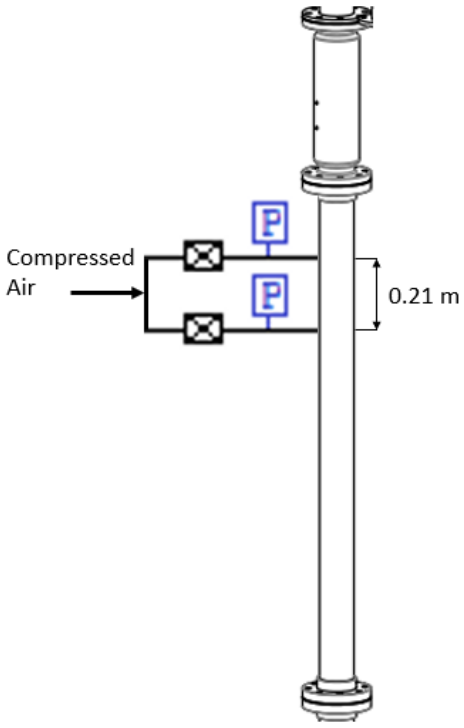

Figure C-1. Location of pressure measurements used for solids flowrate calibration.

Solid flowrates were measured by transferring solids in one direction, from the Reactor to the Heater. Different solids flowrates were achieved by opening the gate valve at the bottom of the Reactor to various degrees. The pressure signal at tap P_4 (see Figure 2-18. Locations of pressure taps using backflushing) in the Reactor was monitored to determine the change in pressure with

time. Using the change in pressure and the reactor cross-sectional area ($A_{Reactor}$), the mass flowrate of solids (F_s) can be calculated as follows:

$$F_s = \frac{\Delta P}{\Delta t} \cdot \frac{A_{Reactor}}{g} \quad \text{(C.1)}$$

An example of the pressure signal at tap P4 as solids were transferred from the Reactor to the Heater is presented in Figure C-2. Due to the capacity of the Reactor, solids were transferred for 20 – 240 s, depending on the flowrate. For the example below, the stable solids flowrate was measured for 170 s after the valve was opened to the target level. The mass of solids transferred during 170s of stable flow was 103 kg, or 2180 kg/hr.

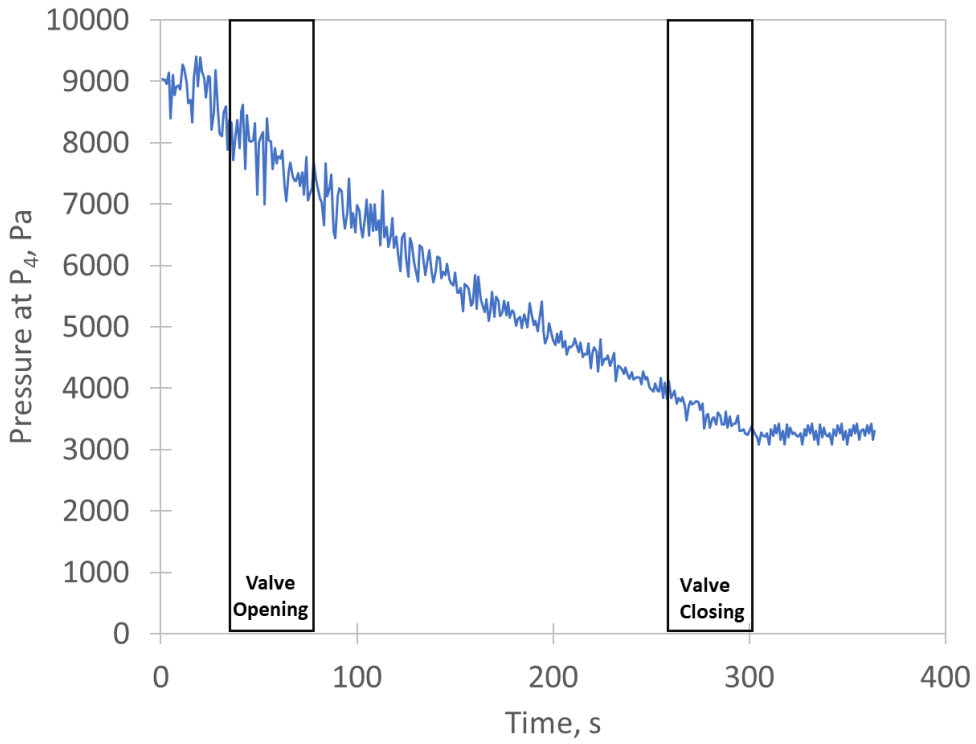

Figure C-2. Example of change in pressure signal at pressure tap P_4 with time as solids exit to Reactor to Heater transfer line.

The pressure drop in the riser was measured simultaneously during the solids transfer to acquire the time average pressure drop. The pressure signal in the riser is shown below. The time average values were used to create the calibration curve for ΔP_{Riser} vs F_s in Figure C-4.

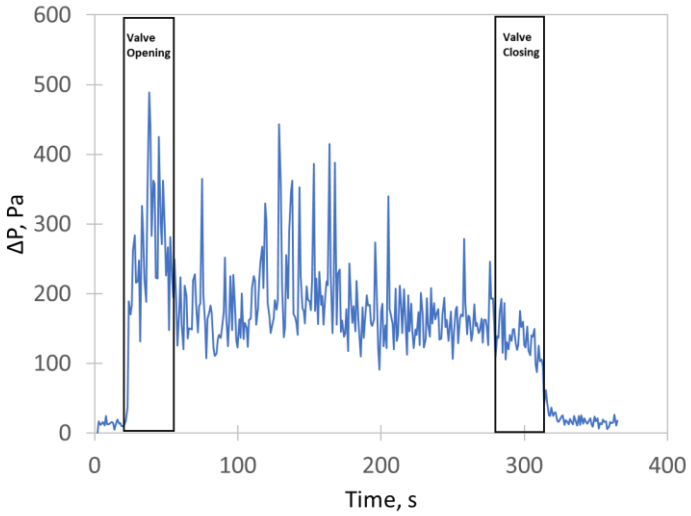

Figure C-3. Example of pressure signal in riser with time as solids were transferred to the Heater.

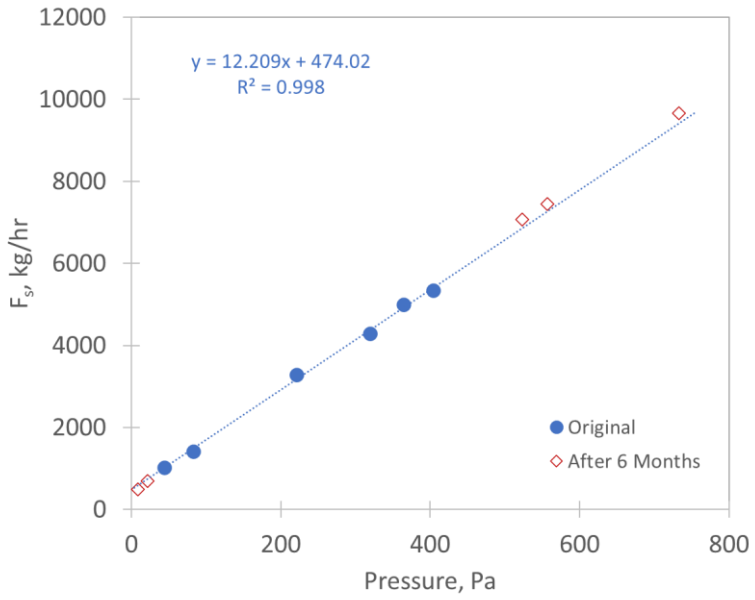

Figure C-4. Calibration between riser pressure drop and solids flowrate (F_s).

Appendix D: Sonic Orifice Calibration Curves

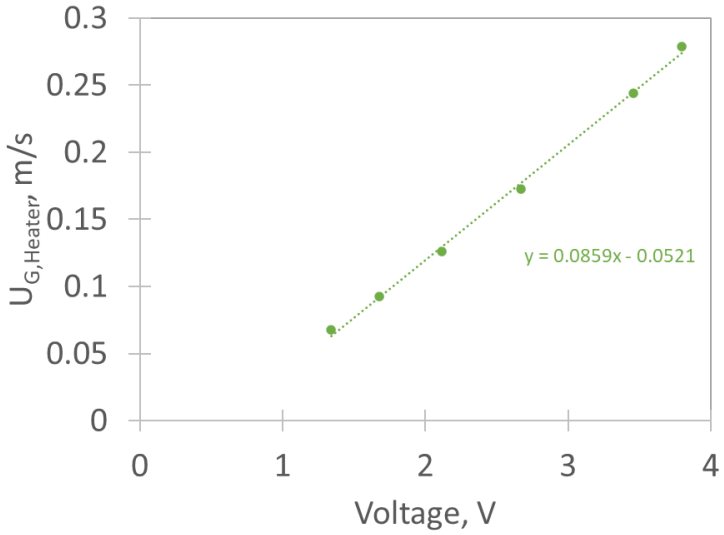

Figure D-1. Change in Heater flow velocity with increasing pressure regulator voltage for the 0.48 inch sonic orifice supplying the Heater.

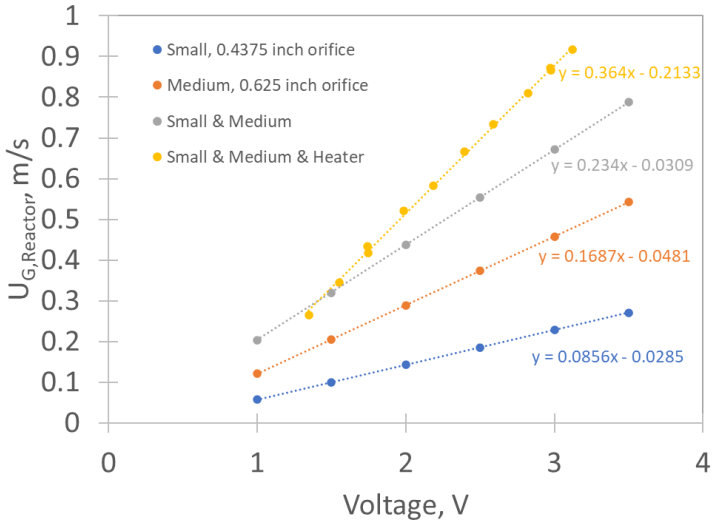

Figure D-2. Change in Reactor flow velocity with increasing pressure regulator voltage for different sonic orifices.

Appendix E: Calibration of Pressure Transducers with Snubbers

Calibration Curves

The Cold Model was originally equipped with pressure transducers with snubbers from the PX2650 Series Bidirectional, Differential Low Pressure Transducers (Omega, 1999). They were calibrated against a U-tube water manometer.

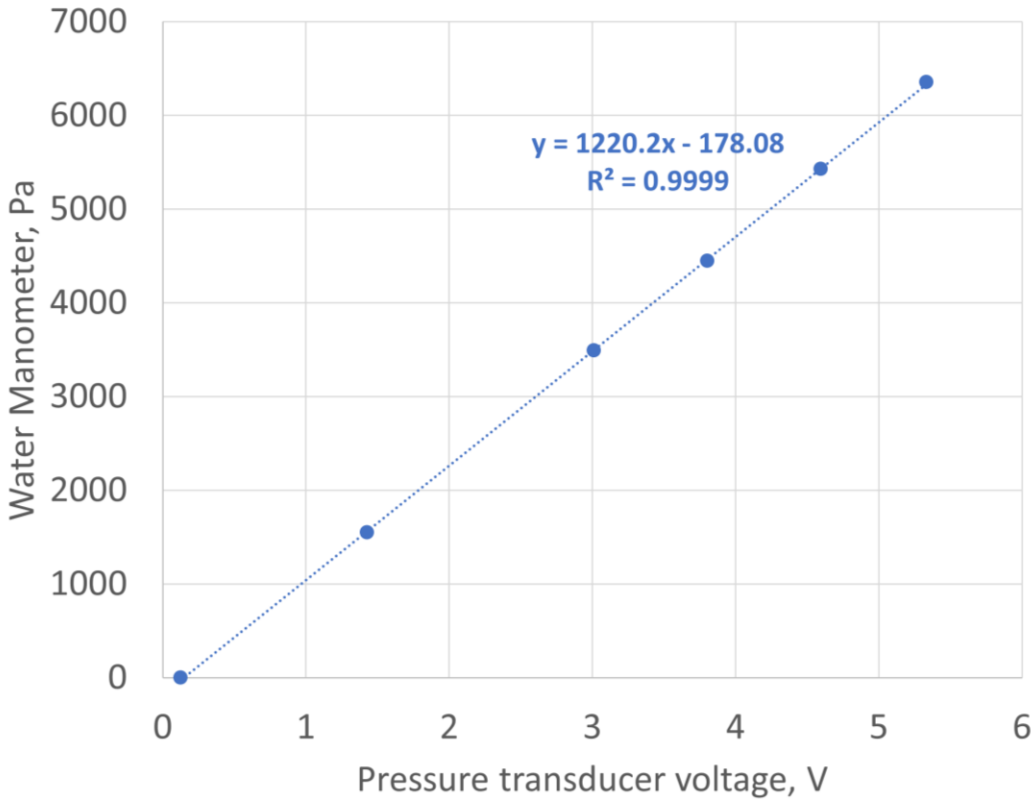

Figure E-1. Differential 0-25 H_2O" pressure transducer PT-301 (PX-2650-25D5V) calibrated against U-tube water manometer.

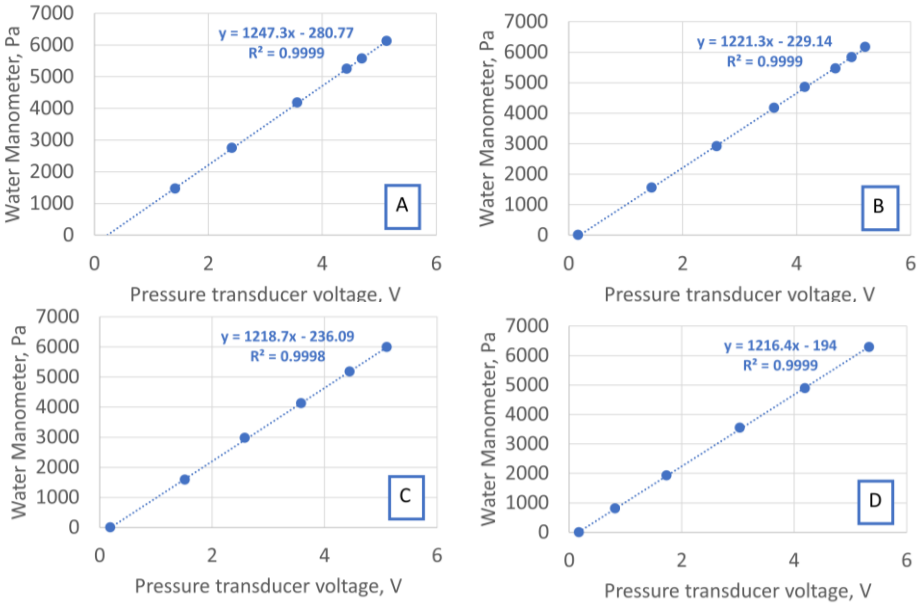

Figure E-2. Differential 0-25 H_2O" pressure transducers (PX-2650-25D5V) calibrated against U-tube water manometer: A) PT-302; B) PT-310; C) PT-415; D) PT-520.

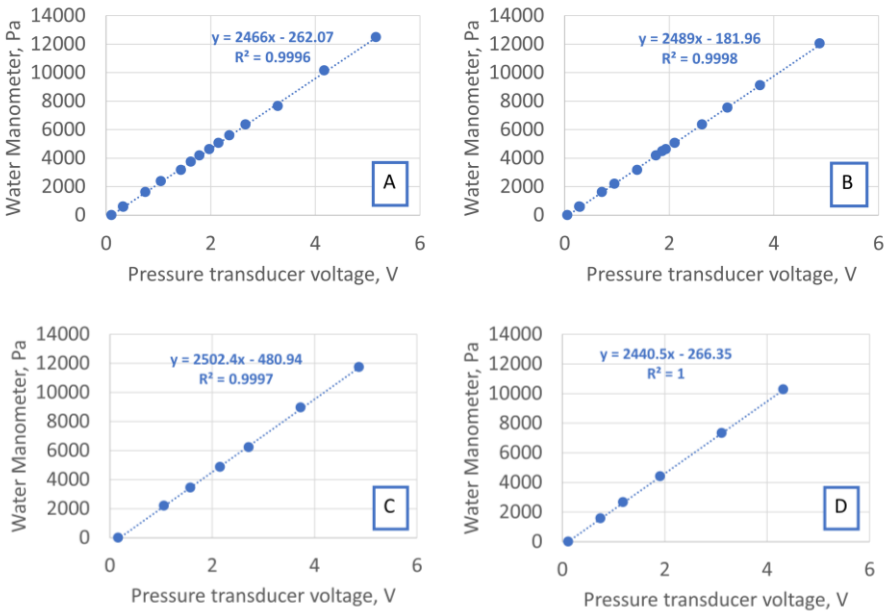

Figure E-3. Differential 0-50 H_2O" pressure transducers (PX-2650-50D5V) calibrated against U-tube water manometer: A) PT-303, B) PT-304, C) PT-407, D) PT-601.

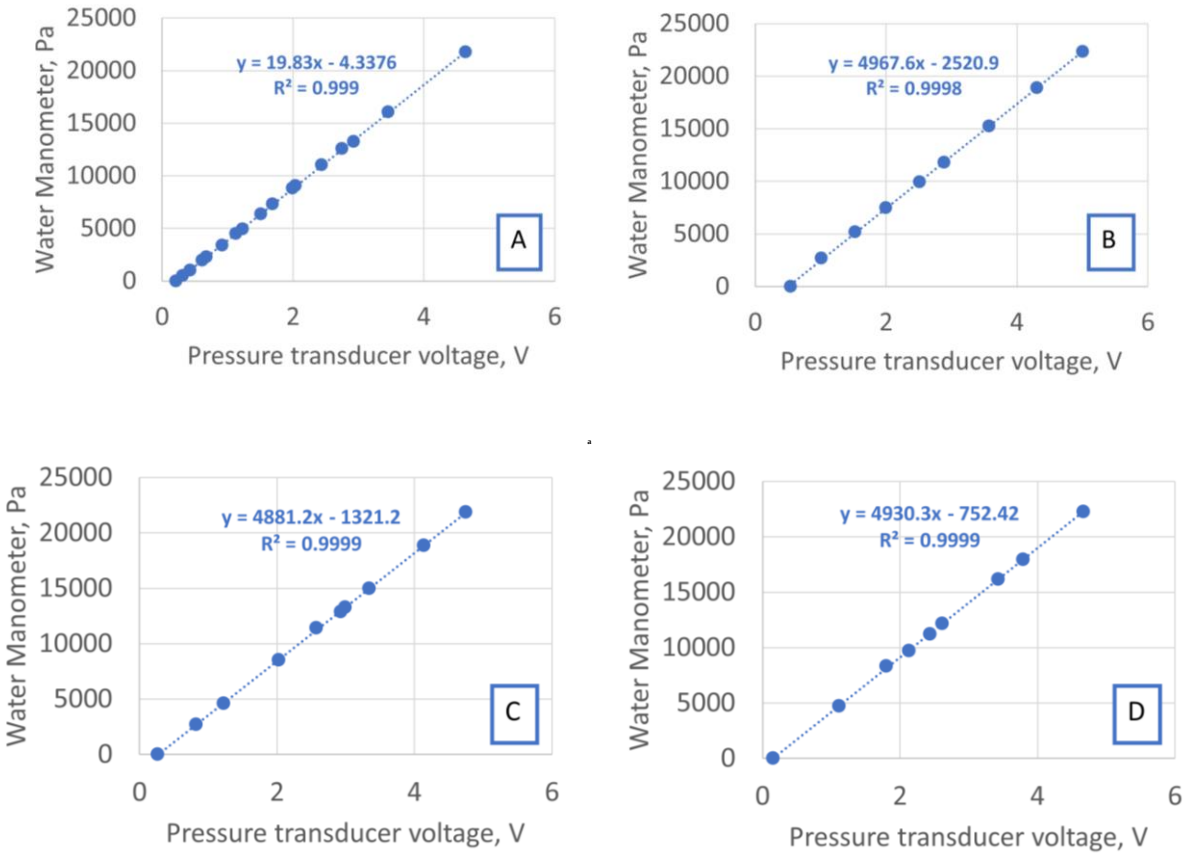

Figure E-4. Differential 0-100 H_2O" pressure transducers (PX-2650-100D5V) calibrated against U-tube water manometer: A) PT-305 B) PT-403, C) PT-410.

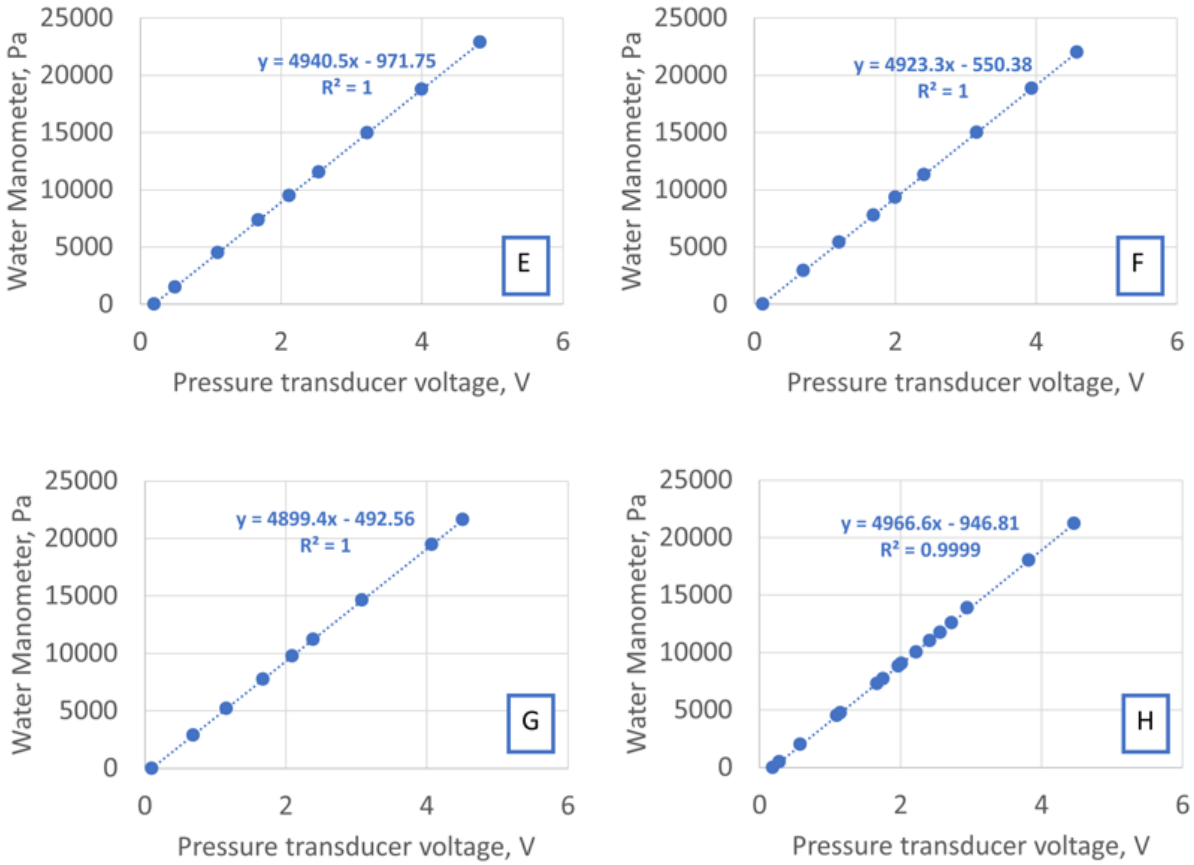

Figure E-5. Differential 0-100 H_2O" pressure transducers (PX-2650-100D5V) calibrated against U-tube water manometer: E) PT-505, F) PT-507, G) PT-510, H) PT-610.

References

Omega Engineering, Inc. (1999). PX2650 Series Bidirectional, Differential Low Pressure Transducers Data Sheet. https://assets.omega.com/pdf/test-and-measurement-equipment/pressure/pressure-transducers/PX2650.pdf

Appendix F: Calibration of Pressure Transducers with Backflushing

To improve the response time of the pressure readings in the Cold Model, differential pressure transducers from the Honeywell Board Mount TruStability® SSC Series (Honeywell, 2014) were used with backflushing gas to prevent clogs. They were calibrated against a U-tube water manometer. To see the impact of the backflushing gas on the pressure readings, calibrations were performed with and without backflushing gas. Figure E-1 shows the apparatus used during calibration.

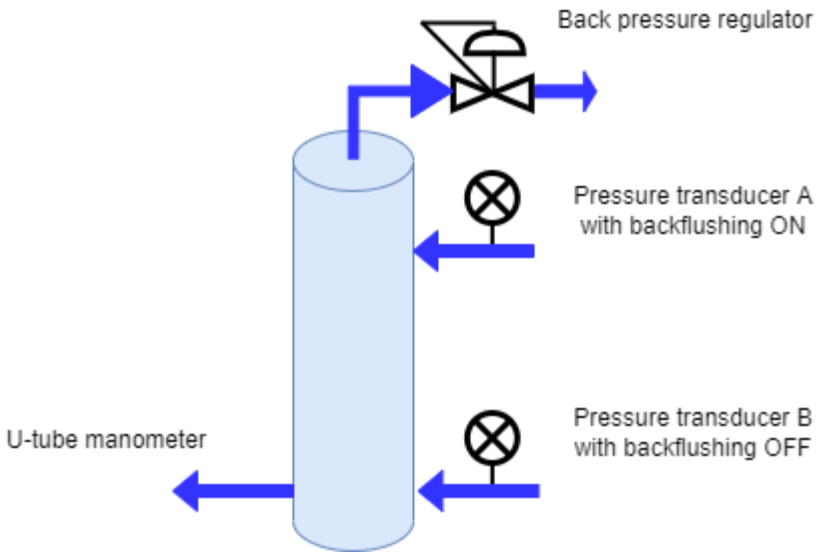

Figure F-1. Apparatus used for calibration of backflushing pressure transducers.

Two transducers, one with backflushing (A) and one without backflushing (B) were connected to a 0.05 m diameter cylindrical vessel to simulate the expansion factor provided by the Cold Model. The vessel was pressurized at various levels using the air flow provided by backflushing gas. A back pressure regulator was used to maintain a constant pressure, and a U-tube water manometer was used to monitor the vessel pressure. The calibration was repeated where transducer A had no backflushing, and transducer B had backflushing.

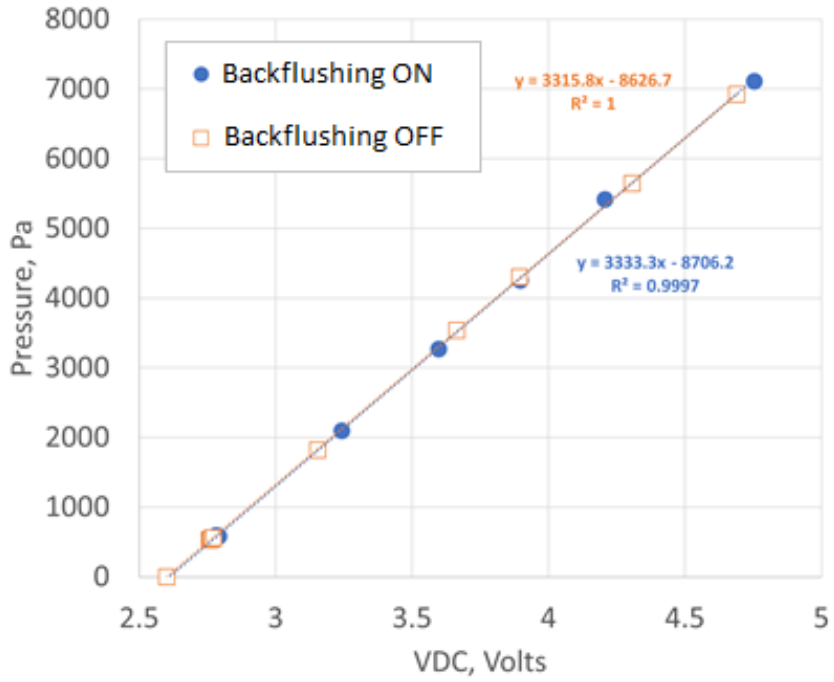

Figure F-2. Differential 1 psi pressure transducer PF-001 (SSCDRRN001PDAA5) calibrated against U-tube water manometer.

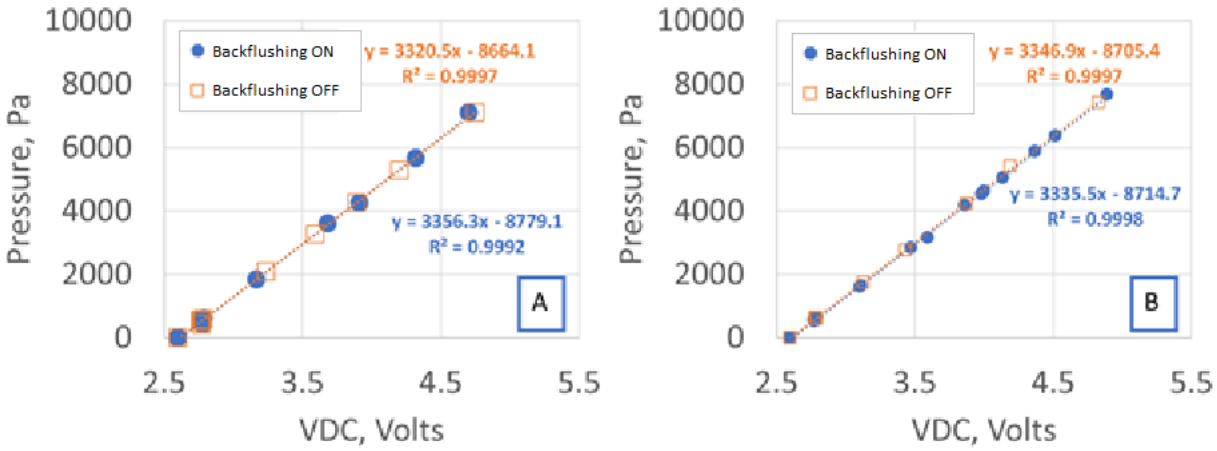

Figure F-3. Differential 1 psi pressure transducers (SSCDRRN001PDAA5) calibrated against U-tube water manometer A) PF-004, B) PF-005.

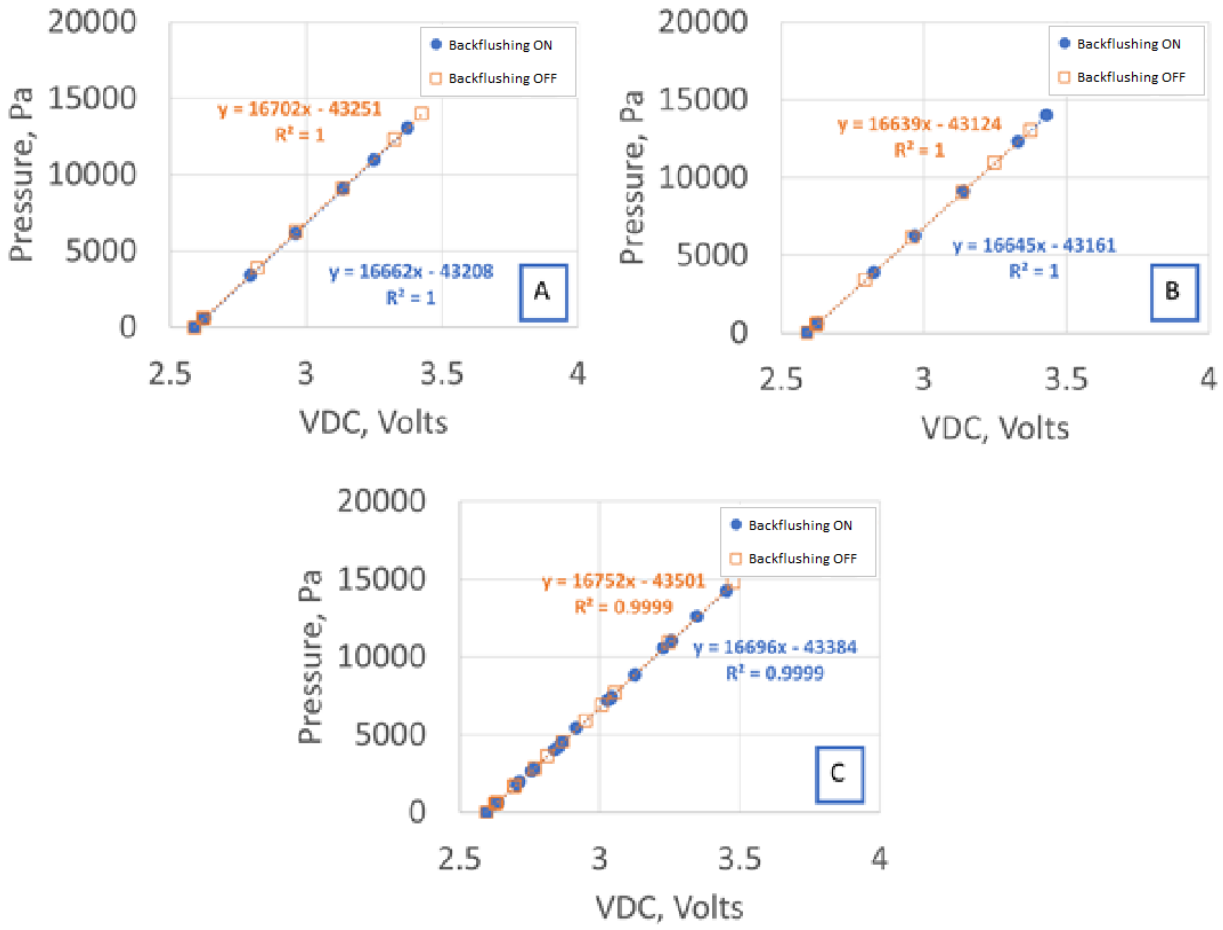

Figure F-4. Differential 0-5 psi pressure transducers (SSCDRRN005PDAA5) calibrated against U-tube water manometer A) PF-002, B) PF-003, C) PF-006 (used in dipleg model).

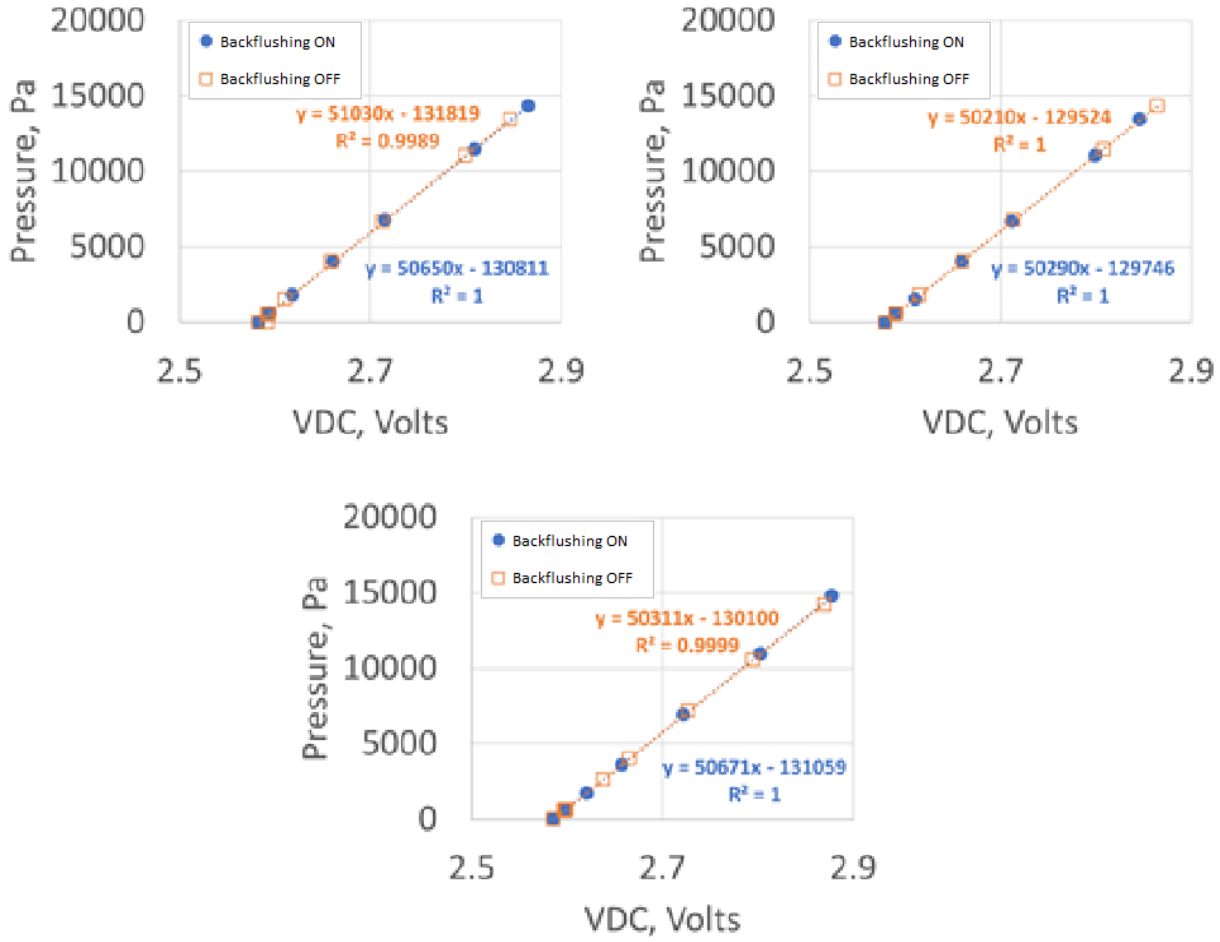

Figure F-5. Differential pressure transducers 15 psi pressure transducers (SSCDRRN015PDAA5) calibrated against U-tube water manometer A) PF-007, B) PF-008, C) PF-009.

References

Honeywell. (2014). *TruStability® Board Mount Pressure Sensors*. https://prod-edam.honeywell.com/content/dam/honeywell-edam/sps/siot/en-us/products/sensors/pressure-sensors/board-mount-pressure-sensors/trustability-ssc-series/documents/sps-siot-trustability-ssc-series-standard-accuracy-board-mount-pressure-sensors-50099533-a-en-ciid-151134.pdf?download=false

Appendix G: Pressure Profiles from Pressure Transducers with Backflushing

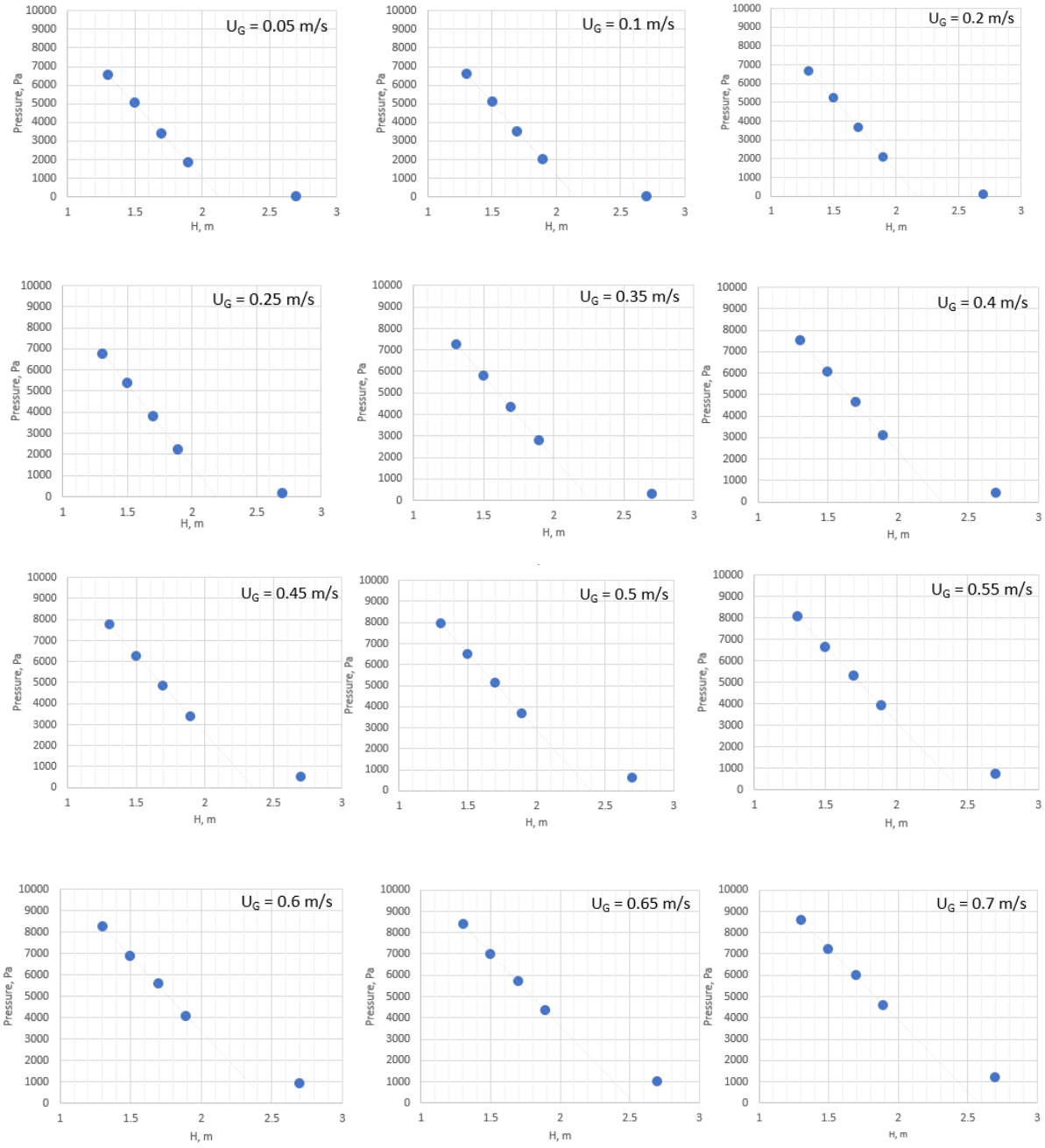

Figure G-1. Pressure profiles with All Spargers gas distribution at $H_{Defluidized}$ = 2.06 m for U_G = 0.05 - 0.7 m/s.

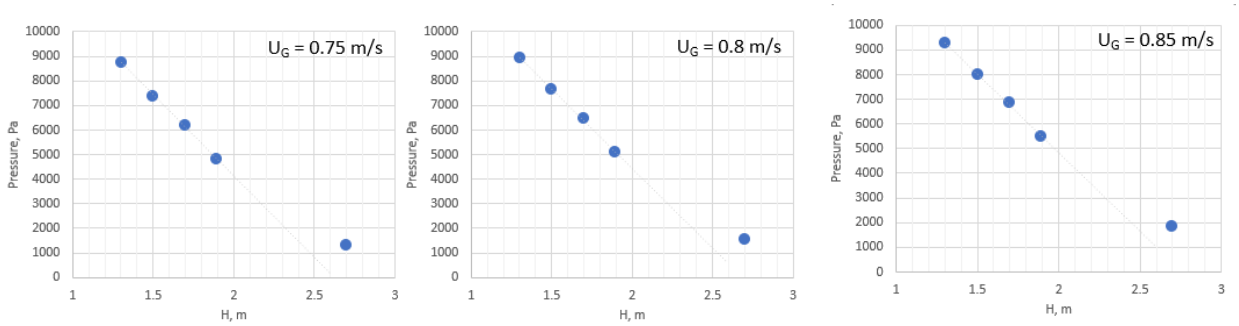

Figure G-2. Pressure profiles with All Spargers gas distribution at $H_{Defluidized}$ = 2.06 m for U_G = 0.75 - 0.85 m/s.

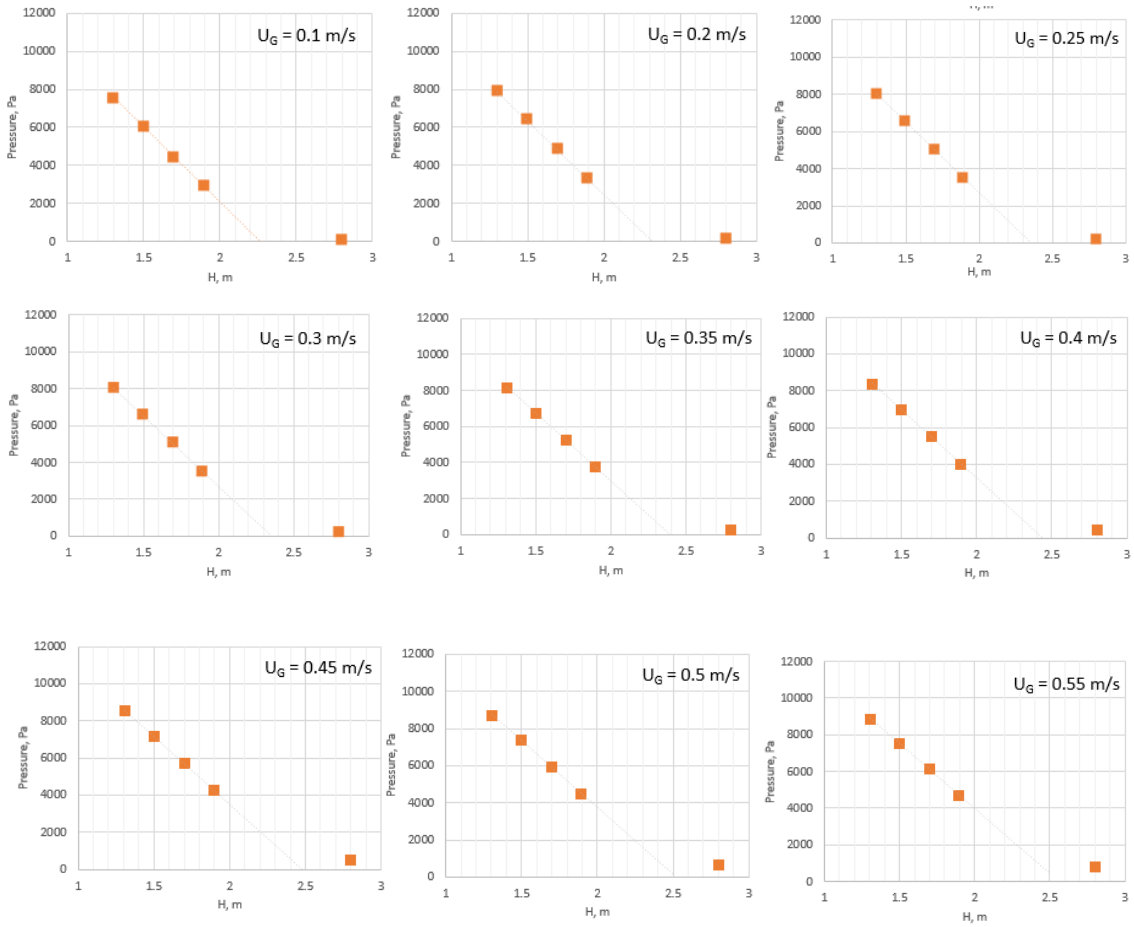

Figure G-3. Pressure profiles with Bottom Spargers Only gas distribution at $H_{Defluidized}$ = 2.06 m for U_G = 0.1 - 0.55 m/s.

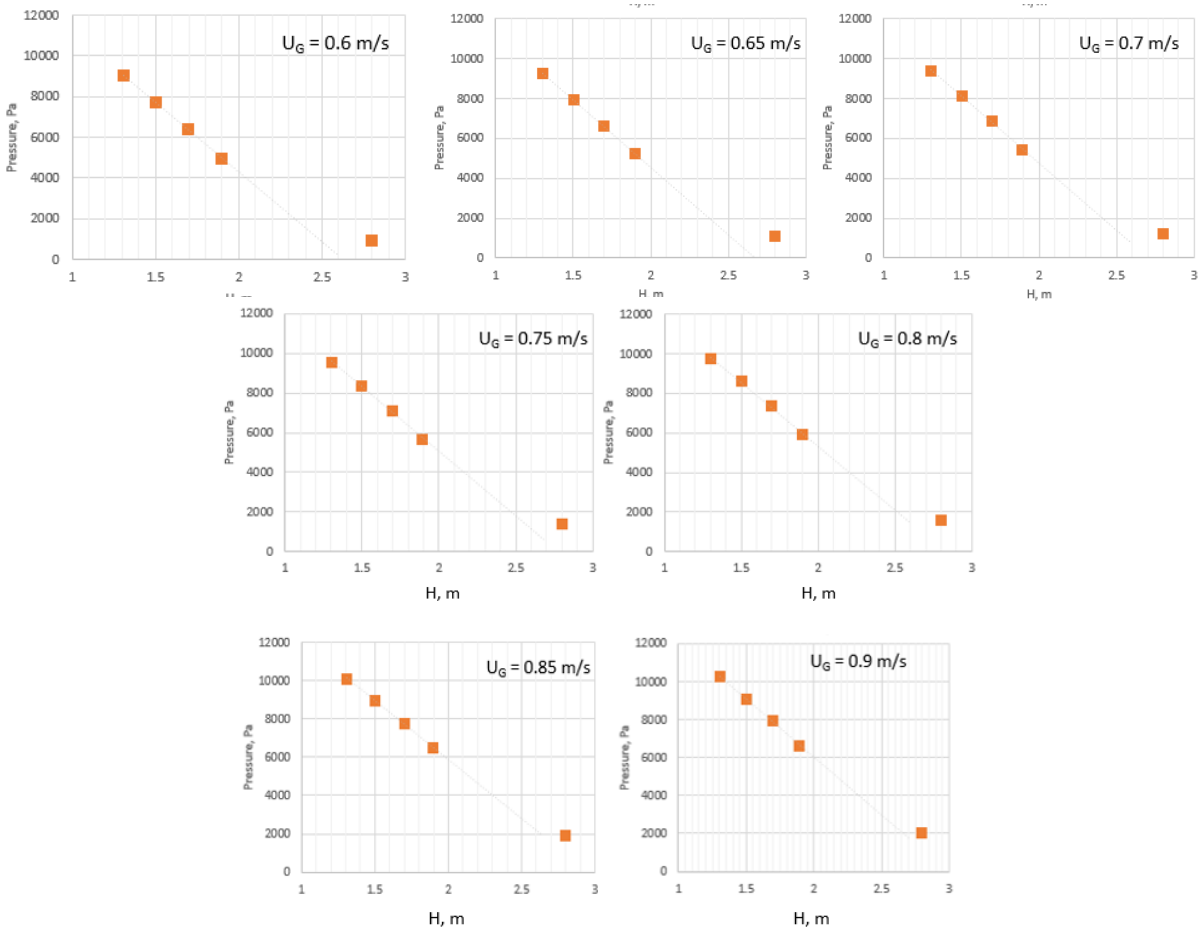

Figure G-4. Pressure profiles with Bottom Spargers Only gas distribution at $H_{Defluidized}$ = 2.06 m. for U_G = 0.55 - 0.85 m/s

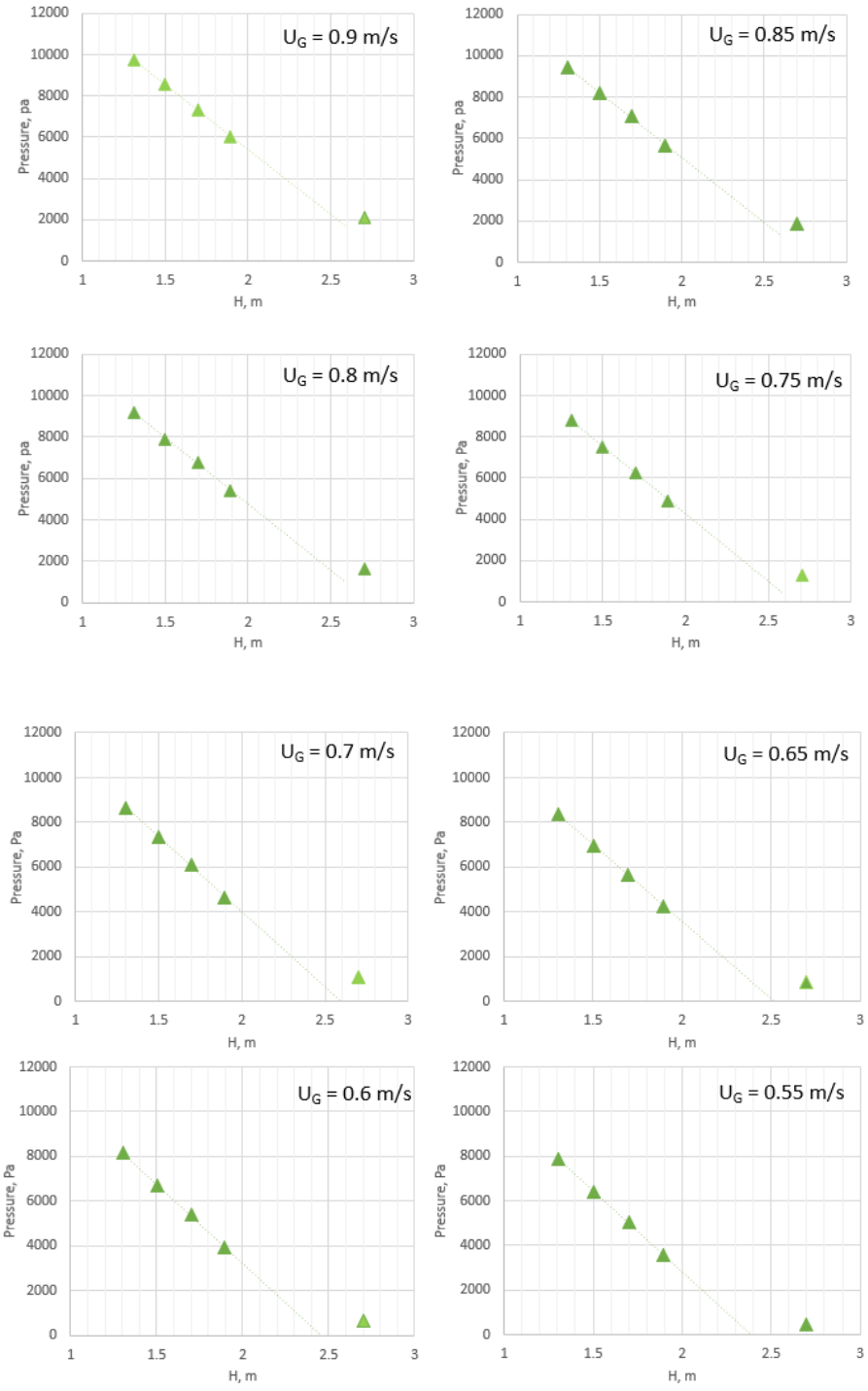

Figure G-5. Pressure profiles with All Spargers – Independent Flow to Bottom Sparger gas distribution at $H_{Defluidized}$ = 2.06 m for U_G = 0.55 - 0.9 m/s.

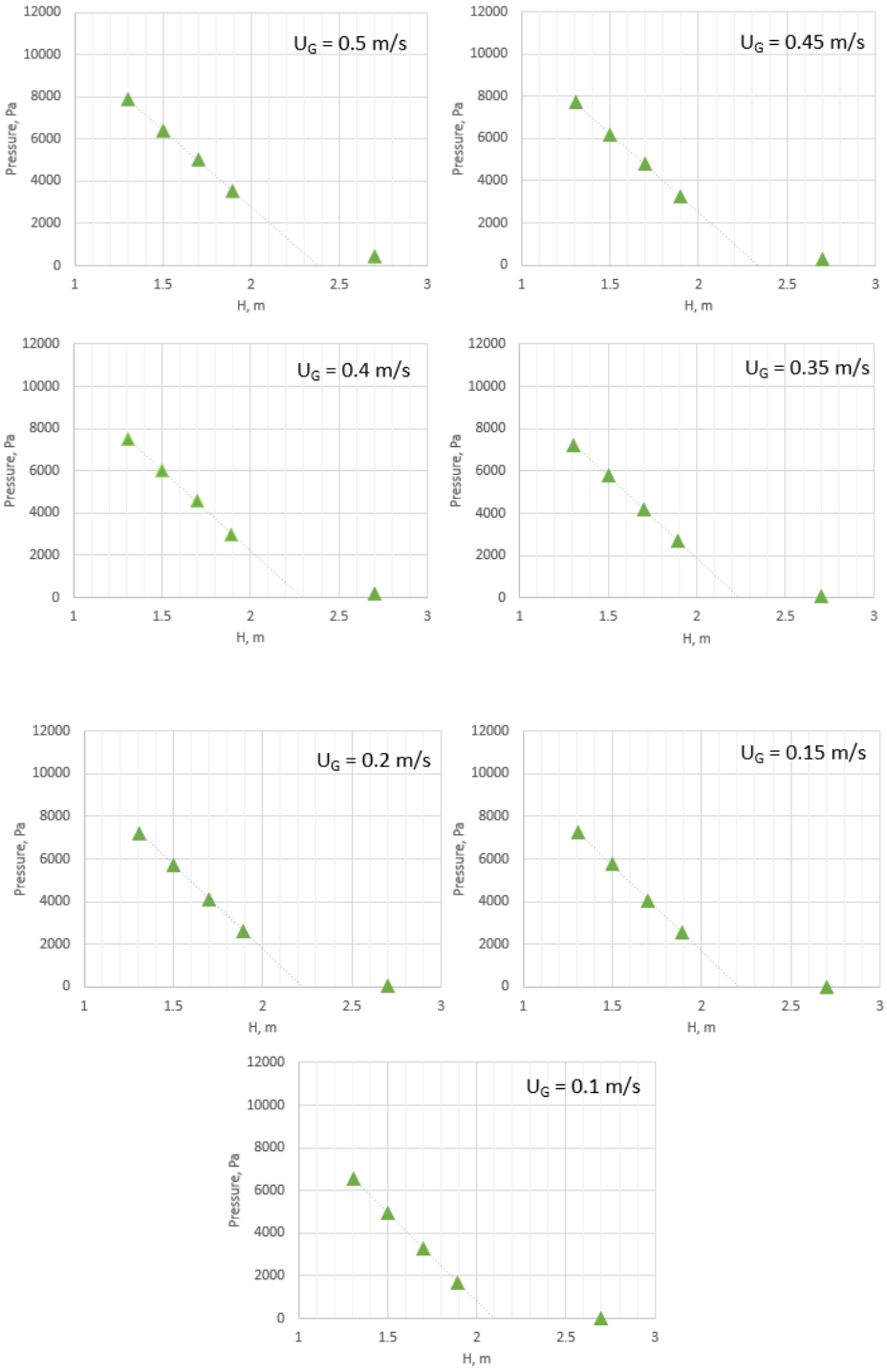

Figure G-6. Pressure profiles with All Spargers – Independent Flow to Bottom Sparger gas distribution at $H_{Defluidized}$ = 2.06 m for U_G = 0.1 - 0.5 m/s.

Appendix H: Method to Determine Solids Losses

The change in bed mass above a specific pressure tap was used to determine solids lost over different operating conditions. A reference pressure measurement was taken when the bed was fluidized at U_G = 0.07 m/s to minimize pressure fluctuations at the bed surface before each experiment. After the experiment, the pressure difference between the freeboard and the pressure just below the bed surface was measured with a u-tube water manometer to determine the solids lost from the cyclone. Figure H-1 shows the apparatus used to measure solids losses

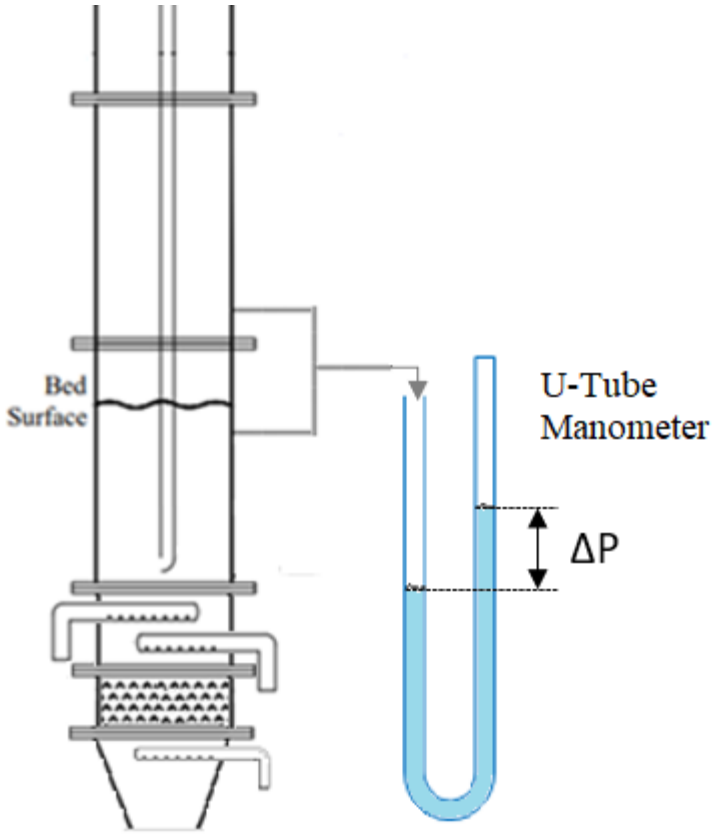

Figure H-1. Apparatus used to determine solids losses during a run

The losses were calculated as follows:

$$\frac{A_{reactor}(\Delta P_{before} - \Delta P_{after})}{g} \quad \text{(I.1)}$$

Appendix I: Size Distributions of Entrained Particles

The particle size distribution of entrained coke particles was measured using a HELOS (H2316) particle size analyzer (Sympatec Gmbh).

Original Design

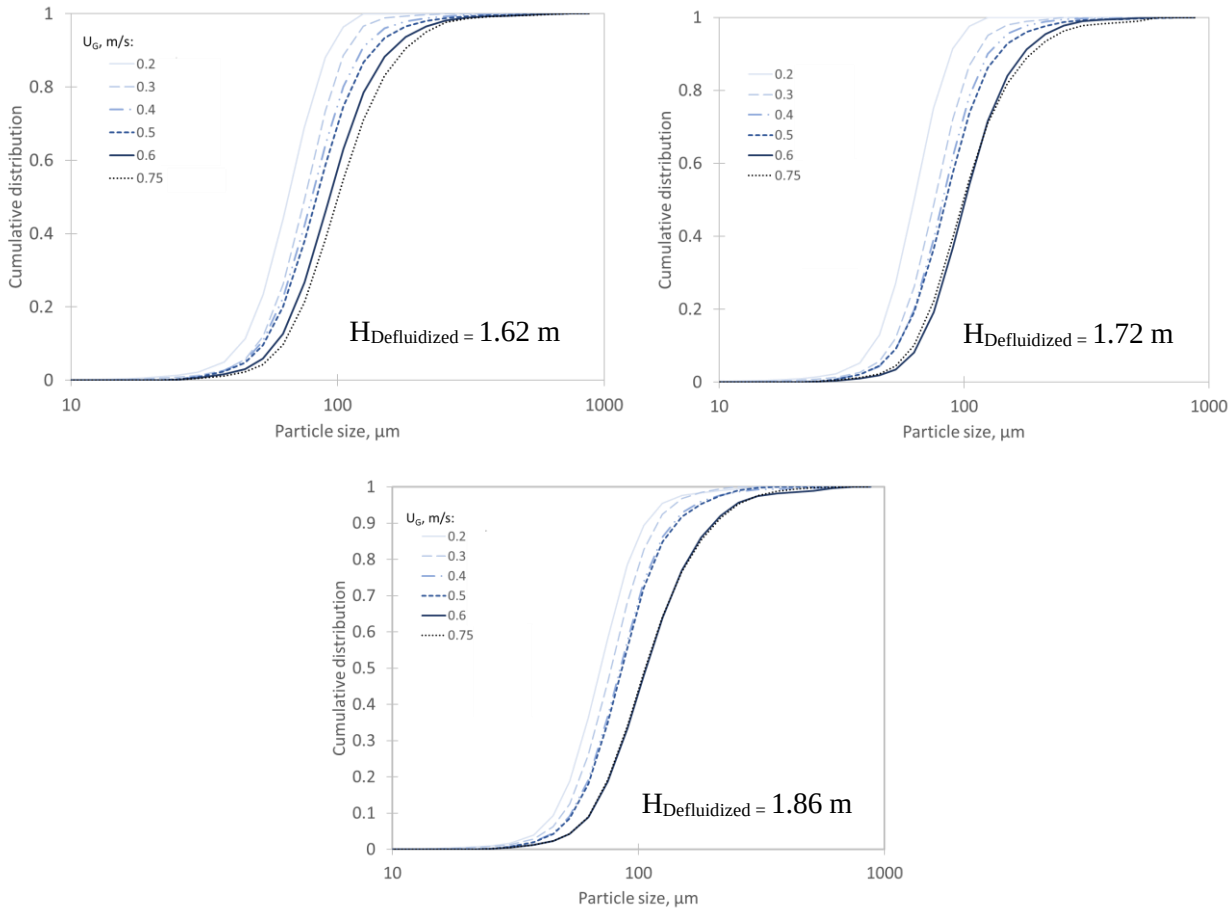

Figure I-1. Particle size distributions of original design at various defluidized bed heights.

Phase 1 of Modifications

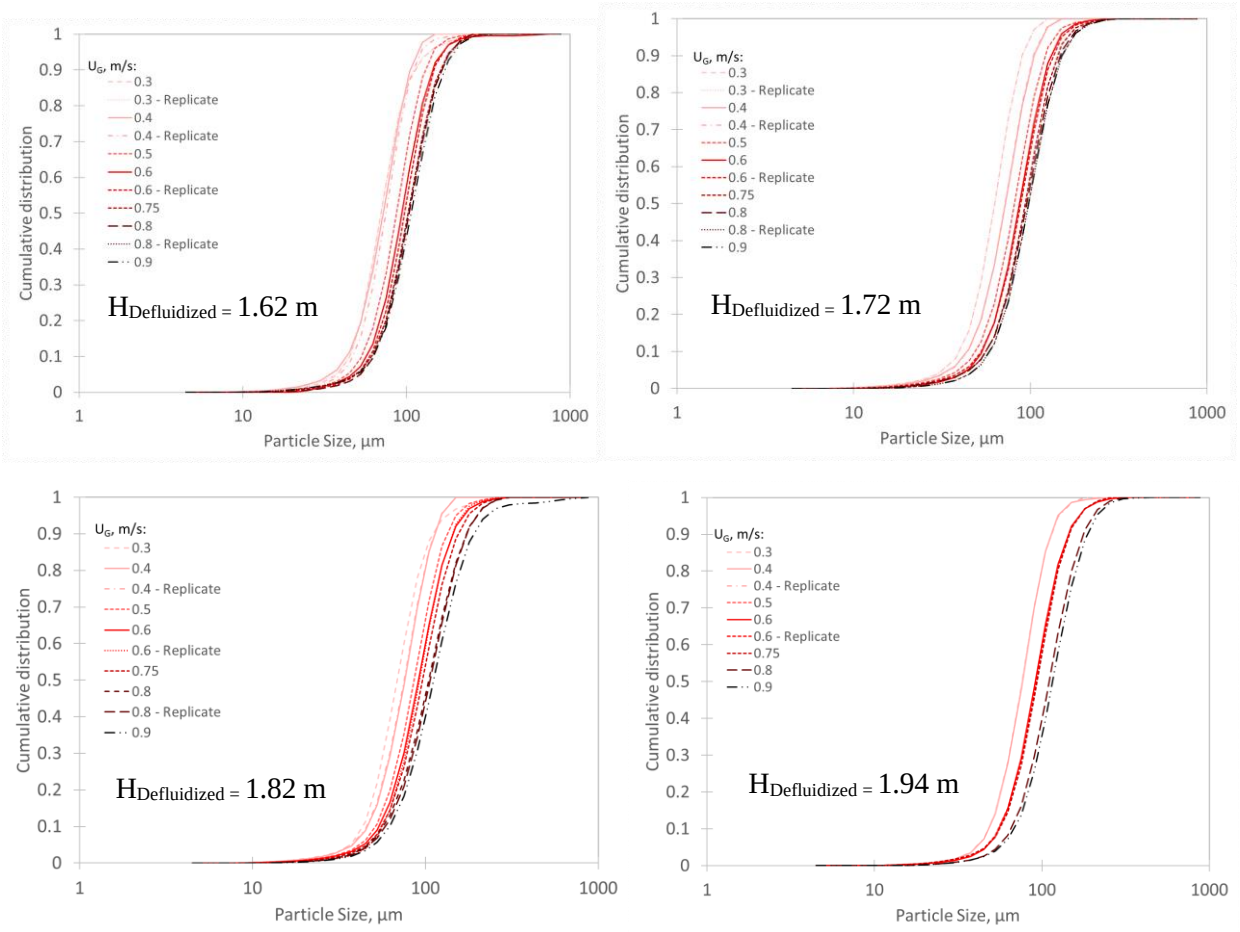

Figure I-2. Particle size distributions after Phase 1 of modifications at various defluidized bed heights from $H_{Defluidized}$ = 1.62 m to 1.94 m.

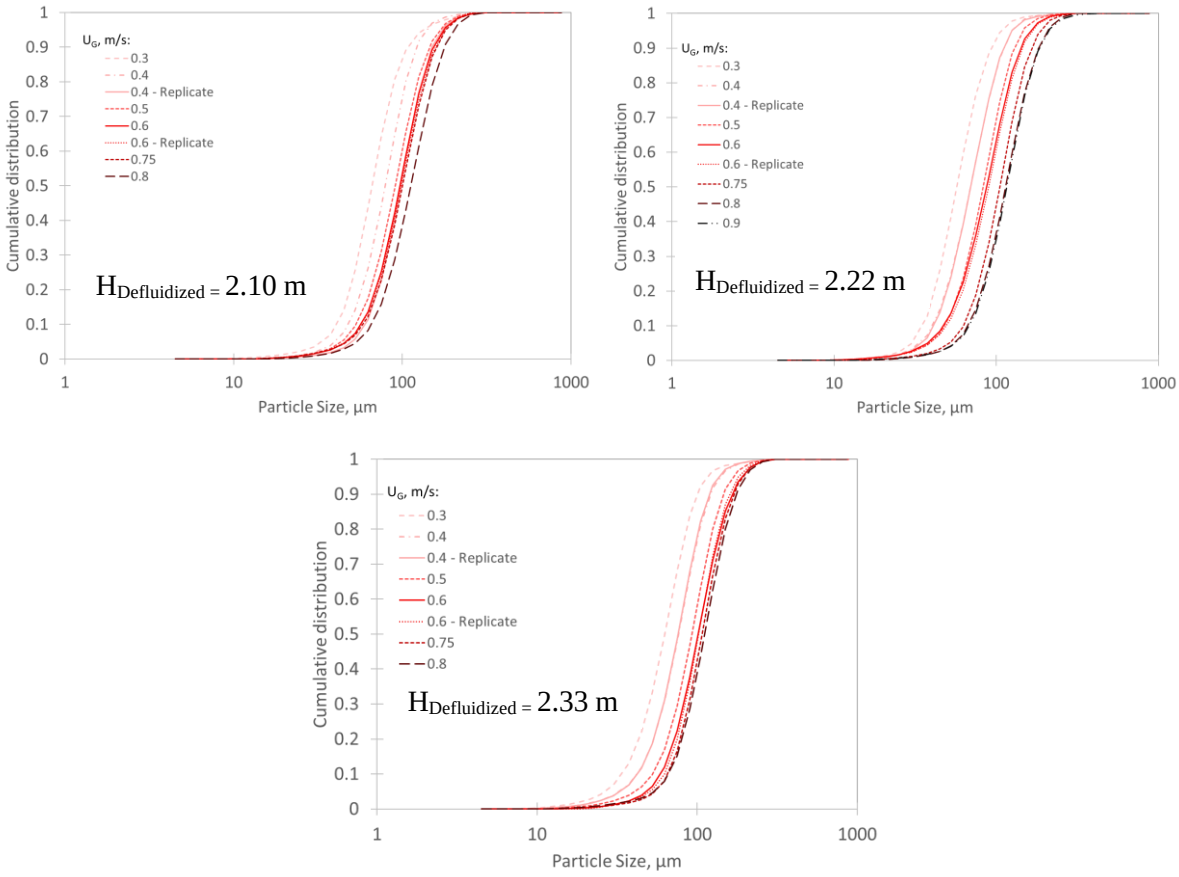

Figure I-3. Particle size distributions after Phase 1 of modifications at various defluidized bed heights from $H_{Defluidized}$ = 2.10 m to 2.33 m.

Phase 2 of Modifications

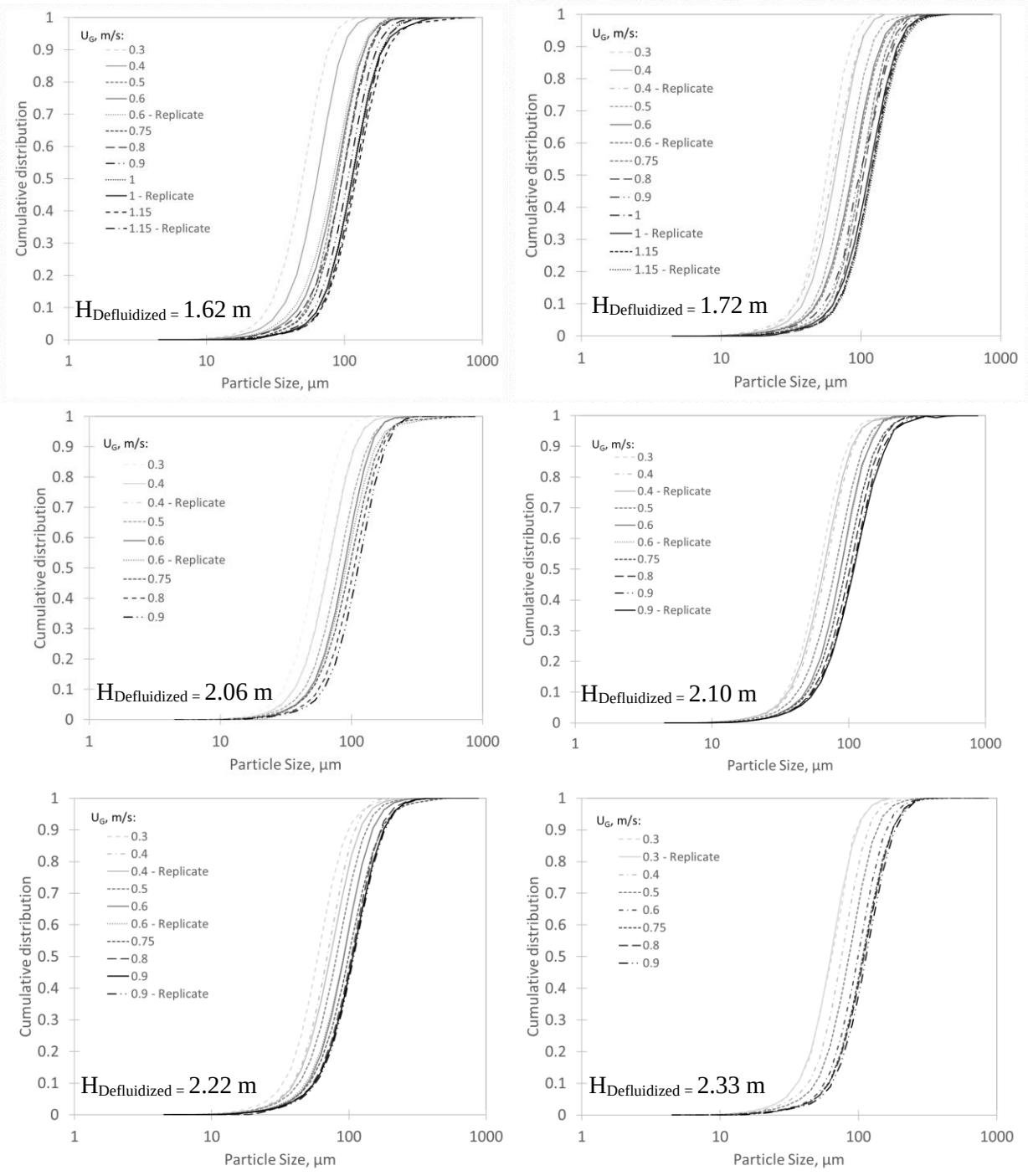

Figure I-4. Particle size distributions after Phase 1 of modifications at various defluidized bed heights.

Appendix J: Comparison in Entrainment Flux Between Phase 1 and Phase 2 of Modifications

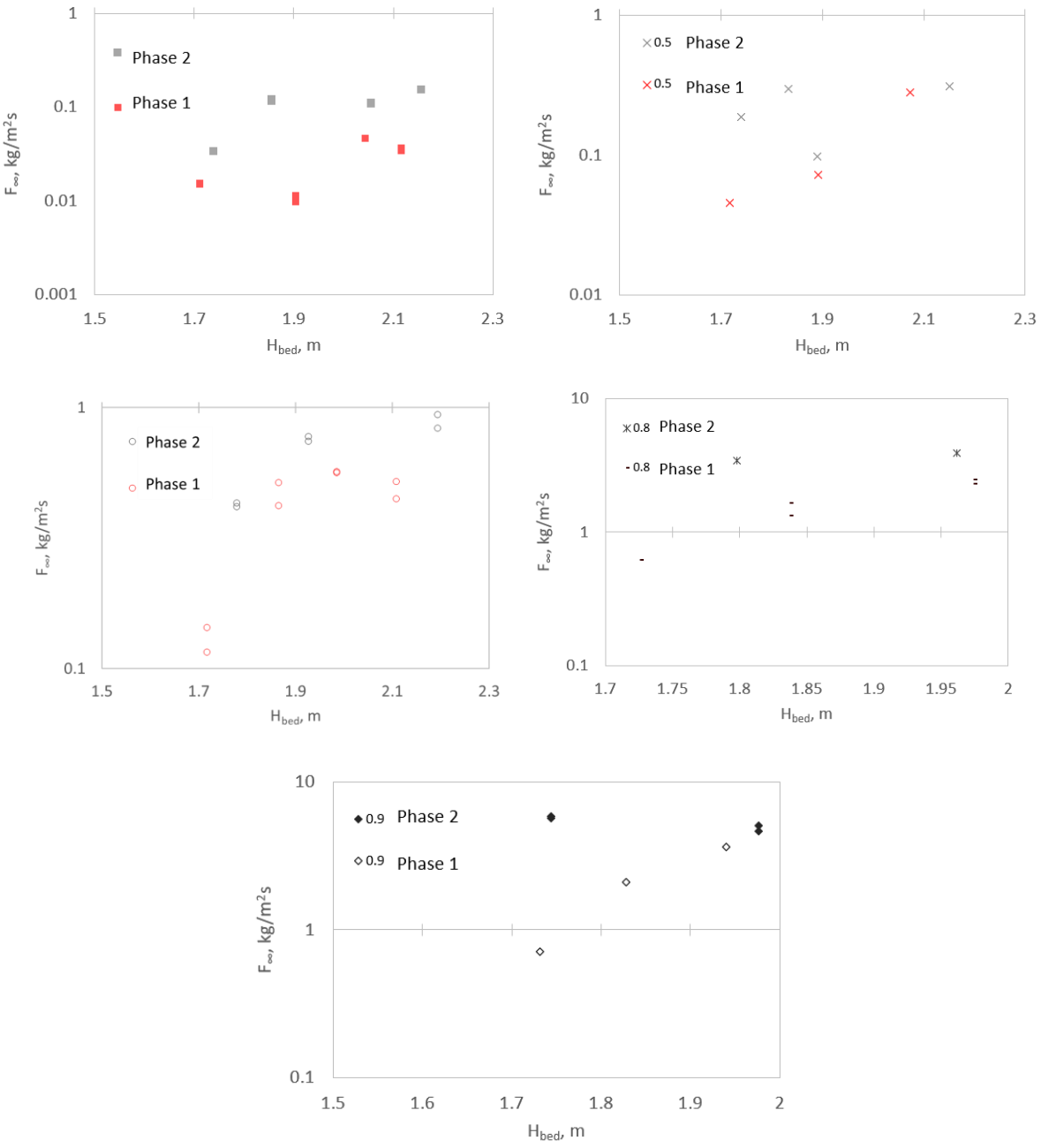

Figure J-1. Entrainment flux in free-board cross section at top of cyclone ad various superficial gas velocities after Phase 1 and Phase 2 of modifications.

Appendix K: Calculated Fraction of Clusters Ejected from the Bed in Cyclone Inlet

Original Design

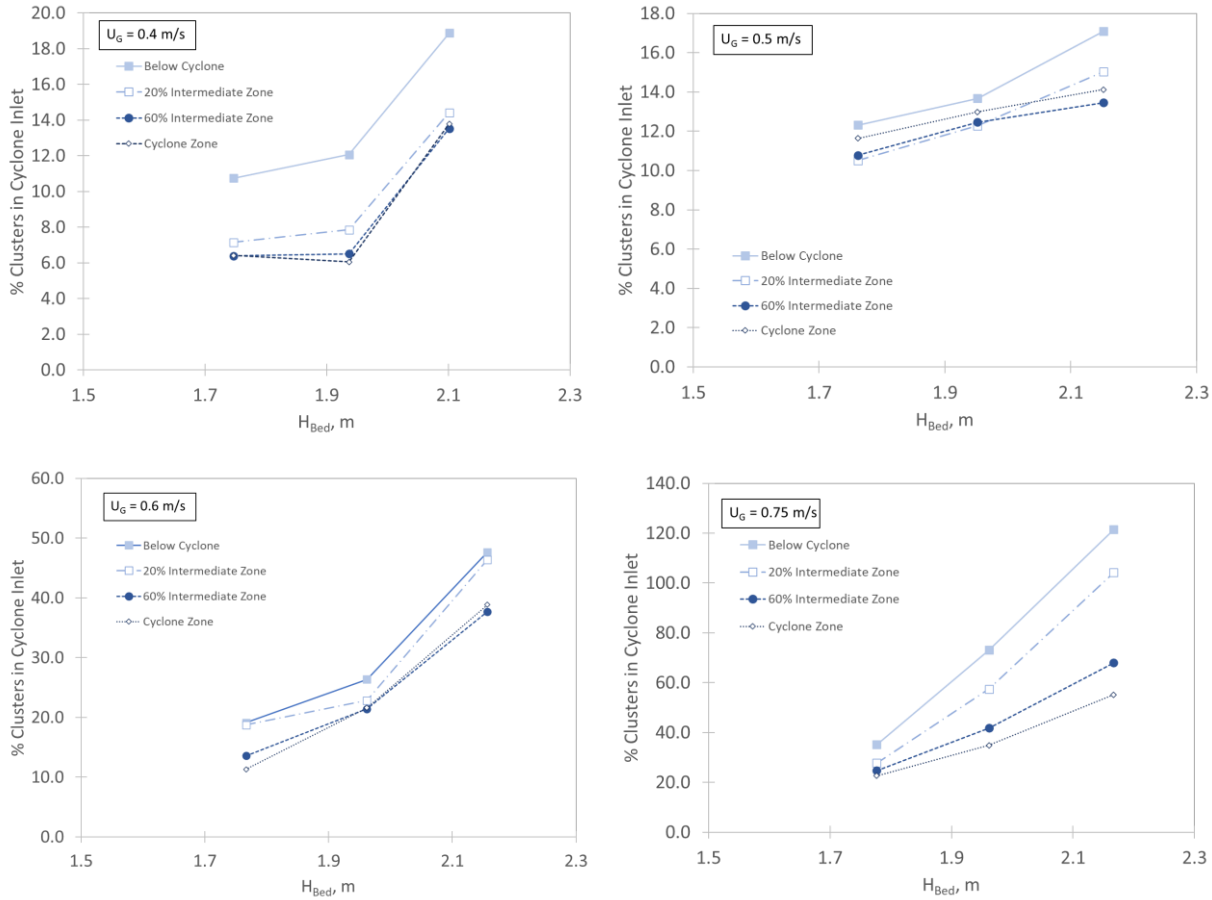

Figure K-1. Change in fraction of clusters ejected from the bed in cyclone inlet with bed height at various superficial gas velocities in original design.

After Phase 1 of Modifications

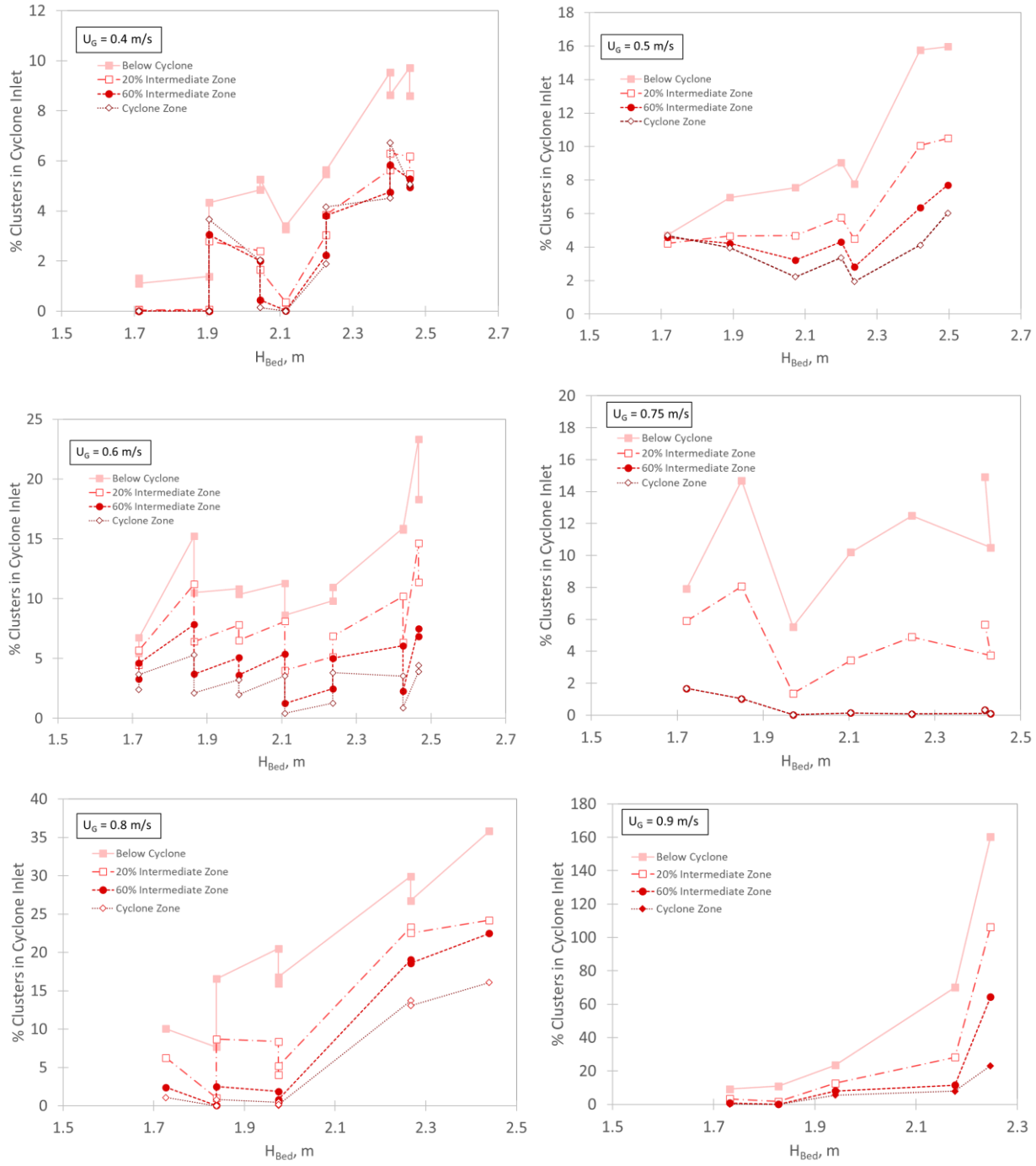

Figure K-2. Change in fraction of clusters ejected from the bed in cyclone inlet with bed height at various superficial gas velocities after Phase 1 modifications.

After Phase 2 of Modifications

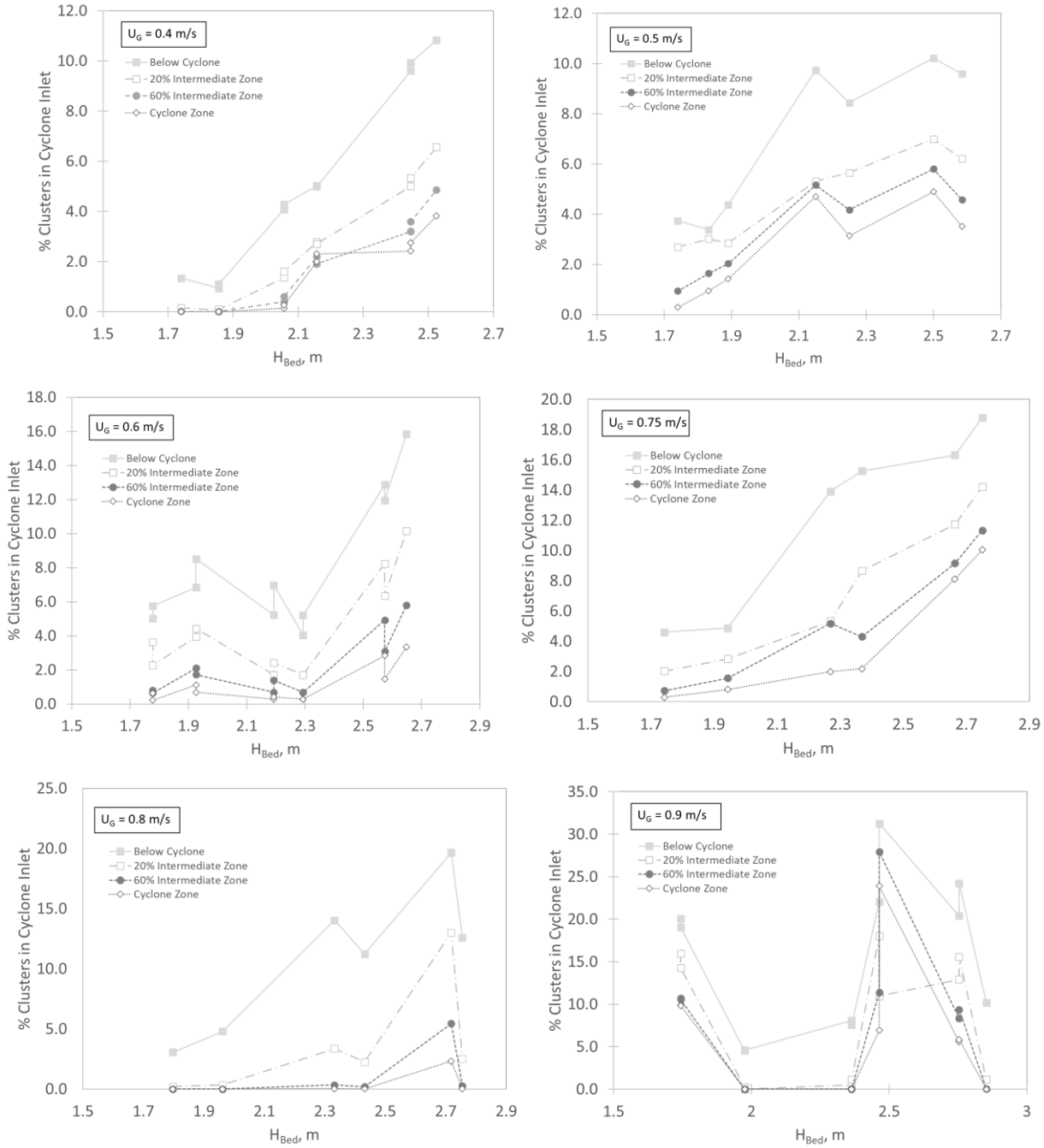

Figure K-3. Change in fraction of clusters ejected from the bed in cyclone inlet with bed height at various superficial gas velocities after Phase 2 modifications.

Curriculum Vitae

Name: Jessica Godin

Post-secondary Education and Degrees:

The University of Western Ontario
London, Ontario, Canada
2020 - 2022, M.E.Sc (Started as M.Eng in 2020, transferred in 2020)

The University of Western Ontario
London, Ontario, Canada
2011-2015 B.E.Sc

Related Work Experience

Teaching Assistant
The University of Western Ontario (Canada)
2021 (Part-Time)

Publications

Godin, J., Sanchez, F., Pjontek, D., Briens, C., & McMillan, J. (2022). Study of hydrodynamics and particle entrainment for a 0.6 m diameter fluidized bed of a large group A powder. *Powder Technology*. Under Review.

Godin, J., Sanchez, F., Pjontek, D., Briens, C., & McMillan, J. (2022). Study of solids flow in the dipleg of the primary cyclone of a 0.6 m diameter fluidized bed of a large group A powder. *Powder Technology*. Under Review.